

Analysis and Quality Assessment of GNSS-Derived Parameter Time Series

der Philosophisch-naturwissenschaftlichen Fakultät
der Universität Bern

vorgelegt von

Luca Ostini

von Sementina (TI, Schweiz)

Leiter der Arbeit:

PD. Dr. Rolf Dach
Astronomisches Institut der Universität Bern

Prof. Dr. G. Beutler
Astronomisches Institut der Universität Bern

Analysis and Quality Assessment of GNSS-Derived Parameter Time Series

der Philosophisch-naturwissenschaftlichen Fakultät
der Universität Bern

vorgelegt von

Luca Ostini

von Sementina (TI, Schweiz)

Leiter der Arbeit:

PD. Dr. Rolf Dach
Astronomisches Institut der Universität Bern

Prof. Dr. G. Beutler
Astronomisches Institut der Universität Bern

Von der Philosophisch-naturwissenschaftlichen Fakultät angenommen.

Der Dekan

Bern, den 27. Februar 2012

Prof. Dr. S. Decurtins

Contents

List of Tables	v
List of Figures	vii
List of Acronyms	xi
1 Introduction	1
1.1 Motivation	1
1.2 Objectives	4
1.3 Structure	5
2 Processing of GNSS Data	7
2.1 Scientific Organizations, Services, Missions, Standards and Products	7
2.2 Global Navigation Satellite Systems	9
2.2.1 Space Segments	9
2.2.2 The Control Segment	14
2.2.3 The User Segment	14
2.3 Basics of Processing	16
2.3.1 Observation Equations	16
2.3.2 Basic Observables	18
2.3.3 Estimation of Parameters	19
2.3.4 Normal Equations and Operation on Parameters	21
2.3.5 Constraints on Parameters	23
2.3.6 Satellite Orbits	24
2.4 Homogeneously Processed GNSS Data at CODE	26
2.4.1 Daily Solution	27
2.4.2 Multi-Day Solutions	29
2.5 Noise in Time Series of Parameters	29
3 A Procedure to Analyze Coordinate Time Series	31
3.1 The Functional Model	32
3.2 The A priori Known Elements	32
3.2.1 Equipment Changes	33
3.2.2 Earthquakes	33
3.2.3 Periodic Functions	34
3.2.4 Outliers from the Test of the Datum Definition	35
3.2.5 User-Defined List of Events	35

3.3	The Procedure	36
3.3.1	General Aspects	36
3.3.2	Controlling the Algorithm	37
3.3.3	The Algorithm	39
3.4	Searching for Discontinuities	41
3.4.1	Mathematical Principle	41
3.4.2	Validation with Synthetic Time Series	45
3.5	Search for Outliers	49
3.5.1	Mathematical Principle	50
3.5.2	Validation with Synthetic Time Series	50
3.6	Search for Velocity Changes	52
3.6.1	Mathematical Principle	52
3.6.2	Validation with Synthetic Time Series	53
3.7	Search for Periodic Functions	56
3.7.1	Mathematical Principle	56
3.7.2	Validation with Synthetic Time Series	56
3.8	More General Examples	60
3.8.1	Iterative Analysis of One-Dimensional Synthetic Time Series	60
3.8.2	Analysis of CODE Reprocessed Time Series	60
3.8.3	Search for all Elements in DCB time series	63
3.9	External Validation	67
4	Cleaning Coordinate Time Series	71
4.1	Station Coordinates and Linear Velocities	71
4.2	Coordinate Time Series	72
4.3	Quality Assessment of Coordinate Time Series	72
4.3.1	Discontinuities and Velocity Changes	73
4.3.2	Outliers	73
4.3.3	Update of Metadata for a Follow-Up Solution	74
4.4	Examples	74
4.4.1	Analysis of Coordinate Time Series	75
4.4.2	Cumulative Solution	83
4.4.3	Cleaned Coordinate Time Series	86
5	Impact of Quality Assessment on Parameter Time Series	93
5.1	Geocenter	93
5.1.1	Impact of Quality Assessment	93
5.1.2	Spectral Analysis	97
5.2	Scale Parameter	99
5.2.1	Impact of Quality Assessment	99
5.2.2	Spectral Analysis	101
5.3	Coordinates	102
5.3.1	Impact of Quality Assessment on Seasonal Variations	102
5.3.2	Global Correlation	104
5.3.3	Spectral Analysis	105

5.4 Earth Rotation Parameters	110
6 Evolution of Mean Orbital Elements	115
6.1 Mean Orbital Elements	115
6.2 Evolution of Mean Elements of GPS Satellites	117
6.2.1 Analysis of the Mean Semi-Major Axes	119
6.2.2 Analysis of the Mean Eccentricity	127
6.2.3 Analysis of the Mean Ascending Node and Inclination	129
6.3 Evolution of Mean Elements of GLONASS Satellites	132
6.3.1 Analysis of the Mean Semi-Major Axes	134
6.3.2 Analysis of the Mean Eccentricity	135
6.3.3 Analysis of the Mean Ascending Node and Inclination	136
7 Summary and Outlook	139
A GPS and GLONASS Satellites	143
B The Tool for the Spectral Analysis	147
Bibliography	151

List of Tables

2.1	IGS final products including GPS broadcast values.	8
2.2	Space segments of GPS, GLONASS, Galileo, and COMPASS.	10
2.3	Intervals with Anti-Spoofing for GPS satellites.	12
2.4	Parameters at the normal equation level to derive CODE final products. . .	26
2.5	Summary of adopted models to derive CODE final products.	28
3.1	Validation of the search for discontinuities. Synthetic time series in one component with one discontinuity.	47
3.2	Validation of the search for discontinuities. Synthetic time series in one component with three discontinuities.	48
3.3	Validation of the search for discontinuities. Synthetic time series in three components with three discontinuities.	48
3.4	Validation of the search for outliers.	52
3.5	Validation of the search for velocity changes.	55
3.6	Validation of the search for periodic functions.	58
3.7	Validation of searches for discontinuities, velocity changes, outliers, and periodic functions.	58
3.8	Time series analysis of daily coordinates of station MAC1.	62
4.1	ADDNEQ2 parameter options for the daily and weekly solutions.	75
4.2	Analysis of CODE daily coordinate time series.	76
4.3	Analysis of CODE weekly coordinate time series.	77
4.4	Equipment changes at station MAD2.	81
4.5	Quality assessment of daily coordinates. Summary of the update step. . . .	83
4.6	Quality assessment of weekly coordinates. Summary of the update step. . .	83
4.7	A posteriori RMS error before and after quality assessment of daily and weekly coordinate time series.	84
4.8	External validation. Discontinuities in the weekly FODITS analysis and in the ITRF2008/IGS realization.	86
4.9	Internal validation of CODE daily coordinate time series.	87
4.10	Internal validation of CODE weekly coordinate time series.	88
5.1	Offsets and drifts of Helmert translation parameters for the interval 1994-2008. .	95
5.2	Offsets and drifts of Helmert translation parameters for the interval 2000-2008. .	95
5.3	Amplitudes of spectral lines in the time series of daily and weekly geocenter motions.	98
5.4	Offsets and drifts of Helmert scale parameters for the interval 1994-2008. . .	99
5.5	Offsets and drifts of Helmert scale parameters for the interval 2000-2008. . .	100

5.6	Amplitudes of spectral lines in the time series of daily and weekly scale parameters.	101
5.7	Determination of the colored noise in daily and weekly coordinate time series.	107
5.8	Amplitudes of spectral lines of daily and weekly stacked amplitude spectra.	108
5.9	RMS of the pole time series w.r.t. to Bulletin A before and after quality assessment.	113
5.10	Pole formal error time series before and after quality assessment.	113
6.1	Validation of the algorithm FODITS to identify repositioning events of GPS satellites.	123
6.2	Results of FODITS detections of repositioning events.	125
6.3	Osculating elements adopted for the simulations.	132
A.1	GPS satellites in the interval from 1994 to 2008.	143
A.2	GLONASS satellites in the interval from 2003 to 2008.	144

List of Figures

2.1	Space segment: artistic designs of GPS, GLONASS, and Galileo satellites.	11
2.2	Examples of monuments and antennas of permanent stations.	15
2.3	Orbital elements a of satellite orbiting the Earth.	25
2.4	The reprocessing procedure at CODE to provide final products.	26
3.1	Selection functions for earthquakes.	34
3.2	The algorithm of FODITS.	39
3.3	Search for discontinuities with space VCI and in simplified form.	44
3.4	Search for discontinuities without and with time re-sampling.	44
3.5	Validation of search for discontinuities with synthetic time series. Discontinuity of +15 mm introduced on 01-Jan-2005.	45
3.6	Validation of search for discontinuities with synthetic time series. Discontinuity of +15 mm introduced on 01-Jan-2002.	46
3.7	Validation of search for discontinuities with synthetic time series. Discontinuity of +15 mm introduced on 01-Jan-2005. Data gap of 3 years.	46
3.8	Validation of search for discontinuities in one-dimensional synthetic time series with three discontinuities.	47
3.9	Validation of search for discontinuities in three-dimensional synthetic time series with three discontinuities.	49
3.10	Validation of the search for outliers with synthetic time series. Standard deviation of observations not considered.	51
3.11	Validation of the search for outliers with synthetic time series. Standard deviation of observations considered.	51
3.12	Validation of the search for velocity changes in one-dimensional synthetic time series with one velocity change.	54
3.13	Validation of the search for velocity changes in one-dimensional synthetic time series with two velocity changes.	54
3.14	Validation of the search for periodic functions in one-dimensional synthetic time series with three signals.	57
3.15	Validation of the search for periodic functions in one-dimensional synthetic time series with three signals and four different noise sizes.	57
3.16	Validation of all searches simultaneously in one-dimensional synthetic time series.	59
3.17	Iteration steps in the analysis of daily coordinate time series of station MAC1.	61
3.18	Validation search for discontinuities. DCB P1-C1 SVN 41 time series analyzed with different levels of significance.	64

3.19	Validation search for outliers. DCB P1-C1 SVN 41 time series analyzed with different levels of significance for outliers.	64
3.20	Validation search for velocity changes. DCB P1-C1 SVN 41 time series analyzed with different levels of significance.	65
3.21	Validation search for periodic functions. DCB P1-C1 SVN 41 time series analyzed with different levels of significance.	66
3.22	Validation of all searches simultaneously. DCB P1-C1 SVN 41 time series analyzed with four different levels of significance.	67
3.23	FODITS analysis of time series of the DOGEx.	68
3.24	Results of the DOGEx.	69
4.1	Quality assessment of coordinate time series in the BSW.	73
4.2	Typical scenario of sub-intervals and relative velocity constraints for a reference site.	74
4.3	Number of stations in daily and weekly solutions resulting from the test of the datum definition for the interval 1994-2008.	78
4.4	Analysis of daily and weekly coordinates—part 1.	79
4.5	Analysis of daily and weekly coordinates—part 2.	80
4.6	Analysis of daily coordinates for stations REYK and MAC1.	82
4.7	Velocity field at epoch 01-Jan-2000 for daily and weekly solutions.	85
4.8	Station CCJM, daily and weekly coordinate time series before and after quality assessment.	89
4.9	Station HOFN, daily and weekly coordinate time series before and after quality assessment.	90
4.10	Histograms of daily and weekly coordinate time series.	91
5.1	Daily and weekly Helmert translation parameter time series for the interval 1994-2008.	94
5.2	Daily and weekly Helmert translation parameter time series for the interval 2000-2008.	96
5.3	Spectral analysis of daily and weekly series of the geocenter motion.	97
5.4	Daily and weekly Helmert scale parameter time series for the interval 1994-2008.	100
5.5	Daily and weekly Helmert scale parameter time series for the interval 2000-2008.	101
5.6	Spectral analysis of daily and weekly series of the scale parameter.	102
5.7	Impact of the quality assessment on the amplitude and phase of the annual signals found in the vertical component of daily and weekly coordinate time series.	103
5.8	Impact of the quality assessment on the amplitude and phase of the semi-annual signals found in the vertical component of daily and weekly coordinate time series.	104
5.9	Evolution of the scale and the mean Up coordinates of daily series.	105
5.10	Stacked power spectra of daily and weekly residual coordinate time series.	109

5.11 Daily series of X and Y pole estimates w.r.t. Bulletin A before and after quality assessment, 1994-2008.	111
5.12 Daily series of X and Y pole estimates w.r.t. Bulletin A before and after quality assessment, 2000-2008.	112
6.1 Osculating and mean semi-major axes of GPS SVN 39.	117
6.2 Evolution of the mean elements of GPS SVN 32.	118
6.3 Validation of the algorithm FODITS to identify repositioning events of GPS satellites.	119
6.4 Repositioning events of GPS satellites between 1994 and 2008.	120
6.5 FODITS analyses of the semi-major axis evolution of GPS satellites.	121
6.6 Instantaneous pulses associated with the repositioning events of GPS satellites in the interval 1994-2008.	122
6.7 Results of the FODITS detection of GPS maneuvers in the evolution of the mean semi-major axis.	126
6.8 Evolution of the mean eccentricity of GPS satellites.	127
6.9 Mean numerical eccentricity evolution of GPS satellites between 1994 and 2008.	129
6.10 Mean numerical eccentricity evolution of GPS satellites between 1994 and 2008.	129
6.11 Analysis of the mean right ascension of the ascending node of GPS satellites.	130
6.12 Evolution of the inclination of GPS satellites.	131
6.13 Inclination versus right ascension of ascending node of GPS satellites.	132
6.14 Evolution of mean elements of the GLONASS SVN 791.	133
6.15 FODITS analyses of the semi-major axis evolution of GLONASS satellites.	134
6.16 Evolution of the mean eccentricity of GLONASS satellites.	136
6.17 Mean numerical eccentricity evolution of GLONASS satellites between 1994 and 2008.	137
6.18 Analysis of the mean right ascension of the ascending node of GLONASS satellites.	137
7.1 Search test for discontinuities in the North component of Ponta Delgada, Portugal.	140
B.1 Validation of the FFT approach with zero padding with a least squares approach.	148

List of Acronyms

AC	Analysis Center
ACC	Analysis Center Coordinator
ADDNEQ2	ADD Normal EQUations 2
AGNES	Automated GPS NETwork of Switzerland
AIUB	Astronomical Institute of the University of Bern
ANTEX	ANTenna format EXchange
APL	Atmospheric Pressure Loading
ARP	Antenna Reference Point
AS	Anti-Spoofing
BSW	Bernese Software
CDMA	Code Division Multiple Access
CF	Center of Figure
CM	Center of Mass
CN	Center of Network
CODE	Center for Orbit Determination in Europe
COSPAR	Committee On SPACe Research
DCB	Differential Code Bias
DFT	Discrete Fourier Transform
DIA	Detection Identification Adaptation
DOGEx	Detection of Offsets in GPS Experiment
DORIS	Doppler Orbitography and Radiopositioning Integrated by Satellite
DSSS	Direct-Sequence Spread Spectrum
DYX	Reference system: (D) towards the Sun, (Y) axis of solar panels, (X) completes the tern
EOP	Earth Orientation Parameter
ERP	Earth Rotation Parameter
EUREF	IAG Reference Frame Sub-Commission for Europe
EVL	EVents List
FDMA	Frequency Division Multiple Access
FFT	Fast Fourier Transform
FOC	Full Operational Capability

FODITS	Find Outliers and Discontinuities in Time Series
GEOSS	Global Earth Observation System of Systems
GGOS	Global Geodetic Observing System
GIA	Glacial Isostatic Adjustment
GIM	Global Ionosphere Map
GIOVE	Galileo In Orbit Validation Element
GLONASS	GLObalnaya NAVigatsionnaya Sputnikovaya Sistema
GLR	Generalized Likelihood Ratio
GMF	Global Mapping Function
GMM	Gauss-Markoff Model
GNSS	Global Navigation Satellite System
GPS	Global Positioning System
GPT	Global Pressure and Temperature
GTR	Ground Track Repetition
GTRF	Galileo Terrestrial Reference Frame
IAG	International Association of Geodesy
IAU	International Astronomical Union
ICRF	International Celestial Reference Frame
ICRS	International Celestial Reference System
ICSU	International Council of Science
IDS	International DORIS Service
IERS	International Earth rotation and Reference systems Service
IGS	International GNSS Service
IGS-CB	IGS Central Bureau
ILRS	International Laser Ranging Service
IONEX	IONosphere map EXchange
ITRF	International Terrestrial Reference Frame
ITRS	International Terrestrial Reference System
IUGG	International Union of Geodesy and Geophysics
IVS	International VLBI Service for geodesy and astrometry
JPL	Jet Propulsion Laboratory
LC	Linear Combination
LEO	Low Earth Orbit
LLR	Lunar Laser Ranging
LOD	(Excess of) Length Of Day
LSE	Least Squares Estimation
MEO	Medium Earth Orbit
MLE	Maximum Likelihood Estimation
NANU	Notice Advisory to NAVSTAR User

NASA	National Aeronautics and Space Administration
NAVSTAR	NAVigation Signal Timing And Ranging
NEQ	Normal EQUation
NEU	North, East, and Up
NNR	No-Net-Rotation
NNT	No-Net-Translation
ORBGEN	ORBbit GENeration
PCO	Phase Center Offset
PCV	Phase Center Variation
PM	Polar Motion
PRN	Pseudo-Random Noise
PZ-90	Parametry Zemli 1990—Earth Parameters 1990
QIF	Quasi-Ionosphere-Free
RHCP	Right Hand Circular Polarization
RINEX	Receiver INdependent EXchange
RMS	Root Mean Squares
RSW	Reference system: (R) radial, (S) along-track, (W) out-of-plane
RTPP	Real-Time Pilot Project
SA	Selective Availability
SINEX	Solution INdependent EXchange
SLR	Satellite Laser Ranging
SVN	Space Vehicle Number
TEC	Total Electron Content
TECU	Total Electron Content Unit
TRF	Terrestrial Reference Frame
TRS	Terrestrial Reference System
UT	Universal Time
UTC	Coordinated Universal Time
VCI	Variance-Covariance Information
VLBI	Very Long Baseline Interferometry
WCRP	World Climate Research Program
WGS-84	World Geodetic System 1984
XYZ	X, Y, and Z
ZPD	Zenith Path Delay

1 Introduction

1.1 Motivation

Today, space geodetic techniques such as **Very Long Baseline Interferometry (VLBI)**, **Satellite Laser Ranging (SLR)**, **Global Navigation Satellite System (GNSS)**, and **Doppler Orbitography and Radiopositioning Integrated by Satellite (DORIS)** are the primary instruments to study size, figure, and deformation of the Earth, and to maintain the *celestial* and the *terrestrial* reference frames (e.g., [Beutler, 2004](#)).

The space geodetic technique **GNSS**, currently tracking signals from the constellations of the American **Global Positioning System (GPS)**, the Russian **GLObalnaya NAVigatsionnaya Sputnikovaya Sistema (GLONASS)**, and test satellites of the European Galileo, is a relatively affordable and flexible technique that allows to survey the Earth on both, global and regional scales ([Segall and Davis, 1997](#)).

Scientific activities related to the **GNSS** technique are supported by the **International GNSS Service (IGS)**¹ of the **International Association of Geodesy (IAG)**². Since January 1, 1994, the **IGS** provides combined operational products of high accuracy such as satellite orbits, **Earth Rotation Parameters (ERPs)**, tropospheric products, and geocentric coordinates of tracking stations to the scientific community. The product combination is performed by the **Analysis Center Coordinator (ACC)**. Contributions for the combination are provided by about ten **Analysis Centers (ACs)** which process **GNSS** observations tracked by permanent stations of the global **IGS** network on a regular basis. The **IGS** global network counts today nearly 400 tracking stations, all maintained worldwide by institutions on a non-commercial basis. A part from freely providing high accuracy combined products, the **IGS** also collects, distributes, and makes freely available **GNSS** observations of all tracking stations of the **IGS** network in near real-time.

The **International Terrestrial Reference Frame (ITRF)**, which constitutes the backbone of all global and regional networks, is derived from a combination of long series of weekly combined solutions from the space-geodetic services **International VLBI Service for geodesy and astrometry (IVS)** ([Schlüter and Behrend, 2007](#)) of the **VLBI** technique, **International Laser Ranging Service (ILRS)** ([Pearlman et al., 2002](#)) of the techniques **SLR** and **Lunar Laser Ranging (LLR)**, **IGS** ([Dow et al., 2009](#)) of the **GNSS** technique, and **International DORIS Service (IDS)** ([Willis et al., 2010](#)) of the **DORIS** technique. About every two years the **International Earth rotation and Reference systems Service (IERS)**³, another service

¹<http://www.igs.org>

²<http://www.iag-aig.org>

³<http://www.iers.org/>

of the **IAG** and of the **International Astronomical Union (IAU)**, issues a new **ITRF** by combining series of **Solution INdependent EXchange (SINEX)** (Dick and Richter, 2008) files containing station coordinate parameters and **Earth Orientation Parameters (EOPs)** (Altamimi et al., 2011). In order to obtain a consistent **ITRF** solution the **IERS** requires **ACs** of all involved space geodetic techniques to adopt the **IERS Conventions** (McCarthy and Petit, 2003; Petit and Luzum, 2010)—physical constants and accepted standards to process geodetic data. **ITRF** realizations, also issued in **SINEX** file format, provide coordinates and linear motions of all stations which contributed to the combination at the reference epoch of the realization. In this context station solutions are given within a validity interval and new **ITRF** realizations contain updated validity intervals by considering the history of known discontinuities in the series.

The **Center for Orbit Determination in Europe (CODE)**, a joint venture of the **Astronomical Institute of the University of Bern (AIUB)**, in Bern, Switzerland, the Swiss Federal Office of Topography (swisstopo), in Wabern, Switzerland, the Bundesamt für Kartographie und Geodäsie (BKG), in Frankfurt am Main, Germany, and the Institut für Astronomische und Physikalische Geodäsie at Technischen Universität München (IAPG, TUM), in Munich, Germany, is one **AC** of the **IGS**. **CODE** also contributes as a Local **AC** to the **IAG Reference Frame Sub-Commission for Europe (EUREF)**⁴ and as an associated **AC** to the **ILRS** activities. Operational products provided by **CODE** are processed by the **Bernese Software (BSW)** (Dach et al., 2007), a software developed at the **AIUB**, where **CODE** is located, as well.

Long time series of operational products usually have not been homogeneously processed. For instance, **ACs** update models and/or change their processing strategies from time to time in order to improve the quality of their products. In addition, **ACs** regularly adopt new realizations of the **ITRF**. Such changes may induce discontinuities in the series of operational products (e.g., Steigenberger, 2009). The discontinuity of up to 20 mm at GPS-week 1400 in the vertical component in nearly all coordinate time series processed at **CODE** (e.g., Ostini et al., 2008a) is a prominent example. Such large discontinuities were mainly caused by switching from relative to absolute antenna calibration models in conjunction with the use of the IGS05 reference frame (Gendt, 2006; Hugentobler, 2006), a more consistent **IGS** reference frame derived from the ITRF2005 (Altamimi et al., 2007).

Recently, in the context of the 1st **IGS** reprocessing campaign, some **ACs** of the **IGS** reprocessed **Receiver INdependent EXchange (RINEX)** (Gurtner, 1994) data from 1994 onwards with the latest models and strategies, providing homogeneously processed products. **CODE** carried out its reprocessing providing reprocessed data spanning from 1994 to 2008 (Steigenberger et al., 2009a). Reprocessed contributions from **ACs** were subsequently combined and made available to the user community as a new **IGS** product. Combined weekly **SINEX** files were furthermore provided to the Product Center of the **IERS** as **IGS** contribution to the latest **ITRF** realization, the ITRF2008 (Altamimi et al., 2011). The **IGS** intends to repeat reprocessing campaigns in the future, possibly at regular basis, because long series of **IGS** reprocessed products are important datasets for the scientific community.

Accumulated solutions are obtained by stacking series of normal equations, in best case

⁴<http://www.euref.eu>

homogeneously processed ones. In this context, coordinate parameters, which represent the points attached to the solid surface of the Earth, must be stacked in order to consider the action of the continuous drift of tectonic plates. For this reason, coordinates in multi-year solutions are typically modelled by means of a linearized model, i.e., by station positions and linear station velocities. If discontinuities and outliers contaminate the underlying coordinate time series, multi-year solutions with coordinates will obviously become inaccurate.

Discontinuities, also known as offsets, occur in almost all long coordinate time series derived from GNSS data (Williams, 2003), even in the reprocessed ones (Steigenberger, 2009). Many discontinuities are caused by model updates and changes of processing strategies, but there may be other sources, as well. Earthquakes, for example, may cause discontinuities and velocity changes in the series of stations near the epicenter. Other discontinuities, mainly present in coordinate time series of single stations, are known to be associated with equipment changes (e.g., due to the replacement of antennas and/or tracking receivers, change of the radome on the antenna, firmware updates, etc.). Discontinuities may also be due to a not logged (i.e., unknown) reason (e.g., malfunctioning equipments, vandalism, human errors, construction of new monuments around the antenna, falling of accumulated snow from the antenna, etc.).

Outliers contaminate most coordinate time series. Often, they are due to systematic errors, e.g., due to adverse atmospheric conditions, anthropogenic impact, short instrumental malfunctioning, etc. From a point of view of statistics the detection of outliers depends on the assumptions made, i.e., on the null and alternative hypothesis, the particular statistical test, and the significance level adopted for the analysis of the dataset (Barnett and Lewis, 1994).

Reprocessing campaigns aim to provide high accuracy series of products. One of the key tasks to obtain high accuracy multi-year solutions is to assess the underlying coordinate time series. Such a key task related to reprocessing campaigns mainly consists of two steps. First, coordinate time series are analyzed, i.e., events such as discontinuities and outliers are identified. Second, the collected analysis information is taken into account to model the coordinate time series in the solution.

High accuracy multi-year solutions, i.e., solutions where the underlying coordinate time series are assessed, are used to study geodetic and geophysical models. Terrestrial Reference Frame (TRF) realizations (e.g., Rülke et al., 2008; Altamimi et al., 2011) are a prominent example where series of normal equations containing coordinates and ERPs are cumulated to estimate sets of station coordinates and linear velocities. Calibration parameters of satellite antennas to obtain high accuracy GNSS parameter estimates, to mention another example, emerge as a multi-year solution by stacking normal equations with coordinate- and antenna-related parameters (e.g., Schmid et al., 2007; Dach et al., 2010). The contribution of GNSS network solutions to model the Glacial Isostatic Adjustment (GIA) process—the gravitational adjustment of Earth’s mantle and lithosphere resulting from deglaciation following the Last Glacial Maximum—is of paramount importance to accurately constrain sea-level rise predictions (e.g., Wöppelmann et al., 2007, 2009; Collilieux and Wöppelmann, 2010). It is recognized that the uncertainty of station velocities have a large impact on the

predicted results (Nerem et al., 2000). Up to now, many analysis confirmed that time series of coordinates are correlated in time, e.g., contain discontinuities, periodic signals, and non-Gaussian noise such as flicker noise or random-walk (Langbein and Johnson, 1997; Williams, 2003; Ray et al., 2008; King and Williams, 2009). In all cases the assumption of unbiased time series of coordinates leads to estimate site velocities with optimistic uncertainties (Williams, 2008). The analysis and the quality assessment of coordinate time series are therefore key processing steps in the context of reprocessing campaigns. These two steps will allow it to obtain more reliable geodetic and geophysical results.

1.2 Objectives

ACs of global and regional geodetic GNSS networks have organized reprocessing campaigns to homogeneously process raw data with the latest models and strategies. The quality assessment of long series of station coordinates is a key task to obtain high accuracy network solutions and series of station coordinates free of inconsistencies such as discontinuities and outliers. Due to the increasing number of geodetic networks of tracking stations constituting these networks, but also due to the need of routinely reprocess raw data, an automated tool to analyze long coordinate time series is required to replace the long, inaccurate, subjective and time consuming manual analysis of time series.

For automated analysis of coordinate time series Salzmann (1993) and Teunissen and Kleusberg (1998b) propose the Detection Identification Adaptation (DIA) procedure to remove errors in time series for both, batch and recursive solutions. For batch solutions, Perfetti (2006) used the DIA procedure to analyze the Italian GPS fiducial network, while Kleijer (2002) employed the same method to analyze the geodetic network in the Netherlands. A procedure based on the Maximum Likelihood Estimation (MLE) which considers stochastic noise models such as flicker noise or random-walk is proposed by (Williams, 2008). De Lacy et al. (2008) propose an algorithm based on the Bayesian detection using a polynomial regression to detect and correct cycle slips in GNSS preprocessing phase.

Our work primarily aims at realizing a tool to analyze and clean coordinate time series in an automated way. More precisely, the tool shall check the significance of lists of predefined events such as lists of equipment changes and of registered earthquakes worldwide, identify discontinuities and outliers in the time series, and create metadata to obtain high accuracy multi-year solutions and long cleaned coordinate time series. As an additional support to the analysis of coordinate time series, but also, more generally, of any other time series, the tool shall be able to identify discontinuities in changes in rates—usually called velocity changes—and in periodic functions.

Our algorithm to analyze the time series is embedded in the BSW program Find Outliers and Discontinuities in Time Series (FODITS) (Ostini et al., 2008a). An introductory description before developing FODITS is given in (Ostini, 2007). The algorithm underlying the program FODITS, the principles of which are the same as those of DIA, tries to optimally represent the time series by a functional model with discontinuity, velocity change, outlier, and periodic function elements. The algorithm advances step-by-step and adapts at

each step the element which removes the largest discrepancy between the functional model and the time series. Elements are either proposed from a priori known lists of events such as the lists of equipment changes and of registered earthquakes worldwide, or identified in the time series by the algorithm. Preliminary versions of the algorithm implemented in **FODITS** are contained in (Ostini et al., 2010a,b), while the latest version is described here.

This work is performed in the context of the **CODE** activities at **AIUB**. Multi-year solutions as well as coordinate time series are obtained by the **BSW** program **ADD Normal Equations 2 (ADDNEQ2)** (Dach et al., 2007). The tool to analyze and clean the time series shall become a new component of the **BSW**, as well.

Un-modelled and mis-modelled signals in **GNSS** data may be discovered by investigating time series of parameters in both, time domain and spectral domain. Our tool for coordinate time series is used as well to analyze time series of other **GNSS** parameters emerging from reprocessing campaigns processed at **CODE**.

1.3 Structure

- Chapter 2: *Processing of GNSS Data*. Missions, scientific organizations, services, notions on processing **GNSS** data, and other fundamental aspects related to this work are described. The time series analyzed in this work emerged from **CODE** reprocessing efforts. Models and strategies underlying such homogeneously processed **GNSS** data are also summarized.
- Chapter 3: *A Procedure to Analyze Coordinate Time Series*. Theory, internal and external validation procedures, and a few applications of the procedure are presented.
- Chapter 4: *Cleaning Coordinate Time Series*. Theory and strategy of the quality assessment of coordinate time series are introduced. The strategy is successively used to clean homogeneously reprocessed coordinate time series at **CODE**. Examples and results are summarized.
- Chapter 5: *Impact of the Quality Assessment on Parameter Time Series*. The impact is assessed on the geocenter, global scale, coordinate, and pole parameter time series. These parameter time series are furthermore studied in spectral domain.
- Chapter 6: *Evolution of Mean Elements of GNSS Satellites*. The mean orbital elements of **GPS** and **GLONASS** satellites emerging from reprocessing efforts at **CODE** are analyzed.

2 Processing of GNSS Data

This chapter introduces the fundamental notions for processing GNSS data used in subsequent chapters. Section 2.1 describes structures and missions of geodetic organizations and services, Sect. 2.2 introduces signals, space, and user segments of GNSS, Sect. 2.3 presents the basic aspects for processing GNSS data, and Sect. 2.4 lists the underlying models and summarizes the processing steps required to obtain long series of homogeneously processed data at CODE.

2.1 Scientific Organizations, Services, Missions, Standards and Products

Today, the IAG, one of the associations of the International Union of Geodesy and Geophysics (IUGG)¹, coordinates international services with the mission of defining standards, collecting and redistributing raw data, and providing intra- and inter-technique geodetic products in support of the geophysical and geodetic communities (Beutler, 2004; Beutler et al., 2004).

The IERS² is responsible for realizing, maintaining, and promoting both, the International Celestial Reference System (ICRS) and the International Terrestrial Reference System (ITRS) (Drewes, 2008; Altamimi et al., 2011). Transformation parameters between the ICRS and the ITRS realizations, the so-called EOPs, are generated, as well. The definition of origin and orientation of the ICRS and origin, orientation, and scale of the ITRS are based on IAU³ and IUGG resolutions. The latest International Celestial Reference Frame (ICRF), which is a ICRS realization, is based on VLBI microwave observations of extragalactic radio sources. On the other hand, ITRFs, the ITRS realizations, are a combination result from the inputs provided by the *space geodetic* services IVS, ILRS, IGS, IDS (see Chapter 1). All services are coordinated by the IAG. As the ITRF is the backbone of the global and of many regional networks, its accuracy has an impact on scientific studies such as Earth rotation monitoring, plate tectonics, sea level changes, etc. Therefore, in order to obtain the highest quality for the combination, the IERS recommends all involved ACs of all participating space geodetic techniques to adopt the IERS Conventions (McCarthy and Petit, 2003; Petit and Luzum, 2010)—containing physical constants and the latest accepted models to process geodetic data.

The IGS provides as a support to the geodetic community the highest quality of data

¹<http://www.iugg.org>

²<http://www.iers.org>

³<http://www.iau.org>

Table 2.1: IGS final products including GPS broadcast values. Source: <http://www.igs.org>.

product	line	system	accuracy	latency	sampling
satellite orbits	broadcast	GPS	~ 100 cm	real-time	daily
satellite clocks	broadcast	GPS	~ 5 ns	real-time	daily
satellite orbits	final	GPS	~ 2.5 cm	12-18 days	15 min
satellite clocks	final	GPS	~ 75 ps	12-18 days	30 sec
satellite orbits	final	GLONASS	~ 2.5 cm	12-18 days	15 min
ERP PM	final		30 μ as	11-17 days	daily
ERP PM rate	final		150 μ as/day	11-17 days	daily
ERP LOD	final		10 μ s	11-17 days	daily
Tropospheric ZPD	final		4 mm	< 4 weeks	2 hours
Ionospheric TEC map	final		2-8 TECU	~ 11 days	2 hours
station positions	final	horizontal	3 mm	11-17 days	weekly
station positions	final	vertical	6 mm	11-17 days	weekly
station velocities	final	horizontal	2 mm/yr	11-17 days	weekly
station velocities	final	vertical	3 mm/yr	11-17 days	weekly

products derived from microwave-based GNSSs such as the American GPS and the Russian GLONASS. Combined products provided by the IGS are: satellite orbits and clock corrections every 15 min in SP3-c file format (Hilla, 2002) together with consistent daily ERPs in IGS file format, additional clock corrections every 5 min and 30 sec in the RINEX file format, weekly station coordinates and velocities (with accuracies of a few millimeters and millimeters/year, respectively) and station-specific tropospheric Zenith Path Delay (ZPD) every 2 hours in SINEX file format (Dick and Richter, 2008), global ionospheric maps every 2 hours with monthly P1-P2 Differential Code Biass (DCBs) in the IONosphere map EXchange (IONEX) file format (Schaer et al., 1998), antenna calibrations in ANTenna format EXchange (ANTEX) file format (Rothacher and Schmid, 2002, 2006), and the IGS reference frame derived from the latest ITRF and consistent with the antenna calibrations. The IGS provides also GNSS observations of the IGS tracking stations with a 30 sec sampling interval as RINEX data. A guide to use IGS products and data including standards and recommendations is provided by (Kouba, 2009).

Currently, the IGS offers the following official product lines: the IGS final (weekly updated with a latency of about 13 days), the IGS rapid (daily updated with a latency of about 17 hours), and the IGS ultra (updated four times a day with a latency of about 3 hours). Table 2.1 summarizes the final products provided by the IGS.

IGS ultra rapid products are divided into *observed* and *predicted* data, where both parts cover an interval of 24 hours. The predicted IGS ultra products may be used for high accuracy real-time navigation and they provide the basis for realizing combined real-time IGS products, see the IGS Real-Time Pilot Project (RTPP)⁴. The ACC performs the combination of IGS products using the contributions of the ACs. In this way, AC contributions may be compared and cross-validated in terms of softwares, models, and processing strategies. The combination allows it to the ACC to identify and reject bad AC solutions. The users benefit from the combination of products by obtaining and using redundant and validated

⁴<http://www.rtigs.net>

products.

Recently, in conjunction with its last important structural reform, the IAG created the **Global Geodetic Observing System (GGOS)**⁵ (Plag and Pearlman, 2009). GGOS acts as the interface between all existing IAG services and all external partners such as the **International Council of Science (ICSU)**, the **World Climate Research Program (WCRP)**, and the **Global Earth Observation System of Systems (GEOSS)**⁶. GGOS will provide time series of the three fundamental geodetic observables and their variations, i.e., the Earth's shape, the Earth's gravity field, and the Earth's rotational motion (Beutler, 2004).

2.2 Global Navigation Satellite Systems

Positioning and navigation are enabled at any time under any weather condition everywhere on and near the Earth's surface by tracking signals broadcast by satellites of **GNSS** orbiting the Earth in **Medium Earth Orbit (MEO)**. GNSS satellites, which have atomic clocks on board, broadcast signals with modulated messages containing satellite clock corrections to GNSS system time and orbit information. Receivers track GNSS signals and messages and compare the signal emission times with the time of signal reception times. The distance between satellite and receiver is subsequently derived by computing the difference between the two clocks multiplied by the speed of light. Four such simultaneous one way measurements eventually allows it to estimate receiver coordinates and receiver clock offset corrections w.r.t. the underlying global reference frame and system time, respectively.

2.2.1 Space Segments

The generic term **GNSS** refers to any global satellite navigation system which provides global coverage. Table 2.2 summarizes important information on the American **GPS**, the Russian **GLONASS**, the European Galileo, and the Chinese COMPASS.

The U.S. GNSS—GPS The U.S.-American **GNSS**, called **NAVigation Signal Timing And Ranging (NAVSTAR) Global Positioning System (GPS)** of the U.S. Department of Defense, has a nominal constellation of 24 satellites deployed in 6 regularly spaced orbital planes, separated by 60° in the Earth's equator. Each orbital plane contains 4 satellites. Orbital planes have an inclination of 55° w.r.t. the Earth's equator. Satellite orbits are near-circular and have semi-major axes of approximately 26,560 km. The full constellation guarantees that at least four satellites are simultaneously visible with an elevation of at least 20° at any time and from any location in the vicinity of the Earth's surface. The sidereal revolution period of satellites is approximately 11 h 58 min, which corresponds to half a sidereal day. The **Ground Track Repetition (GTR)** is one sidereal day (approximately 23 h 56 min), setting the **GPS** satellite orbits into a deep 2:1 resonance with the Earth's rotation. Perturbing forces related to this resonance create long period perturbations with

⁵<http://www.ggos.org>

⁶<http://www.earthobservations.org>

Table 2.2: Space segments of **GPS**, **GLONASS**, Galileo, and COMPASS on 24 December, 2011.

	GPS	GLONASS	Galileo	COMPASS
First satellite	1978	1982	2005	2007
FOC since	1994	(2011)	(2015)	(2020)
No. satellites ^a	24 (+3 spares)	24 (+3 spares)	27 (+3 spares)	27 (+5,+3)
No. active satellites	32	24	(4, as test)	1
Planes/Slot/Deg ^b	6/4/90°	3/8/45°	3/9/40°	3/9/40°
Inclination	55°	64.8°	56°	55°
Semi-major axis	26,560 km	25,510 km	29,610 km	27,840 km
Revolution period	11 h 58 min	11 h 16 min	14 h 05 min	12 h 50 min
GTR	1 day	8 days	10 days	7 days
No. rev./ GTR ^c	2/1	17/8	17/10	13/7
Draconitic year ^d	351.42 days	353.37 days	355.92 days	353.46 days
DSSS	CDMA	FDMA/CDMA	CDMA	CDMA
Fund. clock freq.	10.23 MHz	5.11(10.23) MHz	10.23 MHz	10.23 MHz
Carrier freq.	L1/1575.42 MHz L1/1227.60 MHz L5/1176.45 MHz	L1/1602 MHz band L2/1236 MHz band (L3)/~1205 MHz	E1/1575.43 MHz E5a/1176.45 MHz E5b/1207.14 MHz E6, 1278.75 MHz	B1/1575.42 MHz B2/1191.795 MHz B3/1268.52 MHz
Signal polarization	RHCP	RHCP	RHCP	RHCP
System time	GPS	GLONASS	GST	BDT
Correction to UTC	UTC(USNO)	UTC(SU)	UTC(k) via TSP	Sync. to UTC
Datum	WGS-84	PZ-90	GTRF	CGS2000

^aNominal number of active satellites with nominal number of inactive spare satellites.

^bNumber of orbital planes, number of slots within each orbital plane, and spacing between slots.

^cNumber of orbital revolutions to have the same ground track repetition.

^dApproximation with the only oblateness perturbation (Beutler, 2005).

large amplitudes (Beutler, 2005). This is why **GPS** satellites have to be repositioned about once per year to keep them to their assigned slots.

The first generation of **GPS** satellites, the Block-I satellites with **Space Vehicle Number (SVN)** 1-11, was put in orbit from 1978 to 1985 to validate the navigation concept. Their lifespan was assumed to be 4.5 years, but all operated for at least additional 5 years. All Block-I satellite have now been decommissioned. They are therefore orbiting the Earth as "space debris". The **GPS** satellites of the second generation were designed as Block-II satellites. More precisely, from 1989 to 1990 9 Block-II satellites (**SVN** 13-21) and from 1990 to 1997 19 Block-IIA (**SVN** 22-40) were launched (A denotes "advanced"). Block-I and Block-II/IIA satellites broadcast C/A and P(Y) codes on L1 and P(Y) code on L2. The C/A-code, which repeats itself every millisecond, is a 1023 bits long **Pseudo-Random Noise (PRN)** code sent at 1,023 Mbits/s. The P(Y) code is obtained by encrypting the **PRN** P-code with the secret W-code when the **Anti-Spoofing (AS)** is on (see Table 2.3). The P-code is sent at 10,23 Mbits/s and repeats itself every 266 days with 38 segments of one week. As a consequence, the P-code must be a **PRN** sequence of $2.35 \cdot 10^{14}$ bits.

GPS satellite clocks are generated by Caesium (Cs) or Rubidium (Rb) standards. Block-I satellites were equipped with one Cs and two Rb standard clocks, whereas Block-II/IIA satellites are equipped with two Cs and two Rb clocks. The nominal clock frequency ν_0

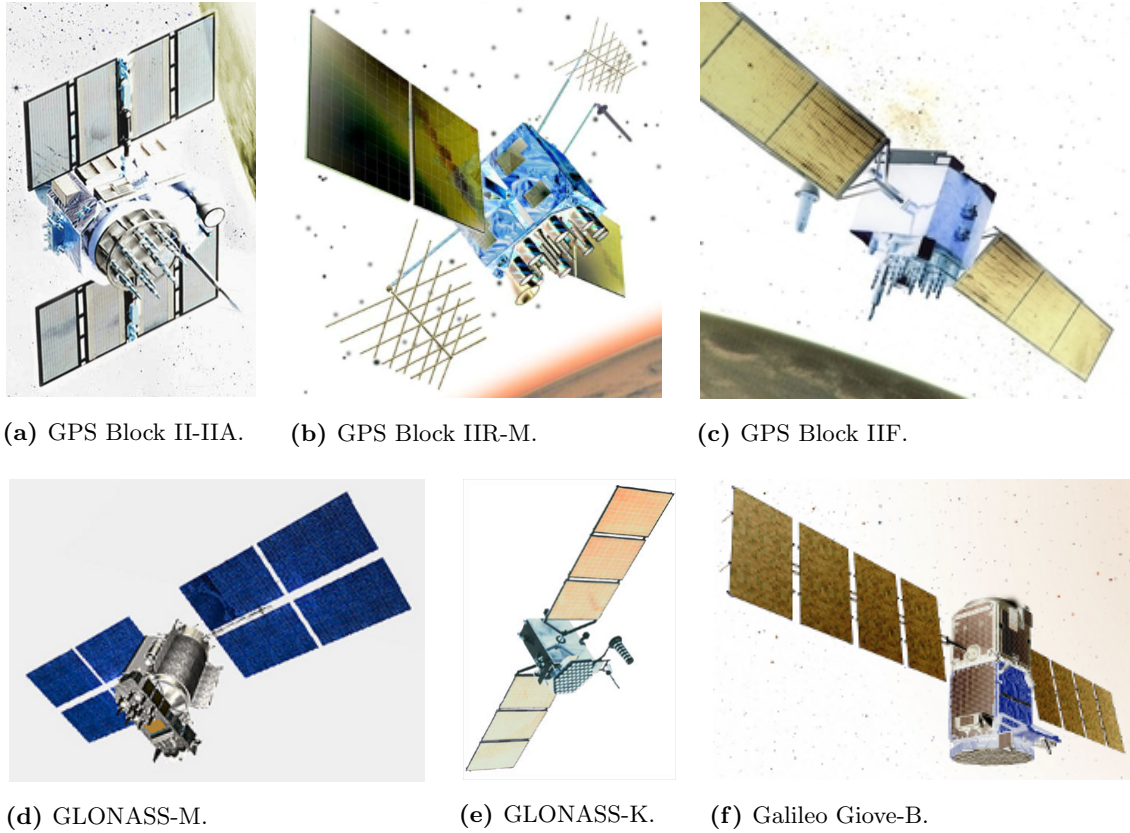


Figure 2.1: Space segment: artistic designs of **GPS**, **GLONASS**, and Galileo satellites.
 Source: <http://www.gps.gov>.

of 10.23 MHz defines the rates of the **PRN** sequences C/A and P(Y) as well as the carrier frequencies:

$$L1 : \nu_1 = 154 \cdot \nu_0 = 1575.42 \text{ MHz} \quad \text{gives} \quad \lambda_1 = c/\nu_1 \simeq 19.0 \text{ cm} , \quad \text{and} \quad (2.1)$$

$$L2 : \nu_2 = 120 \cdot \nu_0 = 1227.60 \text{ MHz} \quad \text{gives} \quad \lambda_2 = c/\nu_2 \simeq 24.4 \text{ cm} . \quad (2.2)$$

The true clock frequency, however, is 4.4647 parts in 10^{-10} lower than its nominal frequency to compensate for relativistic effects (Ashby, 2003).

The **Selective Availability (SA)**, the artificial degradation of the satellite clock accuracy, was switched off on May 1, 2000, in all **GPS** satellites by allowing users to access the error-free L1 signal. Prior to being turned off, the **SA** typically added slowly changing random signal errors of up to 100 m.

From 1997 to 2009 21 Block-IIR satellites (**SVN** 41-61), where R denotes "replenishment", were put in orbit as the third evolution stage of the second generation to increase the number of satellites of the constellation and to replace Block-II/IIA satellites, which were reaching the end of their lifetime. Block-IIR satellites have been equipped with more radiation power, a new attitude control, longer autonomous satellite operation, and reprogrammable

Table 2.3: Intervals with **Anti-Spoofing** for **GPS** satellites (Steigenberger, 2009).

Begin Epoch		End Epoch	
31.01.1994	00:00:00	19.04.1995	20:59:59
10.05.1995	20:00:01	18.06.1995	23:59:59
11.07.1995	00:00:02	09.10.1995	23:59:59
01.11.1995	00:00:01	01.02.1997	23:59:59
24.02.1997	00:00:00	-	-

satellite processors. Block-IIR satellites are further divided into Block-IIR-A and Block-IIR-B, where the latter are equipped with an advanced antenna design. Another evolution step began in September 2005 with the first Block IIR-M satellite, where M stands for "modernized", providing the new military M-code on L1 and L2 and the civil signal L2C on the second carrier frequency (L2). Today, the **GPS** constellation counts 8 Block IIR-M equipped with Rb standards. The last evolution stage of the Block-II generation is the Block-IIF. Its first satellite was launched on May 27, 2010, and in addition to the satellites of other stages it broadcasts the new L5 signal for civil services and commercial aviation purposes. Figures 2.1a-2.1c illustrate the three space vehicles of the Block-II generation.

The future (third) generation of **GPS** satellites is designed as Block-III. Their satellites are expected to have better anti-jam capabilities for the military signals, to broadcast the military M-code signals on L1 and L2 with high-beam power, to supports some safety-of-life applications, to transmit the new international civil signal (L1C), and to have a lifetime of 15 years. The first Block-III satellite is scheduled for launch in 2014. The entire **GPS** constellation is expected to remain fully operational at least through 2030.

The signals transmitted by the **GPS** and other satellites are described in Table 2.2. The carriers are **Right Hand Circular Polarization (RHCP)**. Such circular polarization, compared to horizontal- or vertical-only polarizations, allows to have a full signal strength independently of the antenna orientation and, furthermore, since reflections change the direction of the polarization, allows it to reduce the impact of reflected signals.

The Russian GNSS—GLONASS The Russian **GLO**balnaya **NA**vigatsionnaya **Sputniko**vaya **Sistema** (**GLONASS**) nominally consists of 24 satellites. As opposed to its American counterpart, the **GLONASS** has 3 evenly spaced orbital planes separated by 120° on the Earth's equator, with 8 evenly spaced satellites in each orbital plane (see Table 2.2). Their semi-major axis and inclination are 25,510 km and 64.8° , respectively. With an orbital revolution period of 11 h 16 min **GLONASS** orbits are commensurable with a ratio of 17:8 with the Earth's rotation. No repositioning maneuvers are needed for **GLONASS** satellites since their orbit revolution period are not in deep 2:1 resonance with the Earth's rotation.

The development of the **GLONASS** system began in the late 1970s. The first three test satellites were launched in October 1982. After the test of about twenty other prototypes, the first Block-II satellites were launched in 1985. Initially, their lifetime was about 3 years. The next generation of satellites, the **GLONASS-M** with an expected lifetime up to 7 years (see Fig. 2.1d), were put in orbit from 2003. **GLONASS** and **GLONASS-M** satellites broadcast C/A-code and P-code by an hybrid method **Code Division Multiple**

Access (CDMA)/Frequency Division Multiple Access (FDMA) on the two frequency bands

$$L1 : \nu_1(k) = 1602 \text{ MHz} + k \cdot 0.5625 \text{ MHz} \quad \text{with } k = 1, \dots, n_k \quad (2.3)$$

$$L2 : \nu_2(k) = 1246 \text{ MHz} + k \cdot 0.4375 \text{ MHz} \quad \text{with } k = 1, \dots, n_k, \quad (2.4)$$

where n_k is the number of channels which was originally set to 24, one individual channel number for each satellite of the full constellation. Today, because of interferences with frequencies of radio astronomy, antipodal **GLONASS** satellites transmit on the same channel numbers: From 1998 to 2005 **GLONASS** satellites transmitted on channels $k = 1, \dots, 13$. After 2005, they transmitted on channels $k = -7, \dots, 6$, with $k = +5$ and $k = +6$ reserved for technical purposes (e.g., [Dach et al., 2007](#)). Today, the **GLONASS** constellation counts 24 active satellites. The next generation of satellites, the **GLONASS-K** (see Fig. 2.1e), have a mass of half as much as their predecessors, have a lifetime of up to 10 years, and in addition broadcast civil signals by **CDMA**. The first **GLONASS-K** has been active since 26 February, 2011.

The European GNSS—Galileo As opposed to the American and Russian counterparts the European **GNSS** Galileo will be primarily under civil and not under military control. Currently, four satellites are in orbit: the two test satellites **GIOVE-A** (in 2005) and **GIOVE-B** (in 2008, see Fig. 2.1f), and two In-Orbit Validation (IOV) satellites (in 2011). The full Galileo constellation, which is planned to be **Full Operational Capability (FOC)** in 2015, will have a so-called Walker 27/3/1 configuration. Galileo will consist of 3 evenly spaced orbital planes in the equator with 9 evenly spaced satellites plus one additional inactive spare satellite in each plane (see Table 2.2). The satellite orbits have an inclination of 56° w.r.t. the Earth's equator and are about 3,000 km above the **GPS** constellation. The commensurability of the orbital periods with the Earth's rotation period is of 17:10. No repositioning maneuvers are needed to correct orbital resonance perturbations. The Galileo will basically transmit signals by **CDMA** on three (bands of) frequencies: E1 (1575.43 MHz), which has the same carrier frequency like the L1 of **GPS**, E5 (1191.795 MHz), and E6 (1278.750 MHz). More precisely, the (band of) frequency E5 is divided in the lower E5a (with the carrier at 1176.45 MHz) and the upper E5b (with the carrier at 1207.14 MHz). E5a will coincide with the L5 of **GPS**.

The Chinese GNSS—COMPASS The Chinese **GNSS**, COMPASS, also known as Beidou-2, will also have a constellation of three evenly spaced orbital planes with 9 operational satellites in each plane. The inclination and the semi-major axis will be 55° and 27,840 km, respectively. The commensurability of the revolution period of the satellites with the Earth's rotation period is 13:7, therefore no repositioning maneuvers are needed to correct for the orbital resonance perturbations. A first satellite of the global constellation was put in **MEO** for test purposes and to occupy the assigned frequency. In addition to the global constellation of 30 satellites—27 operational plus 3 in inclined geo-synchronous orbit—COMPASS already consists of 5 satellites in geostationary earth orbit. The full constellation is planned to become active within 2020. COMPASS satellites broadcast civil and military services in three (bands of) frequencies: B1 (1575.42 MHz), B2 (1191.795 MHz)

and B3 (1268.52 MHz). B1 coincides with L1 of GPS and E1 of Galileo, while B2 coincides with the central carrier frequency E5 of Galileo, but different PRNs and different modulations will be broadcast.

2.2.2 The Control Segment

The control segment of a GNSS monitors and maintains the corresponding space segment. It usually consists of few base stations distributed worldwide which have down- and up-link channels to communicate with satellites. Ephemerides, clock corrections, and other information are regularly computed on ground and transmitted to the satellites via ground stations. All satellites simultaneously update their broadcast messages on a regular basis. Repositioning maneuvers and other maintenance operations are preprogrammed via up-link channels, as well.

2.2.3 The User Segment

The user segment of a GNSS consists of all receivers, which are able to track signals from GNSS satellites. Tracking receivers can be hand-held, on board of vehicles, on planes or ships, on Low Earth Orbit (LEO) satellites, on permanent geodetic stations, etc.

Geodetic tracking receivers provide, as opposed to the low cost hand-held or navigation receivers, multi-frequency high accuracy phase (and Doppler) observations. Important characteristics are: GNSS constellations tracked, number of simultaneously tracked channels per GNSS, type of frequencies tracked, real-time functionality, minimum sensitivity, filters, quality, reliability, and (last but not least) the cost (Bossler et al., 2010). From time to time receiver manufacturers provide new firmware, which obviously should be updated as soon as possible in order to have the state-of-art performance. New firmwares, e.g., with multipath filtering, might have an impact on the estimates of station coordinates. Around 2000, the firmware upgrade of the Rogue/TurboRogue GPS receivers of the IGS network lowered their "actual elevation mask" from $\sim 20\text{-}30^\circ$ down to $\sim 10^\circ$. As a result, their number of observations increased and the Root Mean Squares (RMS) of their coordinate time series generally diminished (Tregoning et al., 2004)—see also IGSMails⁷⁸.

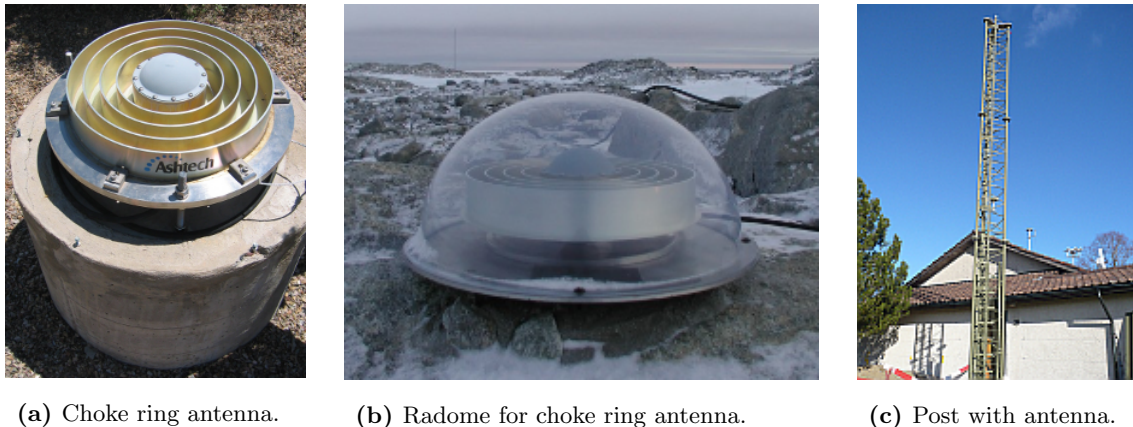
Geodetic GNSS stations consist of a set of dedicated antenna-receiver equipment. Reference networks such as the global IGS, the regional EUREF, or the national AGNES⁹ consist of permanent GNSS tracking stations. Each permanent station has its own description file—LOG file—containing information such as the station name, the equipment history with all antenna and receiver changes, and other technical and general information. The LOG of stations of the IGS tracking network is maintained by the IGS Central Bureau (IGS-CB).

Antennas of GNSS permanent tracking stations are omnidirectional, RHCP consistent to the satellite counterpart (see Table 2.2), and are designed to mitigate signal multipath

⁷[IGSMail-2071]: Rogue Ionosphere Problem.

⁸[IGSMail-2190]: TurboRogue L2 tracking update.

⁹<http://www.swisstopo.admin.ch/>



(a) Choke ring antenna. (b) Radome for choke ring antenna. (c) Post with antenna.

Figure 2.2: Examples of monuments and antennas of permanent stations.

effects. The choke ring antenna (see Fig. 2.2a) is well known within the geodetic community. This antenna, originally designed by **National Aeronautics and Space Administration (NASA)**'s **Jet Propulsion Laboratory (JPL)**, achieves pseudorange multipath mitigation with a number of conductive concentric cylinders around a central antenna. Choke ring antennas are often covered with a protective radome (see Fig. 2.2b). Generally, each antenna comes with the **Antenna Reference Point (ARP)** to accurately relate its distance to the reference marker on the ground. Each single antenna has its own specific electrical characteristics. In order to obtain high accuracy products down to the level of millimeters the antenna of tracking stations need to be calibrated, i.e., to take into account their specific electrical characteristics. For a long time the **IGS** adopted relative antenna calibrations for the antennas of its tracking network. These calibrations consisted of a **Phase Center Offset (PCO)** displacement vector w.r.t. the reference **ARP** and the elevation-dependent **Phase Center Variations (PCVs)**, both estimated w.r.t. the "perfect" antenna **AOAD/M.T** (Allen Osborne Associates Dorne Margolin T) without radome and without any directional dependence (Mader, 1999). During this period the **IGS** used one standard **PCO** for each satellite block. **PCOs** and **PCVs** are frequency-specific. Since **GPS** week 1400¹⁰ the **IGS** switched to absolute antenna calibrations. These are obtained by a robot capable of tilting and rotating the antenna (Menge et al., 1998). Elevation- and Azimuth-dependent **PCVs** are operationally estimated by the **Geo++**¹¹ company since 2000 (Wübbena et al., 2000, 2006). Alternatively, antenna calibration can be performed and validated in an anechoic chamber (e.g., Schupler et al., 1994; Görres et al., 2006). Today, the **IGS** counts 97 different antennas and radome types. 62% of these are absolutely calibrated (Romero, 2010). Consistent with the absolute receiver antenna calibration, the **IGS** provides satellite-specific **PCO** and nadir-dependent **PCVs** for both, **GPS** (Schmid and Rothacher, 2003) and **GLONASS** (Dach et al., 2011) satellites. Satellite and receiver antenna calibrations, both relative or absolute, are provided to the community by an **ANTEX** file (Rothacher and Schmid, 2002, 2006).

¹⁰[IGSMail-5438]: IGS switch to absolute antenna model and ITRF2005.

¹¹<http://www.geopp.de>

Antenna monuments of permanent stations should be as stable as possible and, if possible, provide a place for the antenna to reduce multipath effects to the extent possible. The most common monuments are pillars, concrete blocks, posts, and tripods. Figure 2.2 provides some example.

2.3 Basics of Processing

In this section we describe the most important aspects of GNSS data analysis. As these are mostly valid for all other GNSSs, we restrict ourselves to those of GPS. For more information we refer to (e.g., Mervart, 1995; Schaer, 1999; Dach et al., 2007; Thaller, 2008).

2.3.1 Observation Equations

High accuracy geodetic measurements using the GPS are obtained by tracking both code and phase observations of its signals.

Basic Code Observations GPS receivers track signals broadcast by GPS satellites (see Sect. 2.2). Once the receiver k tracks the signal of the satellite i , the receiver is able to reconstruct the biased receiver-satellite distance, the so-called *pseudorange* (in meters)

$$P_k^i = c(t_k - t^i) + \varepsilon_{k,P}^i, \quad (2.5)$$

where t_k is the arrival time of the signal as measured by the clock of the receiver k , t^i is the transmission time of the signal as measured by the clock of the satellite i , and c is the speed of light. $\varepsilon_{k,P}^i$ is generally the residual error, which contains contributions still to be modelled in order to achieve high accuracy geodetic results. Let us now introduce the GPS system time t (Rockwell, 1984) at signal reception and the signal travelling time τ . Equation (2.5) can be rewritten as follows

$$\begin{aligned} P_k^i &= c[(t + \delta_k) - (t - \tau + \delta^i)] + \varepsilon_{k,P}^i \\ &= c\tau + c\delta_k - c\delta^i + \varepsilon_{k,P}^i \\ &= \varrho_k^i + c\delta_k - c\delta^i + \varepsilon_{k,P}^i, \end{aligned} \quad (2.6)$$

with $\varrho_k^i = c\tau$ the geometric distance, the so-called *slant-range*

$$\varrho_k^i(t) = |\mathbf{r}^i(t - \tau) - \mathbf{r}_k(t)|_{IorE} = |\mathbf{r}_I^i(t - \tau) - \mathbf{R}(t) \cdot \mathbf{r}_{E,k}(t)|, \quad (2.7)$$

defined between satellite \mathbf{r}^i and receiver \mathbf{r}_k positions. The matrix \mathbf{R} performs the transformation from the *Earth-fixed* system (E) to the geocentric *inertial* system (I) (e.g., Rothacher, 1998; Beutler, 2005). The receiver and satellite clock errors w.r.t. the GPS system time t are δ_k and δ^i , respectively.

Basic Phase Observations The geodetic receiver k is able to count the number of zero crossings (negative to positive) of the carrier phase and the fractional part of the phase for each measurement. The sum is the carrier phase measurement (in cycles)

$$\psi_k^i = (\phi_k(t) + \delta_k) - (\phi^i(t - \tau) + \delta^i) + n_k^i + \varepsilon_{k,\psi}^i \quad (2.8)$$

for each sampling epoch. $\phi_k(t)$ is the phase of the local receiver oscillator, $\phi_k(t - \tau)$ is the phase of the signal when it leaves the satellite antenna, and n_k^i is the unknown initial integer number of cycles between satellite and receiver—the so-called *initial ambiguity*—which remains constant as long as the receiver keeps track on the satellite signal. Using the Taylor development $\phi(t - \tau) \simeq \phi(t) - \tau\nu$ with the carrier frequency $\nu = d\phi/dt$ we may rewrite Eq. (2.8) as

$$\psi_k^i = \phi_k(t) + \delta_k - \phi^i(t) + \tau\nu + n_k^i - \delta^i + \varepsilon_{k,\psi}^i . \quad (2.9)$$

The phase difference $\phi_k(t) - \phi^i(t)$ may furthermore be expressed in terms of frequency.

$$\psi_k^i = (\delta_k - \delta^i)\nu + \tau\nu + n_k^i + \varepsilon_{k,\psi}^i . \quad (2.10)$$

By multiplying the above equation with the carrier wavelength λ we obtain the observation equation for phase measurements

$$\begin{aligned} L_k^i &= c\delta_k - c\delta^i + \tau c + \lambda n_k^i + \varepsilon_{k,L}^i \\ &= \varrho_k^i + c\delta_k - c\delta^i + \lambda n_k^i + \varepsilon_{k,L}^i . \end{aligned} \quad (2.11)$$

Compared to the code pseudorange observations (2.6), the phase observations (2.11) contains the additional initial integer phase ambiguity n_k^i that must be determined, see (e.g., Mervart, 1995; Teunissen and Kleusberg, 1998a).

Additional Effects In order to achieve high accuracy GPS measurements, code (2.6) and phase (2.11) observation equations need to take into account:

- The *ionospheric refraction* I_k^i . Approximately, the ionospheric refraction is proportional to $1/\nu^2$, where ν the carrier frequency. By defining I_k^i the delay of ν_1 , we derive from the proportionality factor that the delay of ν_2 (w.r.t. ν_1) becomes $I_k^i \cdot \nu_1^2/\nu_2^2$. By forming the ionosphere-free linear combination (see Sect. 2.3.2), ionospheric refraction is eliminated (to the first order).
- The *tropospheric refraction* T_k^i . Tropospheric refraction is the signal delay caused by the neutral atmosphere. It is the same for both, code and phase measurements.

Modelling the Observables

- A simple model of the tropospheric refraction—without horizontal gradients, see (e.g., Meindl et al., 2004)—reads

$$T_k^i = f_d(z)\Delta T_d + f_w(z)\Delta T_w , \quad (2.12)$$

where $f_d(z)$ and $f_w(z)$ are the mapping functions of the *dry* and *wet* delays as a function of the Zenith distance z of the observations w.r.t. the observing station, respectively, and ΔT_d and ΔT_w are the Zenith hydrostatic delay and Zenith wet delay, respectively.

- The *station position* \mathbf{r}_k in Earth-fixed frame is written as

$$\mathbf{r}_k(t) = \mathbf{r}_k(t_0) + \mathbf{v}_k(t - t_0) + \delta\mathbf{r}_{sol} + \delta\mathbf{r}_{pol} + \delta\mathbf{r}_{ocn} + \delta\mathbf{r}_{atm} + \delta\mathbf{r}_{ant} + \varepsilon_{k,\mathbf{r}_k}^i \quad (2.13)$$

where we have

- $\mathbf{r}_k(t_0) + \mathbf{v}_k$ station coordinates and station velocities,
- $\delta\mathbf{r}_{sol} + \delta\mathbf{r}_{pol}$ solid Earth tides and pole tides,
- $\delta\mathbf{r}_{ocn} + \delta\mathbf{r}_{atm}$ ocean loading and atmosphere loading,
- $\delta\mathbf{r}_{ant}$ antenna **PCO** and **PCVs**.

- The *satellite's antenna position* \mathbf{r}^i in the inertial frame reads as

$$\mathbf{r}^i(t - \tau) = \mathbf{r}_0^i(t^i; a, e, i, \Omega, \omega, T_0; p_1, p_2, \dots, p_d) + \delta\mathbf{r}_{ant}^i + \varepsilon_{k,\mathbf{r}^i}^i \quad (2.14)$$

where

- \mathbf{r}_0^i satellite's center of mass position,
- $\delta\mathbf{r}_{ant}^i$ satellite antenna **PCO** and **PCVs**,
- $a, e, i, \Omega, \omega, T_0$ orbit elements,
- p_1, p_2, \dots, p_d parameters describing the force field.

Precise orbit positions are obtained by numerical integration of the ordinary differential equation which describes the satellite motion in the force field near the Earth (Beutler, 2005).

2.3.2 Basic Observables

The (simplified) *zero-difference* observation equations for the two wavelengths λ_1 and λ_2 of the **GPS** system may be summarized as follows

$$P_{1k}^i = \varrho_k^i + c\delta_k - c\delta^i + I_k^i + T_k^i + \varepsilon_{k,P_1}^i, \quad (2.15a)$$

$$P_{2k}^i = \varrho_k^i + c\delta_k - c\delta^i + \frac{\nu_1^2}{\nu_2^2} I_k^i + T_k^i + \varepsilon_{k,P_2}^i, \quad (2.15b)$$

$$L_{1k}^i = \varrho_k^i + c\delta_k - c\delta^i - I_k^i + T_k^i + \lambda_1 n_{1k}^i + \varepsilon_{k,L_1}^i, \quad (2.15c)$$

$$L_{2k}^i = \varrho_k^i + c\delta_k - c\delta^i - \frac{\nu_1^2}{\nu_2^2} I_k^i + T_k^i + \lambda_2 n_{2k}^i + \varepsilon_{k,L_2}^i. \quad (2.15d)$$

The sign of ionospheric refraction of code measurements is opposite to that of phase measurements. From *Maxwell's equations* we know that the former represents the group delay, the latter the phase advance.

Often, one might not be interested in the satellite (δ^i) and receiver (δ_k) clock corrections. By forming the *single-difference* between the pair of receivers k and l

$$L_{Fkl}^i = L_{Fk}^i - L_{Fl}^i \quad (2.16)$$

one eliminates the satellite clock error δ^i —which is supposed to be constant for a short period of time between the measurements. In a second step, by forming the *double-difference* between the pair of satellites i and j

$$L_{Fkl}^{ij} = L_{Fkl}^i - L_{Fkl}^j, \quad (2.17)$$

one eliminates the receiver clock error δ_k , as well. The resulting double-difference equations are

$$P_{1kl}^{ij} = \varrho_{kl}^{ij} + I_{kl}^{ij} + T_{kl}^{ij} + \varepsilon_{kl,P_1}^{ij}, \quad (2.18a)$$

$$P_{2kl}^{ij} = \varrho_{kl}^{ij} + \frac{\nu_1^2}{\nu_2^2} I_{kl}^{ij} + T_{kl}^{ij} + \varepsilon_{kl,P_2}^{ij}, \quad (2.18b)$$

$$L_{1kl}^{ij} = \varrho_{kl}^{ij} - I_{kl}^{ij} + T_{kl}^{ij} + \lambda_1 n_{1kl}^{ij} + \varepsilon_{kl,L_1}^{ij}, \quad (2.18c)$$

$$L_{2kl}^{ij} = \varrho_{kl}^{ij} - \frac{\nu_1^2}{\nu_2^2} I_{kl}^{ij} + T_{kl}^{ij} + \lambda_1 n_{2kl}^{ij} + \varepsilon_{kl,L_2}^{ij}. \quad (2.18d)$$

Double-differences of code and phase measurements are the basic observables in the **BSW**. Compared to the zero-differences the double-differences are better suited to fix initial phase ambiguities to integer values.

Linear Combinations (LCs) of basic observables—on the zero- and the double-difference levels—are used to eliminate certain parameters and, as a consequence, to obtain new observables containing "only" the parameters of interest. For geodetic tasks the common **LC** is the *ionosphere-free linear combination*

$$L_3 = \frac{\nu_1^2}{\nu_1^2 - \nu_2^2} L_1 - \frac{\nu_2^2}{\nu_1^2 - \nu_2^2} L_2. \quad (2.19)$$

This **LC** eliminates ionospheric refraction when two carrier frequencies are considered. For additional information on other linear combinations consult (Mervart, 1995; Schaer, 1999; Dach et al., 2007).

2.3.3 Estimation of Parameters

We assume that the relationship between the observation vector \mathbf{y} and the parameter vector \mathbf{p} is linear. We furthermore assume that the stochastic model of the observations is known. We then estimate the parameters by assuming a **Gauss-Markoff Model (GMM)**, see (Koch, 1999):

$$\mathbf{E}(\mathbf{y}) = \mathbf{A}\mathbf{p} \quad \text{with} \quad \mathbf{D}(\mathbf{y}) = \sigma^2 \mathbf{P}^{-1}, \quad (2.20)$$

where the first two (central) moments $\mathbf{E}(\mathbf{y})$ and $\mathbf{D}(\mathbf{y})$ correspond to the *functional model* (or mean) and the *stochastic model* (or variance), respectively. Furthermore, we assume

n_{obs}, n_{par}	number of observations, number of unknown parameters,
\mathbf{A}	$n_{obs} \times n_{par}$ the so-called <i>first design matrix</i> ,
\mathbf{p}	$n_{par} \times 1$ vector of unknown parameters,
\mathbf{y}	$n_{obs} \times 1$ vector of observations,
\mathbf{P}	$n_{obs} \times n_{obs}$ positive definite weight matrix,
$\mathbf{E}(\cdot)$	operator of expectation,
$\mathbf{D}(\cdot)$	operator of dispersion,
σ^2	variance of unit weight or variance factor.

The connection between the n_{obs} -vector of observables \mathbf{y} and the n_{par} -vector of unknown parameters \mathbf{p} is given by the system of n_{obs} observation equations

$$\mathbf{v} = \mathbf{y} - \mathbf{A}\mathbf{p} , \quad (2.21)$$

where \mathbf{v} is the vector of residuals describing the discrepancy between the observation \mathbf{y} and the linear functional model $\mathbf{A}\mathbf{p}$.

Once we have collected the observations and defined both the functional and the stochastic model of the observations, the adjustment of the parameters can be carried out.

The **Least Squares Estimation (LSE)** asks that

$$\mathbf{v}^T \mathbf{P} \mathbf{v} = \min , \quad (2.22)$$

where $\mathbf{P} = \mathbf{Q}_{yy}^{-1}$ and \mathbf{Q}_{yy} is the **Variance-Covariance Information (VCI)** matrix of the observations \mathbf{y} . The minimum principle gives the estimates $\hat{\mathbf{p}}$ of the parameters vector \mathbf{p}

$$\hat{\mathbf{p}} = \mathbf{Q}_{\hat{p}\hat{p}} \mathbf{A}^T \mathbf{P} \mathbf{y} \quad (2.23)$$

where

$$\mathbf{Q}_{\hat{p}\hat{p}} = (\mathbf{A}^T \mathbf{P} \mathbf{A})^{-1} = \mathbf{N}^{-1} \quad (2.24)$$

the cofactor matrix $\mathbf{Q}_{\hat{p}\hat{p}}$ is equal the inverse of the normal matrix \mathbf{N} (see Sect. 2.3.4). For hypothesis tests the covariance matrix of residuals may be computed, too:

$$\mathbf{Q}_{vv} = \mathbf{Q}_{yy} - \mathbf{A} \mathbf{Q}_{\hat{p}\hat{p}} \mathbf{A}^T . \quad (2.25)$$

The a posteriori variance of unit weight (or variance factor) is obtained by

$$m_0^2 = \frac{\mathbf{v}^T \mathbf{P} \mathbf{v}}{d} \quad (2.26)$$

as long as the degree-of-freedom (or redundancy)

$$d = n_{obs} - n_{par} > 0 . \quad (2.27)$$

The formal errors of the estimated parameters is given by

$$\delta \hat{\mathbf{p}}_i = m_0 \sqrt{\mathbf{Q}_{\hat{p}\hat{p}(i,i)}} \quad \text{with } i = 1, \dots, n_{par} . \quad (2.28)$$

One often has to deal with a non-linear model $f(\mathbf{p})$ in the parameters \mathbf{p} . In that case the non-linear model must be linearized around the a priori values \mathbf{p}_o by a Taylor series approximation up to the first degree

$$\begin{aligned} f(\mathbf{p}) &= f(\mathbf{p}_o) + \left. \frac{\partial f}{\partial \mathbf{p}} \right|_{\mathbf{p}=\mathbf{p}_o} \cdot \Delta \mathbf{p} \\ &= f(\mathbf{p}_o) + \mathbf{A} \cdot \Delta \mathbf{p} . \end{aligned} \quad (2.29)$$

The first design matrix \mathbf{A} thus corresponds to the term of first degree of the Taylor series, i.e., the Jacobian matrix. The improvements $\Delta \hat{\mathbf{p}}$ w.r.t. the a priori values \mathbf{p}_o are estimated. The parameters of interest are then obtained by adding the improvements to the a priori parameter values

$$\hat{\mathbf{p}} = \mathbf{p}_o + \Delta \hat{\mathbf{p}} . \quad (2.30)$$

If the a priori values \mathbf{p}_o are good enough, the final estimates $\hat{\mathbf{p}}$ may be achieved in one step. This is particularly important for problems with thousands of parameters, because the steps to set up the normal equations with many observations might be very time-consuming.

In space geodesy the **LSE** is the most used estimator type in linear **GMMs**. Nevertheless, for datasets contaminated by *colored noise* such as coordinate time series (Langbein and Johnson, 1997; Williams, 2003; Ray et al., 2008; King and Williams, 2009), the **MLE** method delivers more accurate uncertainties for the estimates when models for *flicker noise* and *random-walk* are considered for the adjustment (Zhang et al., 1997; Mao et al., 1999; Williams et al., 2004; Amiri-Simkooei et al., 2007). Despite the fact that the **MLE** method is implicitly used throughout this work, because it reduces itself to a **LSE** problem in case one assumes normally distributed observations, no further description on the **MLE** method is given in this document.

2.3.4 Normal Equations and Operation on Parameters

The normal equation associated with the **GMM** of Eq. (2.20) reads as

$$(\mathbf{A}^T \mathbf{P} \mathbf{A}) \hat{\mathbf{p}} = \mathbf{A}^T \mathbf{P} \mathbf{y} \quad \text{or} \quad \mathbf{N} \hat{\mathbf{p}} = \mathbf{b} , \quad (2.31)$$

where $\mathbf{N} = \mathbf{A}^T \mathbf{P} \mathbf{A}$ is the $(n_{par} \times n_{par})$ **Normal EQUation (NEQ) matrix** and $\mathbf{b} = \mathbf{A}^T \mathbf{P} \mathbf{y}$ is right hand side of the **NEQ**. By the inversion of Eq. (2.31) one obtains:

the cofactor matrix	$\mathbf{Q}_{\hat{\mathbf{p}}\hat{\mathbf{p}}} = \mathbf{N}^{-1}$,
the estimation of the unknown parameters	$\hat{\mathbf{p}} = \mathbf{Q}_{\hat{\mathbf{p}}\hat{\mathbf{p}}} \mathbf{b}$,
the functional model	$\mathbf{A} \hat{\mathbf{p}}$,
the vector of residuals	$\hat{\mathbf{v}} = \mathbf{A} \hat{\mathbf{p}} - \mathbf{y}$,
the quadratic form	$\Omega = \hat{\mathbf{v}}^T \mathbf{P} \hat{\mathbf{v}}$,
the a posteriori variance of unit weight	$m_0^2 = \Omega/d$.

In order to estimate only the parameters of interest one has the opportunity to apply operations at the normal equation level without going back to the level of observations. Let us review some of these operations.

Transformation of Parameters A general linear transformation from the parameter \mathbf{p} to the parameter $\tilde{\mathbf{p}}$ is given by

$$\mathbf{p} = \mathbf{C}\tilde{\mathbf{p}} + \mathbf{c} \quad (2.32)$$

where \mathbf{C} is the conversion matrix and \mathbf{c} is offset vector. Introducing this transformation into the normal equation system (2.31) and multiplying from left by \mathbf{C}^T we obtain the new **NEQ** which reads

$$\tilde{\mathbf{N}}\tilde{\mathbf{p}} = \tilde{\mathbf{b}} \quad \text{with} \quad \tilde{\mathbf{N}} = \mathbf{C}^T\mathbf{N}\mathbf{C} \quad \text{and} \quad \tilde{\mathbf{b}} = \mathbf{C}^T\mathbf{b} - \mathbf{C}^T\mathbf{N}\mathbf{c} . \quad (2.33)$$

Many transformations at the normal equation level may be reduced to linear transformations.

Stacking Parameters According to the sequential **LSE**, the combination of one and the same parameter at the normal equation level provides the same result as adjusting all observations in one step, as long as these parts are statistically independent (e.g., Brockmann, 1997; Koch, 1999). Therefore, by stacking (let us say a series of n) **NEQs** one obtains the **NEQ** system

$$\tilde{\mathbf{N}}\hat{\mathbf{p}}_c = \tilde{\mathbf{b}} \quad \text{with} \quad \tilde{\mathbf{N}} = \sum_{i=1}^n \mathbf{A}_i^T \mathbf{P}_i^{-1} \mathbf{A}_i \quad \text{and} \quad \tilde{\mathbf{b}} = \sum_{i=1}^n \mathbf{A}_i^T \mathbf{P}_i^{-1} \mathbf{y}_i \quad (2.34)$$

with the vector $\hat{\mathbf{p}}_c$ containing stacked parameters as well as all not stacked ones. Obviously, the combination of parameters in one and the same **NEQ** leads to a reduction of the number of parameters.

Pre-Elimination of Parameters Parameter pre-elimination is an important operation to reduce the size of a **NEQ**. Let us assume that \mathbf{p}_1 are the parameters one wishes to estimate and that \mathbf{p}_2 are the parameters to be pre-eliminated. In such case the **NEQ** can be written in the form

$$\begin{bmatrix} \mathbf{N}_{11} & \mathbf{N}_{12} \\ \mathbf{N}_{21} & \mathbf{N}_{22} \end{bmatrix} \begin{bmatrix} \mathbf{p}_1 \\ \mathbf{p}_2 \end{bmatrix} = \begin{bmatrix} \mathbf{b}_1 \\ \mathbf{b}_2 \end{bmatrix} . \quad (2.35)$$

By solving for \mathbf{p}_2 (assuming that \mathbf{N}_{22} is regular) we have

$$\mathbf{p}_2 = \mathbf{N}_{22}^{-1}(\mathbf{b}_2 - \mathbf{N}_{21}\mathbf{p}_1) , \quad (2.36)$$

and by substituting \mathbf{p}_2 in Eq. (2.35) we obtain

$$(\mathbf{N}_{11} - \mathbf{N}_{12}\mathbf{N}_{22}^{-1}\mathbf{N}_{21})\mathbf{p}_1 = \mathbf{b}_1 - \mathbf{N}_{12}\mathbf{N}_{22}^{-1}\mathbf{b}_2 \quad \text{or} \quad \tilde{\mathbf{N}}\mathbf{p}_1 = \tilde{\mathbf{b}} . \quad (2.37)$$

2.3.5 Constraints on Parameters

Constraints on parameters are usually added at the normal equation level by stacking additional information to the **NEQs** to remove the rank deficiency of a **NEQ** (e.g., [Dach et al., 2007](#); [Thaller, 2008](#)). In the **GMM** such constraints can be described as

$$\mathbf{E}(\mathbf{h}) = \mathbf{H}\mathbf{p} \quad \text{with} \quad \mathbf{D}(\mathbf{h}) = \sigma^2 \mathbf{P}_h^{-1}, \quad (2.38)$$

where

n_{cst}, n_{par}	number of constraints, number of unknown parameters,
\mathbf{H}	$n_{cst} \times n_{par}$, matrix with given coefficients,
\mathbf{p}	$n_{par} \times 1$, vectors of unknown parameters,
\mathbf{h}	$n_{cst} \times 1$, vectors of known constant "observations",
\mathbf{P}_h^{-1}	$n_{cst} \times n_{cst}$, dispersion matrix of constraints.

Non-linear constraints have to be linearized using the pattern of Eq. (2.29). Constraints may be seen as additional pseudo-observations which are stacked to the parameters one wants to constrain

$$\begin{bmatrix} \mathbf{y} \\ \mathbf{h} \end{bmatrix} + \begin{bmatrix} \mathbf{v}_y \\ \mathbf{v}_h \end{bmatrix} = \begin{bmatrix} \mathbf{A} \\ \mathbf{H} \end{bmatrix} \hat{\mathbf{p}} \quad \text{with} \quad \mathbf{D}\left(\begin{bmatrix} \mathbf{y} \\ \mathbf{h} \end{bmatrix}\right) = \sigma^2 \begin{bmatrix} \mathbf{P}_y^{-1} & \mathbf{0} \\ \mathbf{0} & \mathbf{P}_h^{-1} \end{bmatrix}, \quad (2.39)$$

where the n_{cst} -vector \mathbf{v}_h represents the residuals w.r.t. $\mathbf{H}\mathbf{p}$. The resulting **NEQ** system becomes therefore

$$(\mathbf{A}^T \mathbf{P}_y^{-1} \mathbf{A} + \mathbf{H}^T \mathbf{P}_h^{-1} \mathbf{H}) \hat{\mathbf{p}}_c = \mathbf{A}^T \mathbf{P}_y^{-1} \mathbf{y} + \mathbf{H}^T \mathbf{P}_h^{-1} \mathbf{h}. \quad (2.40)$$

Relative Constraints With relative constraints the difference of two parameters are constrained with the user-defined σ_r by

$$\mathbf{h}(p_1, \dots, p_{n_{par}}) = p_i - p_j = 0 \quad \text{with} \quad P_r = \frac{\sigma_0^2}{\sigma_r^2}. \quad (2.41)$$

The derived components $\mathbf{H}^T \mathbf{P}_r^{-1} \mathbf{H}$, equal weights P_r in the diagonal elements and $-P_r$ in the off-diagonal elements of the corresponding parameters, and $\mathbf{H}^T \mathbf{P}_r^{-1} \mathbf{h}$, equal zero, are added to the **NEQ** in Eq. (2.40).

Network Constraints When solving for the coordinates of a network using **GNSS** observations only, it is in general not possible or does not make sense to determine all coordinates of all stations without imposing constraints on them. Datum parameters related to scale, translation, and rotation of the network have to be constrained w.r.t. a known reference network.

This type of constraints assumes that there are two reference frames, an a priori reference frame \mathbf{X} and a reference frame of the resulting coordinates $\tilde{\mathbf{X}}$. The station coordinates of the two reference frames are related by the 7-parameter *Helmert* transformation

$$\begin{pmatrix} \tilde{X}_i \\ \tilde{Y}_i \\ \tilde{Z}_i \end{pmatrix} = (1 + S) \begin{pmatrix} 1 & R_z & -R_y \\ -R_z & 1 & R_x \\ R_y & -R_x & 1 \end{pmatrix} \begin{pmatrix} X_i \\ Y_i \\ Z_i \end{pmatrix} + \begin{pmatrix} T_x \\ T_y \\ T_z \end{pmatrix} \quad (2.42)$$

which could be linearized because rotations R_x , R_y , and R_z and the scale S are small. The index i refers to all (fiducial) stations that define the resulting coordinates reference frame. Equation (2.42) can be rewritten as

$$\tilde{\mathbf{X}}_i = \mathbf{X}_i + \mathbf{B}_i \cdot \boldsymbol{\xi} \quad (2.43)$$

with

$$\boldsymbol{\xi} = (T_x \ T_y \ T_z \ R_x \ R_y \ R_z \ S)^T \quad (2.44)$$

and

$$\mathbf{P}_\xi = \text{diag}(P_{T_x}, P_{T_y}, P_{T_z}, P_{R_x}, P_{R_y}, P_{R_z}, P_S) \quad (2.45)$$

and where

$$\mathbf{B} = \begin{pmatrix} 1 & 0 & 0 & 0 & -Z_i & Y_i & X_i \\ 0 & 1 & 0 & Z_i & 0 & -X_i & Y_i \\ 0 & 0 & 1 & -Y_i & X_i & 0 & Z_i \end{pmatrix} \quad (2.46)$$

contains the station coordinates of the a priori reference frame \mathbf{X} . By collecting $\mathbf{X} = (\mathbf{X}_1, \dots, \mathbf{X}_N)$, $\tilde{\mathbf{X}} = (\tilde{\mathbf{X}}_1, \dots, \tilde{\mathbf{X}}_N)$, and $\mathbf{B} = (\mathbf{B}_1, \dots, \mathbf{B}_N)$, Eq. (2.43) becomes the basic equation to solve for the parameters of Eq. (2.44)

$$\mathbf{B} \cdot \boldsymbol{\xi} - (\tilde{\mathbf{X}} - \mathbf{X}) = \mathbf{v}_h . \quad (2.47)$$

Consequently, the determination of the Helmert parameters reads

$$\boldsymbol{\xi} = (\mathbf{B}^T \mathbf{B})^{-1} \mathbf{B}^T \cdot (\tilde{\mathbf{X}} - \mathbf{X}) , \quad (2.48)$$

which can be rewritten as $\mathbf{H}\mathbf{p} = \boldsymbol{\xi}$ with

$$\mathbf{H} = (\mathbf{B}^T \mathbf{B})^{-1} \mathbf{B}^T \quad (2.49)$$

and $\mathbf{p} = \tilde{\mathbf{X}} - \mathbf{X}$. Minimum constraint conditions are applied when one or more of the 7-parameter transformation are set to zero. A **No-Net-Translation (NNT)** condition is achieved by setting the parameter T_x , T_y , and T_z to zero. A **No-Net-Rotation (NNR)** condition is achieved by setting the parameters R_x , R_y , and R_z to zero. The derived components $\mathbf{H}^T \mathbf{P}_\xi^{-1} \mathbf{H}$ and $\mathbf{H}^T \mathbf{P}_\xi^{-1} \mathbf{h}$ (equal zero) are added to the **NEQ** given by the Eq. (2.39).

2.3.6 Satellite Orbits

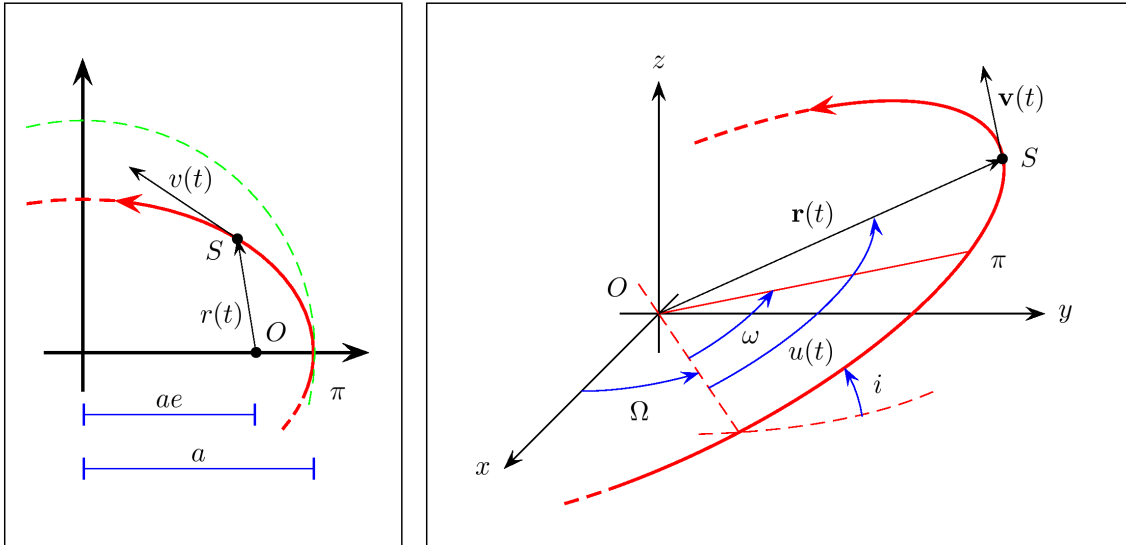
Satellite positions occur in the observation equations (see Sect. 2.3.1). When estimating satellite positions for each observation epoch, the satellite orbit is called *kinematic* (e.g., Bock, 2004). Kinematic orbits are important for Low Earth Orbits (LEOs). Usually, in particular for **GNSS** orbits, the orbit solves the equation of motion (Beutler, 2005)

$$\ddot{\mathbf{r}}(t) = -GM_E \int_{V_E} \rho_E(\mathbf{r}_E) \frac{\mathbf{r} - \mathbf{r}_E}{|\mathbf{r} - \mathbf{r}_E|^3} dV_E - G \sum_{j=1}^{n_{cb}} m_j \left\{ \frac{\mathbf{r} - \mathbf{r}_j}{|\mathbf{r} - \mathbf{r}_j|^3} + \frac{\mathbf{r}_j}{r_j^3} \right\} + \mathbf{a}_{rpr} + \dots \quad (2.50)$$

described in quasi-inertial geocentric system, where n_{cb} is the number of celestial bodies included in the force model, G is the gravitational constant and M_E , V_E , and ρ_E are mass, volume, and density of the Earth, respectively. The first term on the right hand side describes the Earth's gravity field, the second the accelerations due to celestial bodies such as the Moon and the Sun, and the third the acceleration due to the solar radiation pressure. The satellite positions are computed as a particular solution of the ordinary differential equation (2.50) when the initial values, i.e., initial position vector $\mathbf{r}(t_0)$ and initial velocity vector $\dot{\mathbf{r}}(t_0)$ of the satellite at the epoch t_0 , are defined. The initial values may be derived from the osculating orbital elements at t_0 of the two-body problem:

$$\{a_0, i_0, e_0, \Omega_0, \omega_0, u_0\} \longrightarrow \begin{cases} \mathbf{r}(t_0) = \mathbf{r}_0 \\ \dot{\mathbf{r}}(t_0) = \mathbf{v}_0 \end{cases} \quad (2.51)$$

where a is the semi-major axis, i the inclination, e the eccentricity, Ω the right ascension of the ascending node, ω the argument of Perigee, and u argument of latitude, see Fig. 2.3. Orbits derived by Eq. (2.50) with initial values (2.51) are called *dynamic* (e.g., Beutler et al., 1994; Jäggi, 2007).



(a) Orbit in orbital plane.

(b) Orbit plane in inertial geocentric system.

Figure 2.3: Orbital elements of a satellite orbiting the Earth.

On the normal equation level one may set up and solve for stochastic pulses, i.e., instantaneous velocity changes in radial, along-track, and out-of-plane directions (RSW). As a result one obtains so-called *reduced-dynamic* orbits (Beutler et al., 1996; Montenbruck et al., 2005; Beutler et al., 2006; Jäggi et al., 2008), which are continuous in $\mathbf{r}(t)$ and have discontinuities in $\dot{\mathbf{r}}(t)$ at the pulse epoch.

Table 2.4: Parameters at the normal equation level to derive **CODE** final products. (x) estimated. (X) estimated and final product. (p) pre-eliminated. (f) tightly constrained to the results of the weekly 7D solution. (-) no parameter. Table partially derived from (Steigenberger, 2009).

Parameters	Solutions			
	daily 1D	daily 3D	weekly 7D	daily 3F
Coordinates	x	x	X	f
Geocenter	x	x	x	X
Troposphere	x	x	p	X
Orbital elements	x	x	p	X
Radiation pressure	x	x	p	x
Stochastic pulses	x	x	p	x
Satellite PCO	x	x	x	x
Satellite PCVs	x	x	x	x
Earth Rotation Parameters (ERP)	x	x	X	f
Ambiguities	p	p	p	p
Differential Code Bias (DCB) P1-C1	x	-	-	-

2.4 Homogeneously Processed GNSS Data at CODE

Most parameter time series analyzed here are a result of the **CODE** reprocessing effort as contribution to the first **IGS** data reprocessing campaign (see Chapter 1). In agreement with the **IGS** directives, **CODE** provided for this reprocessing contribution homogeneously processed GPS-only data for the interval from January 1994 through December 2008 (Steigenberger et al., 2009a). The remaining few parameter time series analyzed here were derived from the **CODE** reprocessing extension to **GLONASS** observations starting May 2003 (Dach et al., 2011). For both reprocessing efforts the reprocessing procedure is derived from the operational scheme used at **CODE** for the contribution of the **IGS**-final series (Hugentobler et al., 2004). Figure 2.4 presents this procedure on the level of normal equations and of solutions.

```

forall  $i$  days to be reprocessed do
   $1D_i \leftarrow$  processing from RINEX data;
   $3D_{j=i-1} \leftarrow \mathcal{C}\{j-1, j, j+1\}_{1D}$ ;
   $7D_k \leftarrow \mathcal{C}\{j-6, \dots, j\}_{3D}$  if end of GPS-week  $k$ ;
   $3F_{l=i-7, \dots, i-1} \leftarrow \mathcal{C}\{l-1, l, l+1\}_{1D}^*$  if end of GPS-week  $k$ ;
  * with coordinates and ERPs tightly constrained to the values of  $7D_k$ 
end

```

Figure 2.4: The reprocessing procedure at **CODE** to provide final products. Solutions (*SOL*): daily 1D, daily 3D, weekly 7D, and daily 3F. $\mathcal{C}\{\cdot\}_{SOL}$ indicates the combination of *SOL* **NEQs** by **ADDNEQ2**.

The procedure provides four solutions: a 1-day (daily) solution 1D (D denotes "day"), a preliminary 3-days (daily) solution 3D, a 7-days (weekly) solution 7D, and a final 3-days (daily) solution 3F (F denotes "final") (e.g., Steigenberger, 2009). The parameters included

in each solution are summarized in Table 2.4. Station coordinates, ERPs, geocenter parameters, and tropospheric parameters obtained from this processing scheme are provided by CODE as operational products. A more detailed list of products including parameters such as receiver and satellite clock corrections, Global Ionosphere Maps (GIMs), and P1-P2 DCBs may be found in the CODE Analysis Strategy Summary¹². The same summary also contains adopted models and applied strategies to obtain final products. Table 2.5 summarizes adopted models and the parameterization used for the reprocessing effort.

2.4.1 Daily Solution

First, the code observations, the so-called pseudoranges, are smoothed using phase observations (Springer, 2000). Outliers are rejected and large cycle slips are repaired. Cycle slips in phase observations, on the other hand, are not repaired, but marked for a new initial phase ambiguity parameter to be set up.

Station clock corrections, one per observation epoch, are synchronized to GPS time at the zero-difference level (2.15). This allows to determine with good approximation satellite position w.r.t. the signal sending time. Next, single-differences (2.16) are formed by selecting the baselines with the largest number of common observations among all possible baselines (Dach et al., 2007). Successively, preprocessing steps on the double- and triple- (epoch-differences of double-differences) difference levels allow it to detect and correct cycle slips, identify and screen for outliers, and update the list of ambiguities (Dach et al., 2007). If "bad" stations are encountered, the procedure forms new baselines without bad stations.

The next steps of the processing aim at resolving to integer values as many initial phase ambiguity parameters as possible. At first, ambiguities for baselines up to 6,000 km are resolved by the Melbourne-Wüebbena approach (Melbourne, 1985; Wüebbena, 1985), which relies on both, (smoothed) code- and phase-observations. The second step consists of resolving remaining narrow-lane ambiguities in the ionosphere-free solution. In the third step, the Quasi-Ionosphere-Free (QIF) strategy tries to resolve L1 and L2 ambiguities for baselines up to 2,000 km by introducing previously estimated ionosphere maps as known information (Mervart, 1995). The wide-lane/narrow-lane approach attempts to resolve ambiguities for baselines up to 200 km in a similar way like with the Melbourne-Wüebbena approach. At last, L1 and L2 ambiguities are resolved independently for baselines up to 20 km (Dach et al., 2007). The ambiguity resolution procedure may be summarized as follows: (1) resolve all possible ambiguities using a given strategy, (2) insert the resolved ambiguities as known in the observation equations, and (3) screen residuals for outliers after the ambiguity resolution. The percentage of the resolved ambiguities grow from 65% in 1994 to almost 85% at present time (Steigenberger, 2009).

The 1-day 1D final ambiguity-fixed NEQ is obtained by combining the NEQs of four clusters in which correlations are taken into account: One cluster consists of European stations, one of stations in North and South America, and one of stations in Australia, Asia, Africa and Antarctica. The fourth cluster consists of few redundant baselines to connect the other three clusters (Brockmann, 1997). The resulting parameters included

¹²<ftp://ftp.unibe.ch/aiub/CODE/CODE.ACN>

Table 2.5: Summary of adopted models to derive **CODE** final products (Steigenberger, 2009).

General aspects
General a priori sigma of unit weight 1 mm
Elevation cutoff angle of observations 3°
Elevation-dependent weight observations $\cos^2(z)$
Station related models and parameterizations
Reference Datum of the network IGS05 (Gendt, 2006; Altamimi et al., 2007)
Antenna calibration PCO and PCV derived from the IGS05 ANTEX file igs05_1499.atx
Station coordinates aligned by both NNR and NNT conditions to a subset of of IGS05 reference sites
Solid Earth tides and pole tides according to the IERS Conventions, 2003 (McCarthy and Petit, 2003)
Ocean tide loading corrections are considered as they are given in the FES2004 model (Lyard et al., 2006)
Orbit related models and parameterizations
Orbits modelled by 6 orbital elements and 9 solar radiation pressure parameters (Beutler et al., 1994)
Primary equation of motion obtained by a polynomial of degree 10 with integration interval of 1 hour
Variational equation obtained by a polynomial of degree 12 with integration interval of 6 hours
JPL ephemerides DE405/LE405 used to derive positions of major planets (Standish, 1998)
The gravitational field JGM3 is considered up to degree and order 12 (Tapley et al., 1996)
CODE radiation pressure model with constant and periodic terms in the DYX (Beutler et al., 1994)
Pseudo-stochastic pulses every 12 hours in RSW reference system (Beutler et al., 1994)
Eclipsing phases: radiation pressure ignored during transitions of satellites in Earth and Moon shadows
Six orbital parameters tight constrained
Nine dynamical orbital parameters constraints: 10^{-12} m/s ² for (D) and (Y), loose constraints for (X)
Stochastic pulses with sigmas (R) 10^{-6} m/s, (S) 10^{-5} m/s, and (W) 10^{-8} m/s
Block-specific satellite antenna PCOs and PCVs adopted (Schmid and Rothacher, 2003)
Earth rotation related models and parameterizations
Precession model consistent with the IERS Conventions, 2003
Nutation parameters are tightly constrained to the nutation model IAU2000A (Mathews et al., 2002)
ERPs parameterized as continuous piecewise-linear functions with time resolution of 1 hour
First UT1-UTC parameter heavily constrained to the value from Bulletin A (Luzum et al., 2001)
Ocean tide loading model adopted CSR3.0 (Eanes and Bettadpur, 1996)
Sub-daily pole model consistent with the IERS Conventions, 2003
Retrograde sub-daily terms of polar motion blocked at the normal equation level (Hefty et al., 2000)
Atmospheric related models and parameterizations
Hydrostatic tropospheric model (Saastamoinen, 1973) computed with GPT (Böhm et al., 2007) and mapped by GMF (Böhm et al., 2007)
Wet tropospheric delay mapped by wet- GMF (Böhm et al., 2006) and parameterized as piecewise-linear parameters every 2 hours
Gradients estimated in North-South and East-West direction every 24-hours (Rothacher et al., 1997)
Free-ionosphere linear combination used to eliminate the first order-term of the ionospheric refraction

in the (1D) **NEQs** are: station coordinates, site-specific troposphere parameters, orbital parameters (i.e., orbital elements, radiation pressure parameters, and stochastic pulses), **ERPs**, geocenter coordinates, and satellite antenna **PCOs** and **PCVs**, see Table 2.4.

2.4.2 Multi-Day Solutions

The multi-day solutions within the processing scheme at **CODE** consist of daily 3-days solution 3D, a weekly solution 7D, and a daily final 3-days solution 3F, see Fig. 2.4. All multi-day solutions are obtained at the normal equation level by reducing, combining, and estimating **NEQs** as described in Sect. 2.3.4.

The preliminary 3D solution is obtained by combining three 1D **NEQs** with the goal of having a 3-days long arc for satellite orbits. A 3-days arc is obtained from the 1-day arcs by enforcing continuity of satellite position and velocity at the interval boundaries of the middle day (Beutler et al., 1996). The nominal satellite arc length in multi-day solutions is therefore of three days. In the case of satellite modelling problems or satellite repositioning maneuvers, long arcs are split up in shorter arcs to avoid a degradation of results. Seven preliminary 3D **NEQs** are subsequently stacked to obtain a weekly 7D **NEQs** with station coordinates, **ERPs**, and geocenter parameters. These **SINEX** files eventually were sent to the **IGS** for the realization of the **ITRF2008** (see Chapter 1). Weekly solutions are analyzed and stations with a bad repeatability of coordinates are excluded. Finally, the 3F solution is obtained by tightly constraining coordinates and **ERPs** to the corresponding weekly results.

In summary we may state that the processing scheme of Fig. 2.4 allows it to obtain consistent final products, in particular weekly coordinates, weekly **ERPs** with daily values at 12:00 **Coordinated Universal Time (UTC)**, daily orbits with satellite positions and clocks every 15 min, and troposphere parameters with a resolution of 2 hours. Satellite clock corrections (Bock et al., 2009) and **GIM** (Schaer, 1999) consistent to all other final products are separately derived by zero-difference processing procedures.

2.5 Noise in Time Series of Parameters

Series of coordinates are often used to study plate tectonics (e.g., Sella et al., 2002), **GIA** (e.g., Peltier and Andrews, 1976; Peltier, 1976; Sella et al., 2007), and crustal deformations due to earthquakes (e.g., Ergintav et al., 2009), volcanoes (e.g., Larson et al., 2010), or other geophysical phenomena (Segall and Davis, 1997). Rates of coordinates are usually estimated by linear regression assuming that coordinates are normally distributed. Their power spectra, however, reveal that coordinate time series are not only contaminated by white noise but also by power-law processes (Agnew, 1992; Ray et al., 2008), i.e., the assumption that estimates are independent is not correct (Langbein and Johnson, 1997). The uncertainty of coordinate rates are usually too optimistic by up to one order of magnitude when this "white noise" assumption is made (Zhang et al., 1997; Mao et al., 1999; Williams et al., 2004).

A *power spectrum* of a time series represents the relative distribution of the total "energy" in the frequency domain. The so-called *power spectral density* P_i , $i = 1, \dots, m$, with m spectral lines at frequency $i\omega$, corresponds to the square of spectral amplitude \tilde{a}_i per unit

of frequency (e.g., in m^2/Hz) (see (e.g., [Beutler, 2005](#))):

$$P_i = \frac{\tilde{a}_i^2}{P_t} \quad \text{with} \quad P_t = \sum_{i=1}^m \tilde{a}_i^2. \quad (2.52)$$

[Agnew \(1992\)](#) describes power spectra $P_x(\nu)$ of geophysical time series x by fitting the following power-law model

$$P_x(\nu) = P_0 \cdot \left(\frac{\nu}{\nu_0} \right)^\kappa, \quad (2.53)$$

where ν is the frequency, P_0 and ν_0 are normalizing constants, and κ is the spectral index. The author reports how processes with $-3 < \kappa < -1$ are classified as non-stationary or "fractal Brownian", while the ones with $-1 < \kappa < 1$ are classified as stationary or "fractal Gaussian". Moreover, a particular noise emerges by integer spectral indexes: *white* noise for $\kappa = 0$, *flicker* noise for $\kappa = -1$, and *random-walk* noise for $\kappa = -2$. Power spectra are commonly illustrated by periodograms ([Scargle, 1982](#)).

Noise in time series may furthermore be assessed and cross-validated by **MLE** by estimating variance factors of specific covariance matrices describing the assumed noise present in the series, e.g., white noise, flicker noise, random-walk ([Langbein and Johnson, 1997](#); [Zhang et al., 1997](#)). In this context, many investigations using geodetic coordinate time series revealed that, apart from time-correlated noise such as annual, semi-annual, and other signals ([Ray et al., 2008](#)), fractal-white noise dominates at higher frequencies and fractal-Brownian noise at lower frequencies ([Langbein and Johnson, 1997](#)). Using **GPS** coordinate time series ([Zhang et al., 1997](#); [Calais, 1999](#); [Mao et al., 1999](#)) have shown that the best **MLE** solutions result when a combination of white noise and flicker noise models is assumed. The same conclusion was confirmed with slightly different approaches by ([Williams et al., 2004](#); [Amiri-Simkooei et al., 2007](#); [King and Williams, 2009](#)). [Calais \(1999\)](#) demonstrated that colored noise may be drastically reduced by spatially filtering the time series of a regional network. This suggests that the noise may likely originate from common sources such as satellite orbits, rather than a monument motion. [Mao et al. \(1999\)](#) indicated that stations in the Northern Hemisphere are not significantly noisier than stations in the Southern Hemisphere. On the other hand, [Williams et al. \(2004\)](#) showed that the colored noise is in general larger in the Southern than in the Northern Hemisphere, thus inversely proportional to the number of stations in each hemisphere. From other experiments, [Santamaría-Gómez et al. \(2011\)](#) showed by **MLE** with time-dependent variance factors that older data are in general noisier than newer ones within long time series of **GPS** coordinates, again, inversely proportional to the number of stations of the surveying network, this time. Not surprisingly, assuming white noise, from the **LSE** (see Sect. 2.3.3), we know that the size of the noise reduces with the square of the number of observations. This, therefore, may partially explain the results obtained in these latter experiments.

3 A Procedure to Analyze Coordinate Time Series

The automated procedure to analyze coordinate time series presented in this chapter is implemented in the **BSW** program **FODITS** (Ostini et al., 2008b,a, 2010b,a). The analysis of coordinate time series is a key procedure in a reprocessing context, especially when normal equations are cumulated to derive multi-year solutions (see Chapter 1).

The algorithm of the program **FODITS** adapts step-by-step a functional model to the time series containing sets of discontinuities, outliers, velocity changes, and periodic functions. The parameterization of these elements of the functional model is described in Sect. 3.1.

The analysis of coordinate time series by the program **FODITS** is supported by a list of predefined elements. Such a list is created from the information of an external log of earthquakes registered worldwide, from the history of equipment changes, from the test of the datum definition, and from a list of user-defined elements (see Sect. 3.2).

The iterative procedure in the program **FODITS** was originally closely related to the **DIA** procedure proposed by (Teunissen and Kleusberg, 1998b). The algorithm implemented in **FODITS** (see Sect. 3.3) as well as the search for discontinuities (see Sect. 3.4) were, however, rethought and optimized to meet the requirements, e.g., to perform an automated analysis of more than 500 station-specific coordinate time series within an acceptable processing time (see Sect. 1.2).

After having added step-by-step all significant predefined elements in the functional model, program **FODITS** searches for possible elements which help to optimally represent the analyzed time series. Such a search procedure is performed for discontinuities, outliers (see Sect. 3.5), velocity changes (see Sect. 3.6), and periodic functions (see Sect. 3.7). Last but not least, after having added the *most probable* element emerging from the search procedures to the functional model, the algorithm restarts by testing whether other predefined elements optimally describe the time series.

Sections 3.8 and 3.9 conclude the chapter with examples of time series analyses acting as internal and external validation procedures, respectively.

3.1 The Functional Model

The coordinate time series are parameterized in the **NEU** components as

$$\mathbf{f}(t_i) = \mathbf{d}_0(t_0) + \mathbf{v}_0(t_i - t_0) + \sum_{k=1}^{n_d} \mathbf{d}_k \eta_{d,k}(t_i) + \sum_{k=1}^{n_s} \mathbf{s}_k \eta_{s,k}(t_i) + \sum_{k=1}^{n_v} \mathbf{v}_k(t_i - t_k) \eta_{v,k}(t_i) + \sum_{k=1}^{n_p} [\mathbf{p}_{a,k} \cos(\omega_k(t_i - t_0)) + \mathbf{p}_{b,k} \sin(\omega_k(t_i - t_0))] \eta_{p,k}(t_i), \quad (3.1)$$

where $i = 1, \dots, N$ is the index of epoch t_i of the series of N elements. \mathbf{d}_0 and \mathbf{v}_0 are the initial offset and velocity, respectively. The functions $\eta_{d,k}(t_i)$, $\eta_{s,k}(t_i)$, $\eta_{v,k}(t_i)$, and $\eta_{p,k}(t_i)$ are either 0 or 1 to indicate the validity of the n_d discontinuities \mathbf{d}_k , the n_s outliers \mathbf{s}_k , the n_v velocities changes \mathbf{v}_k , and the n_p periodic functions (with phase $\mathbf{p}_{a,k}$ and out-of-phase $\mathbf{p}_{b,k}$ components), respectively.

Changes in horizontal coordinate components (North and East), e.g., after big earthquakes, may likely have an impact on the height (Up) component, too. Alternatively, if the vertical is the primary component affected by a change, e.g., after an equipment change, horizontal components (e.g., the centering of an antenna) may likely experience a change, as well. Since station coordinates are eventually estimated in the geocentric Earth-fixed **XYZ** reference system, it is therefore preferable to consider the time series as a three-dimensional vector defined by Eq. (3.1), rather than analyzing the vectors component-wise.

In order to simplify the analysis and to reduce the processing time coordinate time series of different stations are assumed to be independent. It is therefore possible to analyze time series station-by-station. The functional model given by Eq. (3.1) refers to one single station only. Furthermore, no time correlation is assumed between the data points of the time series. Only the space correlations (in North, East, and Up) are taken into account between components of the time series.

3.2 The A priori Known Elements

The support by predefined information allows it to carry out a more reliable analysis of the time series. It is well known that any equipment change induces a discontinuity in the coordinate time series. In such a case, one may benefit from the knowledge of that event by checking whether the change induced a significant offset in the time series or not. The same principle can be applied to all types of predefined information represented by the elements of the functional model (3.1). The a priori information considered by **FODITS** consists of the history of equipment changes (see Sect. 3.2.1), of a log of earthquakes registered worldwide (see Sect. 3.2.2), of periodic functions (see Sect. 3.2.3), and of a list of user-defined elements (see Sect. 3.2.5).

3.2.1 Equipment Changes

Configuration changes at permanent tracking stations (see Sect. 2.2.3), the so-called equipment changes, may induce systematic offsets and noise changes in the coordinate time series. Whether these changes are significant or not it depends on the assumptions of the statistical tests. Large discontinuities are usually induced by antenna changes such as the antenna (detector) itself, the radome, or imaging effects due to changes in the near field. On the other hand, changes such as that of the tracking receiver or a firmware upgrade often have a lesser impact on the offsets but a larger impact on the noise characteristics.

All changes at permanent tracking stations of the IGS network have been logged since the beginning of the IGS operations in 1992. Agencies operating tracking stations are in charge of keeping station LOG-files updated and to announce station problems and equipment changes via *IGSSTATION* mail—via *IGSMail* before 2004. LOG-files are administered by the IGS-CB and contain all relevant administrative, technical, and historical information.

Using the information in LOG-files ACs are able to create a list of equipment changes. The history of equipment changes at CODE is included in the so-called *station information file* (STA). The program FODITS reads the history information in the STA-file and updates the list of predefined elements: for each equipment change the program adds a discontinuity parameter to the list. No station velocity change is assumed after an equipment change.

Additional information about discontinuities can be exchanged via SINEX files. The officially confirmed discontinuities adopted by both, IGS¹ and EUREF², are related to the validity intervals of their TRF realizations.

3.2.2 Earthquakes

The list of earthquakes introduced in the analysis of the program FODITS is derived from the database of the U.S. Geological Survey (USGS) Earthquake Hazards Program³. Not all tracking stations are affected by the registered earthquakes worldwide. According to (Delle Donne et al., 2010), a station at a distance d_{erq} (in meters) from the epicenter of an earthquake of magnitude M_{erq} has a co-seismic displacement associated with the earthquake if

$$M_{erq,1} \geq -6.40 + 2.17 \cdot \log_{10} d_{erq}. \quad (3.2)$$

This condition, however, is only roughly representative for a permanent co-seismic displacement which an earthquake may cause in coordinate time series. No alternative approximations were found, which relate permanent co-seismic displacements with earthquake magnitudes and distances to epicenters. Nevertheless, from the time series analysis experience we learned that by shifting the offset in Eq. (3.2) by +0.8 magnitudes we obtain

$$M_{erq,2} \geq -5.60 + 2.17 \cdot \log_{10} d_{erq}, \quad (3.3)$$

¹<ftp://igs-rf.ign.fr/pub/discontinuities/soln.snx>

²ftp://epncb.oma.be/pub/station/coord/EPN/EPN_discontinuities.snx

³http://neic.usgs.gov/neis/epic/epic_global.html

which is more representative for permanent co-seismic displacements. Figure 3.1 shows the selection functions Eq. (3.2) and Eq. (3.3) as a function of the distance of the tracking station from the earthquake’s epicenter.

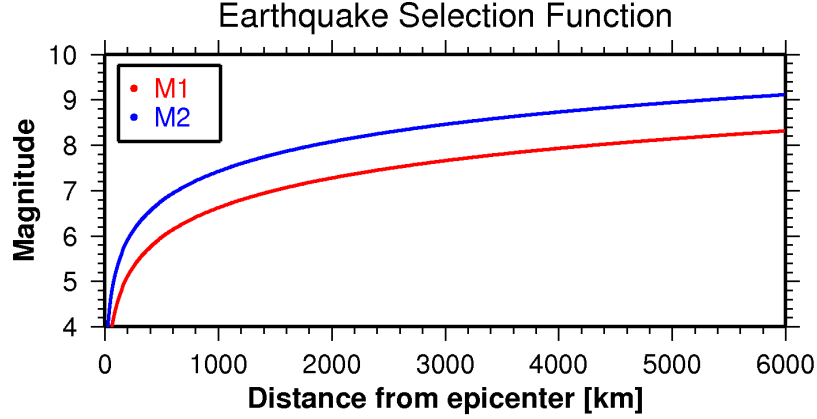


Figure 3.1: Selection functions for earthquakes. (M1) sensitivity function of earthquakes according to (Delle Donne et al., 2010). (M2) selection function adopted in program FODITS.

For each earthquake meeting condition (3.3) we add both a discontinuity and a velocity change to the list of predefined elements. The former, obviously, aims at modeling the permanent co-seismic displacement caused by the event. The latter, on the other hand, is thought to model the actual long-term change of the station velocity after the event.

Large earthquakes are usually followed by a series of aftershocks, which last over weeks or even months, e.g., (Yagi et al., 2001). In these cases, according to the selection criterion given by Eq. (3.3), the list of predefined elements will likely contain the main earthquake as well as many large aftershocks. Currently, for geodetic tasks such as **Terrestrial Reference System (TRS)** realization, there is not yet the need to model post-seismic relaxation phases of earthquakes. Therefore, to avoid modelling these phases by sequences of frequent discontinuities, aftershocks following large earthquakes might be removed from the list of predefined elements. This screening procedure works as follows: starting from the largest earthquake of the list to the smallest (in magnitude), all smaller earthquakes (w.r.t. the major one) appearing after the user-defined time interval Δt_{erq} are removed from the list. As a result, we obtain a list of predefined elements containing only the major earthquakes. From the experience of long time series it emerges that a value of $\Delta t_{erq} = 60$ days optimally removes the events related to post-seismic relaxation phases.

3.2.3 Periodic Functions

Coordinate time series of both, global and regional networks, show apparent quasi-seasonal—annual and semi-annual—signals (VAN DAM and Herring, 1994; Blewitt et al., 2000). Dong et al. (2002) classified these apparent quasi-seasonal signals into three categories, namely (1) of gravitational excitation, e.g., due to solid Earth tides, ocean tides, and atmospheric

tides, (2) of thermal origin coupled with hydrodynamics, e.g., due to thermal expansion of bedrock, wind shear, atmospheric pressure, and (3) due to various errors, e.g., satellite orbit model, atmosphere model, troposphere model, ionosphere model, and local multipath. The same author found that the primary contribution of such apparent signals, with 40% of the power, was identified in surface mass redistribution due to atmosphere, ocean, snow, and soil moisture. Petrov and Boy (2004) developed an Atmospheric Pressure Loading (APL) model based on the knowledge of the surface pressure field over the entire Earth. Dach et al. (2010) evaluated the impact of such APL model on reprocessed GPS data at CODE and found that the repeatability of station coordinates improves by up to 20%. King and Williams (2009) checked on 10 short baselines whether seasonal signals may be associated with thermal expansion, monument motion, multipath, phase center models, or to the cutoff angle. The authors found that monument motion may be a cause of seasonal signals. Within the IGS, products are obtained by processing daily sessions. For this reason un-modeled or mis-modeled sub-daily signals, e.g., of tidal origin, might induce spurious long-period signals such as annual and semi-annual periods (Penna and Stewart, 2003; Penna et al., 2007; King et al., 2008). From the spectral analysis of GPS coordinate time series Ostini (2007); Ray et al. (2008) found anomalous harmonics related to the draconitic year of the GPS constellation, with a length of approximately 352 days (e.g., Beutler, 2005). In addition to the contribution of periodic sources, position time series are also contaminated by non-periodic signals, e.g., signals due to non-tidal ocean loading (VAN DAM et al., 1997), silent earthquakes, and un-modelled snow accumulation on the antennas (Gendt et al., 2009). The composition of the apparent quasi-seasonal signals in the coordinate time series is not yet fully understood. It is recommended to use annual and semi-annual periodic functions when analyzing coordinate time series.

3.2.4 Outliers from the Test of the Datum Definition

Series of station coordinates might be tested epoch-by-epoch against a second set of coordinates by the Helmert transformation (2.42). For each epoch one obtains estimates of the Helmert parameters (2.44) set for the transformation as well as residuals for each station which contributed to the adjustment. This procedure is therefore ideal to identify "outliers" in terms of stations which contribute to the datum definition of the multi-year solution. For each epoch, one-by-one, stations which show residuals larger than user-defined thresholds in NEU components are rejected from the Helmert transformation and added to the list of predefined elements as outliers.

3.2.5 User-Defined List of Events

Predefined elements influencing the analysis may be added by the so-called EVents List (EVL) file. In this context, each element (i.e., a discontinuity, an outlier, a velocity change, or a periodic function) is listed with well-defined attributes. The first attribute defines whether the element is applied (a) unconditionally (i.e., without testing it for significance) introduced into the functional model or (b) checked for significance. A second attribute defines an interval of validity for such an element. This interval can be closed, open, or

even exclusive (i.e., defining an interval in which the element may not be applied). These options give the user the complete control to influence the resulting functional model.

3.3 The Procedure

The *algorithm* is designed to find the set of elements of the functional model (3.1) which optimally represents the analyzed time series. In the **BSW** context, **FODITS** is designed to assess the coordinate time series for a subsequent solution established by the program **ADDNEQ2**. To obtain such a solution, **ADDNEQ2** stacks series of **NEQs** and, according to the metadata-files **STA** (station information file), **FIX** (list of fiducial sites), **CRD/VEL** (a priori set of station coordinates and velocities), derives a so-called network solution, i.e., a set of station coordinates and velocities (**CRD/VEL**). Coordinate time series are generated by **ADDNEQ2**. These are time series delivered in a **PLT**-file format as residuals between the cumulative network solution and each **NEQ** solution of the series. Lists of predefined events support the analysis of coordinate time series, see Sect. 3.2.

3.3.1 General Aspects

The algorithm in **FODITS** step-by-step finds the element, which removes the largest discrepancy between the functional model and the time series. In other words, the analysis consists of classifying the peculiarities of the time series from the largest one down to smaller and smaller ones. A statistical test, based on an a level of significance, terminates the analysis when the functional model represents the time series in a satisfactory way.

The element candidates (discontinuities, outliers, velocity changes, and periodic functions) used in each step of the algorithm are derived either from a priori lists of collected information (see Sect. 3.2) or they are identified in the time series by a search.

The algorithm defines which candidate elements are identified in the time series and in which sequence they are added or removed to/from the functional model. Many strategies may be used. One may step-by-step collect all candidates in one list, check all candidates of such list in the functional model, and add the candidate to the functional model which obtains the largest value of a common test. This strategy underlies our algorithm. The advantage of having normal equations of small dimension to be inverted during the first steps is paid for the time-consuming set up of the functional model from the observations, when normal equations become large. One also could add all candidate elements to the functional model in one step and then step-by-step remove at the normal equation level the candidate, which obtains the smallest value of a common test. This was the strategy of the algorithm in (Ostini et al., 2008a). As opposed to the first strategy, the advantage of not reprocessing all time series at each step is paid for normal equations of large dimension to be inverted in the first steps.

By choosing the analysis strategy one has thus to consider advantages and disadvantages related to it. Other aspects to consider are, e.g., the method to support the analysis by the knowledge of a priori events, and the method to obtain reliable station velocities valid

for a reasonable long interval. Both these aspects could be considered either during the analysis or a posteriori of it.

In the algorithm of **FODITS** outlier elements are administered separately from other elements. Observations identified as outliers are excluded by reprocessing the time series, so that outlier elements are not set up as parameters in the functional model. This choice is dictated by the fact that coordinate time series are often contaminated by a large number of outliers, and a large number of outliers would imply to end up at each step of the analysis with a normal equation containing a large number of parameters. Compared to a **NEQ** describing the full functional model, the inversion of a **NEQ** without outlier parameters significantly reduces the computing efforts and, therefore, the overall processing time. However, no outlier estimates are obtained in such an analysis. For **FODITS** this is not relevant: outliers are derived as values *observed minus computed* after having applied the functional model to the time series, whereas their uncertainties are inherited from the previous step, i.e., from the estimation performed by **ADDNEQ2**.

3.3.2 Controlling the Algorithm

Without external control the algorithm would add more and more elements to the functional model as long as the degree-of-freedom (2.27) of the adjustment is positive. Therefore, in order to terminate the analysis at a reasonable point (when the functional model describes the time series in an acceptable way) the procedure is controlled by user-defined significance levels.

The choice to administer outlier elements in a different way than other elements led to adopt two statistical tests to control the algorithm, one for outlier elements and one for all other elements of the functional model. The drawback of having two statistical tests with two levels of significance to control the algorithm is largely compensated with the advantage of carrying out faster and more flexible analyses.

Test for Discontinuities, Velocity Changes, and Periodic Functions Discontinuity, velocity change, and periodic function elements of the functional model are all checked for significance by a statistical test based on the sum of weighted square residuals. A new element is added to the functional model based on the test value

$$T_t = \left(\frac{v_n^T P v_n}{v_p^T P v_p} - 1 \right) \cdot \frac{n_{obs}}{n_{obs,a}}, \quad (3.4)$$

with $v_n^T P v_n$ the new (after the addition of the element) and $v_p^T P v_p$ the previous (before the addition of the element) weighted sum of square residuals. n_{obs} and $n_{obs,a}$ form the factor to harmonize the test value for all analyzed time series (e.g., of the campaign), where $n_{obs,a}$ is the number of data common of all time series in absence of gaps. In an analog way, for the removal of an element from the functional model the test becomes

$$T_t = \left(\frac{v_p^T P v_p}{v_n^T P v_n} - 1 \right) \cdot \frac{n_{obs}}{n_{obs,a}}. \quad (3.5)$$

An element is added or removed, respectively, if

$$T_t \geq U_t , \quad (3.6)$$

where U_t is the user-defined level of significance for these elements, here also called the *overall level of significance to adapt the functional model*. The test (3.6) tells whether the impact of the added or of the removed element is significant or not. The test values (3.4) and (3.5) are also used to identify the element removing the largest or the smallest discrepancy between the functional model and the time series.

Test for Outliers Outliers, alternatively administered compared to all other elements of the functional model, are considered significant, if

$$T_s = \frac{|\mathbf{s}_c|}{\delta s_C} \geq U_s , \quad (3.7)$$

where δs_c is the formal error of the outlier candidate \mathbf{s}_c and U_s is the user-defined level of significance for outliers.

Additional Criteria for all Parameters Weekly solutions produced by **IGS ACs** are consistent on the 1-2 mm and 3-4 mm level for horizontal and vertical components, respectively (Ferland and Piraszewski, 2009). Therefore, elements of the functional model with absolute values smaller than these accuracy limits, do not have a reliable physical meaning, despite the fact that they have passed the above statistical tests. This is why additional criteria for horizontal, vertical, space, and single components of all elements of the functional model, for a total of 12 additional criteria, may be defined and they must be met. Elements not meeting these additional criteria will be considered as not significant.

Minimum Interval Length for Velocities Station velocities in the program **FODITS** are assumed to be linear in time. According to (Blewitt and Lavallee, 2002), reliable estimates of station velocities emerge from continuous **GNSS** observations spanning over more than 2.5 years.

Changes in the station velocity may typically be induced by earthquakes (see Sect. 3.2.2). Prominent examples are earthquake cycles: the **GPS** technique is often used to monitor inter-, co-, and post-seismic deformations due to earthquakes (Segall and Davis, 1997). Post-seismic phases, often characterized by aftershocks, are associated with the viscoelastic relaxation of the Earth lasting for 6 months or more (e.g., Ergintav et al., 2009; Kositsky and Avouac, 2010).

In order to obtain reliable station velocities the algorithm considers a user-defined *minimum interval length between successive velocity changes* variable Δt_v with default value of 2.5 years. Additional velocity change candidates, e.g., proposed to model a post-seismic phase of a large earthquake, not meeting this criterion are ignored, see Sect. 3.3.3.


```

1 Input: Read input time series from (CRDs) or (CRD/VEL/PLT) files
2 Input: Read predefined elements/events from (STA), (ERQ), or (EVL) files
3 Identify station "outliers" in the datum definition, and add them as outliers to the
  list of predefined elements;
4 forall station time series do
5   repeat identify new elements—iteration loop
6     repeat model screening—screening loop
7       repeat remove elements
8         Remove the non-significant element from the functional model which
          obtained the smallest value of the statistical test (3.6) using test
          value (3.5); At the same time all outliers not meeting the statistical
          test (3.7) are removed from the functional model;
9         until all elements in the functional model are significant;
          Insert in the functional model the significant a priori element candidate,
          which obtained the largest value of the statistical test (3.6) using test
          value (3.4) and meets the minimum interval length between successive
          velocity changes; Add all predefined outliers meeting the statistical test
          (3.7); Additional criteria must be met at the same time;
10        until functional model equal as one of the previous (screening loop) steps;
          Identify in the post-fit residuals the most probable:
          – (epochs of) discontinuities by Eq. (3.19) on page 43;
          – (epochs of) outliers by Eq. (3.20) on page 50;
          – (epoch of) a velocity change by Eq. (3.23) on page 53;
          – (period of) periodic functions by Eq. (3.26) on page 56;
          Collect all identified elements in a list of candidates;
11        Insert the significant identified element candidate into the functional model,
          which obtained the largest value of the statistical test (3.6) based on the
          test value (3.4) and which meets the minimum interval length between
          successive velocity changes; Add all outliers which meet the statistical test
          (3.7); Additional criteria must be met at the same time;
          until functional model equal to one of the previous (iteration loop) steps;
        end
      end
    end
12 Output: Write list of events (EVL) and (OUT) file
13 Output: Write updated (CRD/VEL/STA/FIX) files for successive ADDNEQ2 run

```

Figure 3.2: The algorithm of **FODITS**. Acronyms: (CRD) file of station coordinates, (VEL) file of station velocities, (PLT) file of residual time series, (STA) station information file, (ERQ) list of earthquakes worldwide, (EVL) list of events, (OUT) output file, see (Dach et al., 2007).

3.3.3 The Algorithm

The algorithm of the program **FODITS** is illustrated by Fig. 3.2. It consists of the following steps:

1. Coordinate time series are either read from (a) a list of coordinate files (CRDs) or

- they are (b) reconstructed from the file of residuals (PLT) in conjunction with the coordinate and velocity result files (CRD/VEL). The space **VCI** of the coordinate time series may be provided via file of residuals (PLT) if the case (b) is selected.
2. A list of predefined elements representing equipment changes (STA, see Sect. 3.2.1) and earthquakes (ERQ, see Sect. 3.2.2) is generated from the input files. Additional elements of the functional model can be used via user-interface of the program or predefined by the user via a so-called event list (EVL, see Sect. 3.2.5).
 3. Test epoch-by-epoch the datum definition according to Sect. 3.2.4.
 4. The analysis is performed independently for each station.
 5. The procedure enters the loop to identify new elements in the time series.
 6. The procedure enters the loop to insert a priori elements in the functional model and remove non-significant elements from it.
 7. Elements are removed from the functional model until all remaining elements are significant. No elements are removed during the first iteration step and first screening step because the functional model consists of the solely initial offset and initial velocity.
 8. On the basis of the statistical test (3.6) based on the test value (3.5) the element, which contributes least to describe the time series is removed from the functional model. Simultaneously, according to the statistical test (3.7), all non-significant outliers are removed from the functional model, as well.
 9. The predefined elements (see Sect. 3.2) are checked in the functional model one after the other using the statistical test (3.6) based on the test value (3.4). The condition of a minimum interval length between successive velocity changes is Δt_v (see Sect. 3.3.2) must be met when checking velocity change candidates. Moreover, according to the statistical test (3.7) all significant predefined outlier candidates are added to the functional model, as well. All elements must also meet the additional criteria.
 10. The searches for discontinuities (see Sect. 3.4), outliers (see Sect. 3.5), velocity changes (see Sect. 3.6), and periodic functions (see Sect. 3.7) propose elements which reduce the discrepancy between the functional model and the time series. These proposed elements are collected in a list of candidate elements. In this way it is possible that searches propose more than one candidate per element-type. This feature is exploited by the algorithm in three cases. First, for the search for discontinuities time series are divided in sub-intervals, and for each sub-interval the search proposes one candidate. This is particularly efficient when time series are contaminated by colored noise (see Sect. 3.4 on page 41). Second, the maximum number of outlier candidates is user-defined, i.e., more than only one outlier may be added to the functional model (see Sect. 3.5 on page 49). Last, a velocity change candidate may be proposed in conjunction with each known discontinuity of unknown reason. For analyses of coordinate time series this feature might. e.g., help to model induced effects such as "snow on the antenna" (Gendt et al., 2009).
 11. The candidate elements collected in step 10 are checked one-by-one in the functional

model. Then, the *most probable* element, i.e., the element removing the largest discrepancy between the functional model and the time series, is added to the functional model. Such element must meet the statistical test (3.6) based on the test value (3.4) and the minimum interval length between successive velocity changes Δt_v . At the same time, significant outlier candidates are added to the functional model according to Eq. (3.7). All elements must also meet the additional criteria.

12. Output files are created. All elements of the functional model of all analyzed stations are reported in the event list (EVL, see Sect. 3.2.5).
13. The files for a follow-up **ADDNEQ2** run are updated.

The core algorithm of **FODITS** may be seen as a modified version of the **DIA** procedure (Teunissen and Kleusberg, 1998b) with the opportunity to propose predefined elements. Lists of predefined elements as well as searches can be independently selected.

3.4 Searching for Discontinuities

Time series of coordinates often contain discontinuities. Williams (2003) estimates from an analysis of ten various published data sets that on average time series are contaminated by one offset every 9 years. They are either due to natural events such as earthquakes (see Sect. 3.2.2) or of "artificial origin" (e.g., equipment changes, see Sect. 3.2.1). The latter may also be do to model or strategy changes in data processing, to malfunctioning equipments, to anthropogenic reasons (e.g., vandalism or human errors), to changes in the environment, etc. Not all changes are reported to the **IGS-CB**. Hence, besides discontinuities of known reason, coordinate time series may be contaminated by discontinuities of unknown reason, as well.

According to the step 10 of the algorithm in Fig. 3.2 a search identifies *most probable discontinuities* in the time series of post-fit residuals. The search proposes a discontinuity candidate for each sub-interval emerging from discontinuities and/or velocity changes in the functional model. Therefore, for n discontinuities and/or velocity changes in the functional model the search proposes $n + 1$ discontinuity candidates.

There are two important advantages of proposing one discontinuity candidate for each sub-interval of the time series. First, the search is more reliable, if time series contain only one discontinuity. Second, the search is more reliable, if time series are affected by colored noise. The algorithm **FODITS** especially benefits from these two advantages with the progress of the analysis and, more in particular, with the identification of more and more discontinuities and/or velocity changes.

3.4.1 Mathematical Principle

The search for the epoch of the most probable discontinuity in the time series of the residuals was derived from the theory of quality control proposed by (Baarda, 1968; Teunissen and Kleusberg, 1998b). The theory aims at validating the assumptions for the modification

of functional and stochastic models. For our case there are two assumptions related to the linear **GMM** (2.20): It is assumed that the time series contain only white noise. It is furthermore assumed that the functional model is correct, i.e., it does not contain errors. As we only want to identify the epoch of the discontinuity with the largest discrepancy between functional model and time series, only the second assumption needs to be validated.

According to (Teunissen and Kleusberg, 1998b), an error in the functional model may be verified by formulating the following null and alternative hypotheses

$$\begin{aligned} H_0 &: \mathbf{E}(\mathbf{y}) = \mathbf{A}\mathbf{p}, & \mathbf{D}(\mathbf{y}) &= \mathbf{Q}_{yy} \\ H_A &: \mathbf{E}(\mathbf{y}) = \mathbf{A}\mathbf{p} + \mathbf{C}\nabla, & \mathbf{D}(\mathbf{y}) &= \mathbf{Q}_{yy}. \end{aligned} \quad (3.8)$$

The null hypothesis H_0 states that the functional model is free of errors, while the alternative hypotheses H_A states that the functional model contains the bias $\mathbf{C}\nabla$, with \mathbf{C} the known error and ∇ the unknown size. The statistical test to infer whether the null hypothesis H_0 has to be rejected in favor of the alternative hypothesis H_A has its roots in the **Generalized Likelihood Ratio** (GLR) (Salzmann, 1993; Koch, 1999; Casella and Berger, 2001). The ratio test compares the Likelihood function of H_0 to the one of H_A . According to (Teunissen and Kleusberg, 1998b) the test quantity becomes

$$T_d = \frac{1}{d} \mathbf{v}^T \mathbf{Q}_{yy}^{-1} \mathbf{C} [\mathbf{C}^T \mathbf{Q}_{yy}^{-1} \mathbf{Q}_{vv} \mathbf{Q}_{yy}^{-1} \mathbf{C}]^{-1} \mathbf{C}^T \mathbf{Q}_{yy}^{-1} \mathbf{v}. \quad (3.9)$$

The null hypothesis H_0 is rejected in favor of the alternative hypothesis H_A if

$$T_d \geq F_\alpha(d, \infty, 0), \quad (3.10)$$

where α is the user-defined level of significance, and d the dimension of the test. $F_\alpha(d, \infty, 0)$ corresponds to the F-distribution with d and ∞ degree-of-freedoms.

The d -dimensional matrix \mathbf{C} defines the error considered by Eq. (3.9). According to (Teunissen and Kleusberg, 1998b) one checks in the time series of n_{obs} observations whether a significant discontinuity exists at epoch t_k by defining the one-dimensional test vector

$$\mathbf{c}_k = \begin{cases} 0 & \text{for } i = 1, \dots, k-1 \\ 1 & \text{for } i = k, \dots, n_{obs}. \end{cases} \quad (3.11)$$

The identification step of the **DIA** procedure finds the most probable discontinuity by: (1) testing the alternative hypothesis (3.8) for all n_{obs} epochs of the time series, and by (2) proposing the epoch which obtained the largest value of the statistical test (3.9) as most probable discontinuity—if statistically significant. This implies that the epoch $t_{A,j}$ of the identified discontinuity meets the criterion

$$g(t_{A,j}) = \max(T_{A,1}, \dots, T_{A,n_{obs}}), \quad (3.12)$$

with T_A the one-dimensional test (3.9). For the three-dimensional case Eq. (3.11) is build with identity matrix $I_{3 \times 3}$.

The analysis of time series by the algorithm introduced in Sect. 3.3 together with the search for discontinuities (3.12) is CPU-time intensive. This is particularly true when

daily coordinate time series spanning over more than ten years are analyzed for more than 500 stations. This is why we propose an optimized statistical test for discontinuities by starting from the one-dimensional case of Eq. (3.9)

$$T_1 = \mathbf{v}^T \mathbf{Q}_{yy}^{-1} \mathbf{c} [\mathbf{c}^T \mathbf{Q}_{yy}^{-1} \mathbf{Q}_{vv} \mathbf{Q}_{yy}^{-1} \mathbf{c}]^{-1} \mathbf{c}^T \mathbf{Q}_{yy}^{-1} \mathbf{v} . \quad (3.13)$$

The optimization is based on an heuristic approach. If coordinate time series are not provided along with their **VCI** (as described in step 1 of the algorithm, see Fig. 3.2), the **VCI** of the observations are assumed to be the identity matrix, i.e., $\mathbf{Q}_{yy}^{-1} = \mathbf{I}$. This assumption reduces Eq. (3.13) to

$$T_1 = \mathbf{v}^T \mathbf{c} [\mathbf{c}^T \mathbf{Q}_{vv} \mathbf{c}]^{-1} \mathbf{c}^T \mathbf{v} , \quad (3.14)$$

with $\mathbf{Q}_{vv} = \mathbf{I} - \mathbf{A} \mathbf{Q}_{\hat{p}\hat{p}} \mathbf{A}^T$, see Eq. (2.25). As the F-distribution in Eq. (3.10) refers to the **VCI** of the observations, the original statistical meaning of the test is lost. The denominator $\mathbf{c}^T \mathbf{Q}_{vv} \mathbf{c}$ can therefore be set to one and Eq. (3.14) reduces to

$$T_1 = \mathbf{v}^T \mathbf{c} \mathbf{c}^T \mathbf{v} = (\mathbf{v}^T \mathbf{c})^2 , \quad (3.15)$$

where $(\mathbf{c}^T \mathbf{v})^T = \mathbf{v}^T \mathbf{c}$ was used. Because the only interest of the test is to find which alternative hypothesis H_A in Eq. (3.8) obtains the largest value, Eq. (3.15) may be further simplified to

$$T_1 = |\mathbf{v}^T \mathbf{c}| . \quad (3.16)$$

By using the test matrix \mathbf{c} given in Eq. (3.11) we obtain

$$T_{1,k} = \left| \sum_{i=k}^{n_{obs}} \mathbf{v}_i \right| . \quad (3.17)$$

The new search based on the optimized test (3.17) results in the discontinuity epoch $t_{B,j}$, where

$$g(t_{B,j}) = \max(T_{B,1}, \dots, T_{B,n_{obs}}) \quad \text{with} \quad T_{B,k} = \left| \sum_{i=k}^{n_{obs}} \mathbf{v}_i \right| . \quad (3.18)$$

Figure 3.3 illustrates the normalized search (D-TST) for the most probable discontinuity in the one-dimensional daily coordinate time series 3.3a with the original test Eq. (3.12) and 3.3b with the optimized test Eq. (3.18). The two searches result in slightly different normalized search series, but found the same epoch of the most probable discontinuity, namely 15-Dec-2006. The optimized search $t_{B,j}$ is more than 100 times faster than the original one $t_{A,j}$, about 1sec versus about 160sec, respectively. Both searches found the correct epoch despite the fact that the time series are contaminated by outliers and despite the fact that the discontinuity is not a step function.

The performance of the test (3.18) is reduced in the presence of long gaps. In order to improve the robustness of the test we propose to use

$$g(t_{C,j}) = \max(T_{C,1}, \dots, T_{C,n_{obs}}) \quad \text{with} \quad T_{C,k} = \left| \sum_{i=k}^{n_{obs}} \mathbf{w}_i \right| \quad (3.19)$$

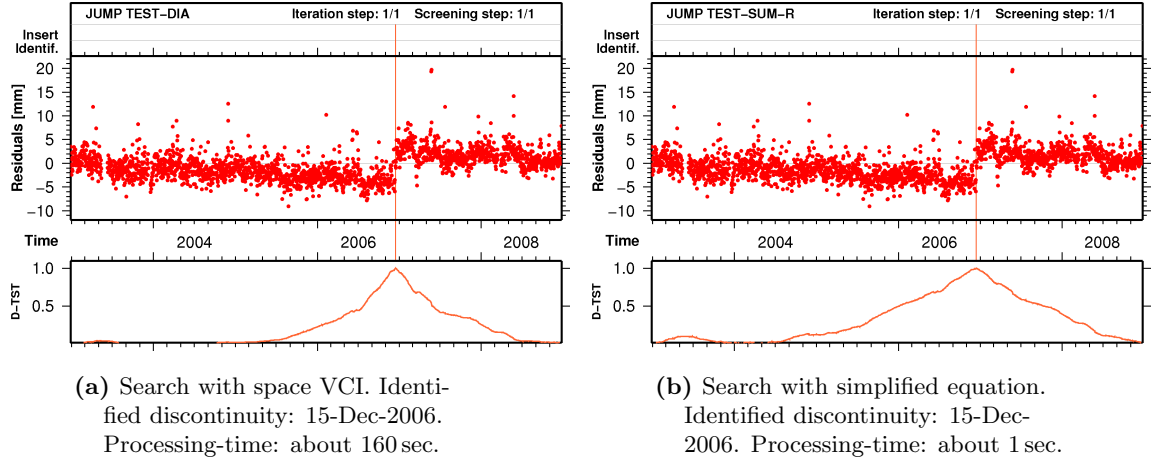


Figure 3.3: Search for discontinuities (a) with space **VCI** and (b) in simplified form. (D-TST): normalized search. Time series: North component of **CODE** daily coordinates, station PDEL 31906M004.

to find the epoch $t_{C,j}$ of the discontinuity, where \mathbf{w} is the time series of residuals obtained from a linear regression through the original time series of the residuals \mathbf{v} , but with the peculiarity $t_i = i$ for $i = 1, \dots, n_{obs}$. In other words, before the fit to obtain the new residuals \mathbf{w} pseudo-observations (i.e., the residuals \mathbf{v}) are artificially spaced in time by a constant unitary amount. Accordingly to the derivation of the test, no **VCI** is taken into account.

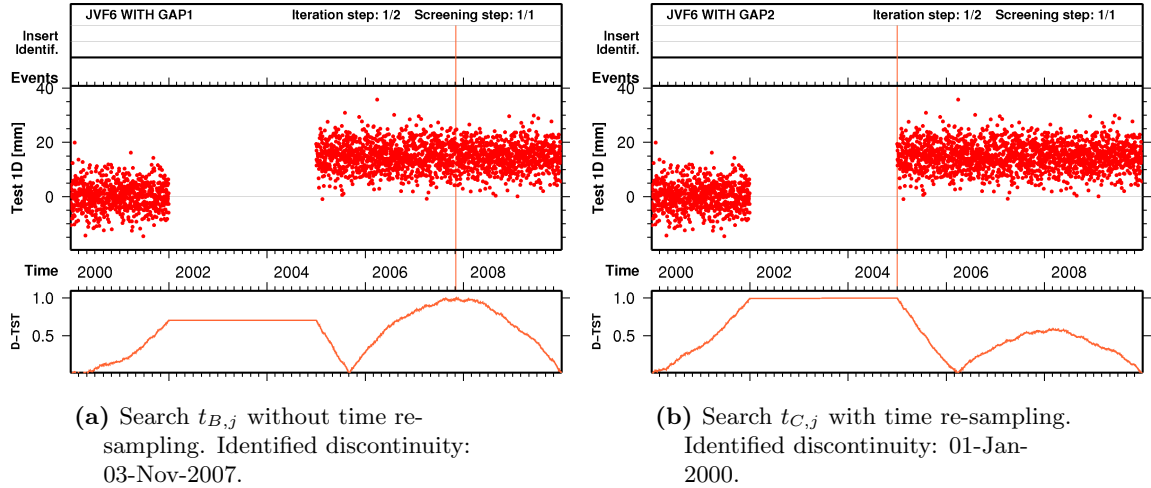


Figure 3.4: Search for discontinuities without (a) and with (b) time re-sampling. (Red) time series: synthetic data $\sim N(0,25)$; discontinuity of +15 mm at the epoch 01-Jan-2002; data gap of 3 years. (D-TST): normalized search.

Figure 3.4 shows the search (D-TST) for both cases, (3.4a) without new sampling ($t_{B,j}$)

and (3.4b) with new sampling ($t_{C,j}$). It is evident that the former test fails and the latter succeeds. For this reason, the implemented search for discontinuities in the algorithm **FODITS** is $t_{C,j}$ given by Eq. (3.19).

Last but not least, the search (3.19) exploits the fact in the context of a **LSE** that if $\sum_{i=k}^{n_{obs}} \mathbf{w}_i^2 = \min$, then $\sum_{i=k}^{n_{obs}} \mathbf{w}_i = 0$. Broadly, such implication might be interpreted as a "first derivative of the minimum principle".

3.4.2 Validation with Synthetic Time Series

The search for unknown discontinuities using Eq. (3.19) is performed with the algorithm implemented in **FODITS** presented in Sect. 3.3. In each figure, the sequence of sub-figures (generally to read from top to bottom, and left to right) shows the progress of the algorithm after each iteration step. The progress is reported in the header of the sub-figures with the exception of the last step, where the final result is shown. The (black) line in the foreground w.r.t. the observations (in background) represents the *current* functional model (3.1) used in the analysis. The search for discontinuities, but indirectly also the algorithm, are validated with one-dimensional and three-dimensional synthetic time series. The overall level of significance to adapt the functional model (3.6) was set to $U_t = 0.002$ for all validations. No additional criteria were used. All synthetic time series contain offsets and white noise. White noise is denoted in each experiment by $\sim N(\mu, \sigma^2)$, with mean value μ in millimeters and variance σ^2 in square millimeters (\sim denotes "proportional to").

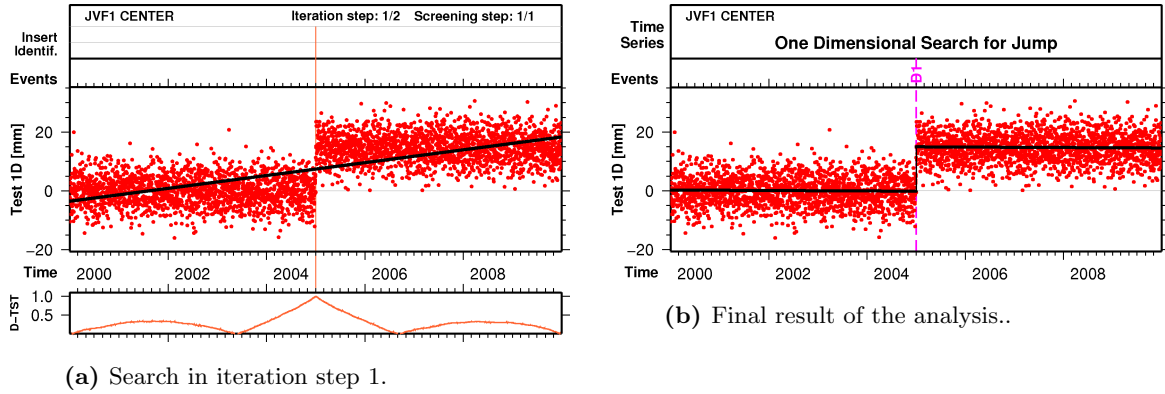


Figure 3.5: Validation of search for discontinuities. (Red) time series: synthetic data $\sim N(0,25)$; discontinuity of +15 mm on 01-Jan-2005; (Black) functional model. (D-TST) normalized search for discontinuities.

Figures 3.5, 3.6, and 3.7 show the validation of the search (3.19) with the one-dimensional synthetic time series containing white noise $\sim N(0,25)$ and one discontinuity of +15 mm, which appears in three different scenarios. For each experiment we see that at the end of the first iteration step the search for discontinuities (D-TST) proposes the epoch $t_{C,j}$ (vertical line). In all three experiments the analysis terminated at the end of the second iteration step after having identified one discontinuity of about +15 mm. Table 3.1 summarizes

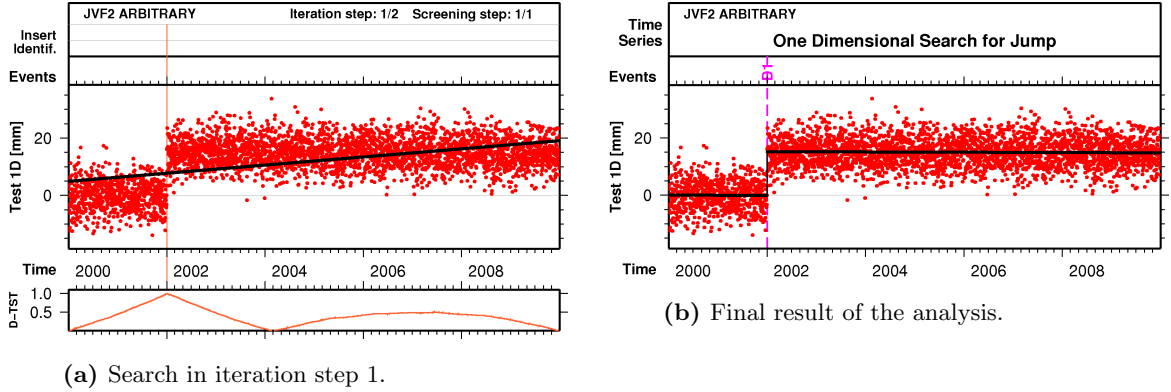


Figure 3.6: Validation of search for discontinuities. (Red) time series: synthetic data $\sim N(0,25)$; discontinuity of +15 mm on 01-Jan-2002; (Black) functional model. (D-TST) normalized search for discontinuities.

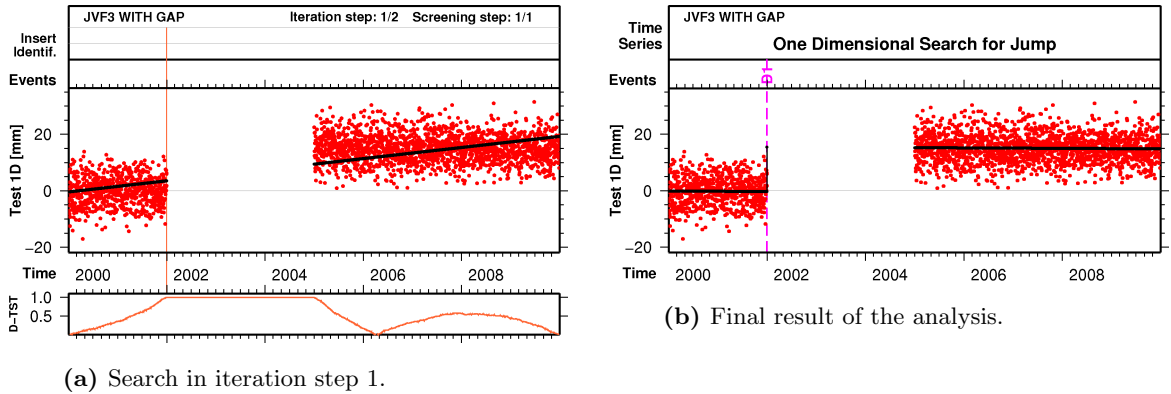


Figure 3.7: Validation of search for discontinuities. (Red) time series: synthetic data $\sim N(0,25)$; discontinuity of +15 mm on 01-Jan-2005; data gap of 3 years. (Black) functional model. (D-TST) normalized search for discontinuities.

the results. Figure 3.7 shows however that the epoch of discontinuity (31-Dec-2001) is associated with the last observation prior to the data gap of 3 years. This is due to the re-sampling performed for the search (3.19), which removed the long gap of data. As a result, the search preferred the epoch priori to the gap. Let us look the RMS error of the estimated discontinuity. As there are fewer data points in the time series (compared to the other two experiments) the formal error (2.28) of the offset (0.542 mm) in Fig. 3.7 must be larger than for the other two experiments. The RMS error is in fact inversely proportional to $\sqrt{n_{obs}}$. The difference of the RMS errors in Fig. 3.5 (of 0.331 mm) and 3.6 (of 0.284 mm) has other sources. Williams (2003) illustrates the variation of the formal error of the estimated discontinuity as a function of its position in the time series: the smallest uncertainties are near 1/4 and 3/4 of the time series, while the uncertainty becomes larger in the middle and at the boundaries. This explains why the uncertainty of the estimated offset in Fig. 3.6

Table 3.1: Validation of the search for discontinuities. Synthetic time series in one component with one discontinuity.

Time series	Label	Introduced [mm]		Identified [mm]		σ
		Epoch	Value	Epoch	Value	
JVF1 CENTER	D1	01-Jan-2005	+15.0	01-Jan-2005	+15.088	0.331
JVF2 ARBITRARY	D1	01-Jan-2002	+15.0	01-Jan-2002	+15.275	0.284
JVF3 WITH GAP	D1	01-Jan-2005	+15.0	31-Dec-2001	+15.777	0.542

is slightly lower than the one in Fig. 3.5. Except for the last experiment, the estimated values of the discontinuities were within the 1σ boundary ranges, see Table 3.1.

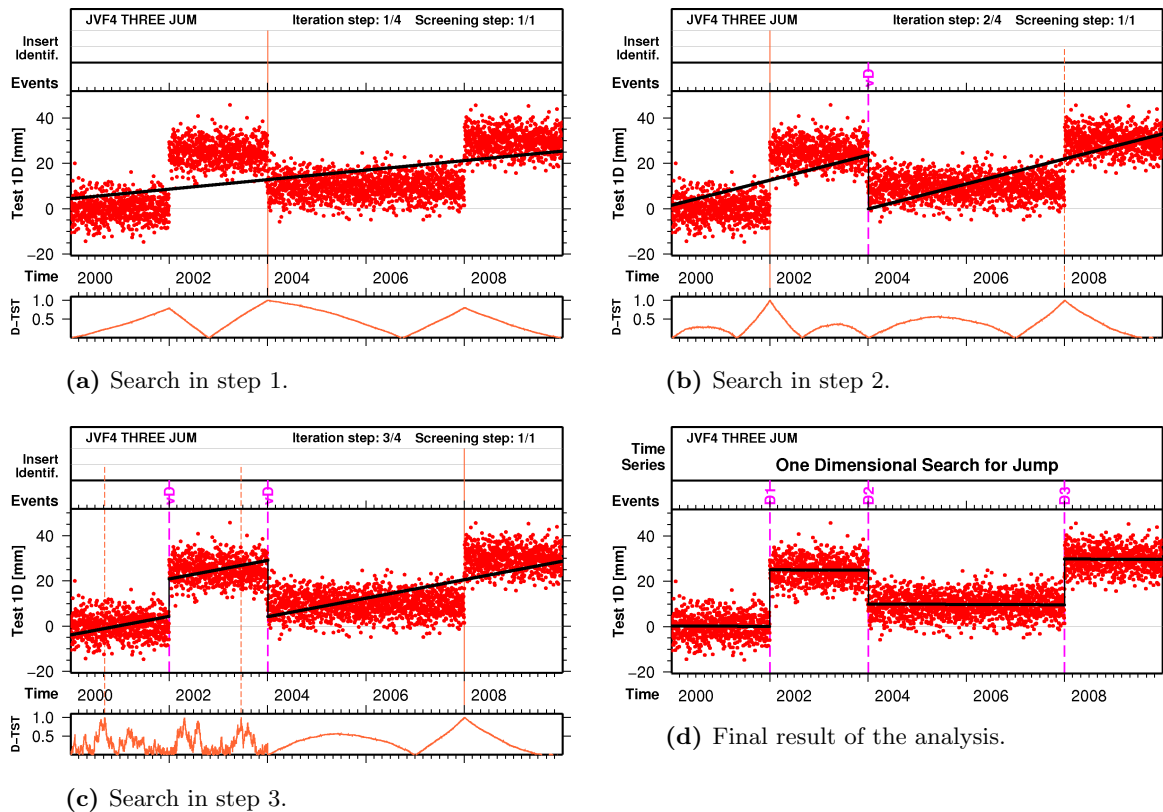


Figure 3.8: Validation of search for discontinuities in one-dimensional time series with three discontinuities. (Red) time series: synthetic data $\sim N(0,25)$. (Black) functional model. (D-TST) normalized search for discontinuities.

Figure 3.8 illustrates the performance of the algorithm with one-dimensional synthetic time series with white noise and three discontinuities. The algorithm needed four iteration steps for the analysis. In the fourth step the procedure terminated because no further significant discontinuity was found. Let us briefly look at the steps. In the first step (see Fig. 3.8a) the algorithm approximates the time series with a linear function (black line),

Table 3.2: Validation of the search for discontinuities. Synthetic time series in one component with three discontinuities.

Time series	Label	Introduced [mm]		Identified [mm]		
		Epoch	Value	Epoch	Value	σ
JVF4 THREE JUM	D1	01-Jan-2002	+25.0	01-Jan-2002	+24.899	0.325
JVF4 THREE JUM	D2	01-Jan-2004	-15.0	03-Jan-2004	-14.910	0.367
JVF4 THREE JUM	D3	01-Jan-2008	+20.0	01-Jan-2008	+20.147	0.367

Table 3.3: Validation of the search for discontinuities. Synthetic time series in three components with three discontinuities.

Time series	Label	Introduced [mm]			Identified [mm]				
		Epoch	Comp.	Value	Epoch	North	East	Up	σ
JVF5 THREE DIM	D1	01-Jan-2002	North	+5.000	31-Dec-2001	+5.1	+0.5	+0.3	0.6
JVF5 THREE DIM	D2	01-Jan-2004	East	-10.000	01-Jan-2006	+0.4	-9.5	-0.7	0.6
JVF5 THREE DIM	D3	01-Jan-2008	Up	+20.000	01-Jan-2008	+0.1	-0.1	+20.9	0.6

and searches for the epoch of the largest discontinuity (D-TST). The three maxima in (D-TST) correspond to the epochs of the three discontinuities. The second one promises to be the most probable one. In the second step (see Fig. 3.8b) the search proposes the next most probable discontinuities. Note that the test value is zero at the epoch of the previously identified offset (vD), because discontinuities are sought separately in all sub-intervals separated by significant discontinuities. Note that the discontinuity at epoch 01-Jan-2008 was also proposed (thin dashed line), but the one on 01-Jan-2002 was selected. In the third iteration step (Fig. 3.8c) the algorithm proceeds in analogy to the second iteration step. No pronounced discontinuities are present in the two first intervals. The final result is illustrated by Fig. 3.8d. Except for the discontinuity (D2), which was identified on 03-Jan-2004 and not on 01-Jan-2004, all other two discontinuities were associated with the correct epoch, see Table 3.2. The same table also reports that all estimated discontinuities are within the 1σ boundary ranges.

Figure 3.9 shows the validation of the algorithm with three-dimensional synthetic time series contaminated by white noise and three discontinuities, one in each component (North, East, and Up). The search (D-TST) seeks for unknown discontinuities in all components simultaneously. According to Eq. (3.19) the test value (D-TST) is obtained as the quadratic mean of each single search per component. The sequence of sub-figures shows that four iteration steps were needed to identify the three discontinuities introduced into the synthetic time series. The figure shows furthermore that the discontinuities were identified from the largest (in the Up component) to the smallest one (in the North component), as expected in the algorithm in FODITS. Figure 3.9d reveals one more detail: the estimated discontinuities are three-dimensional, consistent to the model description in Sect. 3.1. Table 3.3 summarizes the results. All estimated discontinuities are within the 1σ boundary ranges.

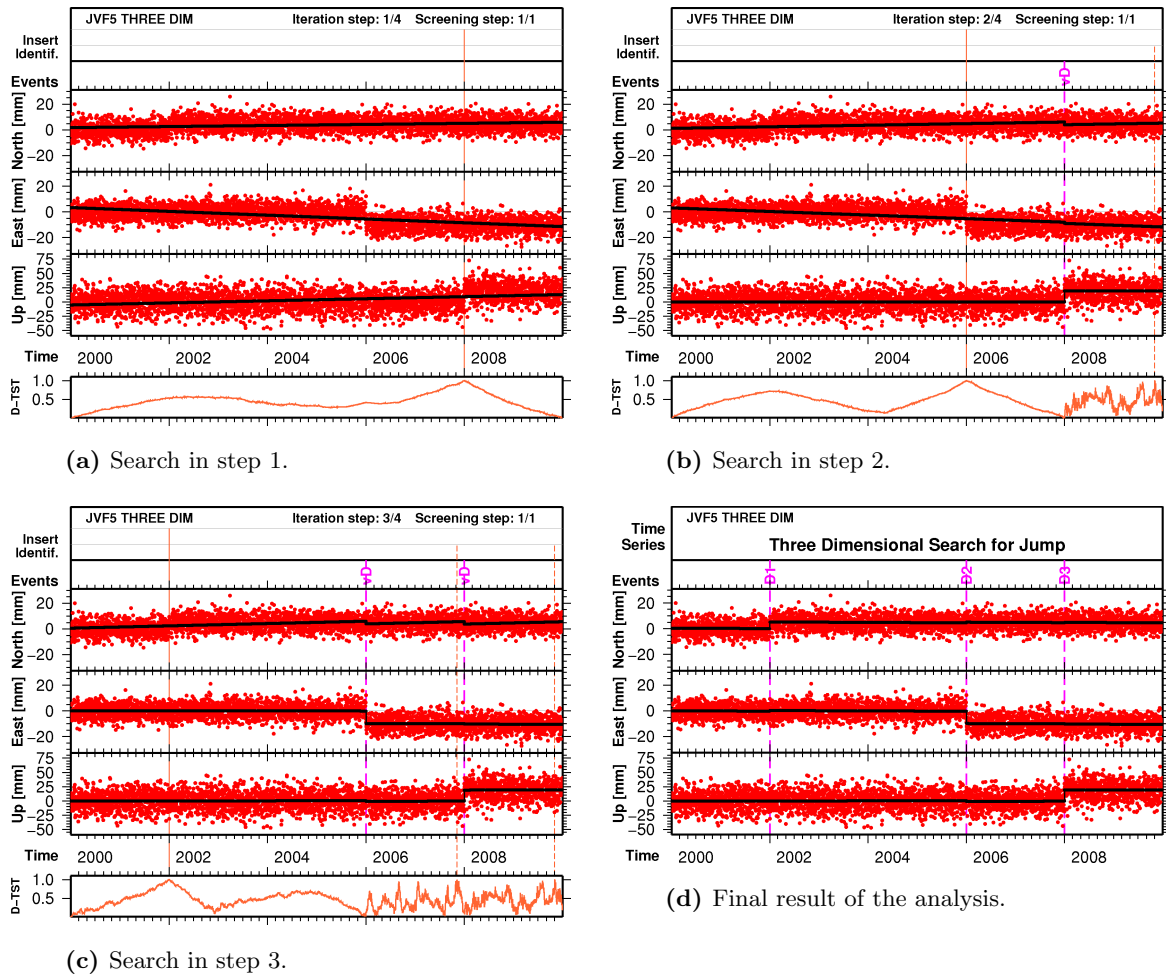


Figure 3.9: Validation of search for discontinuities in three-dimensional time series with three discontinuities. (Red) Time series: synthetic North and East data $\sim N(0,25)$, Up data $\sim N(0,225)$. (Black) functional model. (D-TST) normalized search for discontinuities.

3.5 Search for Outliers

The identification of outliers depends on the statistical assumptions, namely null and alternative hypotheses, statistical test, and the level of significance (Barnett and Lewis, 1994). Baarda (1968) proposed to identify an outlier in a dataset using the theory of reliability and quality control. Forty years later this approach is still studied. Nathan et al. (2010) generalize measures of reliability for multiple outliers. Teunissen and Kleusberg (1998b) propose the **DIA** procedure to identify and remove outliers in the time series. A comparison of several statistic tests applied to **GNSS** derived time series was proposed by (Kern et al., 2005). Outliers in coordinate time series are usually due to systematic errors, instrumental malfunction, image-induced effects, adverse atmospheric conditions, anthropogenic reasons,

etc.

According to the step 10 of the algorithm described in Fig. 3.2 a search identifies the *most probable outliers* in the post-fit residual time series. As described in Sect. 3.3 all observations identified as outliers, significant according to Eq. (3.7), are added to the functional model at step 11 of the algorithm.

3.5.1 Mathematical Principle

The search to identify outliers in the post-fit residuals w.r.t. the functional model (3.1) is based on the statistical test (3.7). An epoch $t_{O,i}$ is assumed to be associated with an outlier, if

$$T_{O,i} = \frac{|\mathbf{v}_i|}{\delta v_i} \geq U_s \quad \text{for } i = 1, \dots, n_{obs}, \quad (3.20)$$

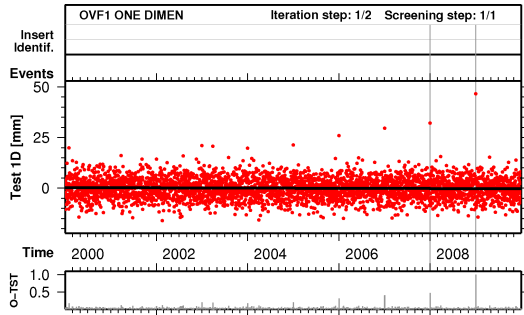
where, U_s is the user-defined level of significance for outliers, $\delta v = m_0 \sqrt{\mathbf{T} \mathbf{Q}_{yy}(\mathbf{v}) \mathbf{T}^T}$ is the **RMS** error of the outlier candidate (residual) \mathbf{v} , with \mathbf{T} the transformation matrix, and m_0 the a posteriori **RMS** of unit weight (see Sect. 2.3.3).

As stated in Sect. 3.3.1, the search for outliers accounts for the **VCI** of the observations (i.e., $\mathbf{Q}_{yy}(\mathbf{v})$) instead of the cofactor matrix derived from the adjustment (i.e., $\mathbf{Q}_{\hat{p}\hat{p}}(\mathbf{v})$). If, however, the **VCI** of the observations is not available, δv takes the value of σ_0 —the value of the user-defined a priori **RMS** of unit weight, which has a conventional value of 1 mm within the **BSW** (Dach et al., 2007).

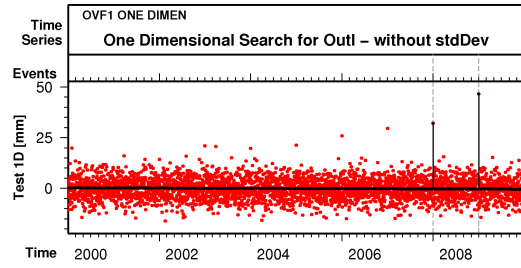
3.5.2 Validation with Synthetic Time Series

The validation of the search for outliers is delivered by two experiments. The time series of both experiments are the same. These mainly consist of white noise $\sim N(0,25)$. Starting from an outlier of 5 mm on January 1, 2001, outliers of $n \cdot 5$ mm are added at the beginning of subsequent years into the time series. In the first experiment, illustrated by Fig. 3.10, outliers are sought without using the **VCI** of the observations, whereas in the second experiment, illustrated by Fig. 3.11, the identification is carried out by using the **VCI**. The progress of the algorithm is documented in the header of the figures with the exception of the final step. The normalized search for outliers is denoted as (O-TST). The results of both experiments are given in Table 3.4.

For the first experiment the level of significance for outliers is set to $U_s = 30$. Figure 3.10 reveals that the algorithm needed two iteration steps. In the first step, in Fig. 3.10a, two observations were identified as outlier candidates: The first on 01-Jan-2008 and the second on 01-Jan-2009. Figure 3.10b shows that both were confirmed to be significant in the next iteration step of the algorithm, the first with a statistical test of value of 32.3 and the second with one of 46.9, see Table 3.4. As stated in Sect. 3.5.1 the standard deviation of the two outliers and of all observations of the dataset is set to 1 mm, because no **VCI** is available.

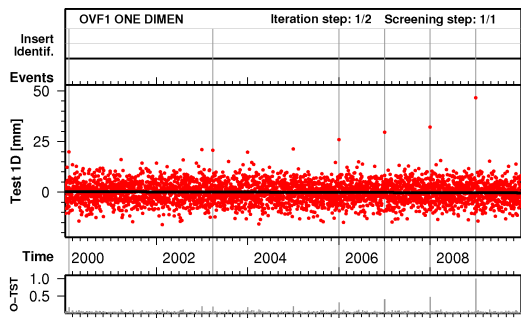


(a) Search in step 1.

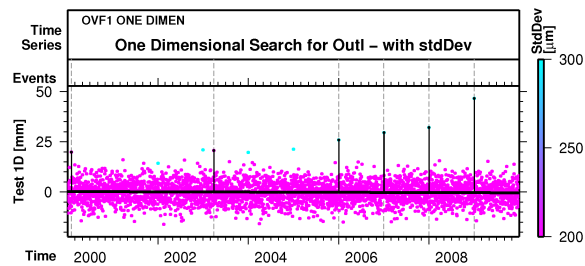


(b) Final result of the analysis.

Figure 3.10: Validation of the search for outliers. Standard deviation of observations not considered. (Red) time series: synthetic data $\sim N(0,25)$; contaminated by outliers. (Black) functional model. (O-TST) normalized search for outliers. Level of significance for outliers $U_s = 30$.



(a) Search in step 1.



(b) Final result of the analysis.

Figure 3.11: Validation of the search for outliers. Standard deviation of observations considered. (Red) time series: synthetic data $\sim N(0,25)$; contaminated with outliers. (Black) functional model. (O-TST) normalized search for outliers. Level of significance for outliers $U_s = 85$.

For the second experiment the level of significance for outliers was set to $U_s = 85$. Again, the algorithm needed two iteration steps for the analysis. As opposed to the first experiment six observations were identified as outliers, see Table 3.4. Two of them, associated with 02-Feb-2000 and 29-Mar-2003, do not correspond to any of the nine artificially added to the synthetic time series. It is clear that if U_s would have been set to a value smaller than 85, many more observations would have been identified as outliers.

Table 3.4 shows that the first and the second experiments identified two and four epochs of the nine "true" outliers, respectively. The epochs agree with the epochs of the "true" outliers. The "estimated" values, however, depart from the "true" values by up to 5 mm because the "true" outliers were added to the white noise $\sim N(0,25)$.

Table 3.4: Validation of the search for outliers. Synthetic time series with white noise $\sim N(0,25)$ and nine outliers. Level of significance $U_s = 30$ and $U_s = 85$ for outliers without and with standard deviation, respectively.

Synthetic outliers added to the time series			Results experiment 1 test without std. dev.				Results experiment 2 test with std. dev.			
Epoch	Value ^a	σ^a	Epoch	Value ^a	σ^a	Test	Epoch	Value ^a	σ^a	Test
01-Jan-2001	5	0.3	01-Jan-2001	-	-	-	01-Jan-2001	-	-	-
01-Jan-2002	10	0.3	01-Jan-2002	-	-	-	01-Jan-2002	-	-	-
01-Jan-2003	15	0.3	01-Jan-2003	-	-	-	01-Jan-2003	-	-	-
01-Jan-2004	20	0.3	01-Jan-2004	-	-	-	01-Jan-2004	-	-	-
01-Jan-2005	25	0.3	01-Jan-2005	-	-	-	01-Jan-2005	-	-	-
01-Jan-2006	30	0.3	01-Jan-2006	-	-	-	01-Jan-2006	26.1	0.3	87.2
01-Jan-2007	35	0.3	01-Jan-2007	-	-	-	01-Jan-2007	29.8	0.3	99.5
01-Jan-2008	40	0.3	01-Jan-2008	32.3	1	32.3	01-Jan-2008	32.3	0.3	107.9
01-Jan-2009	45	0.3	01-Jan-2009	46.9	1	46.9	01-Jan-2009	46.9	0.3	156.5
-	-	-	-	-	-	-	02-Feb-2000	19.7	0.2	98.8
-	-	-	-	-	-	-	29-Mar-2003	20.7	0.2	103.7

^aIn millimeters.

3.6 Search for Velocity Changes

Coordinate time series derived from **GNSS** observations should be continuous and describe only geophysical signatures such as crustal deformations, inter-, co-, and post-seismic phases of earthquakes (Segall and Davis, 1997), or melting processes as permafrost, sliding processes such as soil exploitation, flowing processes such as ice flow in ice sheets (King et al., 2007), etc. In practice, however, one often has to cope with time series containing gaps and colored noise (see Sect. 2.5), artifacts (see Sect. 3.2.1), quasi-periodic signatures due to model deficiencies (see Sect. 3.2.3), and other time correlated signals. All these phenomena, either of geophysical reason or artifacts, might induce true or apparent velocity changes in the coordinate time series.

Because not all velocity changes are known a priori, the algorithm **FODITS** allows it at step 10 (see Fig. 3.2) to search for a velocity change in each sub-interval delimited by velocity changes. If there are n significant velocity changes in the time series the search proposes therefore $n + 1$ velocity change candidates.

3.6.1 Mathematical Principle

In order to identify the epoch of the most likely velocity change in a sub-interval of N observation(s) (epochs) we adopt the following deterministic model:

$$\mathbf{f}_{vc}(t) = \begin{cases} \mathbf{a}_0 + \dot{\mathbf{a}}_0 t & \text{for } t \leq t_k \\ \mathbf{a}_0 + \dot{\mathbf{a}}_0 t + \dot{\mathbf{a}}_{0k}(t - t_k) & \text{for } t \geq t_k \end{cases} \quad (3.21)$$

i.e., the model is linear in the entire sub-interval, but features different slopes before and after the epoch t_k , namely $\dot{\mathbf{a}}_0$, $\dot{\mathbf{a}}_0 + \dot{\mathbf{a}}_{0k}$. The first design matrix associated with the

observations in the selected sub-interval reads as:

$$\mathbf{A}_k = \begin{bmatrix} 1 & t_{a,1} & 0 \\ 1 & t_{a,2} & 0 \\ \vdots & \vdots & \vdots \\ 1 & t_{a,k-1} & 0 \\ 1 & t_{a,k} & t_{b,1} \\ \vdots & \vdots & \vdots \\ 1 & t_{a,N} & t_{b,N-k} \end{bmatrix} \rightarrow \begin{array}{l} t_{a,1} = t_1 \\ t_{a,2} = t_2 \\ \vdots \\ t_{a,k-1} = t_{k-1} \\ t_{a,k} = t_k, \quad t_{b,1} = t_k - t_k = 0 \\ \vdots \\ t_a = t_N, \quad t_{b,N-k} = t_N - t_k, \end{array} \quad (3.22)$$

The most likely epoch $T_{V,k}$ is found by varying k systematically, $k = 2, 3, \dots, N-1$ and to use the a posteriori **RMS** $m_{0,k}$ of the observations associated with the estimates assuming the velocity change at $t = t_k$. To identify $t_{a,k} = t_{V,j}$ we use the following condition

$$g(t_{V,j}) = \max\left(\frac{1}{m_{0,2}}, \dots, \frac{1}{m_{0,N-1}}\right). \quad (3.23)$$

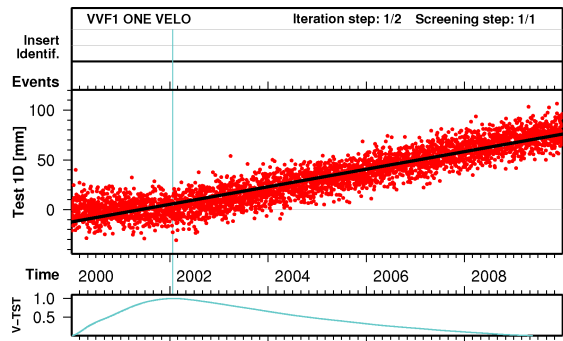
In order to speed up the computation time the search of the maximum velocity change is implemented by assuming that the observations are neither time-correlated nor cross-correlated, i.e., the **LSE** does not take into account the **VCI**. Furthermore, instead of re-computing \mathbf{A}_k and the **NEQ** associated with it for each epoch k , the $N-2$ **NEQs** to be solved

$$\mathbf{N}_k = \begin{bmatrix} N & \sum t_{a,i} & \sum t_{b,j} \\ \sum t_{a,i} & \sum t_{a,i}^2 & \sum t_{a,i}t_{b,j} \\ \sum t_{b,j} & \sum t_{a,i}t_{b,j} & \sum t_{b,j}^2 \end{bmatrix}, \quad \mathbf{b}_k = \begin{bmatrix} \sum y_i \\ \sum t_{a,i}y_i \\ \sum t_{b,j}y_i \end{bmatrix} \quad (3.24)$$

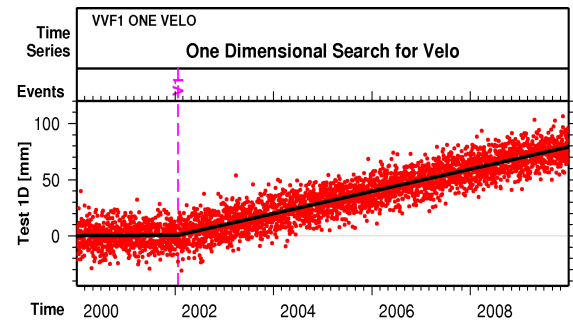
are computed in a time-saving manner by updating $\{\mathbf{N}, \mathbf{b}\}_k$ using $\{\mathbf{N}, \mathbf{b}\}_{k-1}$.

3.6.2 Validation with Synthetic Time Series

The epoch $t_{V,k}$ found with condition (3.23) is validated with a one-dimensional synthetic time series without taking into account the **VCI** of the observations. The user-defined level of significance was set to $U_t = 0.002$ and the minimum interval length between successive velocity changes was set to $\Delta t_v = 0.2$ years. In a first experiment, a time series with white noise $\sim N(0,100)$ and with a velocity change of $+10$ mm/yr on 01-Jan-2002 was analyzed. Figure 3.12 shows the result. The sequence of sub-figures illustrates the results of the iteration steps. In the first iteration step, documented by Fig. 3.12a, the search (V-TST) identifies and proposes a velocity change on 22-Jan-2002. In the second and last iteration step, documented in Fig. 3.12b, the velocity change is estimated to be 9.590 ± 0.432 mm/yr and considered as statistically significant. As no further velocity change was significant the analysis terminated after the second step. The experiment is performed three more times with three different levels of white noise: $\sim N(0,25)$, $\sim N(0,9)$, and $\sim N(0,1)$. The results (V1) are all summarized in Table 3.5.

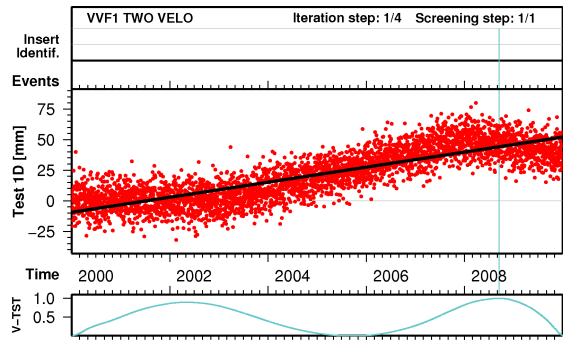


(a) Search in step 1.

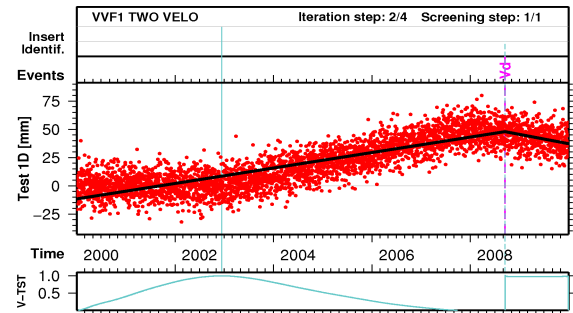


(b) Final result of the analysis.

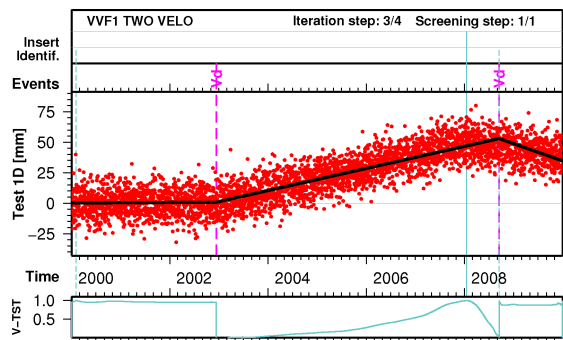
Figure 3.12: Validation of the search for velocity changes in one-dimensional time series with one velocity change. (Red) time series: synthetic data $\sim N(0,100)$. (Black) functional model. (V-TST) normalized search for velocity changes.



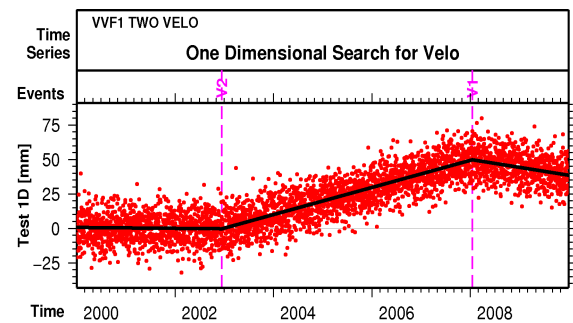
(a) Search in step 1.



(b) Search in step 2.



(c) Search in step 3.



(d) Final result of the analysis.

Figure 3.13: Validation of the search for velocity changes in one-dimensional time series with two velocity changes. (Red) time series: synthetic data $\sim N(0,100)$. (Black) functional model. (V-TST) normalized search for velocity changes.

Table 3.5: Validation of the search for velocity changes. Synthetic time series with up to two velocity changes and four different levels of white noise.

Time series	L ^a	Noise	Introduced [mm/yr]		Identified [mm/yr]		σ
			Epoch	Value	Epoch	Value	
VVF1 ONE VELO	V1	$\sim N(0,100)$	01-Jan-2002	10.0	22-Jan-2002	9.590	0.432
VVF1 ONE VELO	V1	$\sim N(0,25)$	01-Jan-2002	10.0	17-Jan-2002	9.705	0.217
VVF1 ONE VELO	V1	$\sim N(0,9)$	01-Jan-2002	10.0	10-Jan-2002	9.826	0.131
VVF1 ONE VELO	V1	$\sim N(0,1)$	01-Jan-2002	10.0	04-Jan-2002	9.936	0.044
VVF1 TWO VELO	V2	$\sim N(0,100)$	01-Jan-2003	10.0	13-Dec-2002	10.164	0.340
VVF1 TWO VELO	V1	$\sim N(0,100)$	01-Jan-2008	-15.0	15-Jan-2008	-15.568	0.515
VVF1 TWO VELO	V2	$\sim N(0,25)$	01-Jan-2003	10.0	13-Dec-2002	10.108	0.170
VVF1 TWO VELO	V1	$\sim N(0,25)$	01-Jan-2008	-15.0	14-Jan-2008	-15.356	0.257
VVF1 TWO VELO	V2	$\sim N(0,9)$	01-Jan-2003	10.0	10-Dec-2002	10.107	0.102
VVF1 TWO VELO	V1	$\sim N(0,9)$	01-Jan-2008	-15.0	13-Jan-2008	-15.242	0.154
VVF1 TWO VELO	V2	$\sim N(0,1)$	01-Jan-2003	10.0	30-Dec-2002	9.916	0.033
VVF1 TWO VELO	V1	$\sim N(0,1)$	01-Jan-2008	-15.0	22-Jan-2008	-15.463	0.052

^aLabel in the figure.

As expected, the smaller the noise, the more precise the identification of the epoch and the estimated velocity change. This first experiment shows that a velocity change is accurately identified in time series contaminated by only one velocity change.

A second experiment, performed four times with the same four white noise characteristics as in the first experiment, analyzes time series with two velocity changes, the first of +10 mm/yr on 01-Jan-2003 and the second one of -15 mm/yr on 01-Jan-2008. Figure 3.13 illustrates the result of this experiment with $\sim N(0,100)$. In the first iteration step, see Fig. 3.13a, the search (V-TST) proposes 05-Aug-2008, 217 days after the epoch of the true velocity change on 01-Jan-2008. The added element is nevertheless considered as significant and in the next iteration step, see Fig. 3.13b, the search proposes another velocity change on 13-Dec-2002. The latter epoch, compared to the first one proposed, is only 19 days before the true velocity change. After having confirmed the second velocity change (V2) as significant, the search proposes a third element (V1) on 15-Jan-2008, 15 days after the true event, see Fig. 3.13c. In the fourth and last iteration step the algorithm removes the velocity change on 05-Aug-2008 from the function model which, after adding of (V1), is no longer significant in the model. The analysis is then terminated, because the search (V-TST) did not find other significant velocity change. The final result of the analysis is illustrated by Fig. 3.13d. The second experiment shows that the search (3.23) is not able to propose the correct epochs of the velocity changes in time series with more than one velocity change. Nevertheless, if the search is dealing with only one velocity change per sub-interval, the analysis gives the correct result—by removing the first velocity change erroneously accepted at the beginning of the analysis.

Table 3.5 summarizes the result of both experiments. The reports confirm that velocity changes could be identified within a few days from the true epochs and, moreover, their estimates are mostly within the $\pm 1\sigma$ limits.

3.7 Search for Periodic Functions

Seasonal signals (see Sect. 3.2.3) are usually taken into account in the analyses of coordinate time series as elements of the functional model. Coordinate time series, however, might show other apparent periodic signatures, e.g., due to the presence of colored noise (see Sect. 2.5). One might absorb such effects in the time series by setting additional periodic functions. The search for periodic functions may be of interest for other than coordinate time series. For this reason, a search for unknown periodic functions is implemented in the algorithm of FODITS.

3.7.1 Mathematical Principle

The search for the most probable periodic function in the post-fit residual time series is based on the Fourier analysis by LSE (e.g., Beutler, 2005) without accounting for the VCI. The Fourier analysis consist of n_{per} spectral lines starting from the initial period p_{beg} to the final period p_{end} . Spectral lines are thus evenly spaced in the frequency domain. For each spectral line k the following first design matrix (here only for one component)

$$\mathbf{A}_k = \begin{bmatrix} \cos(\omega_k t_1) & \sin(\omega_k t_1) \\ \cos(\omega_k t_2) & \sin(\omega_k t_2) \\ \vdots & \vdots \\ \cos(\omega_k t_N) & \sin(\omega_k t_N) \end{bmatrix}, \quad (3.25)$$

is defined. Parameters are estimated by LSE (see Sect. 2.3.3), and the a posteriori RMS error of unit weight $m_{0,k}$ is computed. The most probable period P_j is found in the residuals by

$$g(\omega_{P,j}) = \max\left(\frac{1}{m_{0,k}}, \dots, \frac{1}{m_{n_{per},k}}\right). \quad (3.26)$$

3.7.2 Validation with Synthetic Time Series

The search for periodic functions (3.26) is validated with a one-dimensional synthetic time series without using the VCI of the observations. Time series consist of white noise $\sim N(0,25)$ and three periodic functions: the first with an amplitude of 15 mm with a period of 100 days, the second with an amplitude of 15 mm with period of 200 days, and third with an amplitude of 15 mm with period of 300 days. The user-defined level of significance is set to $U_t = 0.002$. The analysis is carried out by checking $n_{per} = 500$ spectral lines between $p_{beg} = 10$ days and $p_{end} = 400$ days.

Figure 3.14 documents the search step-by-step. The analysis takes four iteration steps. In the first three steps (see Figs. 3.14a, 3.14b, and 3.14c) the search (P-TST) identifies the three periodic signals, which are in the time series. Figure 3.14d shows the final result.

Figure 3.15 contains the result of the four tests with different noise levels: $\sim N(0,25)$ (see Fig. 3.15a which is Fig. 3.14d), $\sim N(0,100)$ (see Fig. 3.15b), $\sim N(0,225)$ (see Fig. 3.15c), and $\sim N(0,400)$ (see Fig. 3.15d).

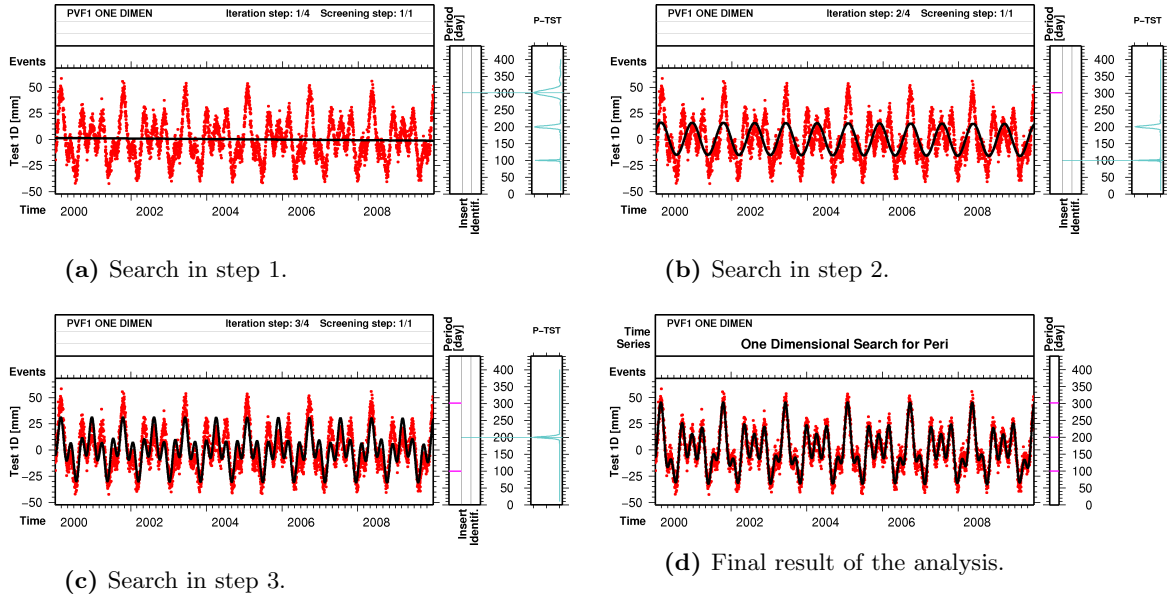


Figure 3.14: Validation of the search for periodic functions in one-dimensional time series with three signals. (Red) time series: synthetic data $\sim N(0,25)$. (Black) functional model. (P-TST) normalized search for periodic functions.

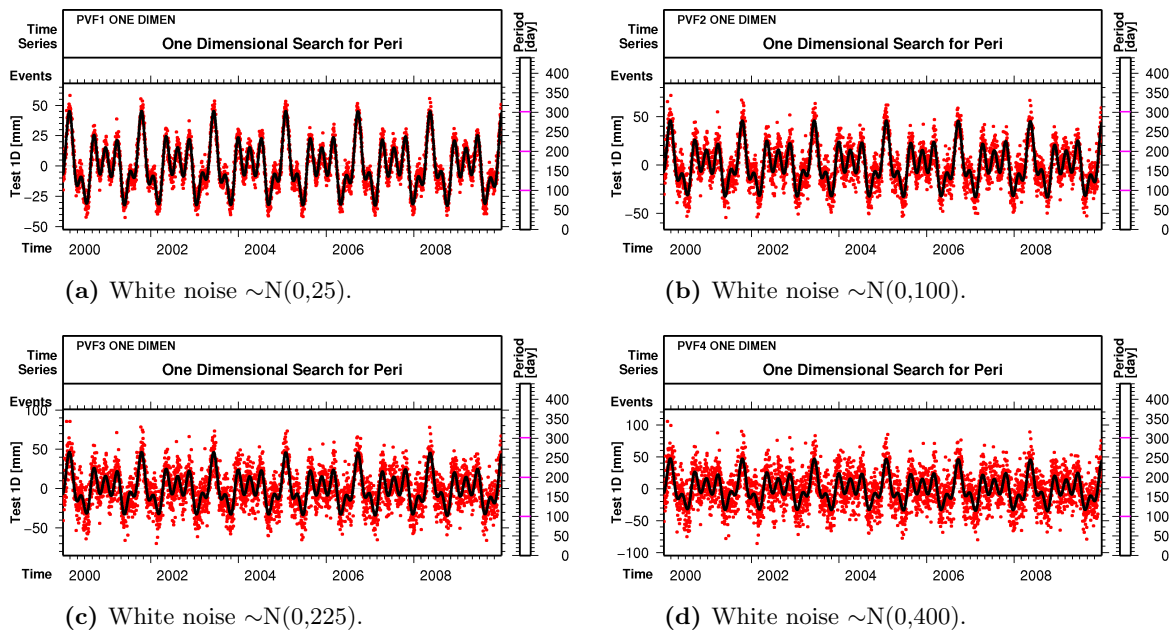


Figure 3.15: Validation of the search for periodic functions in one-dimensional time series with three signals and four different noise sizes. (Red) synthetic time series. (Black) functional model.

Table 3.6: Validation of the search for periodic functions. Synthetic time series with three periodic functions and four different white noise levels.

Time series	Label	Noise	Introduced [day]/[mm]		Identified [day]/[mm]		
			Period	Value	Period	Value	σ
PVF1 ONE DIMEN	P1	$\sim N(0,25)$	100.0000	15.0	99.9836	15.158	0.120
PVF1 ONE DIMEN	P2	$\sim N(0,25)$	200.0000	15.0	200.2812	14.969	0.121
PVF1 ONE DIMEN	P3	$\sim N(0,25)$	300.0000	15.0	301.5504	15.139	0.120
PVF2 ONE DIMEN	P1	$\sim N(0,100)$	100.0000	15.0	99.9836	15.316	0.235
PVF2 ONE DIMEN	P2	$\sim N(0,100)$	200.0000	15.0	200.2812	15.093	0.235
PVF2 ONE DIMEN	P3	$\sim N(0,100)$	300.0000	15.0	301.5504	15.309	0.235
PVF3 ONE DIMEN	P1	$\sim N(0,225)$	100.0000	15.0	99.9836	15.473	0.351
PVF3 ONE DIMEN	P2	$\sim N(0,225)$	200.0000	15.0	200.2812	15.218	0.352
PVF3 ONE DIMEN	P3	$\sim N(0,225)$	300.0000	15.0	301.5504	15.478	0.351
PVF4 ONE DIMEN	P1	$\sim N(0,400)$	100.0000	15.0	99.9836	15.631	0.467
PVF4 ONE DIMEN	P2	$\sim N(0,400)$	200.0000	15.0	200.2812	15.343	0.468
PVF4 ONE DIMEN	P3	$\sim N(0,400)$	300.0000	15.0	301.5504	15.648	0.467

Table 3.7: Validation of searches for discontinuities, velocity changes, outliers, and periodic functions.

Time series	Label	Introduced [mm]/[mm/yr]		Identified [mm]/[mm/yr]		
		Epoch/Period [day]	Value	Period [day]	Value	σ
AVF1 ONE DIMEN	D1	01-Jan-2005	+25.0	01-Jan-2005	+24.155	0.379
AVF1 ONE DIMEN	V1	01-Jan-2008	+15.0	09-Nov-2007	-14.145	0.239
AVF1 ONE DIMEN	P1	200.0	+5.0	200.281	+4.944	0.127
AVF1 ONE DIMEN	- ^a	-	-	-	100	-

^aOutliers do not have a label.

Table 3.6 gives a summary of the final results. The identified periods are the same in all cases: P1=99.9830 days, P2=200.2810 days, and P3=301.5500 days. Their nearest spectral lines (in days) to the true periods were 99.2353 and 100.7351 for P1, 199.1923 and 201.3732 for P2, and 298.8571 and 301.5504 for P3, respectively. Therefore, periods could not be better with the user-defined parameters $n_{per} = 500$, $p_{beg} = 10$ days, and $p_{end} = 400$ days. The larger the noise, the larger the estimates and the associated standard deviations for the amplitudes. For $\sim N(0,25)$ the estimates of P2 is 14.969 ± 0.121 mm, while for $\sim N(0,400)$ it is 15.343 ± 0.468 mm. This corresponds very well with the ratio of the RMS of the white noise $100/25=4$.

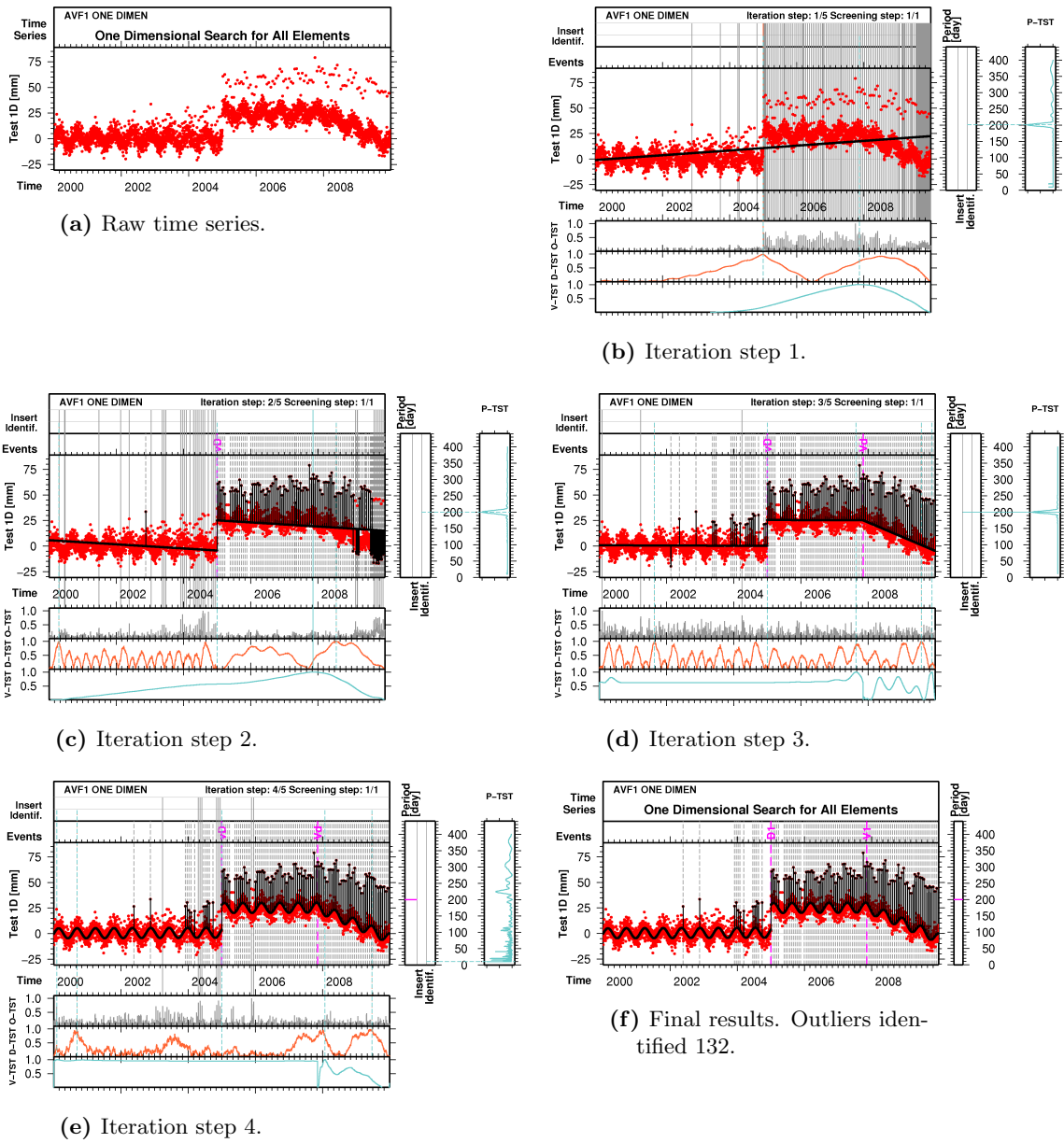


Figure 3.16: Validation of all searches simultaneously in one-dimensional time series. (Red) time series: synthetic data with white noise $\sim N(0,25)$. Search for outliers (O-TST), for discontinuities (D-TST), for velocity changes (V-TST), for periodic functions (P-TST). (Black) functional model.

3.8 More General Examples

3.8.1 Iterative Analysis of One-Dimensional Synthetic Time Series

One-dimensional synthetic time series with white noise $\sim N(0,25)$ and containing one discontinuity of +25 mm on 01-Jan-2005, one velocity change of +15 mm/yr on 01-Jan-2008, one periodic function of +5 mm of period 200 days, and one outliers every 20 observations, are analyzed with **FODITS** with the following user-defined level of significance, for outliers $U_s = 3$ and for other elements $U_t = 0.01$, and $n_{per} = 500$ spectral lines to identify periodic functions starting from $p_{beg} = 10$ to $p_{end} = 400$. Discontinuities (D-TST), outliers (O-TST), velocity changes (V-TST), and periodic functions (P-TST) are sought using the algorithm of Sect. 3.3. The result of the analysis is illustrated in Fig. 3.16. At first, Fig. 3.16a shows the raw time series. The analysis began with the first iteration step (see Fig. 3.16b). The initial functional model (in black) represents the approximation of the observations (in red) by a polynomial of first degree in the time t (linear regression). All searches propose candidates to be added to the functional model as the most probable element which best reduces the discrepancy between the functional model and time series. The discontinuity on 01-Jan-2005 was identified and 200 outliers (the max number per iteration step) were found (28 were not considered to be significant). The discontinuity and the 172 outliers are part of the functional model in the second step. In the next step the velocity change on 09-Nov-2007 is identified and estimated and 27 additional outliers were found (see Fig. 3.16c). In the third step, after the removal of 92 outliers, the periodic function of period 200.281 days and additional 3 outliers were identified (see Fig. 3.16d). In the fourth iteration step (see Fig. 3.16e), after the removal of 11 more outliers, 9 more outliers were found. The analysis terminates with the fifth step (see Fig. 3.16f). Table 3.7 summarizes the results. As expected from the results of the previous validations, the discontinuity (D1) on 01-Jan-2005 and the periodic functions (P1) of period 200.2 days were identified in the time series in a correct manner. The epoch of the velocity change (V1), 09-Nov-2007, differs from the true one by about 2 months.

3.8.2 Analysis of CODE Reprocessed Time Series

The **CODE** daily coordinate time series emerging from the first reprocessing effort (see Sect. 2.4) of station MAC1 (MacQuarie Island) are analyzed with **FODITS**. Here we take the **VCI** of the observations into account. The user-defined level of significance for outliers is set to $U_s = 12$ and that for the other elements of the functional model is set to $U_t = 0.01$. The minimum interval length between successive velocity changes is set to $\Delta t_v = 3$ years. Annual and semi-annual periodic functions, history of equipment changes, and history of earthquakes are added to the list of predefined elements. In addition, we require that the horizontal and vertical discontinuities must be at least 5 mm and 8 mm in size, respectively, and that the amplitude of the periodic functions are at least 1 mm. Only outliers, discontinuities, and velocity changes are identified by the procedure. Furthermore, a velocity change is set up after each discontinuity of unknown reason.

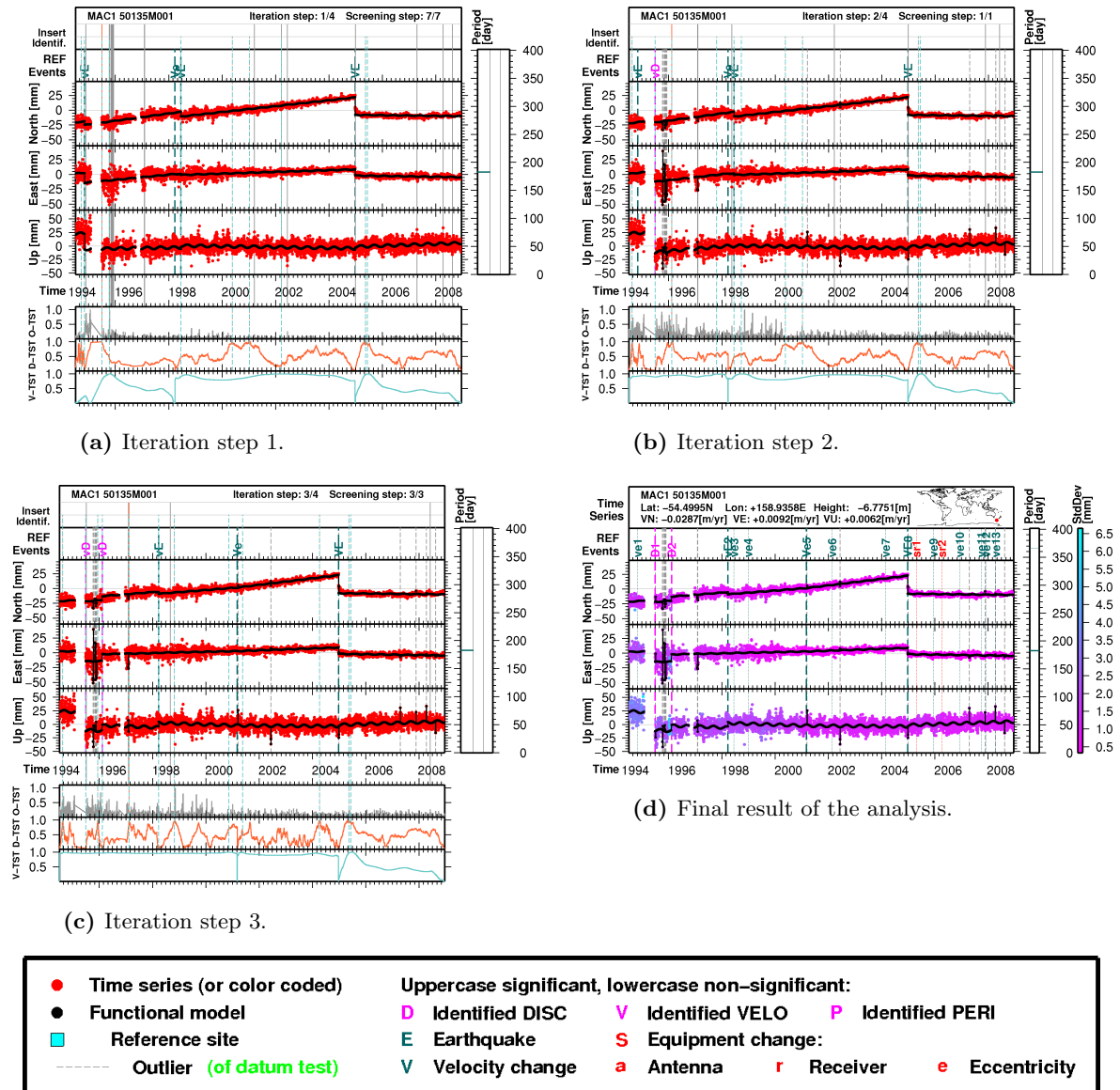


Figure 3.17: Iteration steps in the analysis of daily coordinate time series of station MAC1.

Figure 3.17 illustrates the individual steps of the analysis. The first iteration step is documented in Fig. 3.17a. Seven screening steps were needed to check four significant earthquakes and the significant semi-annual period. Afterwards, searches for outliers (O-TST), discontinuities (D-TST), and velocity changes (V-TST) propose additional candidate elements for the next iteration step. The search for unknown offsets and velocity changes proposes one candidate for each sub-interval (see Sects. 3.4 and 3.6). The most probable

Table 3.8: Time series analysis of daily coordinates of station MAC1.

Time series	Label	E ^a	Epoch/Period [days]	Reason ^b	Size element in [m] and [m/yr]				S ^c
					North	East	Up	σ	
MAC1 50135M001	P1	P	182.6250	PreDef	0.0005	0.0006	0.0024	0.0001	Y
MAC1 50135M001	p2	P	365.2500	PreDef	0.0006	0.0006	0.0004	0.0001	N
MAC1 50135M001	ve1	D	1994-11-05 02:09:36	Erq 6.5/307	-0.0034	0.0001	0.0034	0.0018	N
MAC1 50135M001	ve1	V	1994-11-05 02:09:36	Erq 6.5/307	0.0120	-0.0123	-0.0044	0.0054	N
MAC1 50135M001	D1	D	1995-06-30 11:59:43	Unknown	-0.0038	-0.0181	-0.0331	0.0014	Y
MAC1 50135M001	D2	D	1996-02-12 11:59:43	Unknown	0.0069	0.0122	0.0093	0.0007	Y
MAC1 50135M001	vE2	D	1998-03-25 03:07:21	Erq 8.1/1077	-0.0037	0.0001	0.0083	0.0009	Y
MAC1 50135M001	vE2	V	1998-03-25 03:07:21	Erq 8.1/1077	-0.0020	-0.0008	-0.0055	0.0008	N
MAC1 50135M001	ve3	D	1998-06-16 09:21:01	Erq 6.2/178	-0.0004	0.0021	0.0032	0.0012	N
MAC1 50135M001	ve3	V	1998-06-16 09:21:01	Erq 6.2/178	-0.0020	-0.0008	-0.0056	0.0008	N
MAC1 50135M001	ve4	D	1998-12-30 02:05:34	Erq 4.4/36	-0.0002	0.0013	0.0010	0.0007	N
MAC1 50135M001	ve4	V	1998-12-30 02:05:34	Erq 4.4/36	-0.0022	-0.0018	-0.0065	0.0008	N
MAC1 50135M001	Ve5	D	2001-03-06 09:10:22	Erq 6.4/108	-0.0010	-0.0019	-0.0029	0.0005	N
MAC1 50135M001	Ve5	V	2001-03-06 09:10:22	Erq 6.4/108	0.0020	0.0007	0.0013	0.0002	Y
MAC1 50135M001	ve6	D	2002-02-17 10:05:48	Erq 5.4/45	0.0002	-0.0004	-0.0017	0.0006	N
MAC1 50135M001	ve6	V	2002-02-17 10:05:48	Erq 5.4/45	0.0005	0.0026	0.0024	0.0005	N
MAC1 50135M001	ve7	D	2004-02-26 22:35:02	Erq 6.0/156	-0.0004	0.0018	0.0020	0.0004	N
MAC1 50135M001	ve7	V	2004-02-26 22:35:02	Erq 6.0/156	-0.0002	0.0027	0.0044	0.0009	N
MAC1 50135M001	VE8	D	2004-12-23 14:35:23	Erq 8.1/600	-0.0306	-0.0108	0.0023	0.0002	Y
MAC1 50135M001	VE8	V	2004-12-23 14:35:23	Erq 8.1/600	-0.0060	-0.0023	0.0019	0.0001	Y
MAC1 50135M001	sr1	D	2005-04-22 00:00:00	EqCh R	-0.0044	-0.0013	0.0052	0.0006	N
MAC1 50135M001	ve9	D	2005-12-10 08:03:50	Erq 4.7/2	-0.0026	-0.0010	-0.0008	0.0003	N
MAC1 50135M001	ve9	V	2005-12-10 08:03:50	Erq 4.7/2	0.0063	0.0027	-0.0052	0.0006	N
MAC1 50135M001	sr2	D	2006-04-05 00:00:00	EqCh R	-0.0025	-0.0005	-0.0007	0.0003	N
MAC1 50135M001	ve10	D	2006-12-06 20:23:43	Erq 5.8/57	-0.0005	0.0018	0.0028	0.0006	N
MAC1 50135M001	ve10	V	2006-12-06 20:23:43	Erq 5.8/57	0.0037	0.0009	-0.0019	0.0003	N
MAC1 50135M001	ve11	D	2007-09-30 05:14:04	Erq 7.4/681	0.0036	-0.0002	-0.0013	0.0003	N
MAC1 50135M001	ve11	V	2007-09-30 05:14:04	Erq 7.4/681	0.0045	-0.0002	-0.0037	0.0005	N
MAC1 50135M001	ve12	D	2007-12-01 03:21:19	Erq 5.2/22	0.0034	0.0008	-0.0009	0.0003	N
MAC1 50135M001	ve12	V	2007-12-01 03:21:19	Erq 5.2/22	0.0046	-0.0004	-0.0046	0.0006	N
MAC1 50135M001	ve13	D	2008-04-12 00:18:09	Erq 7.1/132	0.0026	-0.0005	-0.0023	0.0004	N
MAC1 50135M001	ve13	V	2008-04-12 00:18:09	Erq 7.1/132	0.0059	-0.0017	-0.0078	0.0011	N
MAC1 50135M001	Number of identified outliers			24					

^aFunctional model elements. (D): discontinuity. (V): velocity change. (P): periodic function.

^b(Unknown): of unknown reason. (PreDef): predefined. (Erq): earthquake (mag/dist[km]). (EqCh): equipment change, (A) antenna, (R) receiver, (E) eccentricity.

^cElement significance. (Y) yes, (N) no.

element added to the functional model in this first iteration step is the discontinuity on 30-Jun-1995. Note, however, that the discontinuity proposed by (D-TST) is not related to a clear maximum as in Fig. 3.6a. This is because the selected discontinuity is of the order of magnitude of the noise level. The same happens in the second iteration step illustrated by Fig. 3.17b, where the discontinuity on 12-Feb-1996 is added to the functional model as most probable element. In the third iteration step, illustrated by Fig. 3.17c, the search for outliers identifies and adds two additional elements to the functional model. Lastly, the algorithm terminates after the fourth iteration step, because no other significant elements

are found.

The final result of the analysis is illustrated in Fig. 3.17d. Table 3.8 contains the numerical results. The largest discontinuity (VE8) in the time series was induced by the M8.1 earthquake on 23-Dec-2004 with an epicenter at a distance of 600 km from the station MAC1. This earthquake, which preceded the Sumatra M9.0 earthquake by about 3 days (e.g., [Ammon et al., 2005](#)), is associated with co-seismic displacement of -30.6 mm, -10.8 mm, and 2.3 mm in North, East, and Up, respectively, and an uncertainty (for all three components) of about 0.2 mm. [Watson et al. \(2010\)](#) associate the same co-seismic displacement with about 25 mm, 10 mm, and 0 mm in NEU. The two results differ by about 5 mm in the North component. Figure 3.17d suggests that this is due to the non-modelled post-seismic relaxation phase of the earthquake. The analysis identified two more significant elements related to earthquakes. The first, an earthquake of M8.1 on 25-Mar-1998, with its epicenter at 1077 km from the station, induced a discontinuity (vE2) approximately of 3.7 mm in the North component. The second one, an earthquake of M6.4 with its epicenter at 108 km from the station, induced a velocity change (Ve5) of 2.0 ± 0.2 mm/yr on 06-Mar-2001 in the North component. According to ([Watson et al., 2010](#)) the boundary of the tectonic plate predominately extends indeed in the North-South direction. The two equipment changes (sr1) and (sr2) did not generate significant changes (see Table 3.8). The annual signal was not found to be significant and the semi-annual one was found to be significant.

3.8.3 Search for all Elements in DCB time series

In this last test we use FODITS to analyze the CODE DCB time series derived from the first IGS reprocessing effort (see Sect. 2.4). The analysis is performed once with each single search alone and once with all searches together. The level of significance and other parameters are varied to give an impression of the sensitivity of detection.

Figure 3.18 illustrates the results of the search for unknown discontinuities. In the first analysis, illustrated in Fig. 3.18a, the overall level of significance U_t was set to 0.5 and the analysis did not find significant discontinuities. The functional model was polynomial of degree one in time. In the second analysis, illustrated in Fig. 3.18b, four significant discontinuities were found in the time series with $U_t = 0.1$. This result shows that the analysis is quite robust in presence of possible outliers. The result also shows that the search identified discontinuities at epochs where the time series do not show clear offsets. Both facts confirm the characteristics of the search which were already observed in Fig. 3.3. The third analysis, illustrated by Fig. 3.18c, which was performed with $U_t = 0.01$, found three additional offsets w.r.t. the previous analysis. In the last analysis, illustrated by Fig. 3.18d, performed with $U_t = 0.005$, the search identified more and more details, such as the two consecutive double discontinuities at the beginning of 2004 which could also be classified as outliers. These four tests indicate that the optimal representation of the time series heavily depends on the overall level of significance U_t .

Figure 3.19 illustrates two aspects when analyzing the CODE DCB time series with a search solely for unknown outliers. The first aspect, illustrated by Fig. 3.19a and performed with a level of significance $U_s = 200$, and the second, illustrated by Fig. 3.19b and per-

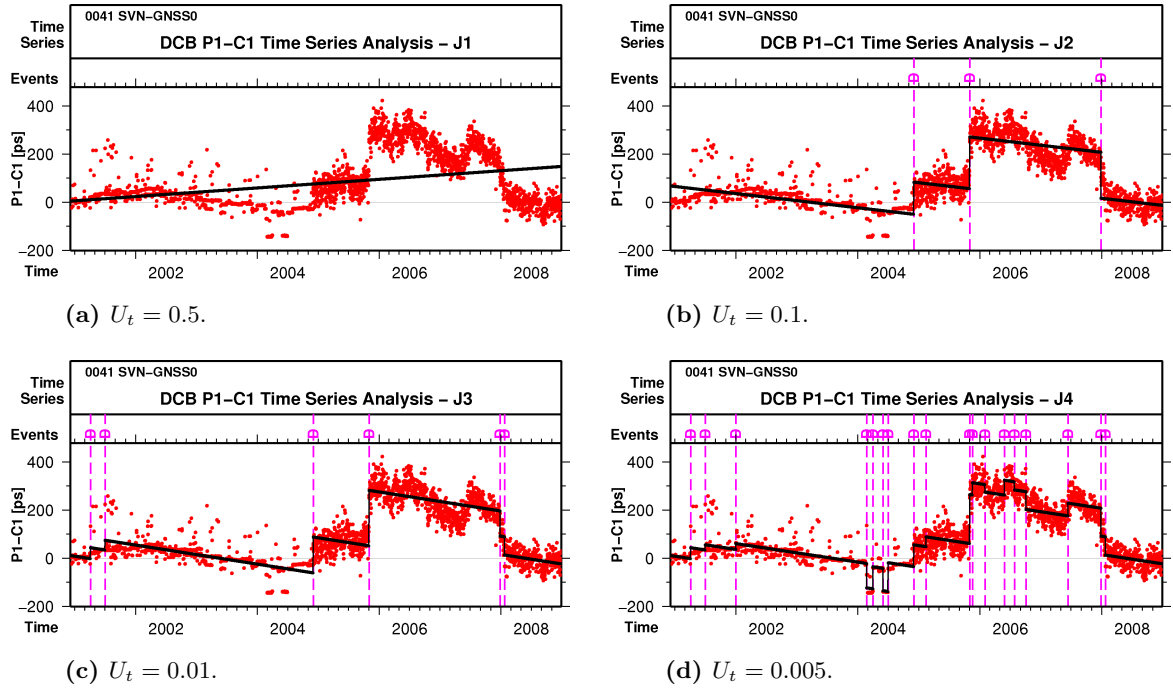


Figure 3.18: Validation search for discontinuities. DCB P1-C1 SVN 41 time series analyzed with different levels of significance U_t . (Red) time series. (Black) functional model. (D) significant discontinuity.

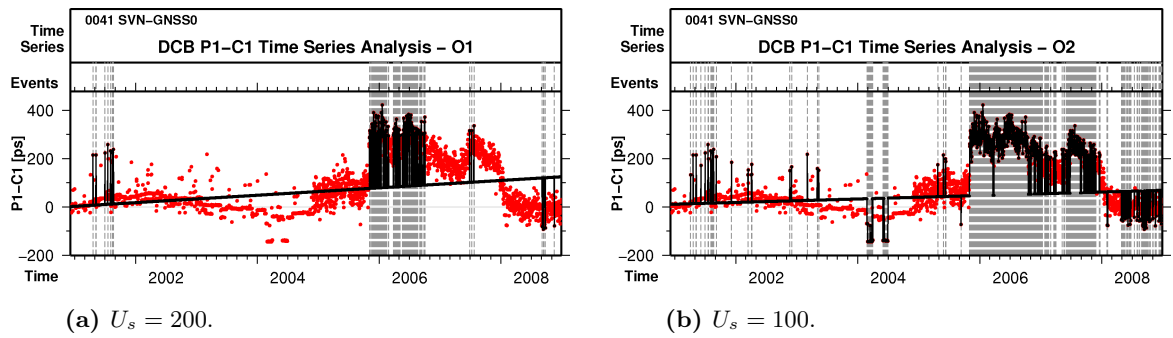


Figure 3.19: Validation search for outliers. DCB P1-C1 SVN 41 time series analyzed with different levels of significance for outliers U_s . (Red) time series. (Black) functional model. Vertical lines are outliers.

formed with $U_s = 100$, demonstrate that the final result depends on the user settings: the lower the level of significance for outliers U_s , the more observations are marked as outliers. Figure 3.19b also shows that, as opposed to Fig. 3.18d (when only discontinuities were sought), the two structures at the beginning of 2004 were identified as outliers—and not as two consecutive discontinuities. It is an open issue, which interpretation is correct.

Figure 3.20 shows four results when analyzing the CODE DCB time series with a search

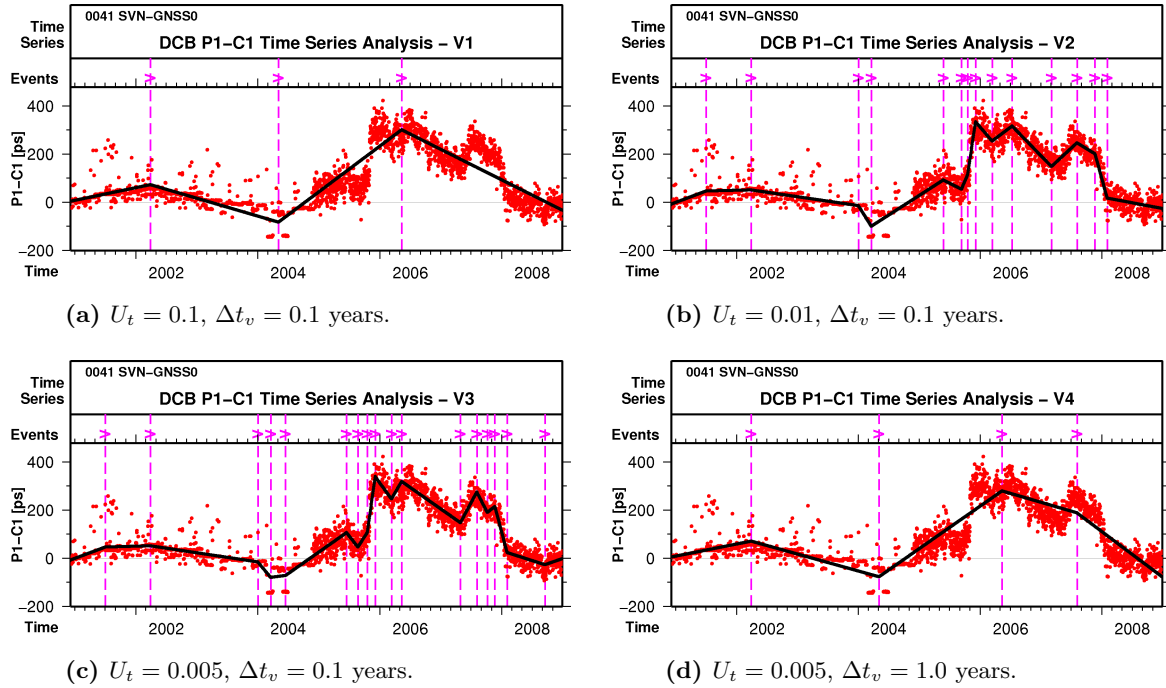


Figure 3.20: Validation search for velocity changes. DCB P1-C1 SVN 41 time series analyzed with different levels of significance U_t and minimum interval length between successive velocity changes Δt_v . (Red) time series. (Black) functional model. (V) Velocity change.

for unknown velocity changes. In Figs. 3.20a to 3.20c the overall level of significance U_t is set to 0.1, 0.01, and 0.005, respectively. For all analyses the minimum interval length between successive velocity changes is set to $\Delta t_v = 0.1$ years. The smaller the overall level of significance U_t , the more velocity changes are found as significant elements. In Fig. 3.20d the level of significance is $U_t = 0.005$, i.e., the same as in Fig. 3.20c, but the minimum interval length between successive velocity changes is now set to $\Delta t_v = 1.0$ years. The result in this latter experiment is similar to the one documented in Fig. 3.20a up to the latter velocity change on the right hand side of the figure. Additional velocity changes could not be added to the functional model due to the constraint related to Δt_v .

Figure 3.21 illustrates the results of four CODE DCB time series analyses by searching only for periodic functions. A maximum of $n_{per} = 500$ spectral lines are sought. In Figs. 3.21a and 3.21b the search is performed for periods from $p_{beg} = 10$ to $p_{end} = 400$ days, while in Figs. 3.21c and 3.21d periods are sought from $p_{beg} = 10$ days through $p_{end} = 1,600$ days. For both ranges the level of significance is first set to $U_t = 0.01$ and then to $U_t = 0.001$. We see that with a larger range of the search the time series are better represented by the functional model. A smaller level of significance leads to more periodic functions.

Figure 3.22 illustrates the result of the analyses of CODE DCB time series by simulta-

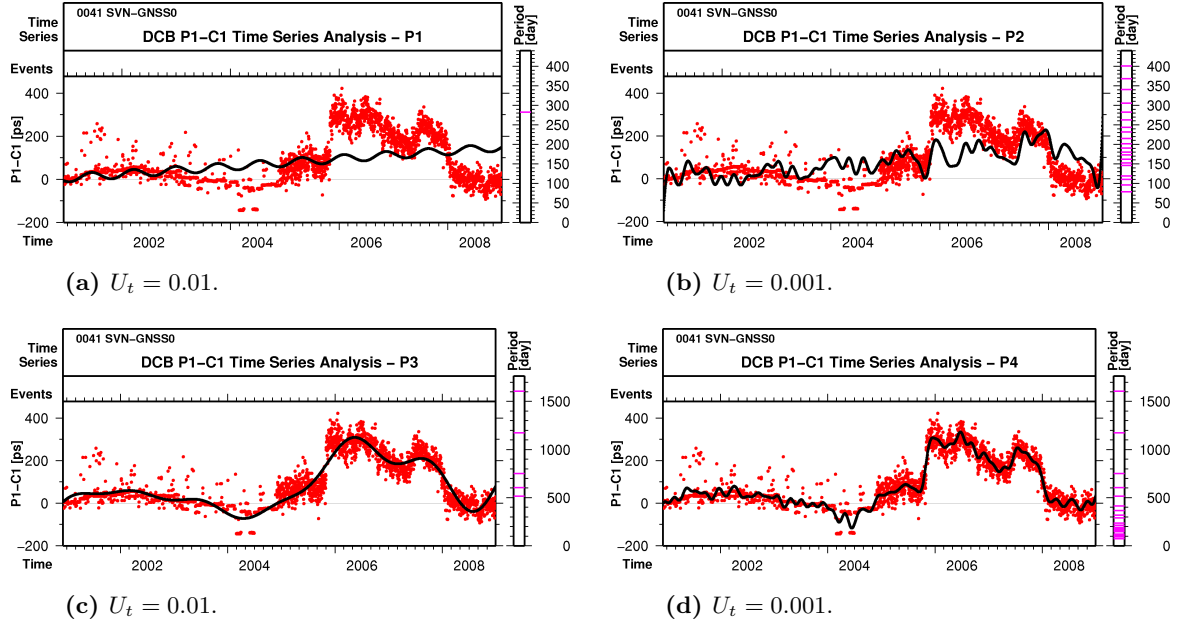


Figure 3.21: Validation search for for periodic functions. DCB P1-C1 SVN 41 time series analyzed with different levels of significance U_t . (Red) time series. (Black) functional model.

neously performing the search for discontinuities, velocity changes, outliers, and periodic functions. The level of significance for outliers is set to $U_s = 100$ and the minimum interval length between successive velocity changes to $\Delta t_v = 1.0$ years. Figure 3.22a illustrates the first result with the overall level of significance set to $U_t = 0.5$. Two discontinuities and tens of outliers were found. With $U_t = 0.1$, see Fig. 3.22b, w.r.t. Fig. 3.22a, the algorithm found one additional velocity change and one additional discontinuity. Compared to the result with $U_t = 0.5$ different outliers disappeared and additional other outliers appeared. With $U_t = 0.01$, see Fig. 3.22c, the analysis finished with significant elements of all types: discontinuities (D), velocity changes (V), outliers (-), periodic functions (-), and velocity changes in conjunction with a discontinuity (DV). This is possible since at step 10 of the algorithm (see Fig. 3.2) a velocity change element is proposed for each discontinuity. With $U_t = 0.005$, see Fig. 3.22d, the analysis identified only one velocity change. Compared to Fig. 3.22d, the latter analysis modelled the time series with more discontinuities. Let us conclude by stating that all analyses show reasonable results and that the time series may be represented by different functional models.

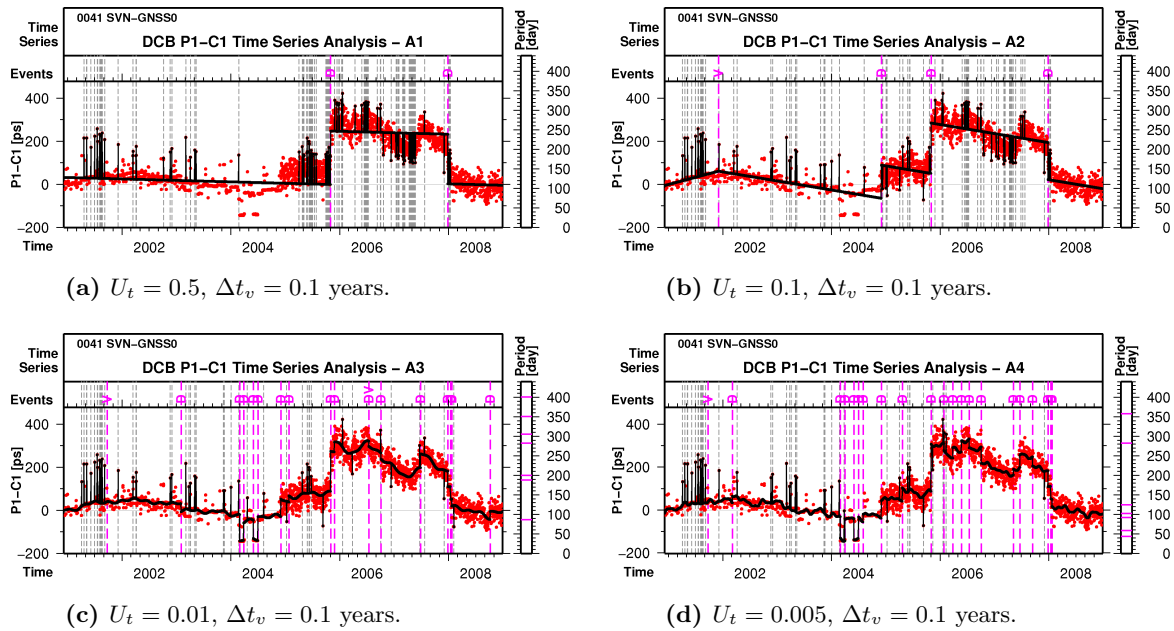


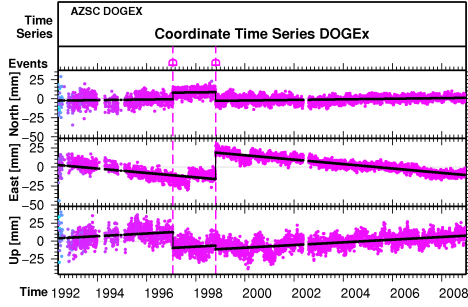
Figure 3.22: Validation of all searches simultaneously. DCB P1-C1 SVN 41 time series analyzed with four different levels of significance. (Red) time series. (Black) functional model. (D) significant discontinuity.

3.9 External Validation

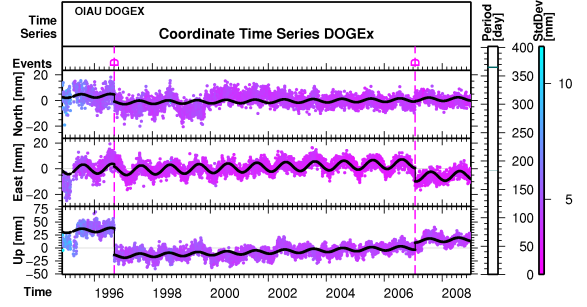
The **Detection of Offsets in GPS Experiment (DOGEx)**⁴ is being conducted in order to test automated offset detection algorithms against a known truth in 50 realistic GPS coordinate time series. These time series cover the time interval from 1992 through 2009, have gaps, contain artificial offsets and colored noise. As the time series were derived from actual GPS time series, their variations and standard deviations in the first years are larger than in the following years. Participants have to identify and estimate offsets and give estimates of the resulting rates, one for each component of the time series.

Figure 3.23 shows the FODITS analysis of two DOGEx time series (AZSC and OIAU) analyzed with the three different levels of significance: $U_t = 0.1$, $U_t = 0.05$, and $U_t = 0.005$. The analysis was carried out in three dimensions simultaneously—North, East, and Up. The examples illustrate the difficulty of selecting the correct level of significance. Figures 3.23a and 3.23b show that with $U_t = 0.1$ not all discontinuities were identified. The second FODITS solution, AIUBCOD2 in DOGEx, was obtained by $U_t = 0.05$ (see Figs. 3.23c and 3.23d). In the two figures we notice that the largest discontinuities were identified. Whether the apparent discontinuity across year 2000 in the East component of

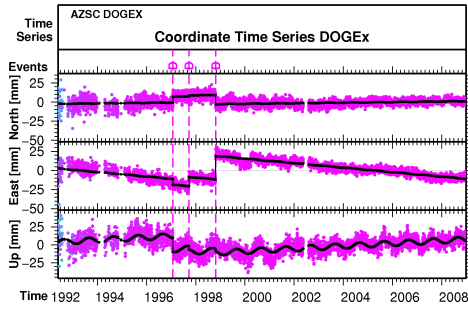
⁴[IGSMail-6211] DOGEx: Detection of Offsets in GPS timeseries Experiment update. The experiment is run jointly by Matt King (Newcastle University, Newcastle upon Tyne, UK, m.a.king@ncl.ac.uk) and Simon Williams (Proudman Oceanographic Laboratory, Liverpool, UK; sdwil@pol.ac.uk)—Working Group 3 of COST Action ES0701 "Improved Constraints on Models of Glacial Isostatic Adjustment".



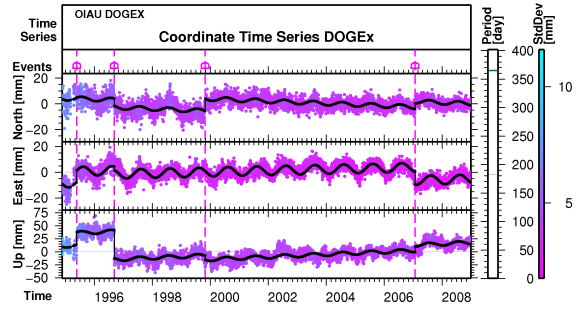
(a) Analysis of AZSC with $U_t = 0.1$.



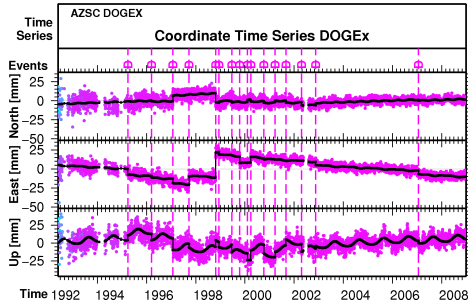
(b) Analysis of OIAU with $U_t = 0.1$.



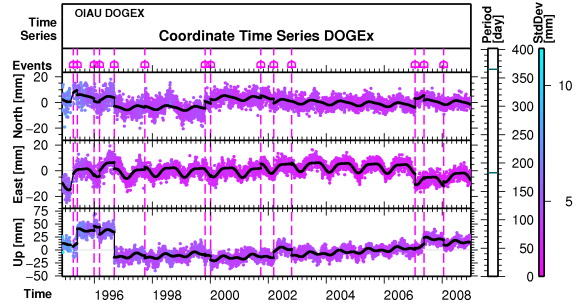
(c) Analysis of AZSC with $U_t = 0.05$.



(d) Analysis of OIAU with $U_t = 0.05$.



(e) Analysis of OIAU with $U_t = 0.005$.

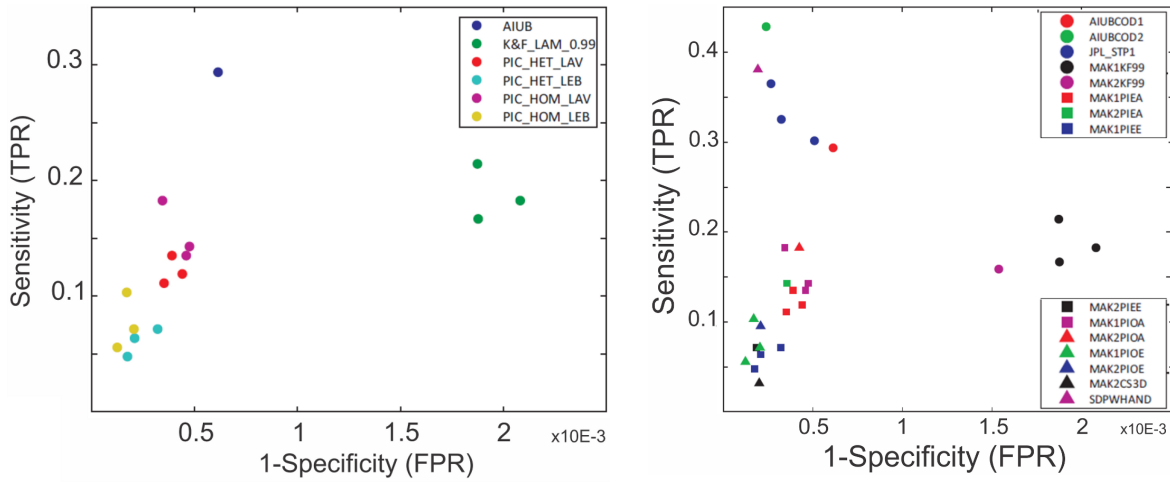


(f) Analysis of AZSC with $U_t = 0.005$.

Figure 3.23: FODITS analysis of time series of the DOGEx with $U_t = 0.1$, $U_t = 0.05$, and with $U_t = 0.005$.

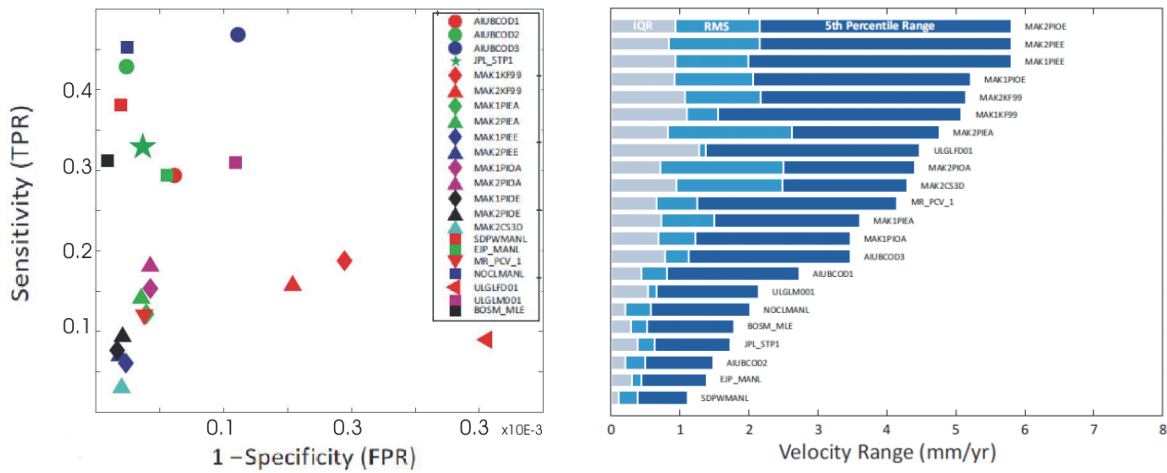
AZSC is a true one it is not known. Figures 3.23e and 3.23f illustrate the analysis with $U_t = 0.005$. As expected, the analysis found more and more discontinuities. In this latter case, however, too many discontinuities were likely identified.

The results of DOGEx, reported from (King and Williams, 2010, 2011), are shown in Fig. 3.24. Different detection algorithms were compared in terms of sensitivity versus specificity. Sensitivity (TPR) is expressed as the ratio $TP/(TP+FN)$, with True Positive (TP) the number of successfully identified offsets and False Negative (FN) the number of actual offsets in the time series that were not identified as TP. Specificity (FPR), on the other hand, is expressed as the ratio $FP/(FP+TN)$, where False Positive (FP) is the



(a) Results of 2009.

(b) Results of 2010.



(c) Results of 2011.

(d) Results of 2011.

Figure 3.24: Results of the DOGEx (King and Williams, 2010, 2011).

number of offsets not corresponding to the actual offsets in the dataset and True Negative (TN) is the complement of FP. If all offsets are correctly identified in the time series the ratio becomes $TPR=1$ and $FPR=0$. The experiment results of the last three updates are documented in Figs. 3.24a, 3.24b, and 3.24c. Figure 3.24d shows in addition the velocity ranges of the last update: the more offsets are identified in the correct position, the smaller becomes the value. In all updates the AIUB/CODE solutions (AIUBCOD1, AIUBCOD2, and AIUBCOD3) achieved excellent results.

DOGEx contributed significantly to the develop of the algorithm implemented in FODITS. The first results shown in Fig. 3.24a were, e.g., obtained by the algorithm presented in (Os-tini et al., 2008a), where the elements were removed step-by-step from the normal equation

system and, moreover, where the most probable discontinuities were sought in the whole interval of the post-fit residual time series (see Sect. 3.3.1). After having realized that many discontinuities could not be identified in this way, the algorithm of **FODITS** was modified to add elements step-by-step to the functional model and, moreover, to search for unknown discontinuities in the sub-intervals delimited by the discontinuities in the functional model (see Sect. 3.4). This latter manner was in fact adopted to overcome the weakness of the search to detect offsets in the presence of colored noise.

4 Cleaning Coordinate Time Series

Assessing the quality of the underlying coordinate time series (see Chapter 1), i.e., cleaning the coordinate time series, is a key processing task when establishing multi-year solutions. This task consists of two principal steps. First, the underlying coordinate time series are analyzed, i.e., events such as discontinuities, outliers, velocity changes, and periodic functions are identified, see the algorithm of FODITS described in Chapter 3. Then the analysis results are taken into account to obtain the final cumulative multi-year solutions.

This chapter documents the strategy to assess the quality of coordinate time series generated by FODITS. Sections 4.1 and 4.2 describe how the BSW program ADDNEQ2 generates both, network solutions and coordinate time series, respectively. Section 4.3 introduces the scheme to assess the quality of the coordinate time series. Finally, Sect. 4.4 presents examples of quality assessment within the CODE reprocessing framework (see Sect. 2.4).

4.1 Station Coordinates and Linear Velocities

The station motion is assumed to be linear in time:

$$\mathbf{x}(t) = \mathbf{x}(t_r) + \mathbf{v}_r (t - t_r) , \quad (4.1)$$

where $\mathbf{x}(t_r)$ (or \mathbf{x}_r) represents the position vector at the reference epoch t_r and $\mathbf{x}(t)$ the position vector at epoch t . Alternatively, Eq. (4.1) may be expressed by the position vector $\mathbf{x}(t_1)$ (or \mathbf{x}_1) and $\mathbf{x}(t_2)$ (or \mathbf{x}_2) at the boundary epochs t_1 and t_2 . From

$$\mathbf{x}(t) = \mathbf{x}(t_1) + \mathbf{v}_r(t - t_1) \quad \text{and} \quad \mathbf{x}(t) = \mathbf{x}(t_2) + \mathbf{v}_r(t - t_2) \quad (4.2)$$

we obtain

$$\mathbf{v}_r = \frac{\mathbf{x}_2 - \mathbf{x}_1}{t_2 - t_1} . \quad (4.3)$$

By inserting Eq. (4.3) in Eq. (4.2) one obtains the alternative parameterization

$$\mathbf{x}(t) = \mathbf{x}_1 \left(\frac{t_2 - t}{t_2 - t_1} \right) + \mathbf{x}_2 \left(\frac{t - t_1}{t_2 - t_1} \right) . \quad (4.4)$$

ADDNEQ2 parameterizes site velocities as piecewise parameters according to Eq. (4.4), see (Brockmann, 1997; Dach et al., 2007). The following steps are accomplished to estimate station velocities. In each NEQ the coordinates are represented by the parameterization (4.4). The original coordinate $\mathbf{x}(t)$, usually valid for a daily or a weekly interval, are

represented by $\mathbf{x}(t_1)$ and $\mathbf{x}(t_2)$ according to the transformation (2.32). **NEQs** are cumulated to form one stacked **NEQ** containing linear station motion and all other parameters of interest. Constraints (e.g., for the datum definition) are added to the parameters of the stacked **NEQ** (see Sect. 2.3.5). Finally, the inversion of the stacked **NEQ** (see Sect. 2.3.3) gives the estimates for the coordinates \mathbf{x}_1 and \mathbf{x}_2 of each station. The set of station coordinates \mathbf{x}_r and velocities \mathbf{v}_r are derived according to Eqs. (4.2) to (4.4) considering the full **VCI**.

The constraints defining the datum of the network must be parameterized in the same manner as the linear station motions. If minimum network constraints such as **NNR** or **NNT** are put on the coordinates \mathbf{x}_1 as described in Sect. 2.3.5, the same constraints must also be put on the coordinates \mathbf{x}_2 to obtain properly constrained linear station motions. Coordinates and velocities must be therefore constrained in the same way. Datum definitions of the network with different constraints for station coordinates and station velocities would hardly be realistic.

4.2 Coordinate Time Series

The **BSW** program **ADDNEQ2** generates time series of residuals. After have computed the multi-year network solution as described in Sect. 4.1, the program generates the residuals: The original **NEQs** are inverted one after the other as in the first phase. As no velocity parameters are estimated, network constraints are only put on the coordinates. Time series of residuals are eventually obtained by comparing each solution of the series obtained in the second part to the multi-year solution obtained in the first part of the program.

For coordinates, the comparison between the first and second parts of the program can be either a simple mathematical subtraction operation or an Helmert transformation (2.42). In the latter case the transformation is obtained similarly to the setting of minimum constraints (see Sect. 2.3.5), but instead of estimating the Helmert parameters (2.44) between the a priori and the estimated network solutions for a set of reference sites, the Helmert parameters are estimated between the combined and the single network solutions for all common sites of the networks. The time series of residuals are transformed from the geocentric equatorial Earth-fixed reference system (**XYZ**) to the **NEU** components.

4.3 Quality Assessment of Coordinate Time Series

Figure 4.1 contains a general quality assessment scheme for coordinate time series in the **BSW**. **ADDNEQ2** generates a first cumulative solution **A1** (see Sect. 4.1) as well as time series of coordinate residuals (see Sect. 4.2) using the **NEQs** and the *metadata* **M0**. The metadata consist of an a priori reference frame (**CRD/VEL**) as datum of the network solution, a list of station information (**STA**) with discontinuities (see Sect. 4.3.1), outliers (see Sect. 4.3.2), and relative velocity constraints, and a list of reference (core) stations (**FIX**). Time series of residuals **A1** are analyzed by **FODITS** by checking and identifying the presence of significant discontinuities, outliers, velocity changes, and periodic functions,

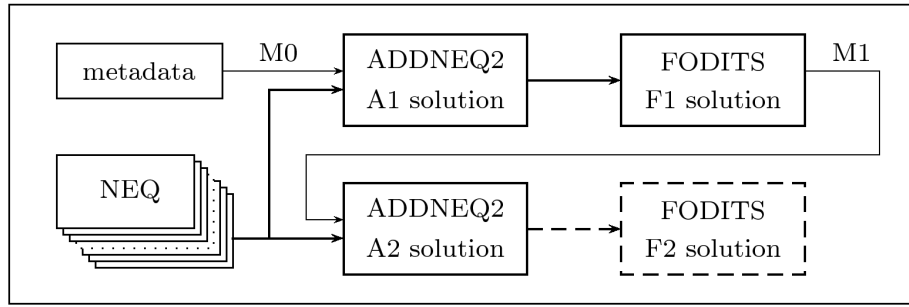


Figure 4.1: Quality assessment of coordinate time series in the **BSW**. (A) refers to **ADDNEQ2**. (F) refers to **FODITS**. (M) refers to metadata.

see Chapter 3. **FODITS** updates metadata M1 for a subsequent cumulative solution. The final solution A2 is obtained by **ADDNEQ2** by taking into account the updated metadata M1. Except for special experiments or for validation no further **FODITS** time series analysis F2 is carried out. As **FODITS** checks and identifies already all elements in analysis F1, no additional elements should be found in the analysis F2.

4.3.1 Discontinuities and Velocity Changes

Discontinuities and velocity changes subdivide the coordinate time series in sub-intervals. For each such interval **ADDNEQ2** estimates a set of station coordinates and velocities according to Eq. (4.4). For n discontinuities one therefore obtains $n + 1$ sets of station coordinates and velocities.

Velocity changes could be realized by tightly constraining the boundary vectors of consecutive sub-intervals—modelled as piecewise-linear parameters in the **BSW** (Dach et al., 2007). This feature is, however, not yet implemented in **ADDNEQ2**. This is why velocity changes are modelled by loosely constraining boundary coordinate parameters ($\sigma_r = 1$ m)—which is equivalent to not using constraints. Discontinuities, on the other hand, are obtained by tightly constraining consecutive station velocities in a relative way ($\sigma_r = 0.00001$ m/sec).

4.3.2 Outliers

Outliers are provided in metadata together with a time interval. All parameters (e.g., coordinates, troposphere, etc.) contained in **NEQs** and contained in such time intervals are pre-eliminated before stacking (see Sect. 2.3.4). Pre-eliminated outliers are redistributed to all other parameters of the **NEQ** before this is stacked. On the normal equation level outliers are assumed to be small otherwise their pre-elimination could affect the estimation of all other parameters. Large outliers are assumed to have been eliminated in the preprocessing steps (see Sect. 2.4).

4.3.3 Update of Metadata for a Follow-Up Solution

A list of reliable reference sites is created by identifying and eliminating (marking) poorly observed stations in the a priori input list.

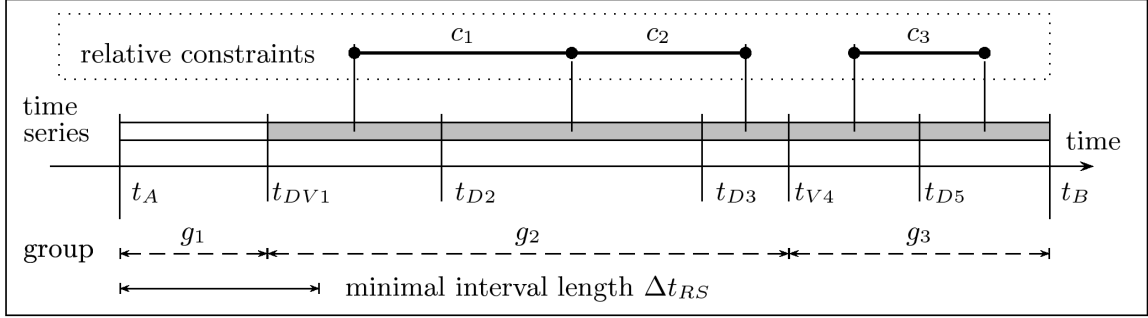


Figure 4.2: Typical scenario of sub-intervals and relative velocity constraints for a reference site. Time series span from t_A through t_B . Sub-intervals emerge from the discontinuities (D) and velocity changes (V). Relative constraints on station velocities are denoted by (c). Groups of sub-intervals with same linear velocity are denoted by (g). Sub-intervals filled in light-gray are included in the list of reference sites. Δt_{RS} is the minimum interval length for reference sites.

FODITS updates the metadata for a subsequent **ADDNEQ2** solutions. Figure 4.2 illustrates a typical result for a reference station. Relative velocity constraints (such as c_1 , c_2 , and c_3) are put on sub-intervals to model the discontinuities. As a result, groups of sub-intervals (such as g_1 , g_2 , and g_3) with identical station velocity are formed. Initially, for a core station, all groups of sub-intervals are considered. In a second step all groups are checked to meet two requirements: (1) a group has the *minimum interval length* Δt_{RS} . (2) the number of observations in a group must have a *minimum percentage of data* p_{RS} . Groups not meeting both requirements become of "non-reference" and, as a consequence, the associated sub-intervals are rejected from the list of reference sites. The first group did not meet the first requirement in Fig. 4.2. For this reason, all sub-intervals of this group are not considered as reference sites for subsequent **ADDNEQ2** runs.

As this strategy depends on the analyzed time series, the update of metadata shall be performed for each analyzed campaign. A well observed reference sites in a first campaign might become a poorly observed reference site in another analyzed campaign, e.g., because the observation interval changed.

4.4 Examples

Daily 1D and weekly 7D coordinate time series of the global network (see Sect. 2.4) are analyzed using the scheme in Fig. 4.1. Table 4.1 summarizes the **ADDNEQ2** parameters for both, cumulative solutions and time series. As **NNT** and **NNR** minimum constraints for both, station coordinates and velocities are required, the difference of the cumulative solution and each single solutions are analyzed.

Table 4.1: ADDNEQ2 parameter options for daily 1D and weekly 7D solutions.

Set up station velocities for a cumulative solution	yes (see Sect. 4.1)
Comparison of cumulative and single solutions	subtraction (see Sect. 4.2)
Datum definition for station coordinates and velocities	minimum constraints
- Minimum constraints NNT	yes with $\sigma = 0.00001$ (mm, mm/yr)
- Minimum constraints NNR	yes with $\sigma = 0.00001$ (mm, mm/yr)
- Minimum constraints for scale	no
Initial list of reference stations	all 117 IGS05 included in the network solution
Geocenter parameters	pre-eliminated before stacking
Earth rotation parameters (ERPs)	transformed to 24 hours and pre-eliminated before stacking
- nutation parameters	deleted, i.e, a priori values of IAU2000A used
- piecewise-linear	1 hour to 24 hours bins
- pole components X and Y	free, 24 hours
- a priori σ UT1-UTC	first parameter fixed to 0.00001 mas

4.4.1 Analysis of Coordinate Time Series

According to the scheme in Fig. 4.1 a first cumulative solution (A1) and coordinate time series (A1) for both, daily 1D and weekly 7D series, are generated by ADDNEQ2 with the settings of Table 4.1. Settings and results for both, daily and weekly FODITS analyses F1, are contained in Tables 4.2 and 4.3, respectively. In both the daily and the weekly time series 234 stations were analyzed by checking the datum definition, equipment changes, earthquakes, and by identifying discontinuities, velocity changes, and outliers. For the 1D analysis the minimum relative improvement and the independent statistical test for outliers were set to $U_t = 0.02$ and $U_s = 15.0$, respectively. For the 7D analysis these were set to $U_t = 0.04$ and $U_s = 50.0$, respectively. A minimum interval length of three years was selected for velocities.

Altogether, the analysis of 1D coordinate time series found 441 discontinuities (384 offsets and 74 velocity changes), 8438 outliers (4496 of them as "outliers" from the test of the datum definition, see Sect. 3.2.4), and 209 annual signals. The number of discontinuities, which corresponds to 1.827 every 10 years, is above that of one per 9 years found by (Williams, 2003). Every 10 years, on the average, 0.456 of the 1.376 predefined equipment changes and 0.597 of the 3.878 predefined earthquakes were found to produce significant changes in the analysis. The number of significant discontinuities and velocity changes of unknown reason, every 10 years, were of 0.675 and 0.104, respectively. The 7D analysis, altogether, found 494 discontinuities (436 offsets and 82 velocity changes), 53 more than the 1D analysis. 116 equipment changes were considered as significant, 6 more than for the 1D series, 168 earthquakes were considered to produce significant effects, 24 more than for the 1D series.

The datum definition, which is checked epoch-by-epoch (see Sect. 3.2.4), rejects one-by-one reference sites if larger differences are encountered than the user-defined values (North: 50 mm, East: 50 mm, Up: 50 mm). Translation and scale were estimated in the Helmert transformation (rotation was fixed). Figure 4.3 shows the number of stations of both reference sites and rejected sites for the 1D and 7D solutions. The rejected sites were considered as outliers in the analysis of time series. As opposed to the total number of

Table 4.2: Analysis F1 of CODE daily coordinate time series 1D.

Settings			
Time interval of the time series; From: 01-Jan-1994, To: 31-Dec-2008			
Time series; daily 1D			
Number of analyzed stations; 234			
Number of data in time series; maximum: 5468, mean: 3356			
Data variance-covariance; VCI of North, East, and Up)			
Identify discontinuities, outliers, velocity changes			
A velocity change is proposed after each discontinuity			
Minimum relative improvement $U_t = 0.02$ (abort criterion)			
Independent statistical test for outliers $U_s = 15.0$ (abort criterion)			
Additional criterion ^a , minimum size for discontinuities (meters) Horizontal: 0.001, Vertical: 0.003			
Additional criterion ^a , minimum size for periodic functions (meters) Space: 0.001			
Minimum interval length for velocities $\Delta t_v = 3$ years			
Check equipment changes			
Check earthquakes			
Check annual and semi-annual signals			
Check the datum definition; North: 50 mm, East: 50 mm, Up: 50 mm; translation and scale			
Analysis results	Mean per site	Mean per 10 year	Total in all sites
Discontinuities and velocity changes	1.885	1.827	441
- discontinuities	1.641	1.591	384
- velocity changes	0.316	0.307	74
Outliers from datum definition test	30.795	18.629	4496
Outliers (total)	36.060	34.963	8438
Annual period	0.893	-	209
Semi-annual period	0.244	-	57
A priori equipment changes	1.419	1.376	332
Equipment changes	0.470	0.456	110
- antenna changes	0.355	0.344	83
- receiver changes	0.295	0.286	69
A priori earthquakes	4.000	3.878	936
Earthquakes	0.615	0.597	144
- discontinuities	0.474	0.460	111
- velocity changes	0.209	0.203	49
Discontinuities of unknown reason	0.697	0.675	163
Velocity changes of unknown reason	0.107	0.104	25

^aSee Sect. 3.3.2.

stations and the number of reference sites, the number of rejected sites decreases with the length of the time interval.

Figures 4.4 and 4.5 document selected results of both daily 1D and weekly 7D coordinate time series.

Figure 4.4a illustrates the analysis of station AMC2 (Colorado Springs, U.S.A.) for the daily series. The receiver change Sr1 on 03-Jul-2002 is proposed by the list of predefined elements. According to the analysis this equipment change induced a significant discontinuity of 8.4 ± 0.4 mm in the vertical component. If the used information is correct, this fact indicates that not only antenna changes, but also receiver changes may induce significant

Table 4.3: Analysis F1 of **CODE** weekly coordinate time series 7D.

Settings			
Time interval of the time series; From: 05-Jan-1994, To: 24-Dec-2008			
Time series; weekly 7D			
Number of analyzed stations; 234			
Number of data in time series; maximum: 779, mean: 495			
Data variance-covariance; VCI of North, East, and Up			
Identify discontinuities, outliers, velocity changes			
A velocity change is proposed after each discontinuity			
Minimum relative improvement $U_t = 0.04$ (abort criterion)			
Independent statistical test for outliers $U_s = 35.0$ (abort criterion)			
Additional criterion ^a , minimum size for discontinuities (meters) Horizontal: 0.001, Vertical: 0.003			
Additional criterion ^a , minimum size for periodic functions (meters) Space: 0.001			
Minimum interval length for velocities $\Delta t_v = 3$ years			
Check equipment changes			
Check earthquakes			
Check annual and semi-annual signals			
Check the datum definition; North: 50 mm, East: 50 mm, Up: 50 mm; translation and scale			
Analysis results	Mean per site	Mean per 10 year	Total in all sites
Discontinuities and velocity changes	2.111	2.057	494
- discontinuities	1.863	1.815	436
- velocity changes	0.350	0.341	82
Outliers from datum definition test	3.342	2.032	488
Outliers (total)	13.167	12.829	3081
Annual period	0.915	-	214
Semi-annual period	0.333	-	78
A priori equipment changes	1.415	1.378	331
Equipment changes	0.496	0.483	116
- antenna changes	0.346	0.337	81
- receiver changes	0.342	0.333	80
A priori earthquakes	3.983	3.881	932
Earthquakes	0.718	0.700	168
- discontinuities	0.568	0.554	133
- velocity changes	0.231	0.225	54
Discontinuities of unknown reason	0.799	0.779	187
Velocity changes of unknown reason	0.120	0.117	28

^aSee Sect. 3.3.2.

discontinuities in the coordinates. King and Watson (2010) indicated the same findings from their analysis experience of **GPS** coordinate time series. Two more discontinuities were identified: one of -5.8 ± 0.4 mm in Up and one of 7.9 ± 0.1 mm in the North components. Therefore, discontinuities of unknown reason are also present in homogeneously processed series (see Sect. 2.4). A significant annual signal of amplitude (North) 1.6 mm, (East) 1.7 mm, and (Up) 1.4 mm with a standard deviation of 0.1 mm and few outliers were also found. As no significant velocity changes were found, all sub-intervals derived from the analysis were assumed to belong to the same group (see Sect. 4.3.3)—a result visualized by the horizontal bar (REF) in the header: colored bars indicate reference site; a particular color indicates a particular group of sub-intervals. Figure 4.4b documents the results for

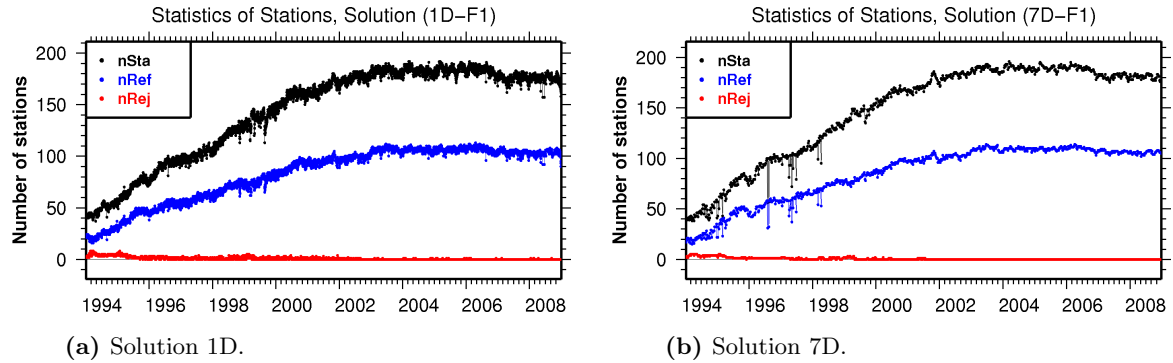


Figure 4.3: Number of stations in daily 1D and weekly 7D solutions resulting from the test of the datum definition for the interval 1994-2008. (nSta) number of stations. (nRef) number of resulting reference sites. (nRej) number of rejected stations with thresholds North: 50 mm, East: 50 mm, Up: 50 mm.

weekly series of the same station. The elements found as significant in the daily analysis were also found as significant in the weekly analysis. The Up component of Sr1 was, e.g., estimated as 8.5 ± 0.5 mm, which agrees to the value found in the 1D analysis.

Figure 4.4c documents the 1D analysis of station ANKR (Ankara, Turkey). Two large earthquakes (VE2 of M7.6 with epicenter at 264 km and vE3 of M7.2 with epicenter at 166 km from the site) were generating significant effects in the horizontal components. The first earthquake induced both, an offset and a velocity change, while the second one induced only an offset. The two co-seismic offsets were confirmed, e.g., by (Ergintav et al., 2009). On 05-Mar-2008 the receiver change Sr1 apparently induced an offset, in particular in the vertical component. One may see that this event shares the same gap with the earthquake (ve10 of M5.7 with epicenter at 64 km) and the equipment change srae2, both apparently not significant. It is not clear which of the three events caused the discontinuity of this kind. Many "special cases" of this kind still need to be implemented into the algorithm for an even more reliable automated analysis of coordinate time series. The analysis found the earthquake vE9 M4.3 with the epicenter at 28 km significant with offsets of 0.4 mm, -1.5 mm, and -5.1 mm in the North, East, and Up directions, and standard deviation of about 0.1 mm. The result of vE9 is not as clear as that for VE2. Figure 4.4d illustrates the analysis result of the weekly ANKR coordinate time series. Compared to the analysis of daily series, FODITS identified the discontinuity D1 with a size of -6.9 ± 0.6 mm in the Up component. It is, however, not clear whether D1 is real.

Figures 4.4e and 4.4f illustrate the results for KOKB (Kokee Park, U.S.) for daily and weekly series, respectively. Both analyses found the discontinuity D1 and the two equipment changes Sra2 and Sa3. The daily analysis shows that between 1994 and 1999 many epochs were identified as "outliers" in terms of datum definition. As Table 4.2 indicates, stations with residuals larger than 50 mm in one or more components were considered outliers. With the same thresholds, see Table 4.3, no such "outliers" were found for the weekly analysis. The analysis of weekly time series found, however, outliers of unknown source between 1994

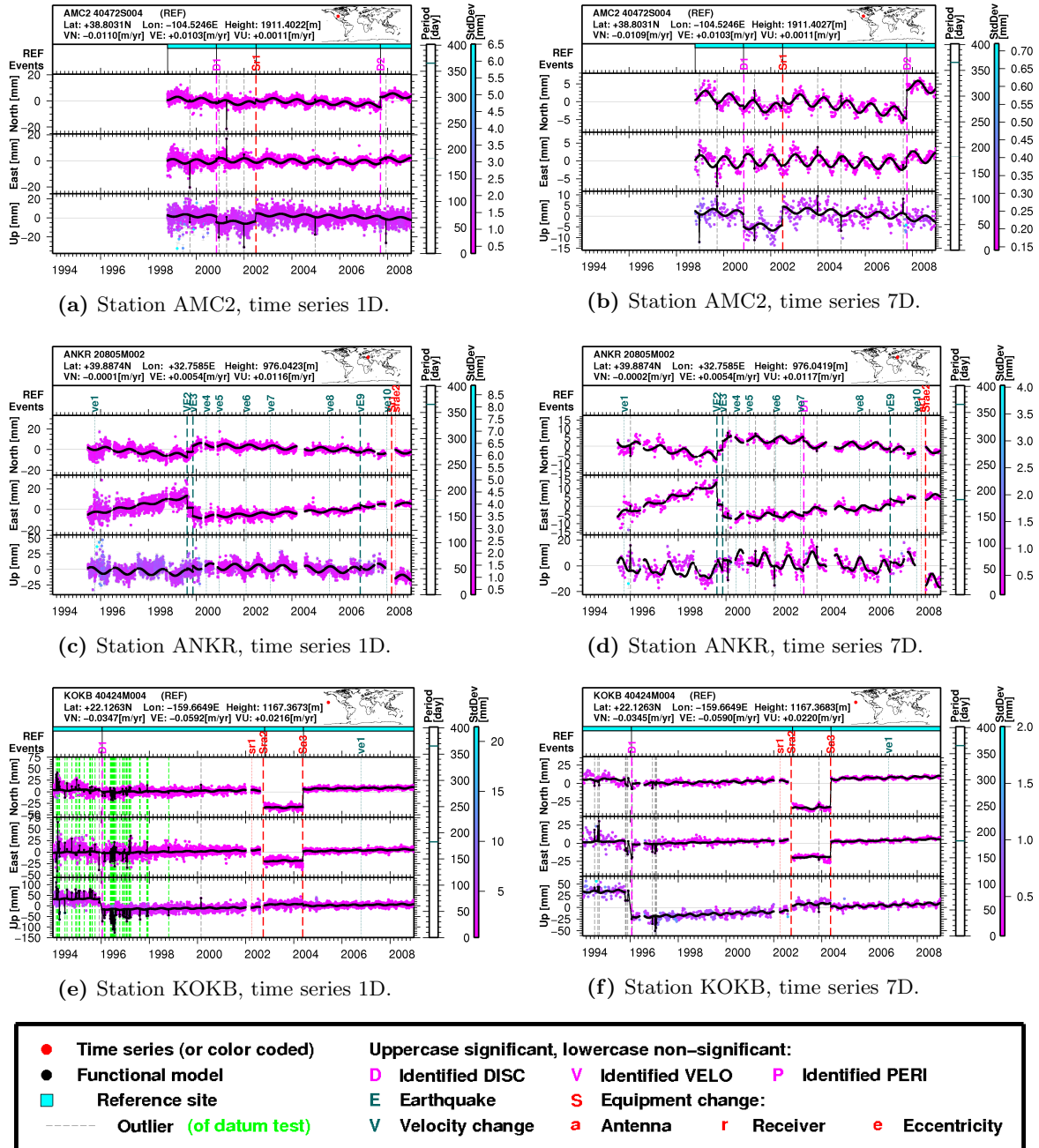


Figure 4.4: Analysis of daily 1D and weekly 7D coordinates—part 1. (Color-coded) time series with standard deviation. (Black) functional model.

and 1997.

Figure 4.5a documents the 1D analysis of station MAD2 (Robledo, Spain). The only (not significant) equipment change known is sr1 on 29-Nov-2004. According to Table 4.4

4 Cleaning Coordinate Time Series

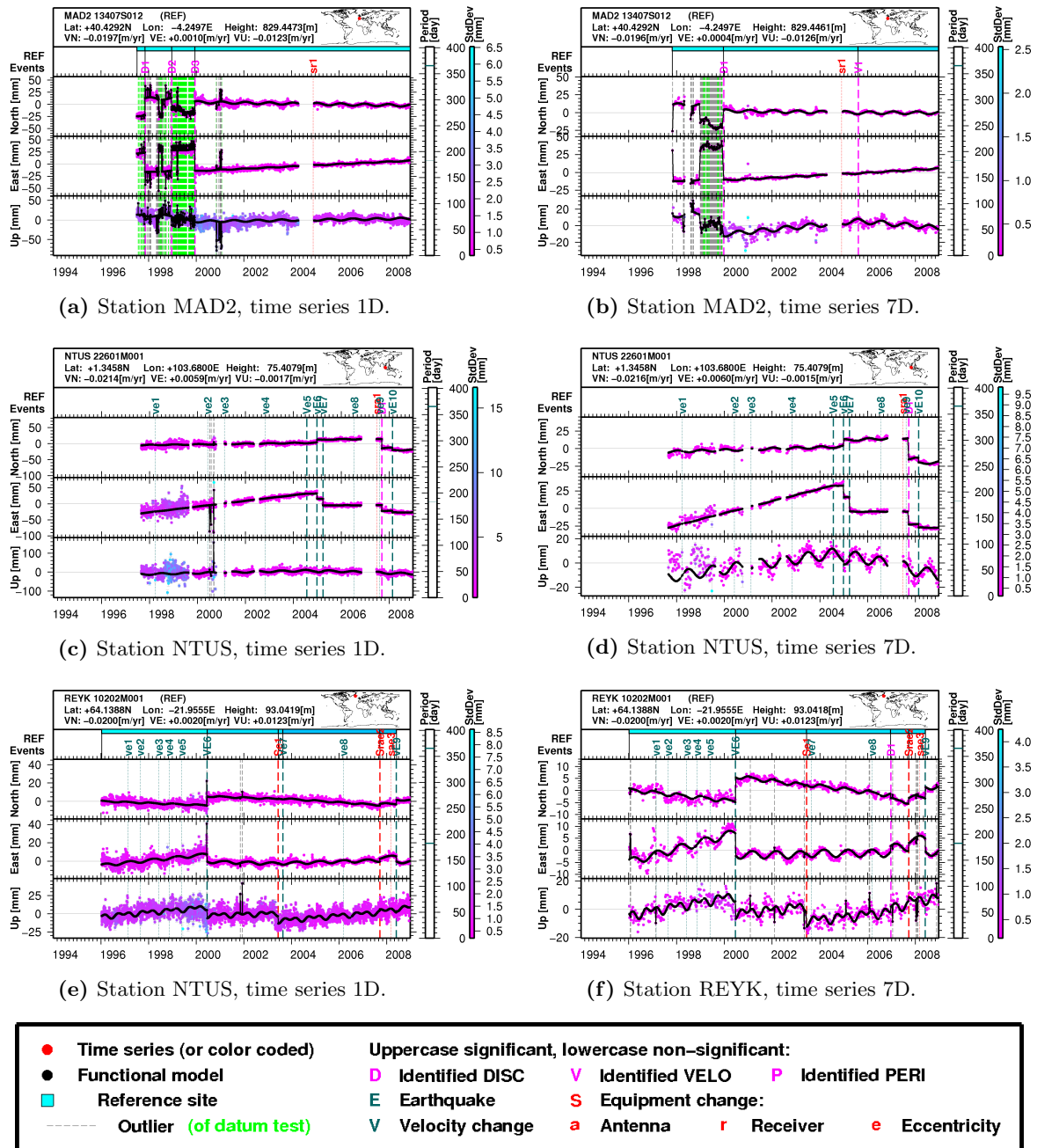


Figure 4.5: Analysis of daily 1D and weekly 7D coordinates—part 2. (Color-coded) time series with standard deviation. (Black) functional model.

(taken from the IGS LOG-file) this event is associated with the firmware upgrade of the receiver ASHTECH Z-XII3T. The analysis identified a sequence of three discontinuities and outliers in the test of the datum definition as significant. By comparing the epochs of such discontinuities with the entries in Table 4.4 we note that D1 on 09-Nov-1997 may

Table 4.4: Equipment changes at station MAD2 from IGS-LOG: <http://igsb.jpl.nasa.gov/igsb/station/log/mad2.20110303.log>. The last column reports the discontinuities identified by FODITS 1D analysis.

Epoch	Type		Serial number	Firmware	In 1D analysis
25-Sep-1996	Antenna	AOAD/M.T	404-B		
30-Oct-1997	Receiver	ROGUE SNR-12 RM	R249	3.2	(D1)
16-Jun-1998	Receiver	ROGUE SNR-12 RM	R202	0.0	(D2)
24-Aug-1999	Receiver	ROGUE SNR-12 RM	R202	3.2.32.8	
19-Nov-1999	Receiver	ROGUE SNR-12 RM	R202	0.0	(D5)
10-Sep-2003	Antenna	AOAD/M.T	4046		
29-Sep-2003	Antenna	AOAD/M.T	404-B		
11-Nov-2003	Antenna	AOAD/M.T	451-U		
29-Nov-2004	Receiver	ASHTECH Z-XII3T	RT920041504	1L01-1D04	

be due to the receiver update on 30-Oct-1997 and D3 on 12-Dec-1999 to the receiver update on 19-Nov-1999. No explanation can be given for D2 on 21-Dec-1998. The two apparent discontinuities in 1998 were interpreted as a sequence of outliers. One of them, on 16-Jun-1998, may be associated with the receiver change from ROGUE SNR-12 RM serial number R249 to the same receiver but serial number R202, see Table 4.4. These results indicate that IGS LOG-files might not be complete. There is, e.g., no information concerning D2. Secondly, the information in the IGS LOG-files is not completely taken into our internal list of equipment changes at CODE. There is, e.g., no information available for the event on 16-Jun-1998. Figure 4.5b shows that, for the same station, the analysis of weekly series identified only the D1 discontinuity. As opposed to the daily series, the analysis of weekly series identified the velocity change V1 to model the apparent subsidence displacement after 2006. As a consequence, a new group of sub-intervals began (as indicated by the change of color in the header, see REF bar), i.e., no relative velocity constraints were put on the two groups (see Sect. 4.3.3).

Figure 4.5c documents the 1D analysis of station NTUS (Singapore, Republic of Singapore). The time series are dominated by the prominent Sumatra Earthquake (vE6 of M9.0 on 26-Dec-2004 with epicenter at 882 km) and its aftershock (vE7 of M8.6 on 28-Mar-2004 with epicenter at 735 km). Before these two large events the analysis found a velocity change on 25-Jul-2004 associated with the earthquake Ve5 of M7.3 with epicenter at 418 km. Towards the end of 2007 the analysis found the discontinuity of unknown source, prominent in the horizontal components. This discontinuity on 13-Sep-2007 is preceded by the equipment change sra1 on 25-Jun-2007 and the earthquake (ve9 of M7.5 on 08-Aug-2007 with epicenter at 897 km). After D1 the horizontal components show a typical relaxation decay related to an earthquake post-seismic phase. As the minimum interval length Δt_v for velocities was 3 years (see Table 4.2), no velocity change was set up to model the decay. This is why FODITS assessed the earthquake vE10 of M7.4 on 20-Feb-2007 with epicenter at 872 km as a significant discontinuity. For more consistent analyses, earthquakes and in particular their post-seismic phases, need a better modelling strategy. The analysis of weekly series 7D is illustrated by Fig. 4.5d. Except for a few outliers, the analysis found the same elements as in the daily series.

Figure 4.5e documents the 1D analysis of station REYK (Reykjavik, Iceland). The earthquake VE6 of M6.5 with epicenter at 73km on 17-Jun-2000, which induced both, a discontinuity and a velocity change, was identified as significant and generated also a prominent outlier. More than 3 years later, the equipment change Se1 was followed by an apparent velocity change in the vertical component due to the earthquake Ve7 of M5.2 with its epicenter at 28 km. These two significant earthquakes, VE6 and Ve7, divided the time series in three distinct groups of sub-intervals (note the three colors in the horizontal bar REF). The algorithm found for 20-Sep-2007 that the equipment change Srae2 induced a small but significant offset in the series. Finally, the earthquake vE9 of M6.3 with epicenter at 48 km had an impact on the horizontal components. As the interval of the last group after vE9 did not meet the minimum length requirement of 3 years, the group was not considered a reference site for the subsequent multi-year solution. Annual and semi-annual signals were also found to be significant. The analysis of weekly series is documented by Fig. 4.5f. As opposed to the daily analysis ve7 was not judged to be significant, but D1 was considered as significant.

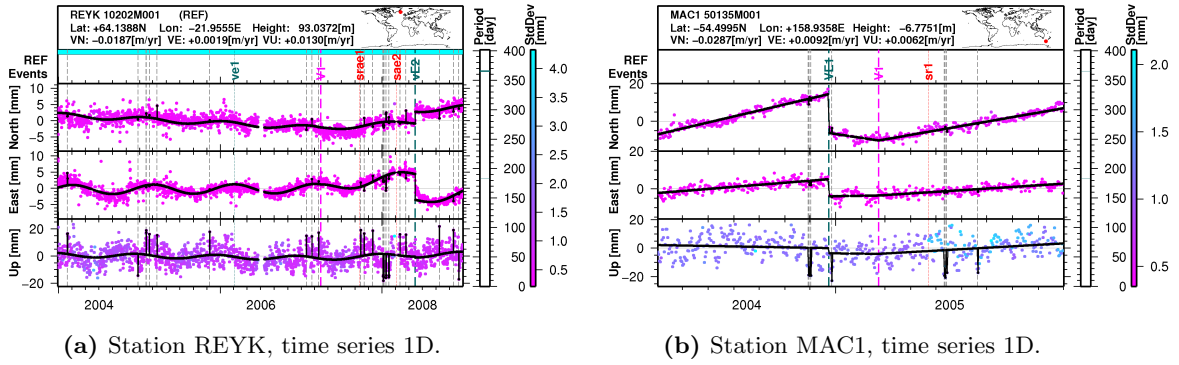


Figure 4.6: Analysis of daily coordinates for stations REYK and MAC1. (Color-coded) time series with standard deviation. (Black) functional model.

In an experiment, the minimum interval length for velocities Δt_v was reduced from 3 years down to 2 months. Figure 4.6a illustrates the new analysis of REYK for the time interval from 2004 to 2008. Compared to the results in Fig. 4.5e the re-analysis associated the velocity change V1 of (North) 2.8 mm/yr, (East) 3.6 mm/yr, and (Up) 2.9 mm/yr with uncertainty 0.3 mm/yr with 29-Mar-2007. As a consequence, the equipment change srae1 was considered as not significant. Figure 4.6b shows an enlarged view of the post-seismic relaxation phase of MAC1 after the M8.1 earthquake on 23-Dec-2004. As opposed to 3.17d the algorithm associated the decay with the velocity change V1 on 21-Feb-2005 of (North) 52.7 mm/yr, (East) 7.7 mm/yr, and (Up) 14.5 mm/yr with an uncertainty of 5.2 mm/yr. These experiments show that the algorithm may be used to analyze relaxation phases associated with earthquakes with the appropriate settings, as well. For even more consistent analyses, the functional model (3.1) might be extended to model such phases, as well.

Let us conclude with a general remark. We saw that weekly series generally have a smaller standard deviation than the daily series. From Sect. 2.4 we know that the former emerge

Table 4.5: Quality assessment of daily coordinates. Summary of the update step.

Minimum interval length for Δt_{RS} core sites (years)	3.0
Minimum percentage of data p_{RS} for core sites	70.0
Number of sites in the network	234
Number of fiducial sites before the analysis	146
Number of fiducial sites after the analysis	106
- number of rejected fiducial sites	40
Number of resulting sub-intervals in fiducial sites	287
Number of discontinuities	672
Number of outliers	8438
Number of relative constraints	272
Mean interval of a fiducial station after the analysis (years)	13.217
Percentage of data of a fiducial station after the analysis (mean)	93.218

Table 4.6: Quality assessment of weekly coordinates. Summary of the update step.

Minimum interval length Δt_{RS} for core sites (years)	3.0
Minimum percentage of data p_{RS} for core sites	70.0
Number of sites in the network	234
Number of fiducial sites before the analysis	146
Number of fiducial sites after the analysis	107
- number of rejected fiducial sites	39
Number of resulting sub-intervals in fiducial sites	330
Number of discontinuities	722
Number of outliers	3081
Number of relative constraints	298
Mean interval of a fiducial station after the analysis (years)	12.861
Percentage of data of a fiducial station after the analysis (mean)	95.269

from the latter and thus they benefit from the combination. Series of weekly observations, however, are less representative than daily series due to the smaller number of data in the series. The analysis showed that the "good setting" for the minimum relative improvement U_t for all stations analyzed is easier to find for daily than for weekly coordinate time series.

4.4.2 Cumulative Solution

ADDNEQ2 generates the multi-year solutions A2 for both, daily and weekly series using the settings of Table 4.1 (see also Fig. 4.1). Tables 4.5 and 4.6 summarize the update steps for the daily and weekly solutions, respectively. Both update steps adopted a minimum interval length Δt_{RS} for core sites of 3 years and a minimum percentage of data p_{RS} for core sites of 70.0%. Initially, 146 of the 234 stations included in the networks were assumed to be core sites. The update step rejected 40 sites for the daily and 39 for weekly solutions. After introducing discontinuities and adding relative velocity constraints, the number of sub-intervals recognized as core for the datum definition became 287 and 330 for the 1D and 7D solutions, respectively. Tables 4.5 and 4.6 furthermore tell that the mean interval of a fiducial station is of about 13 years (out of 15 years) for both solutions. The percentage of data is for both solutions above 93% in these long intervals.

Table 4.7: A posteriori **RMS** error before and after quality assessment of daily and weekly coordinate time series.

Solution	Before quality assessment [mm]	After quality assessment [mm]	Factor improvement
daily 1D	3.47	1.30	2.67
weekly 7D	1.52	1.32	1.15

Table 4.7 lists the a posteriori **RMS** of the multi-year adjustment before and after quality assessment. For daily series this value improves by a factor 2.67, from 3.47 mm to 1.30 mm, while for weekly series the a posteriori **RMS** improves by a factor 1.15, from 1.52 mm to 1.32 mm.

Multi-year solutions consist of intervals of set of station coordinates and velocities. Figures 4.7a and 4.7b illustrate the velocity field of the 1D and 7D solutions for the epoch 01-Jan-2000, respectively. The reference sites are characterized by an arrow. The vertical rates are color-coded. As expected, the two solutions have comparable vector fields. Figures 4.7c and 4.7d illustrate the improvements for the 1D and the 7D solutions, respectively. Generally, the largest improvements are achieved for the non-reference sites. HARK (Hartebeesthoek, Republic of South Africa, Lon: 27.70 E, Lat: -25.89 N) improves by 104.8 mm/yr in the horizontal and -5.1 mm/yr in the vertical components in the 1D series. In the 7D series the largest improvement affects AREQ (Arequipa, Peru, Lon: -71.5 E, Lat: -16.5 N) with 79.3 mm/yr and 0.14 mm/yr in the horizontal and vertical components, respectively. Reference sites show smaller improvements. The largest is observed in the 1D solution for SEY1 (La Misere, Seychelles, Lon: 55.5 E, Lat: -4.7 N) with Hor: 1.5 mm/yr and Ver: -13.3 mm/yr, while the 7D solution impacts the same station with Hor: 1.2 mm/yr and Ver: -10.1 mm/yr. The reference sites with the largest horizontal improvements are GLPS (Puerto Ayora, Ecuador, Lon: -90.3 E, Lat: -0.7 N), for 1D: 5.9 mm/yr and for 7D: 6.0 mm/yr, and COCO (Cocos, Australia, Lon: 96.8 E, Lat: -12.1 N), for 1D: 6.2 mm/yr and for 7D: 5.4 mm/yr. Both, reference and non-reference sites substantially improve their velocities.

The 7D series were delivered in **SINEX** format as the **CODE** contribution to the realization of the **ITRF2008** (Altamimi et al., 2011). The **ITRF2008/IGS** discontinuities¹ in the **IGS** contribution for the **ITRF2008** are compared to the discontinuities identified in the **FODITS** 7D analysis. Table 4.8 lists the results for four tolerance settings. According to the **IGS** contribution for the **ITRF2008** realization the time interval starts 1997 and ends 2008. The common number of stations is 142. For a tolerance of ± 1 day 42 events were found to agree in both series, the 7D and the **ITRF2008/IGS** series. For a tolerance of ± 7 days 122 discontinuities/velocity changes agree, 99 of them are discontinuities-only and 5 velocity changes-only. For a tolerance of ± 21 days there were 151, 122, and 5 common events, respectively. For the interval between 1997 and 2008, the number of events (354) identified in the weekly analysis is larger than the corresponding number in the **ITRF2008/IGS** solution (256). The number of common discontinuities is about 130, i.e., about the half of the total.

¹<ftp://igs-rf.ign.fr/pub/discontinuities/soln.snx>

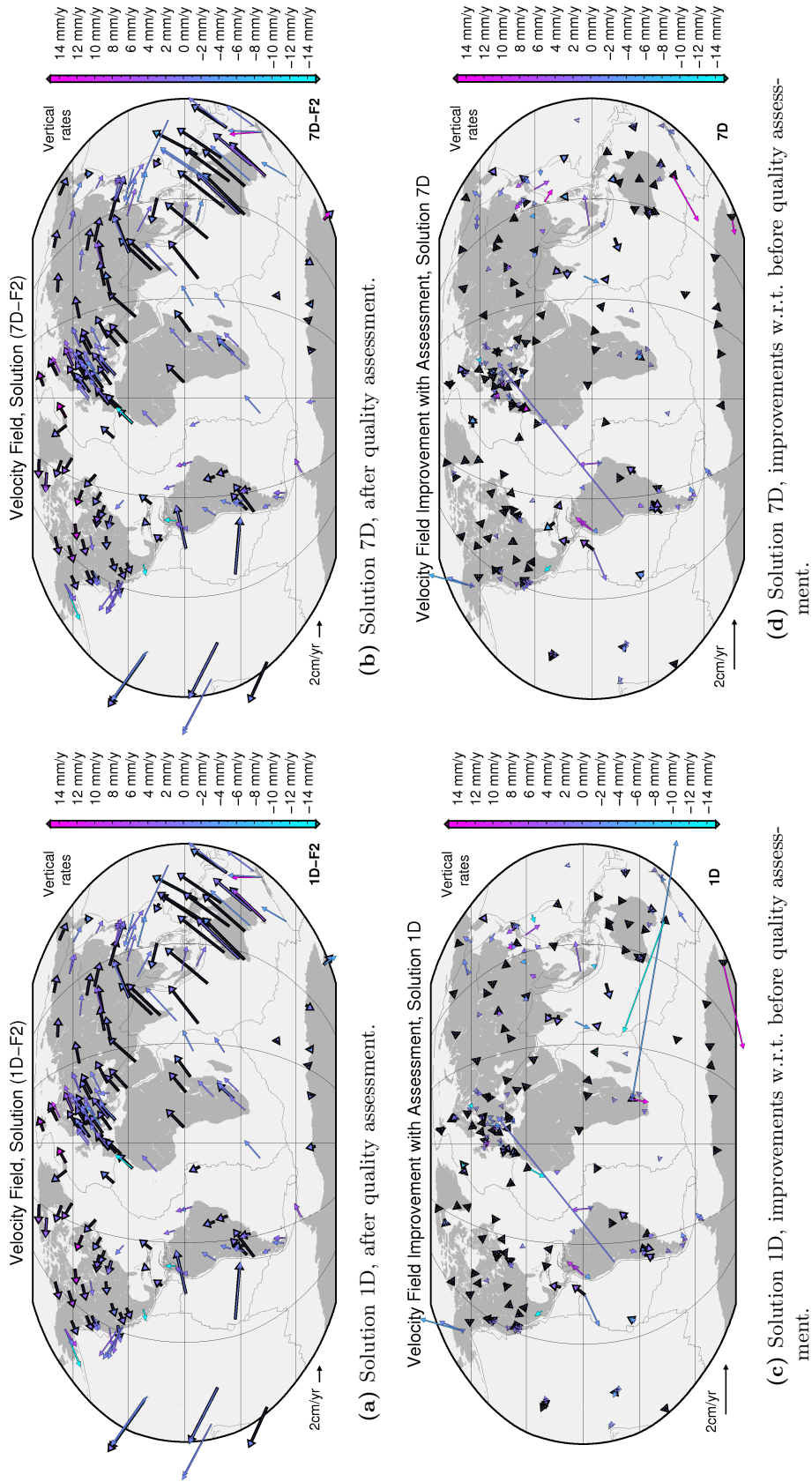


Figure 4.7: Velocity field at epoch 01-Jan-2000 for daily and weekly solutions. (top) solutions quality after quality assessment. (bottom) improvements. Vertical rates are color-coded. Velocities of reference sites have a thick contour.

Table 4.8: External validation. Discontinuities in the weekly **FODITS** analysis and the **ITRF2008/IGS** realization (ftp://igs-rf.ign.fr/pub/discontinuities/soln.snx) (Altamimi et al., 2011). Compared are only the discontinuities in the 142 common stations between 1997.0 and 2008.

Window ^a (days)	ITRF2008/IGS			FODITS 7D analysis			Agreement ^b		
	Disc ^c	VICh ^d	Both ^e	Disc ^c	VICh ^d	Both ^e	Disc ^c	VICh ^d	Both ^e
±1							42	0	42
±7	227	35	256	307	68	354	99	4	122
±11							109	5	135
±21							122	5	151

^aWindow of tolerance in days for epochs comparison **ITRF2008/IGS** and **FODITS** solutions.

^bAgreement of events (i.e., discontinuities, velocity changes, or both of them simultaneously) between **FODITS 7D analysis** and the **ITRF2008/IGS**.

^cTotal number of discontinuities.

^dTotal number of velocity changes.

^eTotal number of discontinuities and velocity changes.

4.4.3 Cleaned Coordinate Time Series

As a last step **ADDNEQ2** generates coordinate time series for validation F2, see Fig. 4.1. The **ADDNEQ2** and **FODITS** settings for the A2 and F2 solutions, respectively, are exactly the same as those for the A1 and F1 solutions. Therefore, from analyses F2 we do not expect to see discontinuities or outliers.

The result of the validation of the daily series is documented by Table 4.9. Compared to the analysis before quality assessment, the number of data in the time series was reduced from 5468 (see Table 4.2) to 5445. This is explained by the elimination of outliers (see Sect. 4.3.2). After quality assessment the number of significant discontinuities in the time series is 13 (10 due to earthquakes and 3 due to receiver changes), the number of outliers is 38 (all identified in the test of the datum definition (see Sect. 3.2.4), the number of velocity changes is 0, and the number of annual periods 211 (2 more than in the analysis before quality assessment). No further discontinuities and velocity changes of unknown reason were identified.

The validation of the weekly series is documented in Table 4.10. In analogy to the 1D series, the number of data was reduced from 779 (see Table 4.3) to 771. After the validation of the coordinate time series more events were identified than in the 1D series. The number of discontinuities is 36 (24 of unknown reason, 8 earthquakes, and 4 equipment changes), the number of velocity changes 4 (3 of unknown reason and 1 due to an earthquake), the number of outliers is 374 (2 of them identified in the test of the datum definition), and the number of annual periodic functions 231.

Both validations, that of the 1D and of 7D coordinate time series, confirm that the number of identified events after quality assessment is substantially reduced. In the daily series 97% of the discontinuities and almost 100% of the outliers were removed, whereas 92% of the discontinuities and 88% of the outliers were removed for weekly series. Once more, more consistent results are obtained for the daily series—as compared to the weekly

Table 4.9: Internal validation F2 of **CODE** daily coordinate time series 1D.

Settings			
Time interval of the time series; From: 01-Jan-1994, To: 31-Dec-2008			
Time series; daily 1D			
Number of analyzed stations; 234			
Number of data in time series; maximum: 5445, mean: 3320			
Data variance-covariance; VCI of North, East, and Up			
Identify discontinuities, outliers, velocity changes.			
A velocity change is proposed after each discontinuity			
Minimum relative improvement $U_t = 0.02$ (abort criterion)			
Independent statistical test for outliers $U_s = 15.0$ (abort criterion)			
Additional criterion ^a , minimum size for discontinuities (meters) Horizontal: 0.001, Vertical: 0.003			
Additional criterion ^a , minimum size for periodic functions (meters) Space: 0.001			
Minimum interval length for velocities $\Delta t_v = 3$ years			
Check equipment changes			
Check earthquakes			
Check annual and semi-annual signals			
Check the datum definition; North: 50 mm, East: 50 mm, Up: 50 mm; translation and scale			
Analysis results	Mean per site	Mean per 10 year	Total in all sites
Discontinuities and velocity changes	0.056	0.054	13
- discontinuities	0.056	0.054	13
- velocity changes	0.000	0.000	0
Outliers from datum definition test	0.000	0.158	38
Outliers (total)	0.000	0.158	38
Annual period	0.902	-	211
Semi-annual period	0.226	-	53
A priori equipment changes	1.419	1.376	332
Equipment changes	0.013	0.012	3
- antenna changes	0.000	0.000	0
- receiver changes	0.013	0.012	3
A priori earthquakes	4.000	3.878	936
Earthquakes	0.043	0.042	10
- discontinuities	0.043	0.042	10
- velocity changes	0.000	0.000	0
Discontinuities of unknown reason	0.000	0.000	0
Velocity changes of unknown reason	0.000	0.000	0

^aSee Sect. 3.3.2.

series. From the fact that the number of events after quality assessment is larger than zero we conclude that the analyses and the quality assessment strategy could be further improved.

Figure 4.8 documents the analyses F1 and the validations F2 of station CCMJ (Ogasawara, Japan). The analysis of daily series, illustrated by Fig. 4.8a, identified five earthquakes vE9 of M4.9 with epicenter at 62 km, vE14 of M5.9 at 95 km, vE15 of M4.2 at 28 km, vE23 of M7.5 at 565 km, and vE24 of M6.2 at 39 km, two discontinuities of unknown reason, D1 and D2, an annual signal, and few outliers. The analysis of weekly series, shown in Fig. 4.8b, obtained similar results. The earthquake ve9 was not found to be significant, and the absence of observations after the large discontinuity in the Up component associated a

Table 4.10: Internal validation F2 of **CODE** weekly coordinate time series 7D.

Settings			
Time interval of the time series; From: 05-Jan-1994, To: 24-Dec-2008			
Time series; weekly 7D			
Number of analyzed stations; 234			
Number of data in time series; maximum: 771, mean: 481			
Data variance-covariance; VCI of North, East, and Up			
Identify discontinuities, outliers, velocity changes.			
A velocity change is proposed after each discontinuity			
Minimum relative improvement $U_t = 0.04$ (abort criterion)			
Independent statistical test for outliers $U_s = 35.0$ (abort criterion)			
Additional criterion ^a , minimum size for discontinuities (meters) Horizontal: 0.001, Vertical: 0.003			
Additional criterion ^a , minimum size for periodic functions (meters) Space: 0.001			
Minimum interval length for velocities $\Delta t_v = 3$ years			
Check equipment changes			
Check earthquakes			
Check annual and semi-annual signals			
Check the datum definition; North: 50 mm, East: 50 mm, Up: 50 mm; translation and scale			
Analysis results	Mean per site	Mean per 10 year	Total in all sites
Discontinuities and velocity changes	0.171	0.168	40
- discontinuities	0.154	0.151	36
- velocity changes	0.017	0.017	4
Outliers from datum definition test	0.000	0.008	2
Outliers (total)	1.590	1.558	374
Annual period	0.910	-	213
Semi-annual period	0.316	-	74
A priori equipment changes	1.410	1.382	330
Equipment changes	0.017	0.017	4
- antenna changes	0.004	0.004	1
- receiver changes	0.017	0.017	4
A priori earthquakes	3.970	3.891	929
Earthquakes	0.038	0.038	9
- discontinuities	0.034	0.034	8
- velocity changes	0.004	0.004	1
Discontinuities of unknown reason	0.103	0.101	24
Velocity changes of unknown reason	0.013	0.013	3

^aSee Sect. 3.3.2.

discontinuity to vE13 of M5.7 at 71 km instead. After quality assessment, the validation of the 1D series of CCJM did not find additional events, see Fig. 4.8c. Except for two outliers, the same is true for the validation of the same station in the weekly series, see Fig. 4.8d.

Figure 4.9 documents the analyses F1 and the validations F2 for the station HOFN (Hoefn, Iceland). Figure 4.9a shows that outliers were identified in the daily series (judged as significant by the test of the datum definition and identified during the iterative **FODITS** procedure). The discontinuity of unknown reason D1, the velocity change of unknown reason V1, the equipment change Srae2, and an annual signal were identified. Except for the outliers and for the semi-annual signal, the analysis of weekly series, documented by Fig. 4.9b, generated the same results. Both validations, of the daily and weekly series of

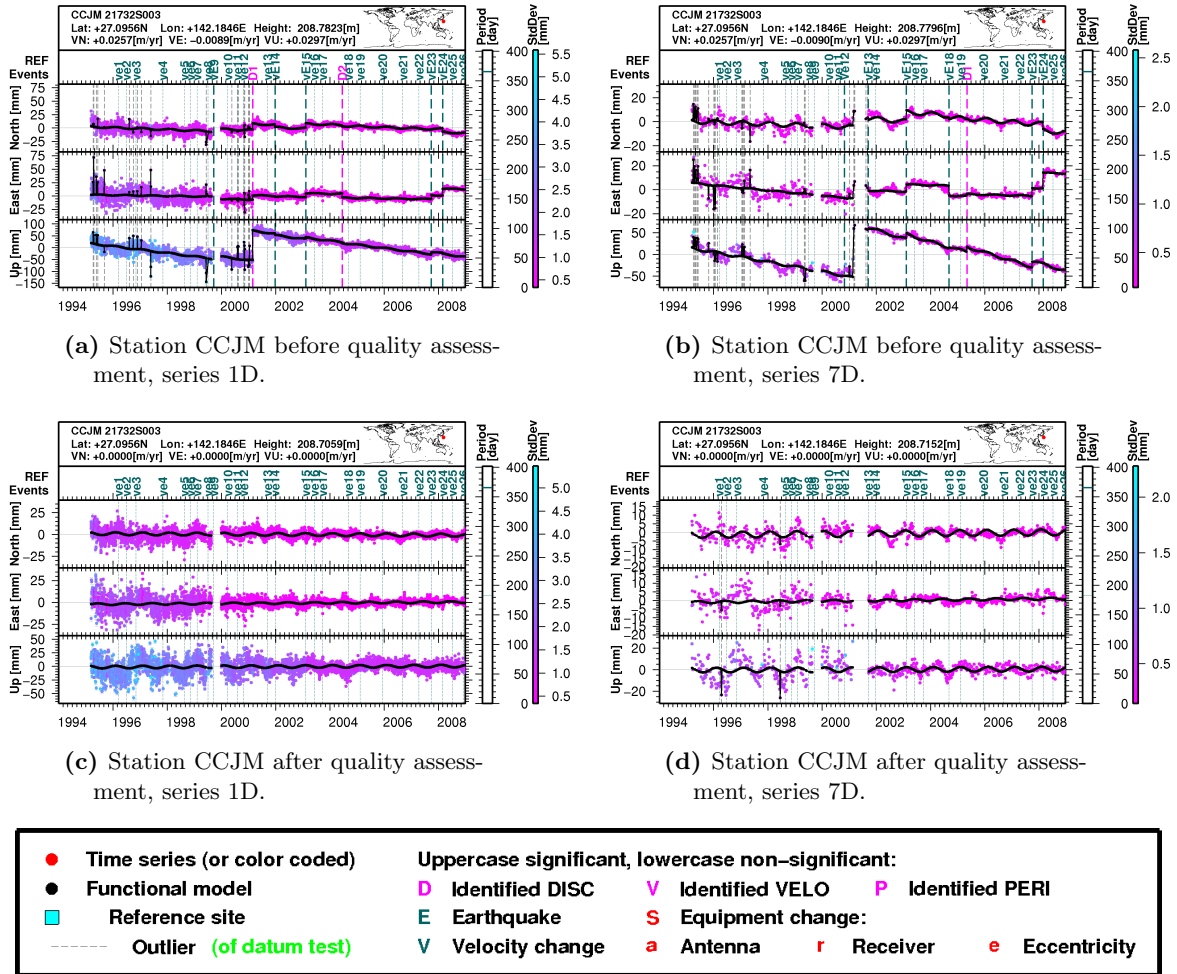


Figure 4.8: Station CCJM, daily and weekly coordinate time series before and after quality assessment.

HOFN, did not find further events afterwards, see Figs. 4.9c and 4.9d, respectively.

Figure 4.10 illustrates the distributions of the residuals of the coordinate time series w.r.t. the model in histograms. For each component, namely North, East, and Up, a histogram was computed from the series of residuals of all stations, for daily and weekly solutions, and once before and once after the validation of coordinate time series. Generally, after quality assessment the distributions have a mean closer to zero, a smaller RMS and, as a consequence, an higher maximum in frequency after validation. Moreover, histograms of daily series, compared to those of weekly series, are smoother in appearance. This is particularly true for the Up components of the solutions. The effect is caused by the greater amount of data in the daily series.

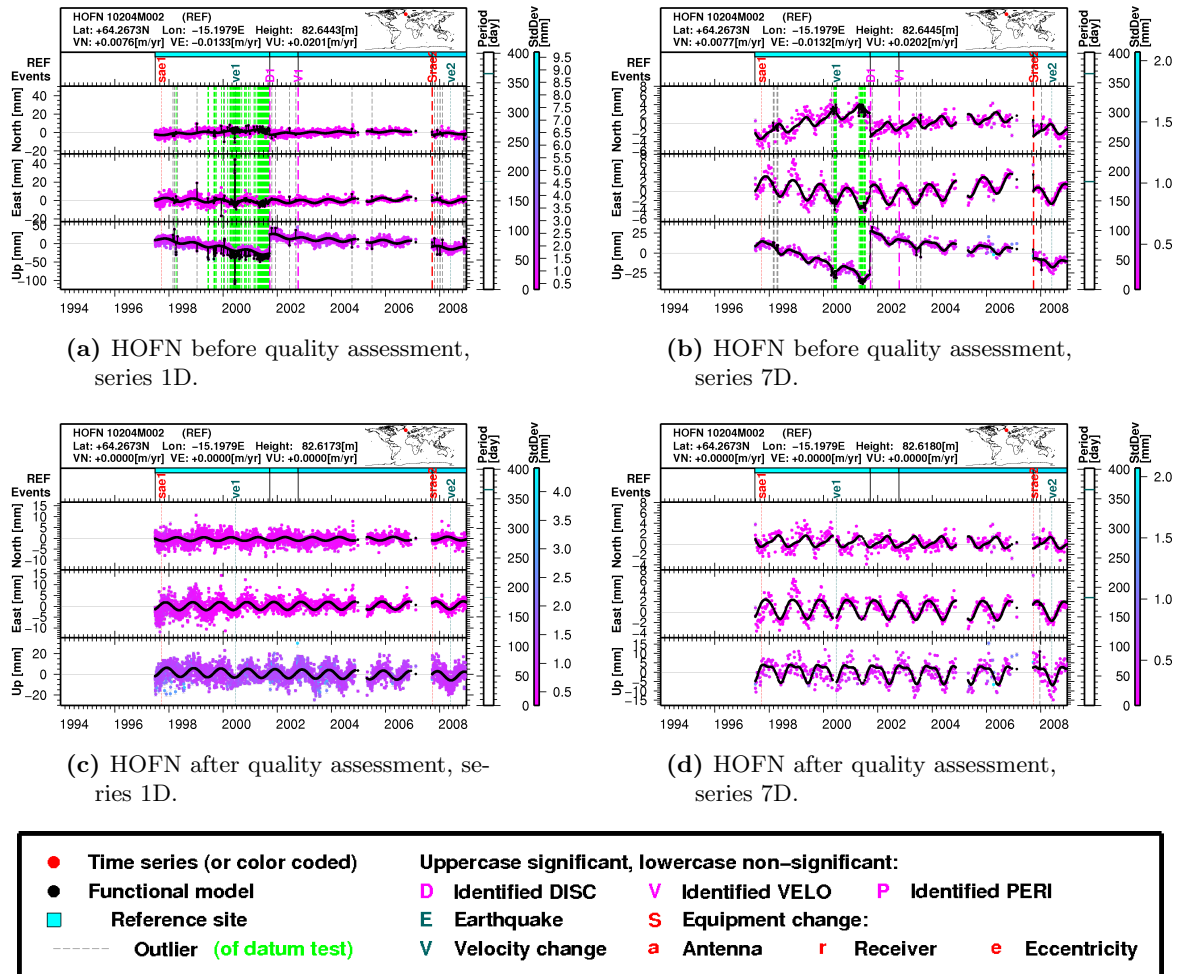


Figure 4.9: Station HOFN, daily and weekly coordinate time series before and after quality assessment.

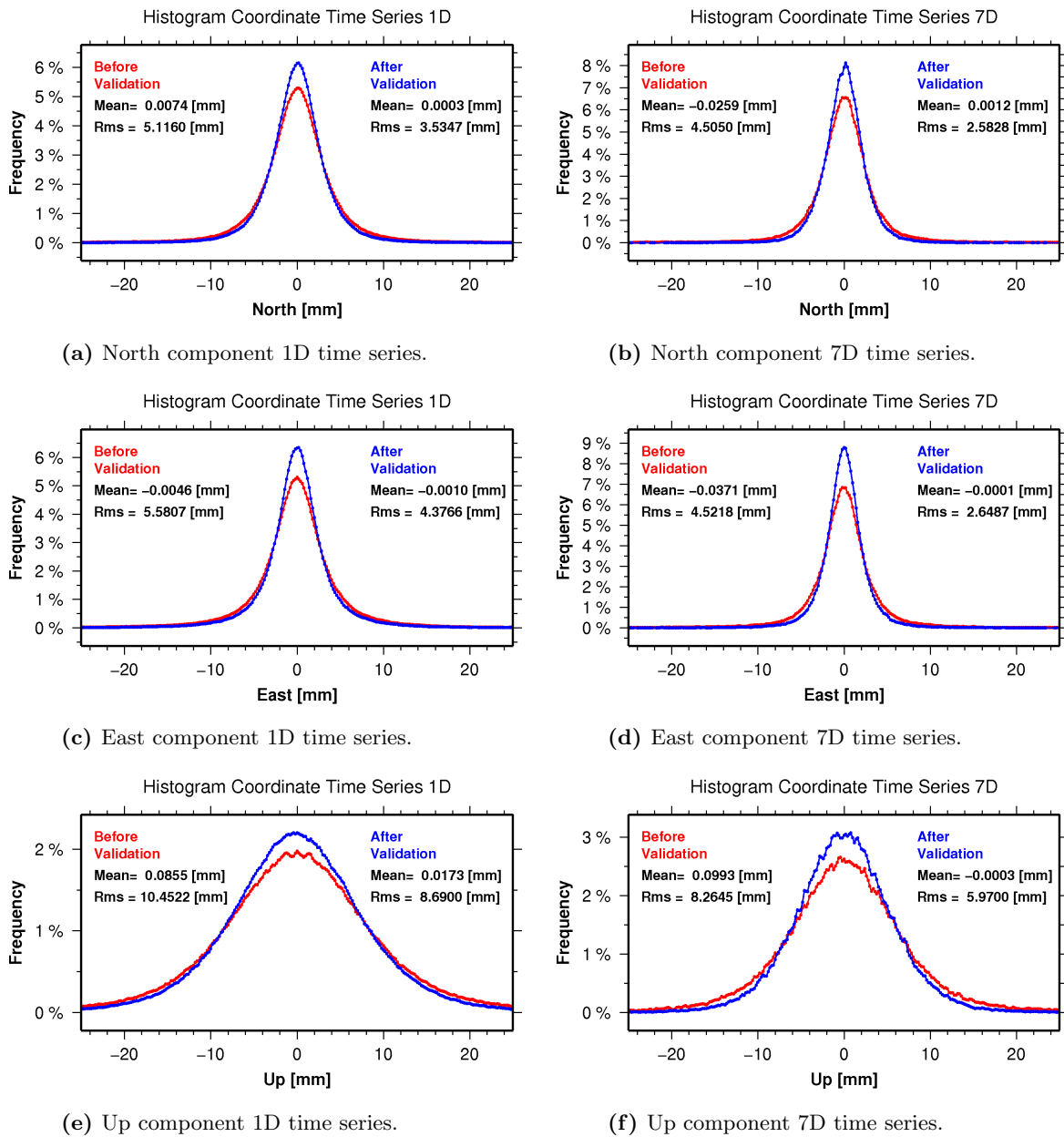


Figure 4.10: North, East, and Up histograms of daily 1D and weekly 7D coordinate time series. Bin width 0.2 mm. In (red) before quality assessment. In (blue) after quality assessment.

5 Impact of Quality Assessment on Parameter Time Series

This chapter evaluates the impact of quality assessment on time series of global parameters obtained from the first **CODE** reprocessing campaign (see Sect. 2.4). Section 5.1 studies the time series of the Helmert translation parameters of the global network. The impact on the geocenter parameters of quality assessment of coordinate time series is provided for daily and weekly solutions (as in Chapter 4). Section 5.2 analyses the time series of the scale parameter. We also show the correlation between the scale and the coordinate parameters related to periodic signals. Section 5.3 documents aspects of the coordinate time series not yet analyzed in Chapter 4. Series of geocenter, scale, and coordinate parameters are spectrally analyzed, as well. Section 5.4 deals with the impact of quality assessment of the coordinate time series on the **ERP** time series.

5.1 Geocenter

The "geocenter motion" is defined as the motion of the **Center of Figure (CF)** of the solid Earth w.r.t. the **Center of Mass (CM)** of the Earth with ocean and atmosphere (Blewitt, 2003; Dong et al., 2003). As the **Center of Network (CN)** of a global network of tracking sites can approximately be interpreted as the **CF**, the geocenter motion can be established via the translation parameters of the Helmert transformation (2.42) between the estimated and the reference network solutions. Series of the Helmert translation parameters therefore give the geocenter motion as a function of time.

5.1.1 Impact of Quality Assessment

At first, we evaluate the impact of quality assessment of the coordinate time series on the resulting *geocenter* time series. The adopted scheme for quality assessment has been provided in Fig. 4.1. The general settings of the program **ADDNEQ2** are those listed in Table 4.1. In order to study the motion of the geocenter parameters, we imposed **NNR**, but not an **NNT** condition. Furthermore, we imposed **CF** equal **CM**. In this way, the resulting coordinate time series implicitly contained the contribution of both, translation and scale parameters. The geocenter time series were subsequently estimated in **FODITS** by testing simultaneously translation and scale parameters w.r.t. the **ADDNEQ2** cumulative multi-year network solution (see Sect. 3.2.4). Both cumulative multi-year network solution and time series were provided in **ITRF2005/IGS**. Differently than in **ADDNEQ2**, the estimation of the Helmert parameters in **FODITS** provides the standard deviations of the parameters.

The experiment was carried out for four series: daily 1D and weekly 7D series spanning from 1994 to 2008, and daily 1R and weekly 7R series spanning from 2000 to 2008 (R denotes "reduced"). The 1R and 7R series, created to provide more results, were a subset of the 1D and 7D series, respectively. The minimum relative improvement (3.6) for the 1D and 7D series is given in the Tables 4.2 and 4.3. For the 1R and 7R solutions the significance levels were set to $U_t = 0.07$ and $U_t = 0.10$. The independent statistical tests for outliers, Eq. (3.7), are given in Tables 4.2 (for daily series) and 4.3 (for weekly series).

In order to evaluate the impact of quality assessment, the list of reference sites was screened in a preliminary processing step. For such a preliminary step, but also for all other processing steps, the minimum interval length Δt_{RS} and the minimum percentage of data for core sites p_{RS} were set to 3 years and to 70.0%, respectively. In this way, "bad" reference stations were rejected from the list of reference sites prior to the start of the experiment.

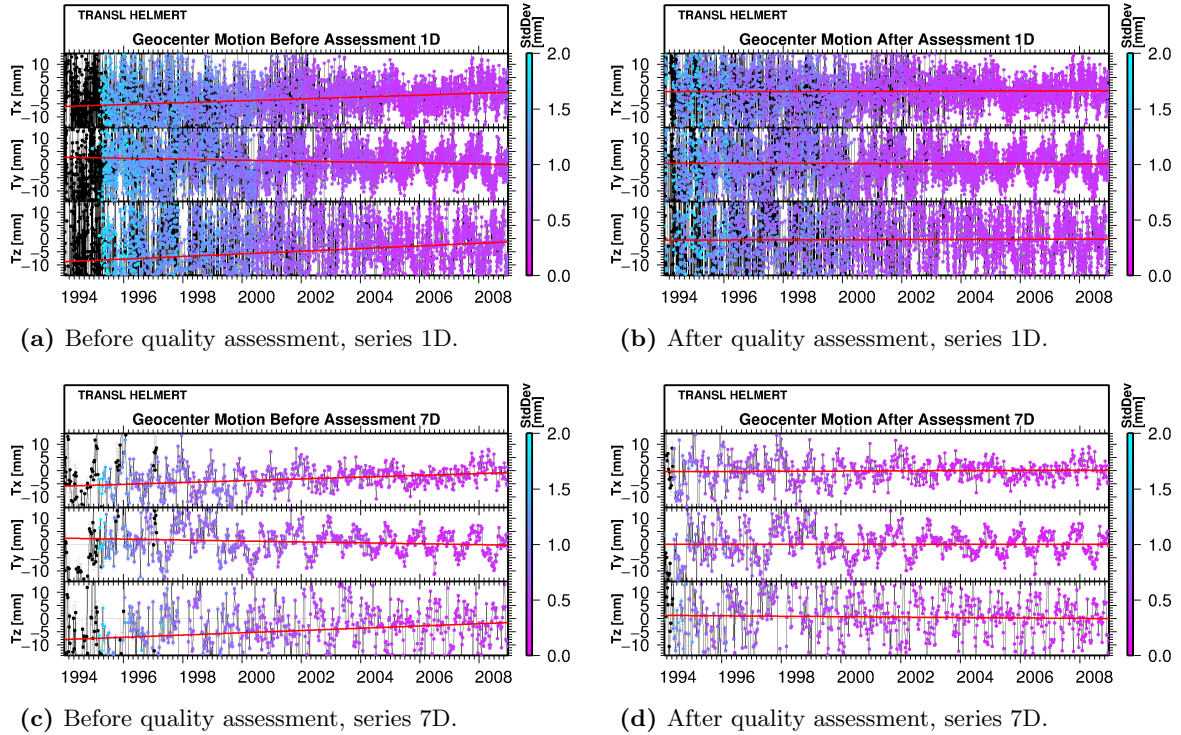


Figure 5.1: Daily 1D and weekly 7D Helmert translation parameter time series for the interval 1994-2008. (left) time series before quality assessment. (right) after quality assessment. (red) linear regression through the time series.

Figure 5.1 shows the impact of quality assessment on the daily 1D and weekly 7D geocenter time series. The vertical axes are defined in such a way as to magnify the offsets and the drifts of the series (shown as straight lines (red) in all components T_x , T_y , and T_z). For both, daily and weekly series, offsets and drifts after quality assessment (Figs. 5.1b and 5.1d) are clearly smaller than before quality assessment (Figs. 5.1a and 5.1c). In other

Table 5.1: Offsets and drifts of Helmert translation parameters before and after quality assessment of coordinate time series, solutions 1D and 7D for the interval 1994-2008.

Interval		Offsets ^a [mm]			Drifts [mm/yr]		
		Before ^b	After ^c	Factor	Before ^b	After ^c	Factor
1994-2008							
Translation X	1D	-3.377±0.113	-0.332±0.106	10.2	0.349±0.025	0.027±0.024	12.9
Translation Y	1D	1.346±0.122	0.334±0.115	4.0	-0.177±0.027	-0.016±0.026	11.1
Translation Z	1D	-5.075±0.235	-0.390±0.218	13.0	0.494±0.053	0.021±0.050	23.5
7D							
Translation X	7D	-3.374±0.176	-0.207±0.161	16.3	0.344±0.039	0.037±0.038	9.3
Translation Y	7D	1.001±0.226	0.111±0.199	9.0	-0.174±0.051	0.005±0.047	-34.8
Translation Z	7D	-4.705±0.415	0.570±0.366	-8.3	0.428±0.094	-0.083±0.087	-5.2

^aGiven at the epoch 1 January, 2000.

^bBefore quality assessment of coordinate time series.

^cAfter quality assessment of coordinate time series.

words, coordinate time series in a cumulative multi-year global network solution may be responsible for offsets and drifts of the resulting geocenter time series.

The estimates of offsets and drifts in Fig. 5.1 are provided in Table 5.1. As expected, the estimates after quality assessment are smaller than before quality assessment, and for daily series they are more accurate than for weekly series. The largest factor (ratio of the offset or drift before and after quality assessment) results is for offsets 16.3 (T_x of the 7D series) and for drifts -34.8 (T_y of the 7D series). As all absolute factors are larger than 1, all offsets and drifts became smaller. After quality assessment geocenter offsets are within a 3σ interval, and geocenter drifts are within a 1σ interval, i.e., geocenter drifts are no more significant.

Table 5.2: Offsets and drifts of Helmert translation parameters before and after quality assessment of coordinate time series, solutions 1R and 7R for the interval 2000-2008.

Interval		Offsets ^a [mm]			Drifts [mm/yr]		
		Before ^b	After ^c	Factor	Before ^b	After ^c	Factor
2000-2008							
Translation X	1R	-3.160±0.098	-0.129±0.097	24.5	0.912±0.039	-0.033±0.039	-27.6
Translation Y	1R	1.279±0.106	0.588±0.105	2.2	-0.538±0.043	-0.001±0.042	538.0
Translation Z	1R	-4.578±0.216	-0.114±0.214	31.8	0.930±0.087	-0.219±0.086	-4.24
7R							
Translation X	7R	-2.982±0.157	-0.010±0.152	298.2	0.708±0.058	0.018±0.057	39.3
Translation Y	7R	0.639±0.198	-0.280±0.190	-2.3	-0.399±0.073	0.046±0.071	-8.7
Translation Z	7R	-3.666±0.366	0.546±0.352	-6.7	0.424±0.135	-0.143±0.132	-3.0

^aGiven at the epoch 1 January, 2000.

^bBefore quality assessment of coordinate time series.

^cAfter quality assessment of coordinate time series.

The same experiment was performed for the daily 1R and weekly 7R series. Figure 5.2 illustrates the results. Qualitatively, we observe a similar impact of quality assessment on the series as in Fig. 5.1, i.e., the offsets and drifts of the geocenter time series became smaller. Table 5.2 gives the estimates. The absolute value of the factors are larger than 1. The largest factor results for offsets 298.2 (T_x of the 7R series) and for drifts 538.0 (T_y

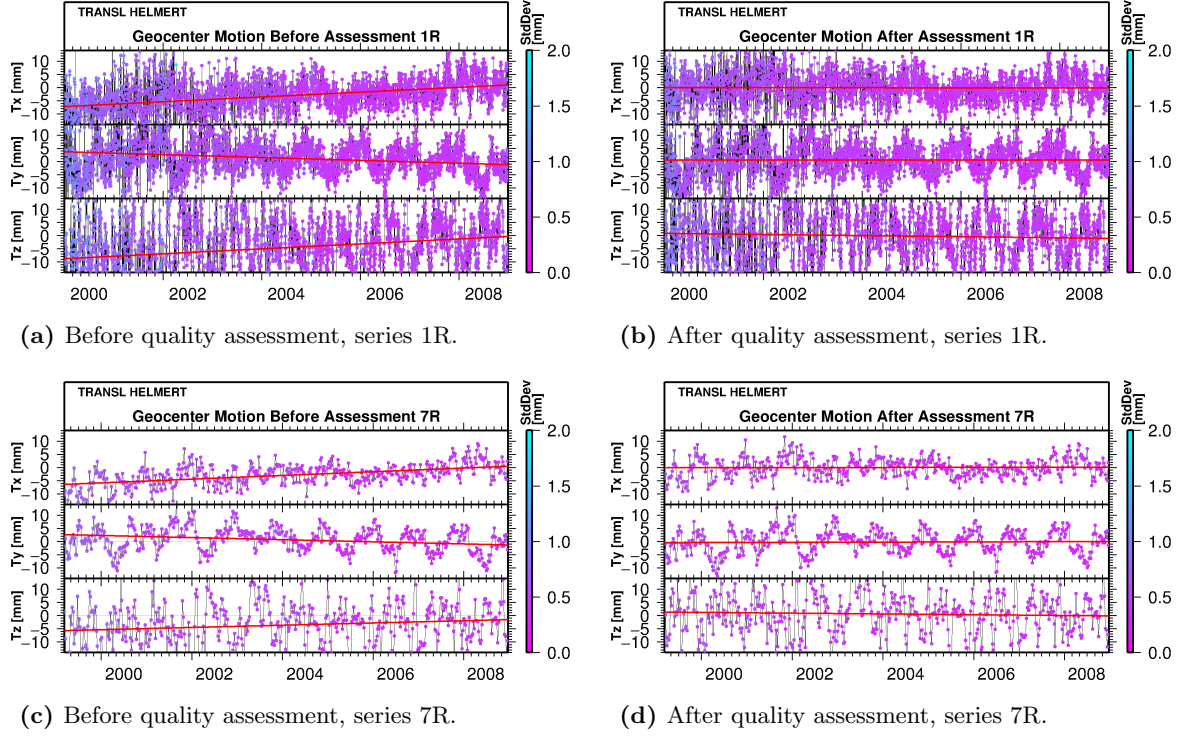


Figure 5.2: Daily 1R and weekly 7R Helmert translation parameter time series for the interval 2000-2008. (left) time series before quality assessment. (right) after quality assessment. (red) linear regression through the time series.

of the 1R series). Before quality assessment, the absolute offsets are less than 4.6 mm and the absolute drifts less than 1.0 mm/yr. After quality assessment, the absolute offsets are less than 0.6 mm and absolute drifts less than 0.3 mm/yr.

Not surprisingly, the quality assessment of coordinate time series also had a positive impact on the standard deviation of the geocenter time series. Figures 5.1 and 5.2 show that the standard deviation of the data are color-coded. Before quality assessment, the standard deviation is larger than 2.0 mm during the first years of the series 1D. Then, the standard deviation decreases with the increasing number of stations contributing to the Helmert transformation. After quality assessment the standard deviation is less than 2.0 mm throughout the whole series. As there are no more discontinuities and outliers in the coordinate time series, the discrepancy between each two frames participating to the Helmert transformation is smaller than before quality assessment.

In the case of a more permissive analysis of coordinate time series (i.e., more events identified by reducing the levels of significance), we obtained comparable results as those provided in Tables 5.2 and 5.1. From Chapter 4 we know, however, that after quality assessment a FODITS analysis still found a few discontinuities in the coordinate time series (see Tables 4.9 and 4.10). Thus, we conclude that further investigations should firstly aim to improve the algorithm FODITS (see Chapter 7).

5.1.2 Spectral Analysis

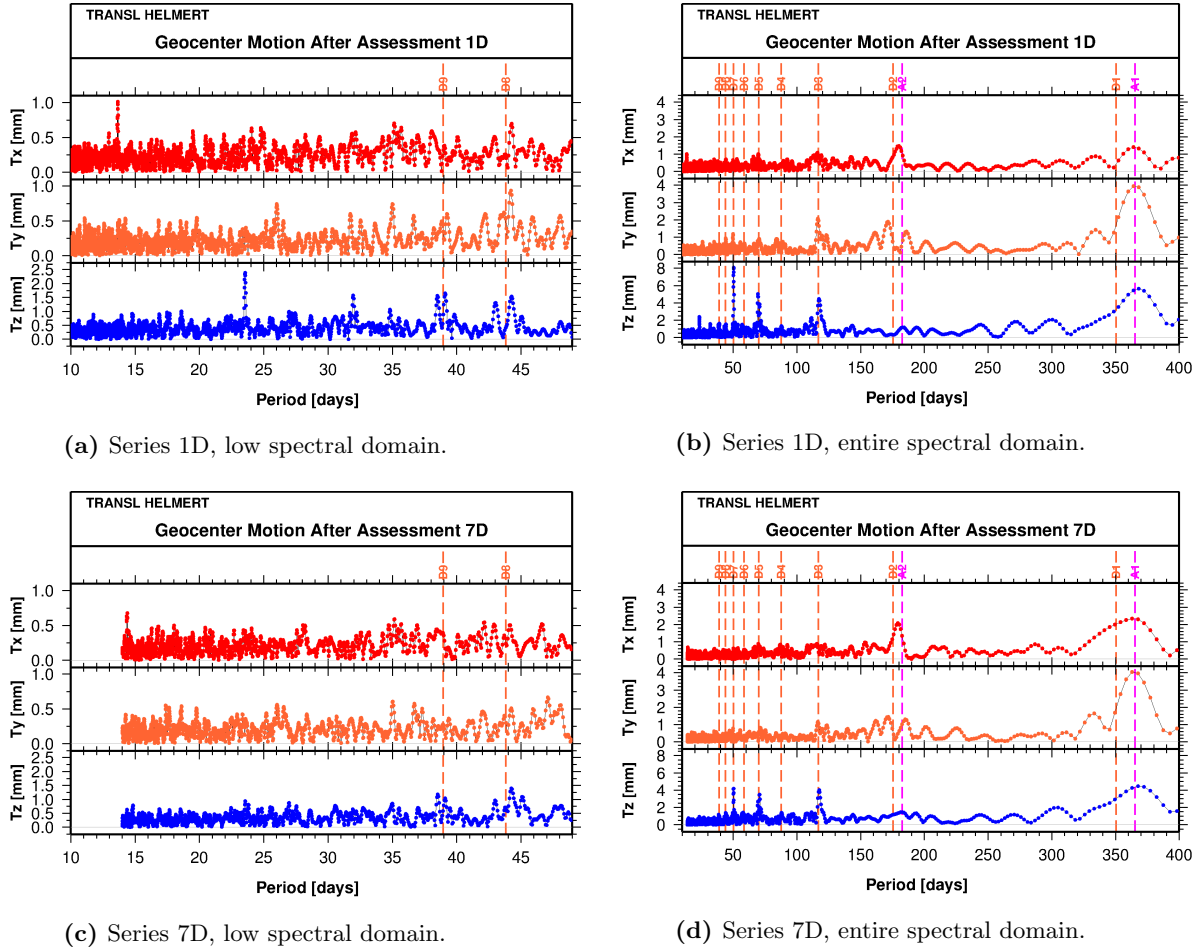


Figure 5.3: Spectral analysis of daily and weekly series of the geocenter motion (amplitude spectra). Lines of the seasonal signals (A1 and A2) and of the signals associated with the draconitic year of the GPS constellation (352 days) (from D1 to D9) are shown.

Figure 5.3 shows the amplitude periodograms for the daily and the weekly time series of geocenter motion after quality assessment. The lower part of the spectra, shown by Figs. 5.3a and 5.3c, is for the daily series from 2 to 49 days and for the weekly series from 14 to 49 days. The entire spectra reach 400 days for both the daily and weekly series.

The amplitude spectra were obtained by **Fast Fourier Transform (FFT)**. The time series were therefore extended, in a first step, to the next power of two, i.e., to 8,192 epochs for daily series and to 1,024 epochs for weekly series. In order to gain more resolution in the spectral domain, however without gaining effectively more information, before computing the **FFT** the time series were furthermore extended by zero-padding (i.e., completion with zeros) to (for daily series) 32,768 and (for weekly series) 8,192 epochs. The spectra were finally divided by the number of data in the original time series. Appendix B gives the

Table 5.3: Amplitudes of spectral lines in the time series of daily and weekly geocenter motions.

Amplitude spectra ^a		Spectral line in [mm] and [day]						
		365	365/2	352/3	352/5	352/7	Other spectral lines	
Daily series after quality assessment	X	1.40	1.47					1.01
		364.1	180.0					13.66
	Y	3.96	1.90	2.08			0.75	
		364.1	171.6	116.6			35.00	
	Z	5.65		4.47	5.03	8.11		1.58 2.40
		368.2		117.4	69.6	50.4		31.97 23.56
Weekly series after quality assessment	X	2.34	2.08					0.61
		362.9	179.2					14.40
	Y	4.04	1.44				0.68	
		362.9	171.7				35.05	
	Z	4.49		4.04	3.50	4.20		5.13 0.94
		367.6		117.5	70.8	50.4		32.00 23.56

^aSpectral lines from the discrete results are given in terms of amplitude (above) and period (below).

validation of such extended **FFT**.

The daily series contain an annual signal (line A1), see Fig. 5.1b. Table 5.3 tells that the amplitude in the three components T_x , T_y , and T_z are 1.40 mm, 3.96 mm, and 5.65 mm, respectively. As the spectra are discrete, the maxima were registered at periods of 364.1 days, 364.1 days, and 368.2 days, respectively. Such seasonal variations in the geocenter time series maybe due to the mass redistribution within the Earth system, in particular in the atmosphere, oceans, and continental water (Chen et al., 1999). No clear semi-annual signals are present. The spectrum T_z shows significant spectral lines at $352/n$, with $n = 3, 5, 7$, associated with three odd harmonics of the draconitic year of the **GPS** constellation. These may be caused by systematic errors associated with the **GPS** technique (e.g., Ray et al., 2008). Fig. 5.3a shows that the amplitude of the harmonics $352/n$, with $n = 8, 9$, are small.

Four barely significant spectral lines are present in the lower part of the periodogram of daily series. The first, of about 35.00 days, of unknown reason, affects the T_y component. The second, of 31.96 days, known from the list of long-period tidal variations (Petit and Luzum, 2010), mainly affects the T_z component. The third, of 23.56 days, of unknown reason, affects the T_z component. And the fourth, of 13.66 days, known to the M_f (Moon fortnightly), is only present in the T_x component.

The periodograms of weekly series show similar spectral lines as the daily series (compare Figs. 5.3b and 5.3d). The annual variation is present in all three components and have amplitudes of 2.34 mm, 4.04 mm, and 4.49 mm. The amplitude of the annual signals in daily and weekly series are thus comparable (signals of long period do not benefit from the weekly combination). The largest amplitude of the seasonal signal is registered in the T_z component. Short periods benefit from the weekly combination. The spectral lines $352/n$, with $n = 3, 5, 7$, of weekly series have amplitudes smaller (about halved for $n = 7$) w.r.t. the same spectral lines for daily series, see Table 5.3.

The spectral lines with periods of about 35 days, about 32 days, and 23.56 days are

present in both periodograms, of daily and weekly series (compare Figs. 5.3a and 5.3c and see Table 5.3). The spectral line at 13.66 days is not present in the weekly periodogram due to the minimum sampling frequency of 14 days (Nyquist frequency). From the T_x component of weekly series emerges however a spectral line at 14.40 days of unknown reason, which is not present in the periodograms of daily series.

5.2 Scale Parameter

The measured scale of the figure of the Earth is derived directly from the speed of light. The scale parameter, on the other hand, is the parameter of the Helmert transformation (2.42), which gives the ratio between the dimension of the two investigated TRFs. The scale parameters are highly correlated to the station heights (e.g., Ostini et al., 2007; Collilieux et al., 2011), the tropospheric ZPD (e.g., Krügel et al., 2007), and to the satellite antenna offset and phase center variations (e.g., Ge et al., 2005). On the zero-difference level (2.15), the scale parameter is also highly correlated to the clock correction parameters (Zhu et al., 2003). The scale parameters aim therefore to absorb modelling deficiencies.

5.2.1 Impact of Quality Assessment

Using the same analysis schema as in Sect. 5.1 we study the impact of quality assessment of the coordinate time series on *scale* time series. Scale and translation parameters were simultaneously estimated and the experiment was carried out for the four series: daily 1D and weekly 7D (from 1994 to 2008), and daily 1R and weekly 7R (from 2000 to 2008).

Table 5.4: Offsets and drifts of Helmert scale parameters before and after quality assessment of coordinate time series, solutions 1D and 7D for the interval 1994-2008.

Interval	Offsets ^a [ppb]			Drifts [ppb/yr]			
		Before ^b	After ^c	Factor	Before ^b	After ^c	Factor
Scale 1D		-0.053±0.006	-0.047±0.005	1.2	0.011±0.001	0.005±0.001	2.2
Scale 7D		-0.081±0.013	-0.037±0.011	2.2	0.018±0.003	0.005±0.002	3.6

^aGiven at the epoch 1 January, 2000.

^bBefore quality assessment of coordinate time series.

^cAfter quality assessment of coordinate time series.

Figure 5.4 shows the impact of quality assessment on the daily 1D and weekly 7D scale time series. The red line in each figure represent the linear fit of the time series. As for the geocenter time series, offsets and drifts are clearly reduced after quality assessment (compare figures on the left hand side to those on the right hand side). Alternatively, the original coordinate time series in a cumulative multi-year global network solution may (and usually do) generate offsets and drifts in the resulting scale time series.

Table 5.4 lists the estimates of offsets and drifts seen in Fig. 5.4. The factors are larger than 1 for all offsets and drifts. After quality assessment the offsets are less than 0.05 ppb

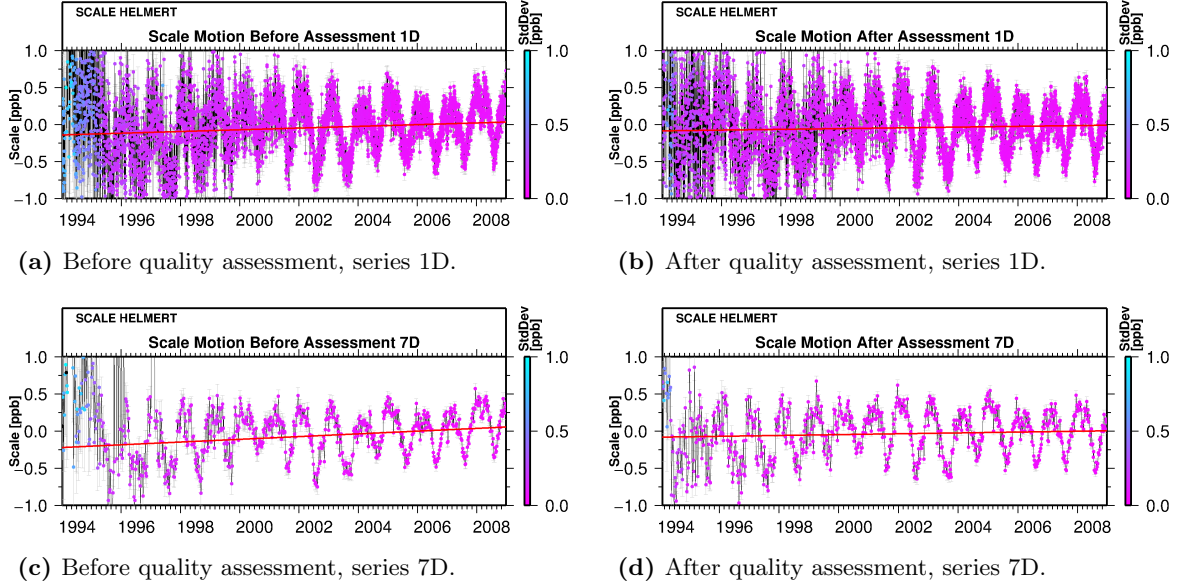


Figure 5.4: Daily 1D and weekly 7D Helmert scale parameter time series for the interval 1994-2008. (left) time series before quality assessment. (right) after quality assessment. (red) linear regression through the time series.

(i.e., less than 0.3 mm) and the drifts ≤ 0.002 ppb/yr (i.e., < 0.013 mm/yr)—at the Earth’s surface 1 ppb corresponds to 6.37 mm.

By comparing Fig. 5.4c to Fig. 5.4d we see that the quality assessment of coordinate time series removed large outliers in the scale time series (visible in the first figure between 1994 and 1997).

Table 5.5: Offsets and drifts of Helmert scale parameters before and after quality assessment of coordinate time series, solutions 1R and 7R for the interval 2000-2008.

Interval	Offsets ^a [ppb]			Drifts [ppb/yr]			
		Before ^b	After ^c	Factor	Before ^b	After ^c	Factor
1994-2008							
Scale	1R	0.008±0.005	-0.011±0.005	-0.7	-0.002±0.002	-0.004±0.002	0.5
Scale	7R	0.017±0.012	-0.010±0.012	-1.7	-0.005±0.004	-0.002±0.004	2.5

^aGiven at the epoch 1 January, 2000.

^bBefore quality assessment of coordinate time series.

^cAfter quality assessment of coordinate time series.

The same experiment was performed for the daily 1R and weekly 7R series. Figure 5.5 illustrates the results, Table 5.5 lists them. For daily 1R series the impact of quality assessment gave factors less than 1 for both, the offset and the drift. Offsets and drifts before and after quality assessment are however not significantly different from zero. Furthermore, as for the 1D and 7D series, no significant change of the standard deviation of the data between before and after quality assessment is visible from the color-coded information.

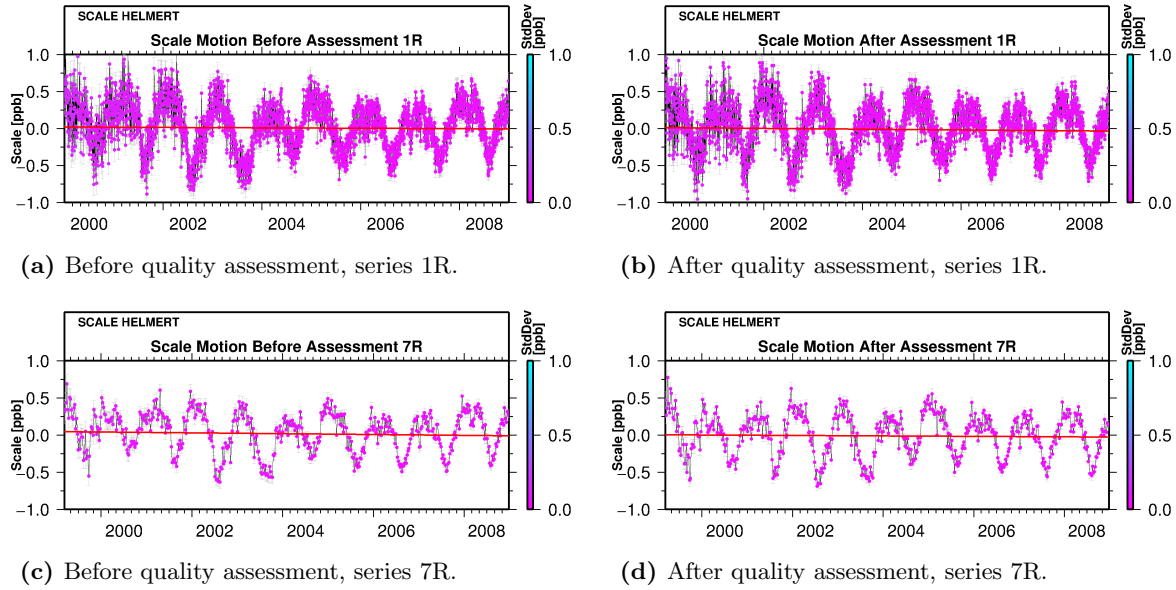


Figure 5.5: Daily 1R and weekly 7R Helmert scale parameter time series for the interval 2000-2008. (left) time series before quality assessment. (right) after quality assessment. (red) linear regression through the time series.

5.2.2 Spectral Analysis

Table 5.6: Amplitudes of spectral lines in the time series of daily and weekly scale parameters.

Amplitude spectra ^a		Spectral line in [mm] and [day]						
		365	365/2	Others	352/5	352/6	Other spectral lines	
Daily series after quality assessment	Scale	2.24	0.68		0.28	0.30	0.41	0.59
		364.1	182.0		70.0	58.2	27.56	13.66
Weekly series after quality assessment	Scale	2.10	0.52	0.40	0.25	0.26	0.31	0.28
		367.6	183.8	139.2	86.6	70.1	27.57	14.35

^aSpectral lines from the discrete results are given in terms of amplitude (above) and period (below).

Figure 5.6 shows the amplitude periodograms of the daily and the weekly time series of scale parameter after quality assessment. The amplitude spectra are provided from 2 days to 400 days (for the entire spectra) and from 2 days to 49 days (for the lower part of the spectra). Spectral analyses were computed by FFT with zero-padding extension to obtain interpolated information in spectral domain (see Sect. 5.1 and Appendix B).

The annual signal (line A1) is the dominating period in the spectra of the scale. Their amplitudes in daily and weekly spectra are 2.24 mm and 2.10 mm, respectively (see Table 5.6). As opposed to the spectra of the geocenter time series, the scale spectra have a significant semi-annual spectral line and do not have the spectral lines associated with the draconitic year of the GPS constellation. The amplitudes of the semi-annual signals are

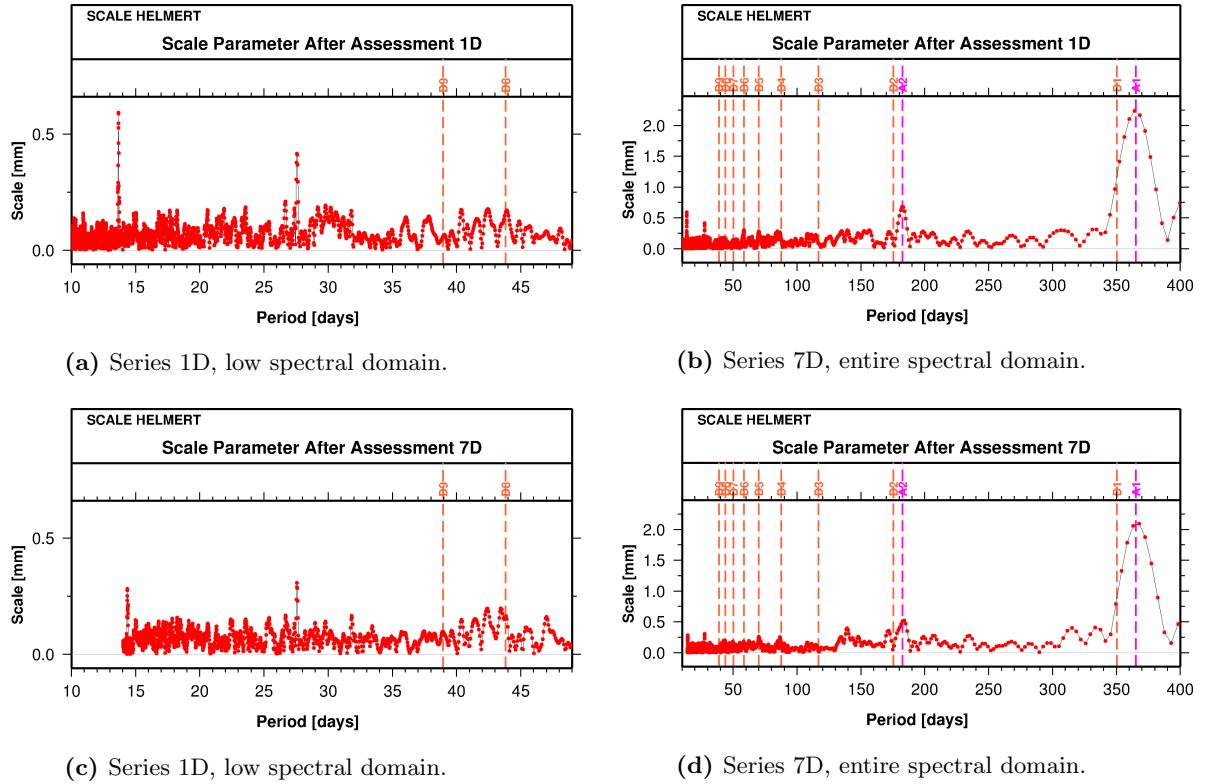


Figure 5.6: Spectral analysis of daily and weekly series of the scale parameter (amplitude spectra). Lines of the seasonal signals (A1 and A2) and of the signals associated with the draconitic year of the GPS constellation (352 days) (from D1 to D9) are shown.

about 4 times smaller than those of the annual signals. The lower part of the spectra show other spectral lines (see Figs. 5.6a and 5.6c). The spectral line at 27.56 days, associated with the long-period tidal variation M_m (Petit and Luzum, 2010), is present in both spectra (see Table 5.6). Then, as in the geocenter time series, the spectral lines at 13.66 days and 14.35 days are present. Due to the not uniform global distribution of tracking stations geocenter and scale parameters are however correlated (e.g., Collilieux et al., 2011).

5.3 Coordinates

5.3.1 Impact of Quality Assessment on Seasonal Variations

The FODITS analysis of daily and weekly coordinate time series found significant seasonal signals, see Tables 4.2 and 4.3. The impact of the quality assessment on the seasonal variations is evaluated.

Figure 5.7 documents the impact of the quality assessment on the amplitudes and phases of the annual signal found in the vertical component of the daily and weekly residual

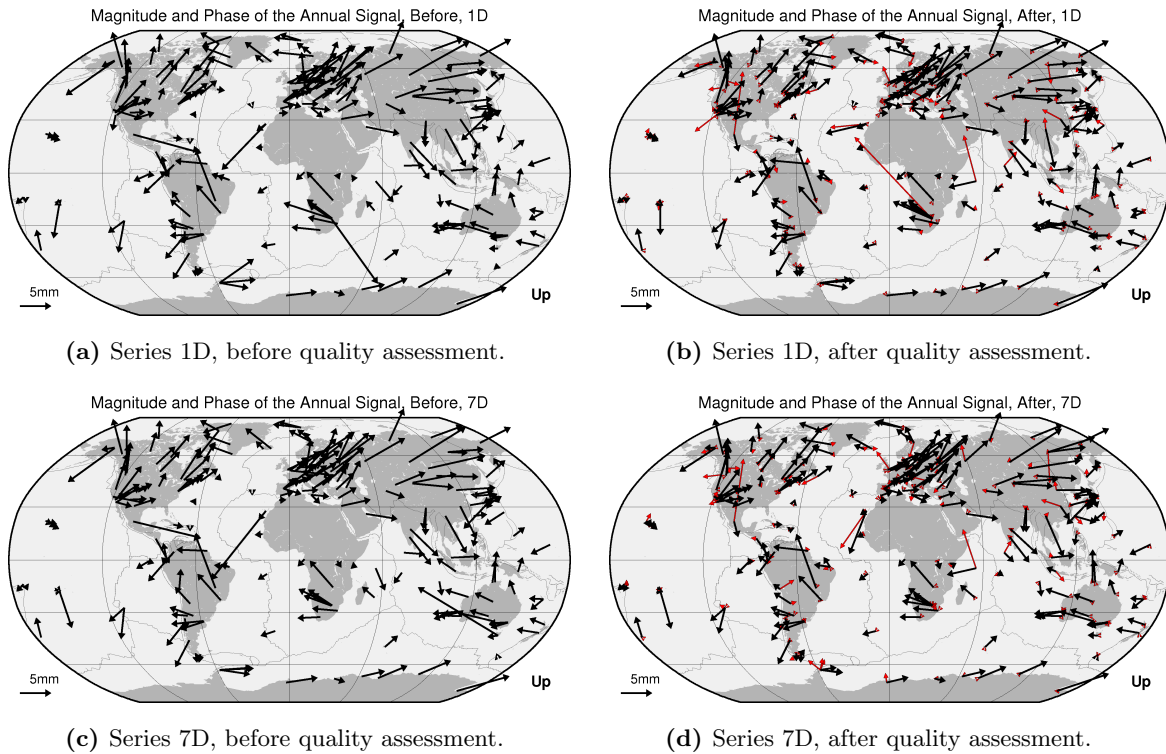


Figure 5.7: Impact of the quality assessment on the amplitude and phase of the annual signals found in the vertical component of daily and weekly coordinate time series. (Red) significant differences between before and after quality assessment.

coordinate time series. Stations with an amplitude of the annual signal larger than 15 mm in the Up component were excluded. The phase 0° , i.e., t_0 in Eq. (3.1), is for all stations 1 January, 2000. The angles are defined as positive in the counter-clockwise direction. A reference amplitude and phase of 5 mm and 0° , respectively, is shown in each figure (see bottom-left corner). Regional correlations of amplitudes and phases are visible before and after quality assessment. Similar regional correlations were found in 128 globally distributed sites by [Dong et al. \(2002\)](#). [Ostini et al. \(2007\)](#) found similar regional correlations in all components *XYZ* for the period of 352 days. Regional correlations of near seasonal variations could be confirmed also by stacked amplitude spectra of baseline time series ([Ostini, 2007](#)). A regional correlation of near seasonal signals indicates the presence of a common source, rather than site-specific local effects. The figures show furthermore a latitude-dependent variation.

Figures 5.7b and 5.7d show the amplitudes and phases of the annual signals as well as their differences w.r.t. before quality assessment. For few stations the differences are larger than 5 mm in amplitude and have a phase change larger than $\pm 90^\circ$. The differences are mainly due to discontinuities present in the residual coordinate time series before quality assessment and no more present after quality assessment. Differences of daily and weekly solutions are not all the same. After quality assessment the maps of daily and weekly

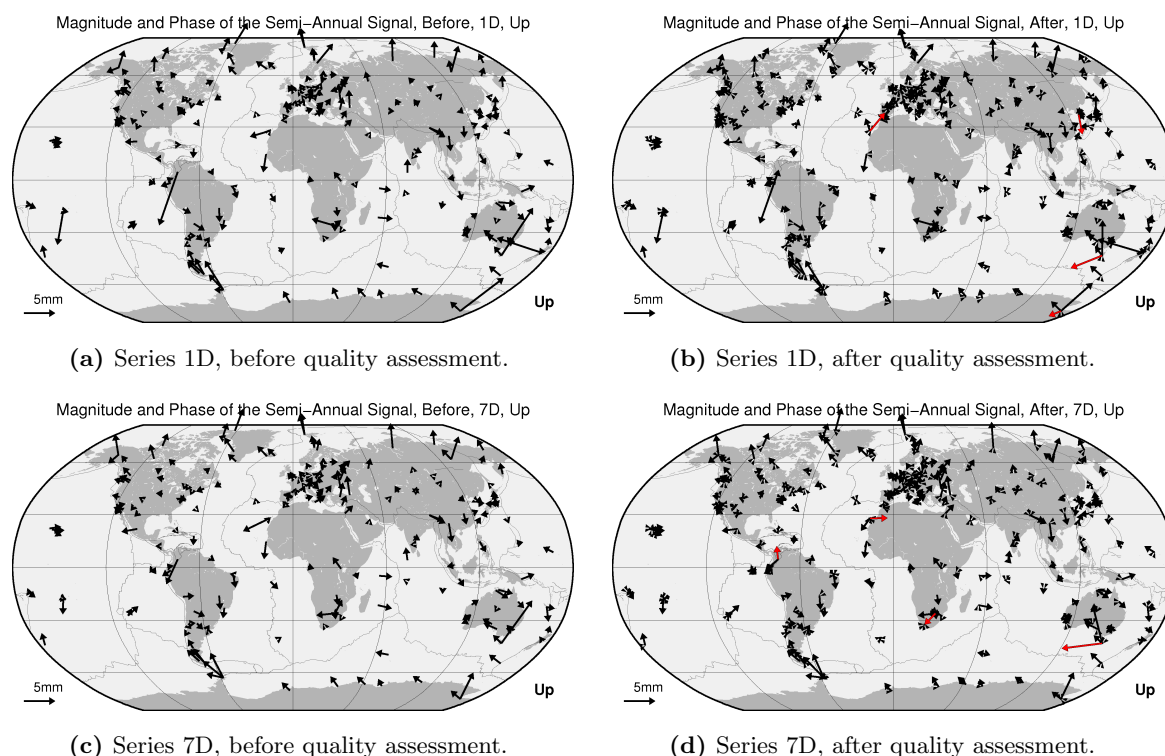


Figure 5.8: Impact of the quality assessment on the amplitude and phase of the semi-annual signals found in the vertical component of daily and weekly coordinate time series. (Red) significant differences between before and after quality assessment.

series are however in good agreement. This implies that the annual variation in daily and weekly residual coordinate time series after quality assessment are comparable (see also Chapter 4).

Figure 5.8 shows the impact of the quality assessment on the amplitudes and phases of the semi-annual signal in vertical component of residual coordinate time series. A semi-annual signal is mainly present at stations of high-latitude in the northern hemisphere. A latitude-dependence of semi-annual signals, however of the 352 days' period, was found by (Tregoning and Watson, 2009, 2011). The impact of the quality assessment is for the semi-annual signals smaller than for the annual signals (compare differences between Figs. 5.7 and 5.8). The amplitude and phase of the semi-annual signals are for daily and weekly series in good agreement—however with more exceptions compared to the annual signal in the daily and weekly series. In fact, the semi-annual signal profits more from the weekly combination as the annual signal.

5.3.2 Global Correlation

Collilieux et al. (2011) showed that the variation of the global scale is highly correlated to the residuals in the Up component. Ostini et al. (2007) showed that in the interval 2003-

2006 the variation of the global scale is comparable to the mean accumulated residuals in the Up component. Let us confirm the latter result using the daily series in the interval 1994-2008.

For both solutions **ADDNEQ2** adopted **NNT** and **NNR** condition for both, station coordinates and velocities. The scale time series was obtained by comparing each **NEQ** solution to the network solution using the Helmert transformation based on all stations. For the time series of residuals, on the other hand, the comparison of each **NEQ** solution to the network solution was carried out by a simple mathematical subtraction operation (see Sect. 4.2). The series of mean accumulated residuals of the Up components were computed in a second step, also using all stations.

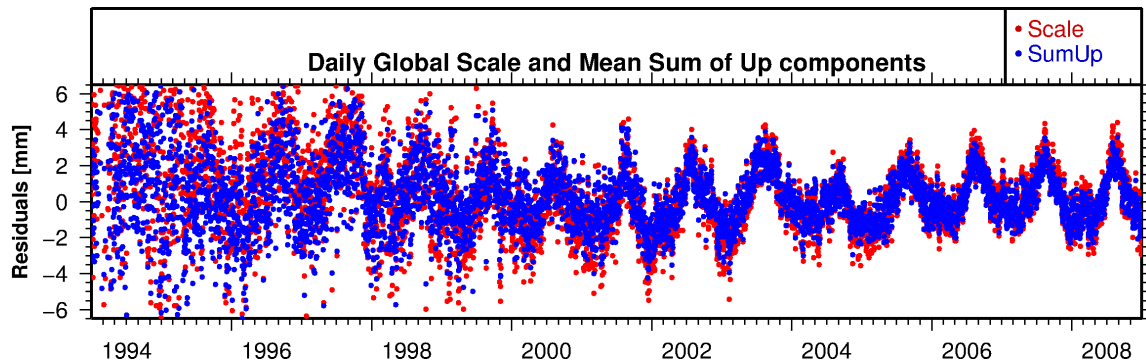


Figure 5.9: Evolution of the scale (red) and the mean Up coordinates (blue) of daily series.

Figure 5.9 illustrates the results. The high degree of correlation between the scale time series and the mean sum of the Up residual coordinate time series is confirmed for the interval 1994-2008. Coordinate time series are thus expected to suffer from both, regional (see Sect. 5.3.1) and global correlations. The **RMS** of scale and sum of the Up residual series are 2.51 mm and 1.94 mm, respectively. The **RMS** of the differences is 0.99 mm. By considering only data points from 1 July, 1998, the three **RMS** are 1.75 mm, 1.42 mm, and 0.50 mm respectively. The series of differences still contain an annual signal.

5.3.3 Spectral Analysis

Power spectra were computed to assess the noise in the daily and weekly coordinate time series (see Sect. 2.5). Following Ray et al. (2008), the power spectra of each station were stacked to amplify the spectral lines common to all stations. As a result we obtained stacked power spectra for the components North, East, and Up. Power spectra were computed by **FFT** with zero-padding extension to obtain interpolated information in spectral domain (see Sect. 5.1 and Appendix B). Stations of daily series with less than 4,000 data points and of weekly series less than 500 data points were not used to reduce systematic errors induced by the **FFT**.

The mean stacked power spectra of daily and weekly series were fitted with a least-squares approach (see Sect. 2.3.3) using the model proposed by (Langbein and Johnson, 1997; Mao

et al., 1999)

$$P(\nu) = P_0 \cdot (\nu_0^{-\kappa} + \nu^{-\kappa}) , \quad (5.1)$$

with the constant P_0 , the crossover frequency ν_0 , and the spectral index κ parameters to be estimated. This model, an extension of the original model (2.53), takes into account both, white noise and colored noise with spectral index κ . Taking the logarithm of both sides

$$\log(P(\nu)) = \log(P_0) + \log(\nu_0^{-\kappa} + \nu^{-\kappa}) , \quad (5.2)$$

the estimation converges more rapidly. With initial values $\log(P_0) = 0$, $\nu_0 = 0.1$, and $\kappa = 1.5$ the optimal fit of the parameters was achieved after four iteration steps.

Figure 5.10 shows the stacked power spectra of daily and weekly residual coordinate time series in three scenarios. In the first scenario (top part) the residual coordinate time series were obtained by the first **ADDNEQ2** run of scheme 4.1, i.e., prior to quality assessment. In the second scenario (center part) the time series emerged from the second **ADDNEQ2** run of the same scheme, i.e., after quality assessment. In the third scenario (bottom part) the time series originated from the second **FODITS** run of the same scheme, after removing the seasonal signals (annual and semi-annual).

As opposed to the first two scenarios, the stacked spectra of the third scenario do not contain the spectral lines associated with the seasonal variations ($365.25/n$, with $n = 1, 2$). The spectral lines associated with the draconitic year of the **GPS** constellation ($352/n$, with $n = 1, \dots, 8$) are present in all components (North, East, and Up) of all scenarios. In both, daily and weekly stacked spectra, two additional spectral lines are present in the lower part of the spectra. In the spectra of daily series these are the prominent signals of 13.66 days and 27.52 days associated with long-period tidal variations M_f and M_m , respectively (see Sect. 5.2.2). In the spectra of weekly series, on the other hand, we found M_m (27.55 days) and the spectral line at 14.35 days. Due to the minimum sampling frequency of 14 days (Nyquist frequency), M_f does not show up in the spectra of the weekly series.

The largest impact of quality assessment on the stacked power spectra is visible for the low frequencies (i.e., long periods), see Fig. 5.10. This is in agreement with the principle of the analysis procedure presented in Chapter 3: errors in the functional model are step-by-step removed to obtain normally distributed residuals. The stacked power spectra of the second and third scenarios (middle and bottom parts) do no longer show the power-law trend visible in the stacked spectra of the first scenario (top part).

Table 5.7 gives the estimates obtained when fitting the model (5.1) (red lines in Fig. 5.10) to the daily and the weekly stacked power spectra (blue signals in Fig. 5.10). In all components the spectral index is $\kappa \approx 1$. This indicates that both, daily and weekly coordinate time series mainly contain a combination of white noise and flicker noise (see Sect. 2.5). This result confirms the findings of other investigations on other coordinate time series (e.g., Zhang et al., 1997; Calais, 1999; Mao et al., 1999; Williams et al., 2004). The spectral index of the Up component is generally smaller than the spectral index of the horizontal components. Before quality assessment κ is larger in weekly series than in daily series.

Table 5.7: Determination of the colored noise in daily and weekly coordinate time series.

Stacked power spectra	Sta	North		East		Up	
		$1/\nu_0$	κ	$1/\nu_0$	κ	$1/\nu_0$	κ
Daily before quality assessment	87 ^a	12.5	1.17±0.02	20.2	1.19±0.01	6.9	1.04±0.05
Daily after quality assessment I ^b	84 ^a	12.6	0.99±0.03	20.1	0.97±0.02	5.9	0.88±0.09
Daily after quality assessment II ^c	86 ^a	12.5	0.98±0.03	20.5	0.98±0.02	5.6	0.85±0.10
Daily series northern hemisphere	149 ^d	10.8	1.02±0.03	15.3	0.98±0.02	3.5	0.80±0.19
Daily series southern hemisphere	75 ^d	13.9	0.98±0.03	21.7	0.92±0.02	11.0	0.85±0.05
Daily series latitude > 60°	34 ^d	7.7	1.02±0.05	8.7	1.00±0.05	0.5	0.77±1.54
Daily series latitude < 60°	190 ^d	13.1	1.00±0.03	19.9	0.95±0.02	8.1	0.83±0.07
Daily series Europe	63 ^d	7.8	1.02±0.05	9.6	0.93±0.05	1.1	0.76±0.68
Daily series North America	38 ^d	9.6	1.00±0.04	14.3	1.03±0.02	4.4	0.87±0.12
Daily series Africa	19 ^d	17.5	0.97±0.02	24.3	0.90±0.01	23.5	1.04±0.01
Daily series South America	6 ^d	18.0	1.05±0.02	37.8	0.97±0.01	21.3	0.82±0.02
Daily series Australia	25 ^d	13.2	0.94±0.03	21.6	1.01±0.01	11.2	0.84±0.05
Weekly before quality assessment	120 ^e	20.2	1.32±0.07	26.3	1.29±0.05	21.7	1.22±0.08
Weekly after quality assessment I ^b	110 ^e	0.9	0.79±6.39	2.7	0.78±2.78	2.3	0.80±3.12
Weekly after quality assessment II ^c	114 ^e	0.9	0.75±7.23	4.7	0.80±1.76	0.9	0.71±7.69

^aOnly stations with more than 4,000 data points.

^bResiduals of coordinates after quality assessment.

^cResiduals of coordinates after quality assessment and after rejection of seasonal signals.

^dStations of daily series after quality assessment with more than 300 data points.

^eOnly stations with more than 500 data points.

Vice versa, after quality assessment, κ is larger in daily series than in weekly series. The quality assessment of coordinate time series changes the colored noise from non-stationary ($\kappa > 1$) to stationary ($\kappa < 1$), see Sect. 2.5. The period of the smooth transition $1/f_0$ from white noise to white noise and flicker noise is obtained from the estimation of the crossover frequency ν_0 . In stacked spectra of the daily series $1/\nu_0$ is larger for the horizontal components than for the vertical component. In the stacked power spectra of weekly coordinate time series, on the other hand, the crossover period are ≈ 20 days and ≈ 2 days before and after quality assessment, respectively (see also Fig. 5.10).

More investigations were made to obtain different region-specific spectral indices κ (see Table 5.7). The spectral indices were computed after quality assessment and after the removal of the seasonal variations. The results tell that no significant difference exists between the spectral indices of different regions. This result is in agreement with the findings of (Mao et al., 1999), where the investigation was made with about 3 years of GPS coordinates. On the other hand, Williams et al. (2004), by analyzing GPS time series of global and regional solutions spanning about 10 years, pointed out that the amplitude of white and flicker noises are larger in the Southern Hemisphere than in the Northern Hemisphere. More investigations in this context need therefore to be undertaken.

Table 5.8: Amplitudes of spectral lines of daily and weekly stacked amplitude spectra. Daily series included only stations with more than 4,000 data points. Weekly series included only stations with more than 500 data points.

Stacked amplitude spectra ^a		Spectral line in [mm] and [day]									
		365	365/2	352/3	352/4	352/5	352/6	352/7	27.50	14.35	13.66
Daily series before quality assessment	North	1.42	0.54	0.34	0.29	0.24	0.44				0.27
		364.1	184.1	117.0	88.6	69.4	58.5				13.66
	East	1.16	0.53	0.32	0.34	0.34	0.32				0.23
		364.1	172.5	115.4	87.6	71.2	58.5				13.65
	Up	3.73	1.32	0.92	0.90	0.65	0.76	0.76	0.71		1.09
		364.1	182.0	114.6	87.6	70.6	58.3	51.0	27.58		13.66
Daily series after quality assessment I ^b	North	1.46	0.50	0.29	0.25	0.20	0.44				0.26
		364.1	184.1	117.9	88.1	69.4	58.5				13.65
	East	0.99	0.49	0.32	0.29	0.29	0.30				0.21
		364.1	172.5	115.4	87.6	69.7	58.5				13.65
	Up	3.45	1.23	0.71	0.79	0.51	0.69	0.45	0.66		1.02
		364.1	182.0	114.6	88.1	70.6	58.3	50.1	27.58		13.66
Daily series after quality assessment II ^c	North	0.58	0.48	0.29	0.25	0.20	0.44				0.26
		341.3	176.2	117.9	88.1	69.4	58.5				13.65
	East	0.62	0.48	0.33	0.29	0.31	0.30				0.21
		341.3	172.5	115.4	87.6	69.7	58.5				13.65
	Up	1.22	1.04	0.73	0.79	0.52	0.70	0.45	0.66		1.00
		341.3	174.3	114.6	88.1	70.6	58.5	50.1	27.58		13.65
Weekly series before quality assessment	North	1.46	0.59	0.32	0.27	0.22	0.33				0.18
		367.6	183.8	117.5	88.5	69.6	58.5				14.36
	East	1.15	0.58	0.35	0.32	0.28	0.29				0.18
		367.6	174.8	115.6	87.4	69.6	58.5				14.35
	Up	3.68	1.37	0.72	0.80	0.52	0.63	0.48	0.61	0.65	
		367.6	181.5	114.7	88.0	70.3	58.5	51.0	27.57	14.36	
Weekly series after quality assessment I ^b	North	1.40	0.53	0.26	0.26	0.23	0.29				0.17
		367.6	183.8	117.5	88.0	69.6	58.8				14.36
	East	0.90	0.51	0.30	0.26	0.27	0.28				0.15
		358.4	174.8	115.6	88.0	69.6	58.5				14.36
	Up	3.29	1.15	0.65	0.70	0.46	0.58	0.40	0.53	0.62	
		367.6	181.5	118.5	88.0	69.3	58.5	51.0	27.57	14.36	
Weekly series after quality assessment II ^c	North	0.52	0.48	0.27	0.25	0.21	0.30				0.16
		341.3	177.0	117.5	88.5	69.3	58.5				14.36
	East	0.63	0.49	0.30	0.26	0.26	0.28				0.15
		341.3	174.8	115.6	88.0	69.6	58.5				14.35
	Up	0.91	1.05	0.64	0.71	0.46	0.56	0.39	0.56	0.64	
		341.3	177.0	119.5	88.0	69.9	58.5	50.8	27.57	14.36	

^aSpectral lines from the discrete results are given in terms of amplitude (above) and period (below).

^bResiduals of coordinates after quality assessment.

^cResiduals of coordinates after quality assessment and after rejection of seasonal signals.

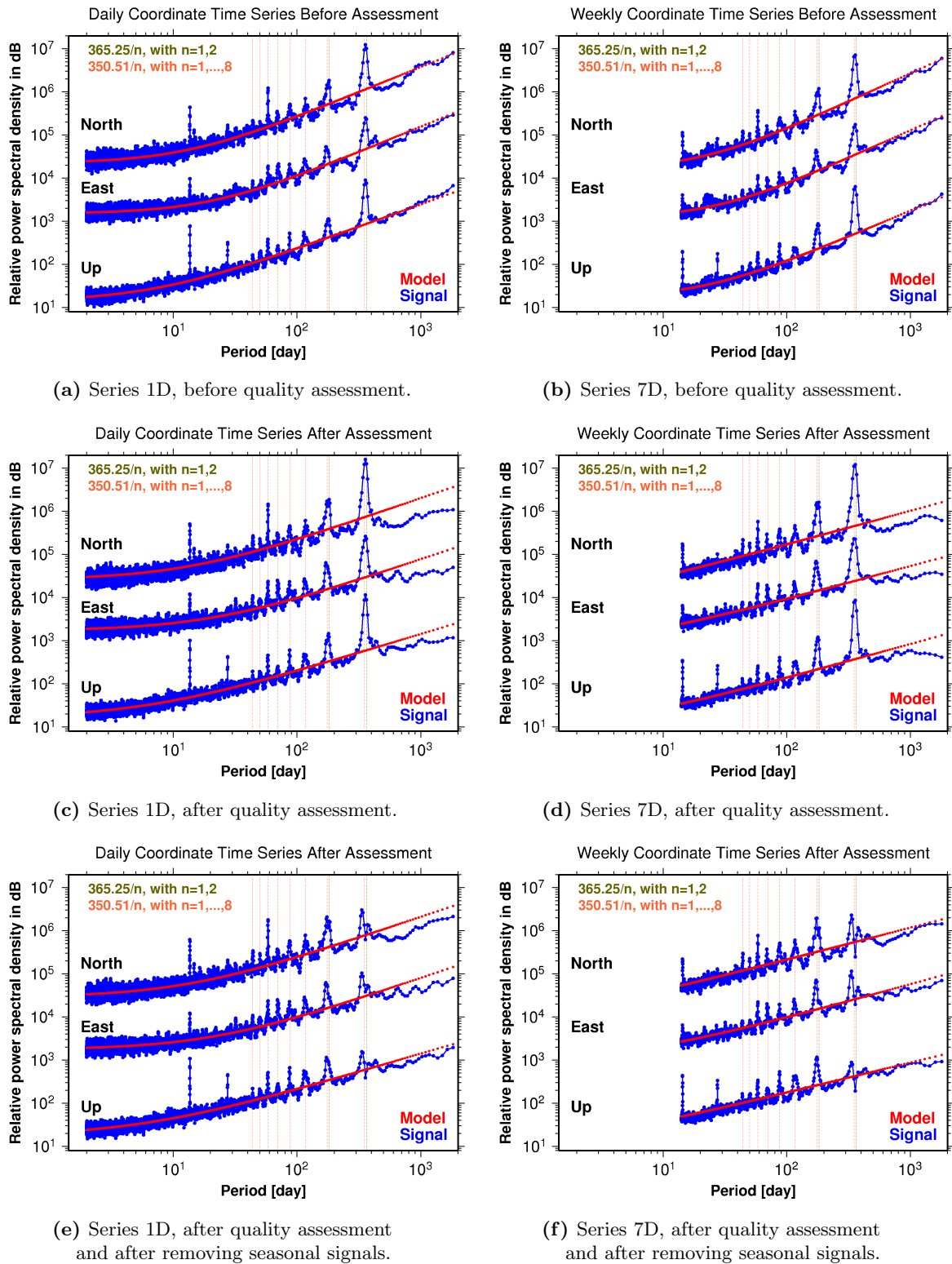


Figure 5.10: Stacked power spectra of daily and weekly residual coordinate time series.

The amplitude of the relevant spectral lines identified in the stacked amplitude spectra, obtained before computing the stacked power spectra of Fig. 5.10, are listed in Table 5.8. The amplitude of the spectral lines ($352/n$, with $n = 4, 6$) are larger than the amplitude of the spectral lines ($352/n$, with $n = 5, 7$). In the spectral analyses of the geocenter series we found only odd harmonics (see Sect. 5.1.2). Hence, concerning the draconitic year of the GPS constellation, the even harmonics ($352/n$, with $n = 4, 6$) characterize the coordinates and the odd harmonics ($352/n$, with $n = 3, 5, 7$) the Z-component of the geocenter parameters. One reason is likely a not uniform global distribution of tracking stations. $352/6$ could be associated with the number of orbital planes of the GPS constellation.

The spectral analysis of the time series of the global scale gave no evidence of spectral lines associated with the draconitic year of the GPS constellation (see Sect. 5.2.2). As the time series of the global scale are highly correlated with the time series of the mean sum of the Up residuals (see Sect. 5.3.2), it is understandable that no harmonics of the GPS-year are present in the spectra of the mean sum of the Up residual either. Figure 5.10 showed, however, that the stacked power spectra of the Up component have such harmonics. Further investigation were not carried out.

5.4 Earth Rotation Parameters

The EOPs (i.e., the nutation parameters ψ and ϵ , the UT1-UTC, and the pole parameters X and Y), elements of the matrix \mathbf{R} in Eq. (2.7), describe the transformation between the inertial and the Earth-fixed reference systems. In a narrow sense, the ERPs are the subset of the EOPs, but without the nutation parameters (e.g., Yibin, 2006).

The GNSS technique cannot estimate the nutation and the UT1-UTC parameters (e.g., Thaller, 2008). The GNSS technique can, however, estimate the first derivation of these parameters, i.e., $\Delta\psi$, $\Delta\epsilon$, and (Excess of) Length Of Day (LOD), with high temporal resolution.

The impact of quality assessment of coordinate time series was studied on the series of ERPs, in particular on the series of X and Y pole parameters. ADDNEQ2 estimates the ERPs as a piecewise-linear function. Daily and weekly NEQs from the first CODE reprocessing contain the nutation rate parameters $\Delta\psi$ and $\Delta\epsilon$, the LOD parameters, and the X and Y poles parameters, all with 1 hour time resolution (see Sect. 2.4). All ERPs were first transformed to 24 hours resolution. The first parameter of the nutation rate parameters and the LOD parameters of each NEQ were heavily constrained to the values of the model IAU2000A (Mathews et al., 2002) and Bulletin A (Luzum et al., 2001), respectively. NNT and NNR were adopted for both, station coordinates and velocities. The geocenter parameters were pre-eliminated before stacking. The result is a piecewise-linear representation of daily X and Y poles over 15 years with one day resolution. The X and Y pole estimates, provided at 24:00 UTC of each day, were linearly interpolated to have their values at 12:00 UTC.

Figure 5.11 shows the impact of quality assessment on the daily series of X and Y poles from 1994 to 2008. The (top) four figures illustrate the solution obtained from daily NEQs,

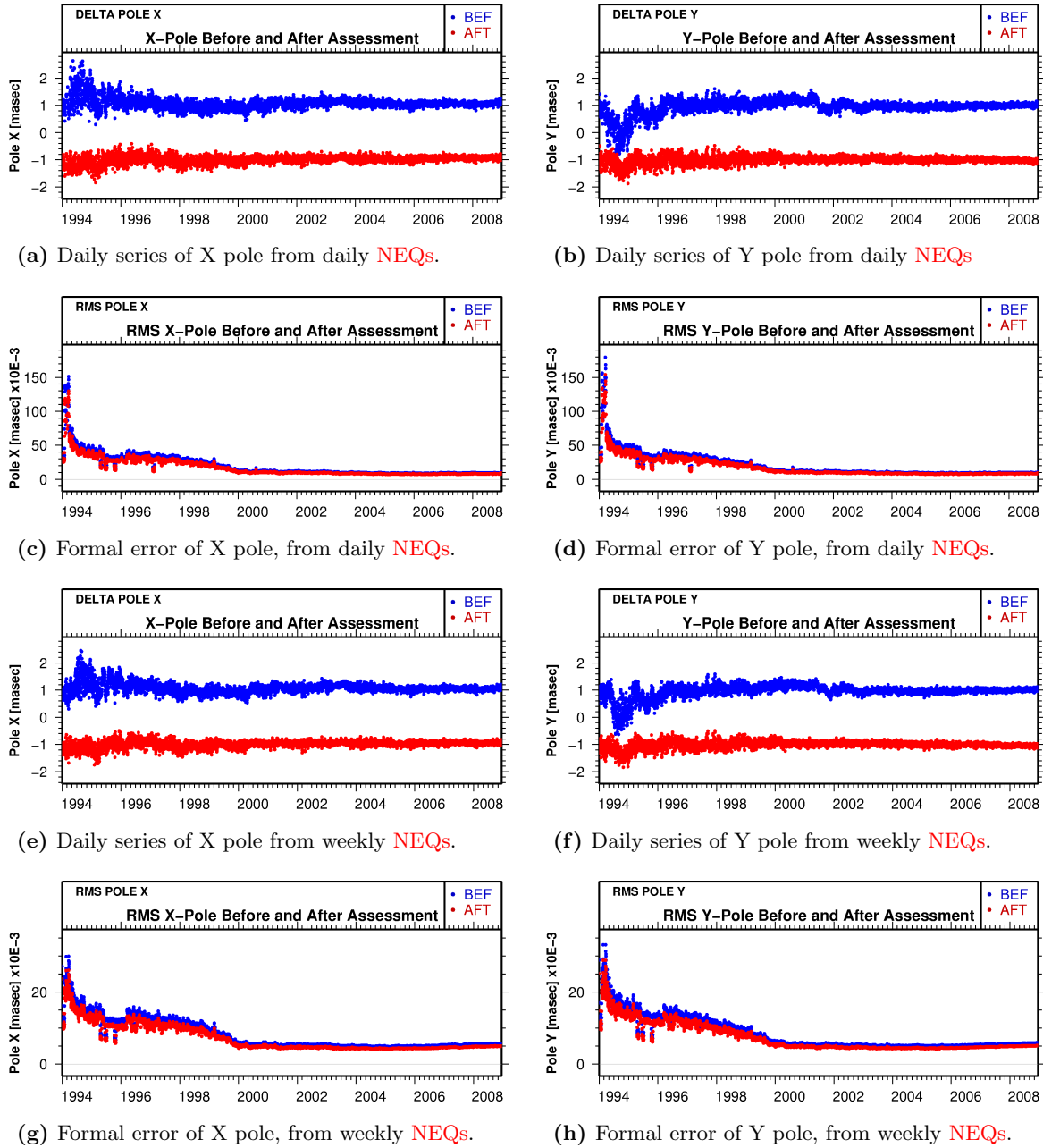


Figure 5.11: Daily series of X and Y pole estimates w.r.t. Bulletin A before and after quality assessment, 1994-2008.

while the four (bottom) figures display the solution obtained from weekly NEQs. The series of estimates w.r.t. to Bulletin A and their formal errors are given for each solution. The series before quality assessment of the coordinate time series are given in blue (BEF), and the series after quality assessment of coordinate time series in red (AFT).

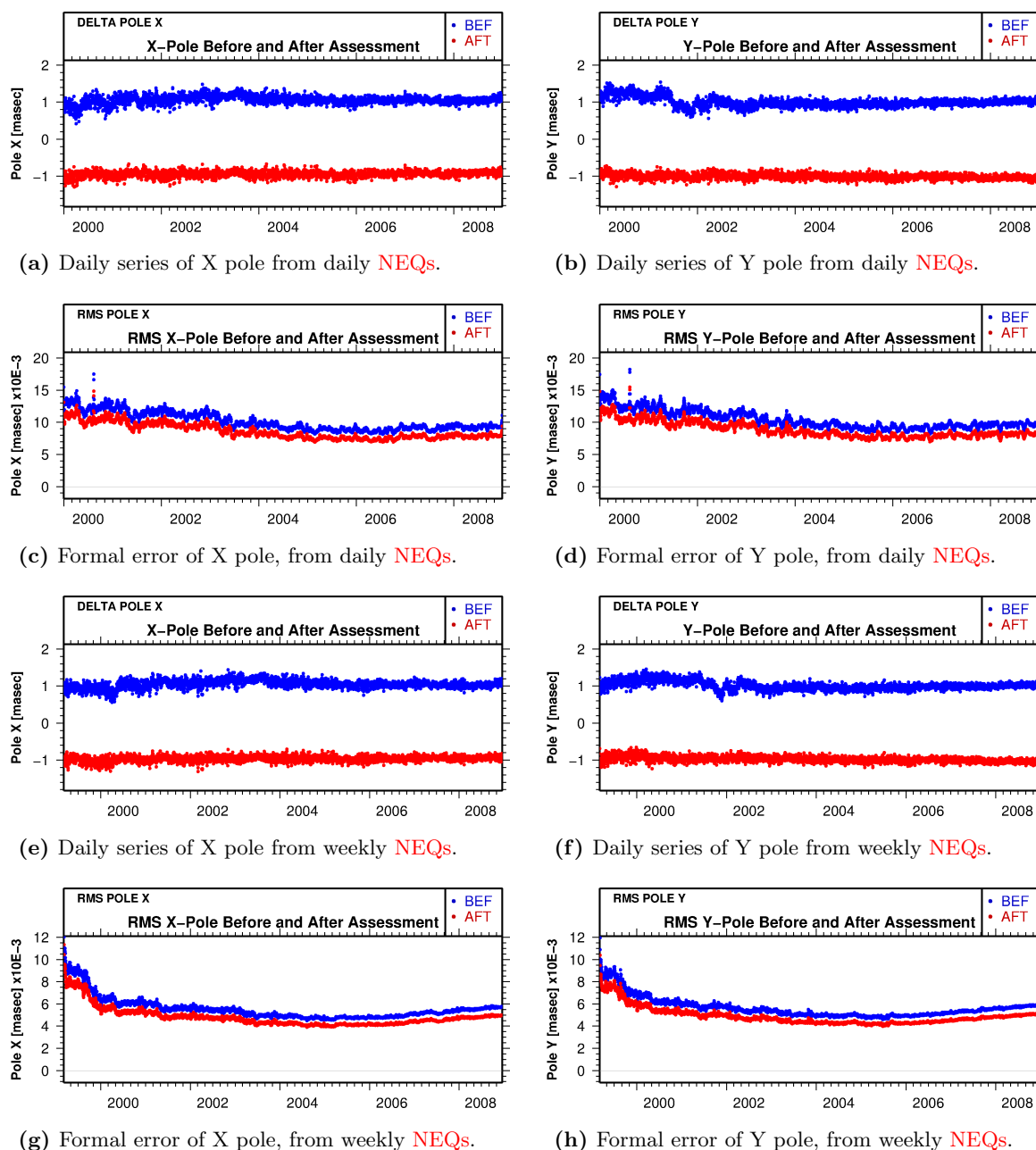


Figure 5.12: Daily series of X and Y pole estimates w.r.t. Bulletin A before and after quality assessment, 2000-2008.

The largest impact of quality assessment is achieved in the early years of the series, i.e., the large variations w.r.t. the official IERS time series between 1994 and 1996 in both, the X and Y time series could be significantly reduced. The quality assessment of coordinate time series also completely removed the offset around 2001 visible in Figs. 5.11b and 5.11f.

The removal of offsets is even more apparent in Fig. 5.12, where the series span from 2000 to 2008.

Table 5.9: RMS of the pole time series w.r.t. to Bulletin A before and after quality assessment.

[masec] ^a	Daily, 1994-2008			Weekly, 1994-2008			Daily, 2000-2008			Weekly, 2000-2008		
	Bef.	Aft.	%	Bef.	Aft.	%	Bef.	Aft.	%	Bef.	Aft.	%
X pole	0.250	0.175	29.9	0.209	0.154	26.4	0.144	0.111	23.0	0.133	0.104	21.9
Y pole	0.313	0.169	45.8	0.254	0.155	39.0	0.153	0.104	32.0	0.135	0.101	25.0

^a(Bef.) before and (Aft.) after quality assessment.

The RMS and the percentage of improvement in all X and Y pole time series of Figs. 5.11 and 5.12 are given in Table 5.9. Before quality assessment the RMS of the X and Y pole time series are in part different. After quality assessment they turn out to be on the same level. The improvement in RMS of the pole series from not reprocessed data to reprocessed data was about 30% (Steigenberger et al., 2009b). By the quality assessment of coordinate time series in the multi-year solution a further improvement in RMS of more than 20% (see Table 5.9) could be achieved in all pole series.

Table 5.10: Pole formal error time series before and after quality assessment.

[μasec] ^a	Daily, 1994-2008			Weekly, 1994-2008			Daily, 2000-2008			Weekly, 2000-2008		
	Bef.	Aft.	%	Bef.	Aft.	%	Bef.	Aft.	%	Bef.	Aft.	%
X pole	13.29	11.40	14.2	9.48	8.25	13.0	13.54	11.48	15.2	9.63	8.34	13.4
Y pole	13.88	11.91	14.2	9.85	8.57	13.0	14.13	11.99	15.1	10.00	8.67	13.3

^a(Bef.) before and (Aft.) after quality assessment on December 31, 2008.

Figures 5.11 and 5.12 show also the time series of the formal errors of the X and Y pole estimates. The improvement is apparent in all series. A comparison of Figs. 5.12c and Fig. 5.12g) shows that the formal errors of the series based on daily NEQs is about a factor 2 larger than the formal errors of the series based on weekly NEQs. As the a posteriori RMS of unit weight of the adjustment of both multi-year solutions is ≈ 1.3 mm, the difference of formal errors from daily and weekly NEQs originates from the cofactor matrix $\mathbf{Q}_{\hat{p}\hat{p}}$ associated with the LSE (see Sect. 2.3.3). Using weekly NEQs the formal errors of the pole estimates are better than using daily NEQs (a more precise value is computed below).

The improvements of the formal errors of the pole time series before and after quality assessment are given in Table 5.10. The comparison was carried out for the last epoch of the series, namely for 31 December, 2008. For the series spanning from 1994 to 2008 the formal error associated with the weekly NEQs is a about of a factor 1.4 smaller than the one associated with daily NEQs. The same factor of about 1.4 was found for the series from 2000 to 2008. Using the same dataset as in this work, Steigenberger et al. (2009b) found an improvement of the formal error (however for subdaily ERPs) of about 30%. The additional improvement in the formal error obtained through quality assessment of coordinate time series is in all pole series larger than 13%.

Last but not least, the time series of the pole formal errors contain jumps attributed

to the deactivation and reactivation of **AS**. When **AS** is deactivated the formal error become smaller. The jumps are in agreement with the intervals of Table 2.3—intervals of deactivated **AS** from 19-Apr-1995 to 10-May-1995, from 18-Jun-1995 to 11-Jul-1995, from 09-Oct-1995 to 01-Nov-1995, and from 01-Feb-1997 to 24-Feb-1997. The same impact of **AS** was seen by [Steigenberger et al. \(2009b\)](#).

6 Evolution of Mean Orbital Elements

The analysis of the evolution of the satellite orbital elements, i.e., semi-major axis a , inclination i , eccentricity e , right ascension of the ascending node Ω , argument of Perigee ω , and argument of latitude $u(t)$, see Fig. 2.3, describes the long-term temporal behavior of satellite orbits in space. The program **FODITS** introduced in Chapter 3, originally designed to analyze coordinate time series, is used here to study the evolution of orbital elements of **GPS** and **GLONASS** satellites.

GPS orbits are processed at **CODE** since the beginning of the **IGS** activities in 1992 (Rothacher et al., 1999). The processing of **GLONASS** orbits, on the other hand, began in 1998 (Habrich, 1999). Reprocessed **GPS** and **GLONASS** orbits are available with a daily spacing from the years 1994 and 2003, respectively (see Sect. 2.4).

The revolution time of **GPS** (11 h 58 min) and **GLONASS** (11 h 16 min) satellites is shorter than one solar day. The analysis of orbital elements averaged over an entire number of revolutions, i.e., of the so-called *mean elements* (Beutler, 2005), allows it to studying the behavior of satellite orbits over years. Section 6.1 introduces the computation of the mean elements. The analysis of the evolution of the mean elements of **GPS** and **GLONASS** satellites are documented in Sects. 6.2 and 6.3, respectively.

6.1 Mean Orbital Elements

A particular solution of the equation of motion (2.50) with initial values (2.51) consists of a state vector (i.e., satellite position $\mathbf{r}(t)$ and satellite velocity $\dot{\mathbf{r}}(t)$) for each epoch t . A set of orbital elements is associated with each epoch t (in this context also called *osculating epoch*):

$$t : \{ \mathbf{r}(t), \dot{\mathbf{r}}(t) \} \longrightarrow \{ a(t), e(t), i(t), \Omega(t), \omega(t), u_0(t) \} . \quad (6.1)$$

These orbital elements are called *osculating elements*. Osculating elements represent the instantaneous unperturbed (Keplerian) orbit of a satellite. Time series of osculating elements visualize therefore the impact of the perturbing forces on the Keplerian elements.

Mean elements are computed to study the long-term evolution of osculating elements by averaging the osculating elements over a number of full revolutions (Beutler, 2005). A mean element

$$\bar{I}(t) \in \{ a(t), e(t), i(t), \Omega(t), \omega(t), u_0(t) \} \quad (6.2)$$

at the epoch t is obtained by

$$\bar{I}(t; \Delta t(t)) = \frac{1}{\Delta t} \int_{t-\Delta t/2}^{t+\Delta t/2} I(t') dt' , \quad (6.3)$$

where $\Delta t(t)$ corresponds to the averaging time interval covering an entire number of revolution periods.

Mean elements are computed by a modified version of the **BSW** program **ORBbit GENERATION (ORBGEN)**. In the program the averaging time interval $\Delta t(t)$ is of one revolution period for all **GNSS** satellites.

An average time $\Delta t(t)$ of one satellite revolution corresponds to the unperturbed revolution period U at the epoch t . Using the Kepler's third law

$$\mu = n^2 a^3 \quad (6.4)$$

in the energy theorem of a two-body problem for an ellipse

$$v^2 = \mu \left(\frac{2}{r} - \frac{1}{a} \right) , \quad (6.5)$$

and considering that the mean satellite motion is $n = 2\pi/U$, one obtains the revolution period at the epoch t as

$$U = 2\pi\mu \sqrt{\frac{r^3}{(2\mu - v^2 r)^3}} . \quad (6.6)$$

As the perturbing forces have an impact on the osculating revolution period, $\Delta t(t)$ varies as a function of time. Therefore, $\Delta t(t)$, i.e., in this context the revolution period (6.6), is computed for each day from r and v at time t .

Each integration interval of 1 hour the satellite orbits are represented as polynomials of degree 10 (Table 2.5). It is obvious that a spacing of one hour is not sufficient to compute accurate mean elements. For this reason, in the modified version of **ORBGEN** mean elements are computed with a spacing of one second using the hourly polynomial functions obtained from the numerical integration.

Figure 6.1 illustrates the evolution of both, the osculating and the mean semi-major axis, of the **GPS** satellite **SVN 39 (PRN 09)**. The evolution of the osculating semi-major axis is dominated by a signal with period of about 6 hours (see (Beutler, 2005), Vol 2, pp. 134). The evolution of the mean semi-major axis, on the other hand, mainly contains a signal with period of about 352 days, corresponding to the draconitic year of the **GPS** constellation (Beutler, 2005). The discontinuities visible in both evolutions are due to the repositioning events (satellite maneuvers).

The analyses in the next sections refer to analyses of the mean elements.

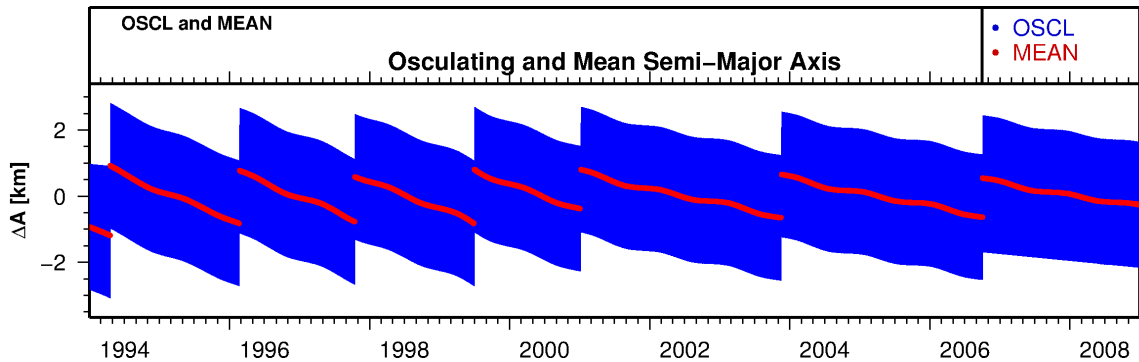


Figure 6.1: Osculating (OSCL) and mean (MEAN) semi-major axes of GPS SVN 39, Block IIA, plane A, PRN 09.

6.2 Evolution of Mean Elements of GPS Satellites

With their deployment in orbit, GPS satellites obtain unique SVN and Committee On SPace Research (COSPAR) numbers. Active GPS satellites are also characterized by a unique PRN, characterizing their code signal (see Sect. 2.2.1). This is why we analyze time series of orbital elements using SVNs and not PRNs. Table A.1 lists the SVNs and PRNs for the GPS satellites between 1994 and 2008.

Figure 6.2 shows the evolution of the mean orbital elements of SVN 32 from 1994 to 2008. Each gray vertical line indicates when the satellite was *eclipsed*, i.e., when it entered the Earth’s shadow once per revolution. For a GPS satellite, the maximum length of an eclipse phase is about 56 minutes (Beutler, 2005). This occurs when the Sun is in the orbital plane of the satellite. *Eclipsing seasons* occur twice per year for each satellite (actually for each orbital plane).

Repositioning events of GPS satellites are accomplished by short accelerations in the along-track direction (e.g., Beutler, 2005; Dach et al., 2009). Such a repositioning event causes a rather large discontinuity in the evolution of the semi-major axis and a smaller discontinuity in the evolution of the other elements eccentricity, and argument of Perigee (see Fig. 6.2). The evolutions of the right ascension of the ascending node Ω and of the inclination i should not be affected by discontinuities because accelerations in the along-track direction do not affect the natural evolution of the orbital plane. Figure 6.2 also shows that few repositioning events were performed during eclipsing seasons. These repositioning events were however performed outside the eclipsing phases, because GPS satellites do not maintain the correct (nominal) attitude during these phases (Kouba, 2008).

SVN 32 was launched on 22 November, 1992. From 1994 to the day of its decommission, on 17 March, 2008, the satellite broadcasted signals as PRN 1¹. Although no official information could be found, from 1994 to begin 1996 SVN 32 occupied slot 6 on plane F (i.e., slot F6). By a sequence of two maneuvers, the first on 30 January, 1999 (NANU 1999015), and the second on 21 January, 2000 (NANU 2000012), the satellite was moved

¹<ftp://tycho.usno.navy.mil/pub/gps/gpsb2.txt>

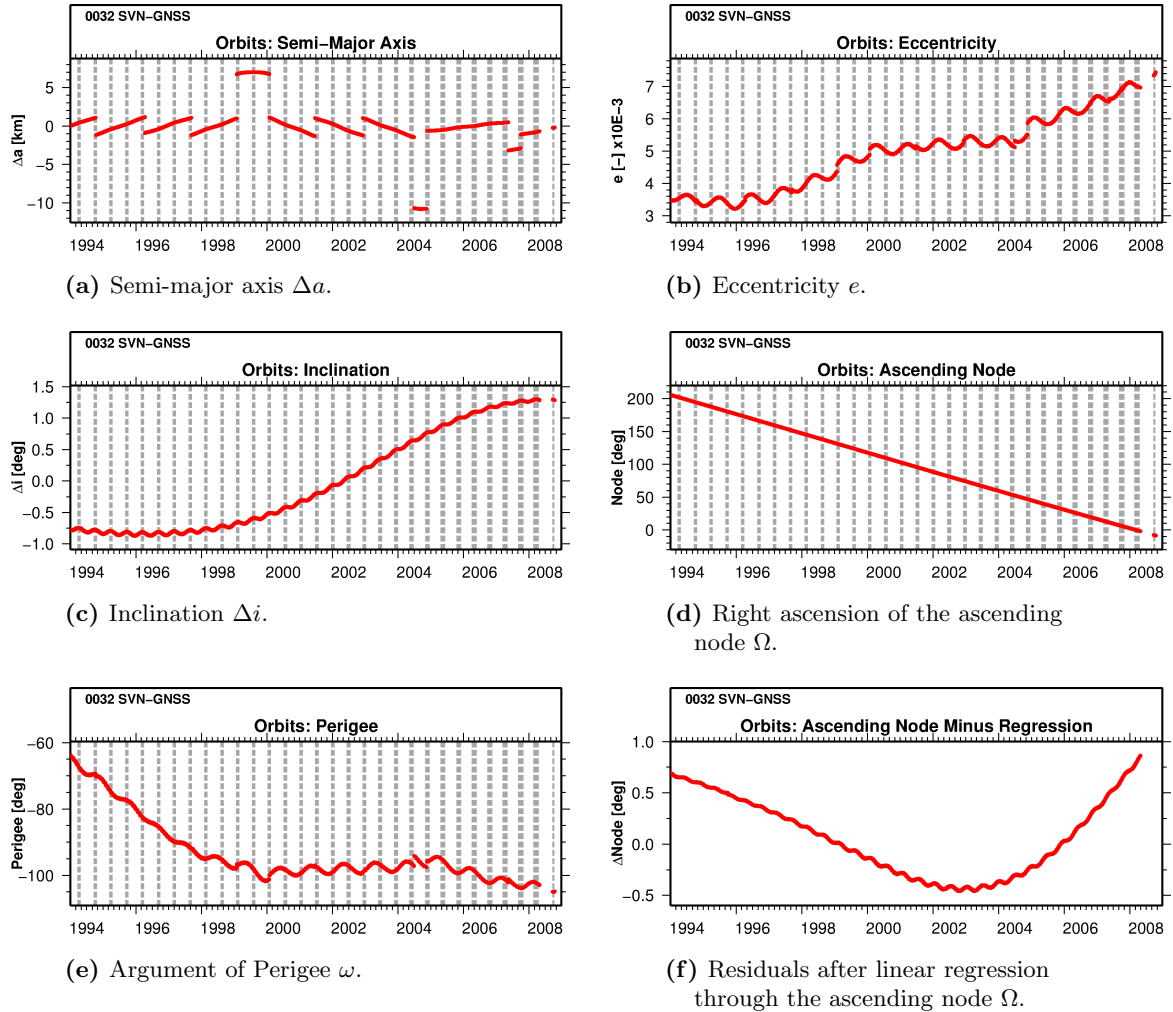


Figure 6.2: Evolution of the mean elements of **GPS SVN 32**, Block IIA, plane F, **PRN 1** from 22-Nov-1992 to 17-Oct-2008. Daily eclipsing phases are shown by the gray dashed vertical lines.

to slot F4. This double maneuver is clearly visible in Fig. 6.2a. Towards the end of its lifetime, the satellite was moved back to slot F6, again by a double maneuver, the first on 28 June, 2004 (**NANU 2004076**) and the second on 18 November, 2004 (**NANU 2004120**). Both events are clearly visible in Fig. 6.2a. Shifts within the orbital plane are therefore performed by a pair of maneuvers to temporary lowering or rising the satellite's altitude.

A perturbation with a period of one **GPS** draconitic year is present in the semi-major axis, in the eccentricity, and in the argument of Perigee. The inclination evolution is perturbed by a period of half draconitic year. After removing the secular regression, the evolution of the right ascension of the ascending node shows perturbations of period of half a draconitic year, as well (see Fig. 6.2f). Inclination and right ascension of the ascending node describe the precession of the orbital plane w.r.t. the Equatorial plane.

6.2.1 Analysis of the Mean Semi-Major Axes

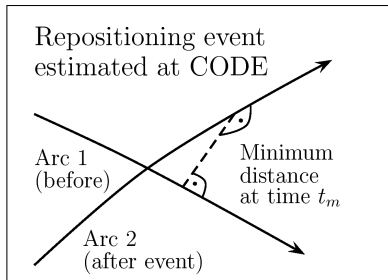
Ground Truth The evolution of the semi-major axis of GPS satellites is characterized by discontinuities associated with repositioning events, see Fig. 6.1. In order to validate the identification of repositioning maneuvers by the algorithm in FODITS, we derived the ground truth, i.e., the list of all maneuvers of GPS satellites between 1994 and 2008.

The repositioning events are regularly announced via Notice Advisory to NAVSTAR User (NANU) messages². Despite that, the *ground truth* for the validation of the FODITS detection was derived from the list of satellites' maneuvers followed at CODE since the beginning of its activities in 1992.

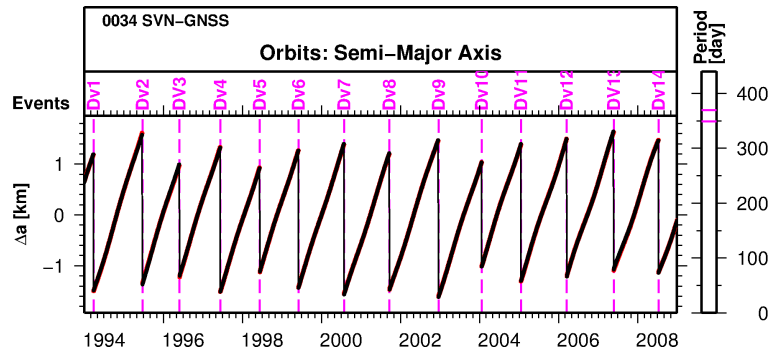
From 2003 onwards CODE estimates the thrust associated with each repositioning event (Hugentobler et al., 2006). The Gaussian perturbation equations (see, e.g., (Beutler, 2005), Vol 1, pp. 215) give the relation between the change in the semi-major axis Δa on one hand, and the thrust $T \cdot \Delta t = \Delta v$ in the along-track direction, on the other hand. In a (T, N, W) system (where T is a tangential component in the direction of the velocity vector) such thrust can be approximated by the instantaneous velocity change

$$\Delta v = \frac{\mu}{2a^2} \cdot \frac{1}{v} \cdot \Delta a, \quad (6.7)$$

where v (in meter/sec) is the velocity of the satellite. The epoch of a repositioning event t_m is identified as that of the minimum distance between the two orbital arcs, the first before and the second after the repositioning event, see Fig. 6.3a. As a result, CODE, from 2003 onward, collected a list of repositioning events with the epoch, the minimum distance, and the pulse Δv in the T -system of the event.



(a) Principle of the minimum distance to identify the epoch t_m of the repositioning events at CODE from 2003 onwards.



(b) Validation of the algorithm of FODITS to estimate repositioning events in the evolution of the mean semi-major axis of SVN 34.

Figure 6.3: Validation of the algorithm FODITS to identify repositioning events of GPS satellites. (6.3a) scheme to estimate repositioning events at CODE. (6.3b) analysis of the semi-major axis evolution of GPS SVN 34, Block IIA, plane D, PRN 4 from 26-Oct-1993. (D) identified repositioning event. (V) change in drift added by the analysis.

²<http://www.navcen.uscg.gov/>

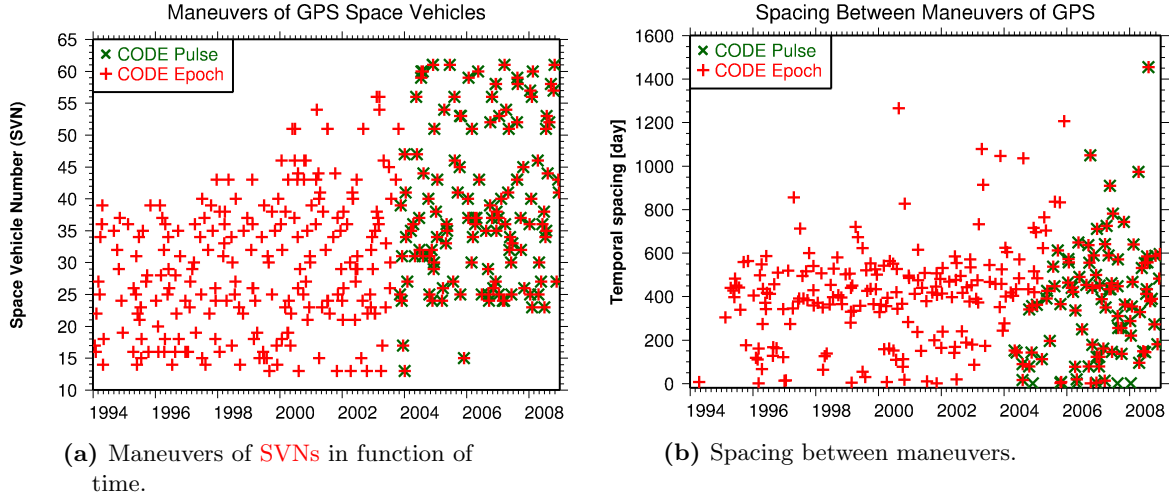


Figure 6.4: Repositioning events of GPS satellites between 1994 and 2008. (CODE Pulse, Green) maneuvers performed at CODE by the principle of minimum distance from 2003 onwards. (CODE Epoch, Red) maneuvers known at CODE (ground truth).

Figure 6.4 shows statistics on the epochs of repositioning events of the SVNs derived from the CODE list (CODE Epoch, ground truth, in red) and from the list of the estimates of the thrust associated with each repositioning event (CODE Pulse, in green). Figure (6.4a) shows the events of two lists in function of time. Figure (6.4b) shows the spacing between the events for each SVN. The epochs in the two lists perfectly agree because the CODE list (i.e., the ground truth in our case) provides the ground information for estimating the thrusts associated with each repositioning event. From Fig. 6.4b one can observe that the majority of repositioning events were repeated about every 450 days. Few maneuvers were repeated with few days spacing. According to the figure, no SVN registered a spacing longer than 5 years.

At first, FODITS was used to analyze the evolution of the semi-major axis by proposing the ground truth as known. The settings were the following: The overall level of significance was set to $U_t = 0.005$. Changes in drift were identified and, after each discontinuity, the procedure proposed a new change in drift. The minimum size accepted for a discontinuity (i.e., repositioning event) was 200 m. The minimum interval length between successive drift changes was $\Delta t_v = 1.0$ year. For each series 10 periodic functions were sought between 340 and 390 days.

Figure 6.5 documents the semi-major axis's analysis of six SVNs. Let us mention some peculiarities by beginning with the evolution of SVN 15 (see Fig. 6.5a). After the three repositioning events DV1, DV2, and DV3 to keep the satellite in slot D2—and to avoid the drift due to the deep 2:1 resonance with the Earth's rotation (see Sect. 2.2.1)—two larger maneuvers, DV5 and DV6, moved the satellite to slot D5. From the vertical bar on the right hand side of the figure we notice that the analysis did not just introduce a signal of 352 days. Due to the shift from one to the other slot along the orbital plane the underlying

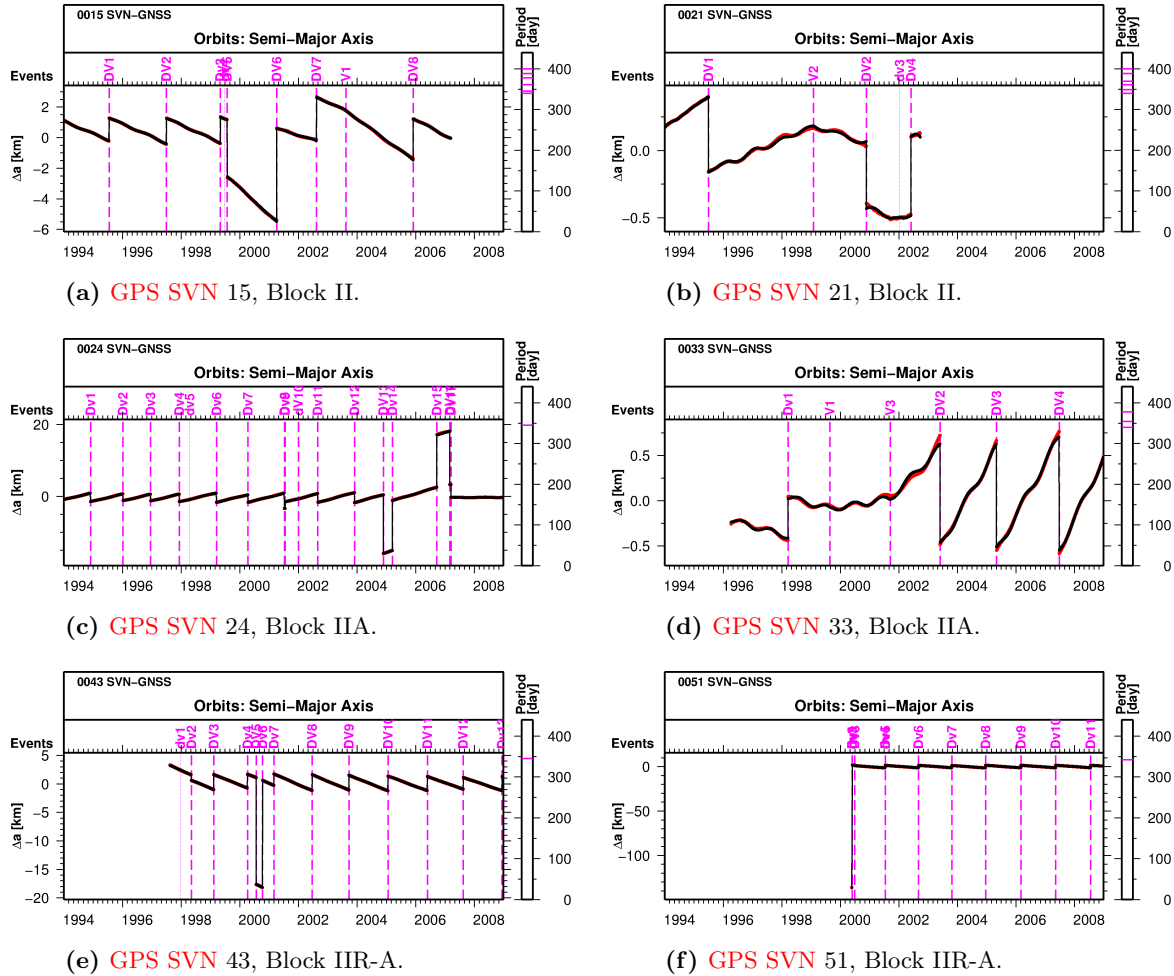
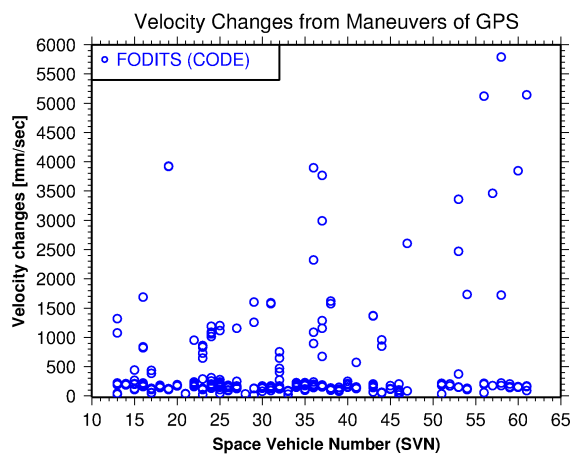


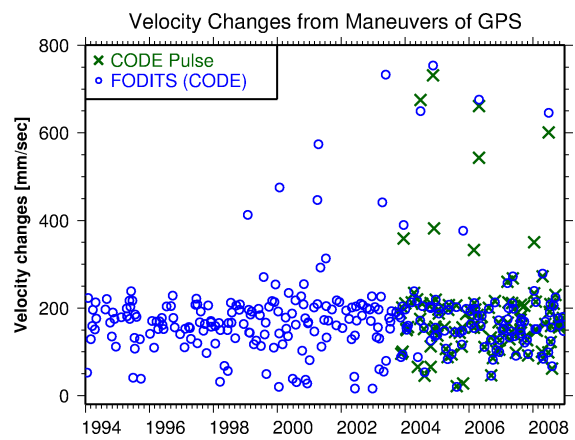
Figure 6.5: FODITS analyses of the semi-major axis evolution of GPS satellites. Epochs of the maneuvers introduced as predefined from the CODE database. (D) identified maneuver. (V) change in drift. (Red) time series. (Black) functional model.

signal of 352 days has a shift in phase, as well. Shifts in phase occur after each repositioning event. For this reason the optimal representation of the underlying signal for the SVN 15 was obtained by 6 periodic functions proposed between 340 days and 390 days. Figure 6.5b shows the evolution of the orbit of SVN 21. The drift due to the 2:1 resonance, which almost depends on the position of the satellites in the orbital plane, is significantly smaller than that of SVN 15. This allows it to better see the quasi-seasonal signal associated with the draconitic year of the GPS constellation. The shift in phase of the signal is visible across DV2 (compare the functional model in black to the underlying semi-major axis's evolution in red). Again, the optimal representation of the series was found by 6 periodic functions. The analysis of SVN 21 also underscores the importance of proposing changes in drifts to obtain a satisfying analysis result (see, e.g., the change in drift V2). Not all events known from the ground truth were found to be significant, e.g., dv3. Figure 6.5c

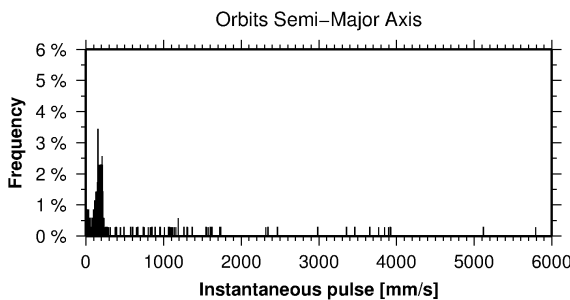
shows the evolution of the semi-major axis of **SVN 24**. The analysis could be carried out by proposing only one periodic function. In 2001 two small maneuvers were found with a spacing of 10 days. After 2004 two pairs of repositioning events shifted the satellite twice along the orbit. Repositioning events of the order of 1 km (corresponding to a velocity change of 73 mm/sec) are visible in Fig. 6.5d. As the minimum interval length between successive drift changes was 1 year, no additional drift changes could be proposed to better fit the functional model to the time series. Figure 6.5e shows in particular that the pair of maneuvers carried out by **SVN 43** for a shift along the orbit were each of about 1.3 m/sec. Last, Fig. 6.5f shows that the **SVN 51** was moved into its slot by an initial maneuver which equates to 10 m/sec.



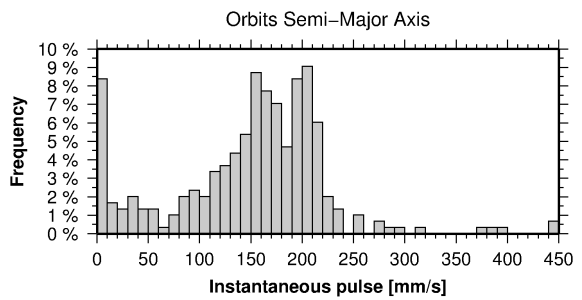
(a) Velocity changes by **SVN** due to maneuvers.



(b) Velocity changes by time due to maneuvers (note y-axis range has been reduced to see detail).



(c) Histogram of the velocity changes.



(d) Histogram of the velocity changes (zoom).

Figure 6.6: Instantaneous pulses associated with the repositioning events of **GPS** satellites in the interval 1994-2008. For the **FODITS** analysis, the epochs of all maneuvers were provided from the ground truth. (Green) maneuvers performed at **CODE** by the principle of minimum distance from 2003 onwards. (Blue) identified in the **FODITS** analysis.

Figure 6.6a gives the estimates of the instantaneous velocity changes obtained by the **FODITS** analysis with proposed ground truth. Three velocity changes above 6.0 m/sec

(the largest of them of 13.2 m/sec) were not reported in Fig. 6.6b. Maneuvers with instantaneous velocity change larger than 1.0 m/sec were mainly carried out to shift satellites along their orbits. Figure 6.6b shows the same instantaneous velocity changes, but up to 800 mm/sec and in function of time. The major number of maneuvers were carried out with pulses between 150 mm/sec (corresponding to a discontinuity of about 2.1 km) and 200 mm/sec (corresponding to a discontinuity of about 2.7 km). This result confirms the approximation provided by Dach et al. (2009). Figure 6.6b shows furthermore that before 1999 no repositioning event had an instantaneous velocity change larger than 250 mm/sec. This implies that before 1999 no slot changes were made, i.e., maneuvers were only carried out to keep satellites in their assigned slots. Last, Fig. 6.6b reports also the pulses estimated at CODE (CODE Pulse, in green). Except for few cases, pulses estimated by FODITS with proposed ground truth are comparable to the pulses estimated at CODE.

Figures 6.6c and 6.6d report the estimated instantaneous velocity changes by FODITS (with proposed ground truth) in histograms. We notice that maneuvers to keep satellites in their slot had peaks in frequency for pulses around 150 mm/sec and 200 mm/sec. A large number of maneuvers had pulses less than 10 mm/sec. dv3 in Fig. 6.5b is an example.

The program FODITS can be used to identify and estimate the repositioning events in the evolution of the semi-major axis. The settings for the validation, except that discontinuities are in this case identified, are the same as for the analysis with proposed ground truth (see above).

Table 6.1: Validation of the algorithm FODITS to identify repositioning events of GPS satellites. Summary of the analysis of the semi-major axis evolution of GPS SVN 34.

Event	Epoch	Discontinuity size ^a [m]	Velocity change of maneuvers [mm/sec]		
			FODITS	CODE	Difference
(D1)	29-Mar-1994	-2,747.0 ± 1.53	-200.4 ± 0.1	n.a.	
(D2)	23-Jun-1995	-2,986.4 ± 1.28	-217.9 ± 0.1	n.a.	
(D3)	30-May-1996	-2,240.8 ± 1.56	-163.5 ± 0.1	n.a.	
(D4)	12-Jun-1997	-2,896.5 ± 1.27	-211.3 ± 0.1	n.a.	
(D5)	11-Jun-1998	-2,092.5 ± 1.51	-152.7 ± 0.1	n.a.	
(D6)	04-Jun-1999	-2,735.3 ± 1.30	-199.5 ± 0.1	n.a.	
(D7)	29-Jul-2000	-2,980.9 ± 1.22	-217.5 ± 0.1	n.a.	
(D8)	21-Sep-2001	-2,688.3 ± 1.35	-196.1 ± 0.1	n.a.	
(D9)	18-Dec-2002	-3,089.4 ± 1.20	-225.4 ± 0.1	n.a.	
(D10)	22-Jan-2004	-2,029.0 ± 1.51	-148.0 ± 0.1	-149.4	1.4
(D11)	19-Jan-2005	-2,680.1 ± 1.46	-195.5 ± 0.1	-196.4	0.9
(D12)	17-Mar-2006	-2,706.5 ± 1.33	-197.4 ± 0.1	-197.1	-0.3
(D13)	25-May-2007	-2,752.8 ± 1.36	-200.8 ± 0.1	-197.8	-3.0
(D14)	11-Jul-2008	-2,655.1 ± 1.49	-193.7 ± 0.1	-191.5	-2.2

^aIdentified by FODITS.

Figure 6.3b shows the result of the analysis for the satellite SVN 34, which was active for the entire interval 1994-2008. 14 repositioning events were identified, each with a discontinuity of about 2 km, about one every 14 months (about 420 days). The list of the 14 identified repositioning events is given in Table 6.1. For each identified repositioning event the table lists the epoch, the size of the discontinuity, and the approximated instantaneous

velocity change according to Eq. (6.7). As a result, we found that the pulses derived by the two independent methods, i.e., by **FODITS** and by the identification at **CODE**, are in good agreement. This result confirms the finding illustrated in Fig. 6.6b.

FODITS Detection The ground truth is used to assess the sensitivity of the algorithm implemented in **FODITS** by detecting discontinuities associated with repositioning maneuvers in the evolutions of the semi-major axes. The assessment is carried out for four strategies.

Obviously, for all strategies discontinuities were identified. In addition, the first strategy proposed changes in drift and 10 periodic functions with periods between 340 and 390 days. The overall level of significance was set to $U_t = 0.001$. The minimum size accepted for a discontinuity was for this strategy 100 m. The minimum interval length between successive drift changes was $\Delta t_v = 1.0$ year. A change in drift was proposed for each discontinuity in the functional model. The second and the third strategies had the same settings of the first strategy, but the minimum size accepted for a discontinuity were 200 m and 500 m, respectively. The fourth strategy was the same as the second strategy, but no periodic functions were proposed, and the minimum interval length between successive drift changes was $\Delta t_v = 0.2$ years. Hence, the minimum size accepted for a discontinuity was 200 m.

The comparison between the epochs identified by the analysis and those of the ground truth had to accept tolerances. For each strategy the comparison was repeated for tolerances of ± 0.5 , ± 1.0 , ± 1.5 , ± 2.0 , and ± 2.5 days. For each strategy and each tolerance we computed the sensitivity and the specificity of the detection, as proposed by (King and Williams, 2011). If all discontinuities were correctly identified w.r.t. the ground truth the sensitivity (TPR) is equal one and the specificity (FPR) is equal zero. More information on sensitivity and specificity are given in Section 3.9.

The results of the **FODITS** detection for all strategies are given by Table 6.2. The table indicates that for all strategies the results obtained with tolerances of ± 2.0 and ± 2.5 days were the same. Moreover, for all strategies the number of identified discontinuities in agreement with the ground truth with tolerances of ± 0.5 , ± 1.0 , and ± 1.5 days are smaller than with tolerances of ± 2.0 and ± 2.5 days. This indicates that the comparisons must be made with a tolerance of ± 2.0 days between the analysis results and the ground truth.

The results of the **FODITS** detection are given in a TPR versus FPR representation (TFR) and by histograms of the frequency of instantaneous pulses (see Fig. 6.7). In the TFRs each point gives the number of equivalent analysis results (each analysis of the evolution of the semi-major axis gives one analysis result, i.e., maximum number of equivalent results equals maximum number of **SVNs**). The tolerance assumed for both, TFRs and histograms, was of ± 2.0 days.

First, Fig. 6.7 tells that most discontinuities were identified by all four strategies, i.e., most **SVN** analyses provided TPR equal one and FPR equal zero. Only for few time series **FODITS** did not correctly identified the maneuvers.

Let us compare the first three strategies. These strategies have the same settings, but different minimum size accepted for a discontinuity (100 m, 200 m, and 500 m, respectively).

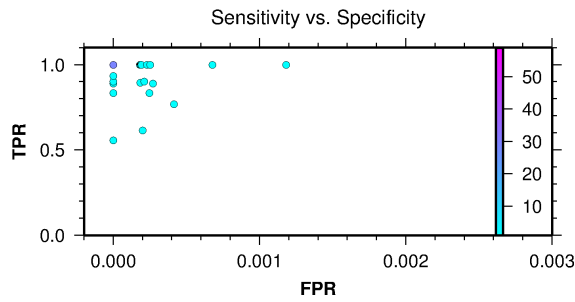
Table 6.2: Results of **FODITS** detections of repositioning events.

Strategy	\pm tolerance detection [day]	Minimum size [m]	Repositioning events					
			Total ^a	TP	FN	FP	TPN	FPR
Strategy 1 versus ground truth	± 0.5	100	451	116	335	44	0.364	0.000429
	± 1.0	100	451	334	117	37	0.777	0.000322
	± 1.5	100	451	385	66	26	0.880	0.000218
	± 2.0	100	451	419	32	17	0.935	0.000148
	± 2.5	100	451	419	32	17	0.935	0.000148
Strategy 2 versus ground truth	± 0.5	100	451	116	335	44	0.364	0.000429
	± 1.0	100	451	334	117	36	0.777	0.000317
	± 1.5	100	451	385	66	25	0.880	0.000213
	± 2.0	100	451	419	32	14	0.935	0.000134
	± 2.5	100	451	419	32	14	0.935	0.000134
Strategy 3 versus ground truth	± 0.5	100	451	114	337	43	0.362	0.000426
	± 1.0	100	451	266	185	35	0.683	0.000314
	± 1.5	100	451	306	145	23	0.771	0.000205
	± 2.0	100	451	329	122	13	0.811	0.000130
	± 2.5	100	451	329	122	13	0.811	0.000130
Strategy 4 ground truth	± 0.5	100	451	116	335	44	0.364	0.000429
	± 1.0	100	451	332	119	36	0.770	0.000317
	± 1.5	100	451	383	68	24	0.873	0.000209
	± 2.0	100	451	416	35	8	0.926	0.000105
	± 2.5	100	451	416	35	8	0.926	0.000105

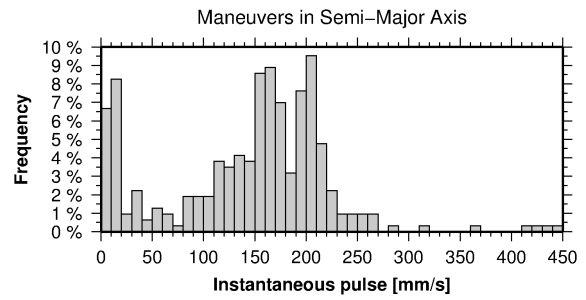
^aTotal number of discontinuities known in the ground truth.

From the TFRs we notice that the larger is the minimum acceptable size, the fewer is the number of wrongly identified discontinuities. The three TFRs tell furthermore that the number of correctly identified discontinuities increases by diminishing the minimum size accepted for a discontinuity. The three histograms associated with the first three strategy results give more details on the mechanism behind these three results. For the smallest minimum size accepted (100 m) (see Fig. 6.7b) we see the two known groups of maneuvers with velocity changes around 150 mm/sec and 200 mm/sec, and the group of maneuvers with pulses smaller than 50 mm/sec. By comparing the latter group to the same group of small pulses in Fig. 6.6d, we understand that **FODITS** detected small discontinuities to help to the optimally represent the semi-major axes' evolutions. The larger the minimum acceptable size, the smaller the group of maneuvers with pulses smaller than 50 mm/sec, but also the smaller the number of correctly identified discontinuities. The second strategy gave therefore the best results, see Fig. 6.7c.

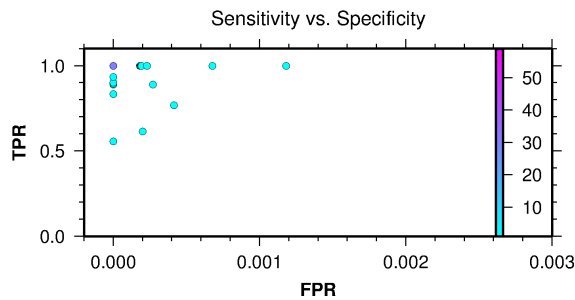
By the fourth strategy **FODITS** introduced changes in drifts with $\Delta t_v = 0.2$ years. By comparing the TFR of the second strategy (see Fig. 6.7c) and the fourth strategy (see Fig. 6.7g), we notice that the latter strategy detected slightly less events but also had less detection errors than the former strategy. Analyses with the proposed periodic functions give therefore more wrongly identified discontinuities. The reason is known (from the above analyses): shifts in phase of the 352 days' signal force the algorithm to add discontinuities.



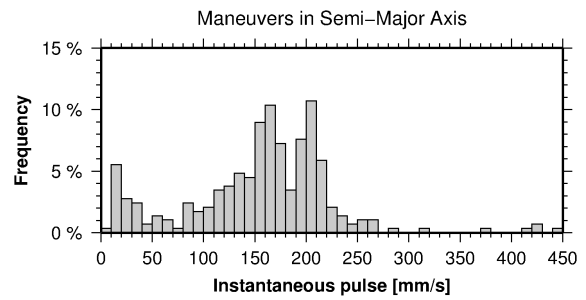
(a) Strategy 1, TPR versus FPR.



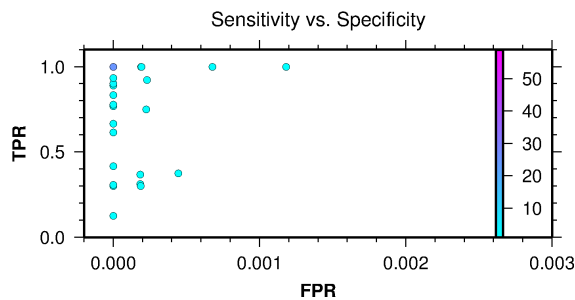
(b) Strategy 1, histogram.



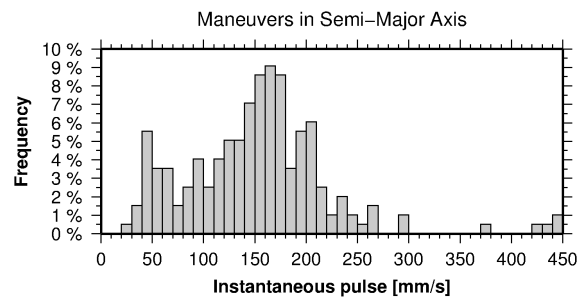
(c) Strategy 2, TPR versus FPR.



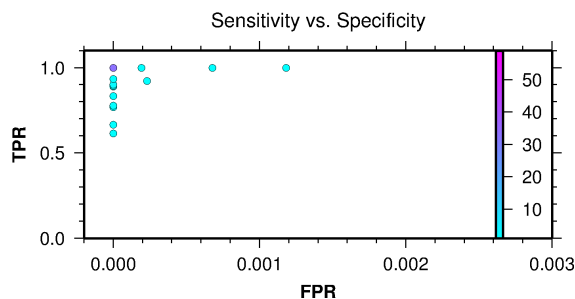
(d) Strategy 2, histogram.



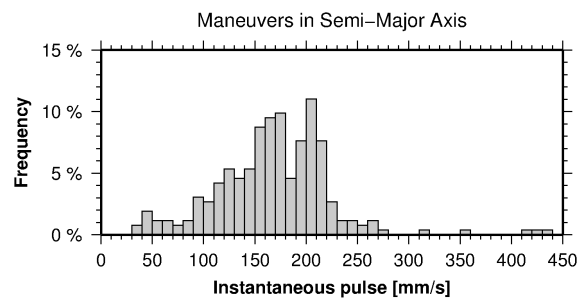
(e) Strategy 3, TPR versus FPR.



(f) Strategy 3, histogram.



(g) Strategy 4, TPR versus FPR.



(h) Strategy 4, histogram.

Figure 6.7: Results of the FODITS detection of GPS maneuvers in the evolution of the mean semi-major axis. (Color-coded) are the number of SVNs with same results.

Table 6.2 points out that none of the four strategies obtained a 100% correct detection of maneuvers. The second and the fourth strategies successfully identified 92.9% (419 of 451) and 92.3% (416 of 451) discontinuities, respectively. From the above investigations we know that few maneuvers were not significant and, moreover, other maneuvers were carried out with few days spacing. These aspects indicate that the obtained percentages of detection success are rather pessimistic. For the two strategies the percentage of wrongly identified discontinuities were 3.1% (14 of 451) and 1.8% (8 of 451). The fourth strategy collected therefore the best results.

6.2.2 Analysis of the Mean Eccentricity

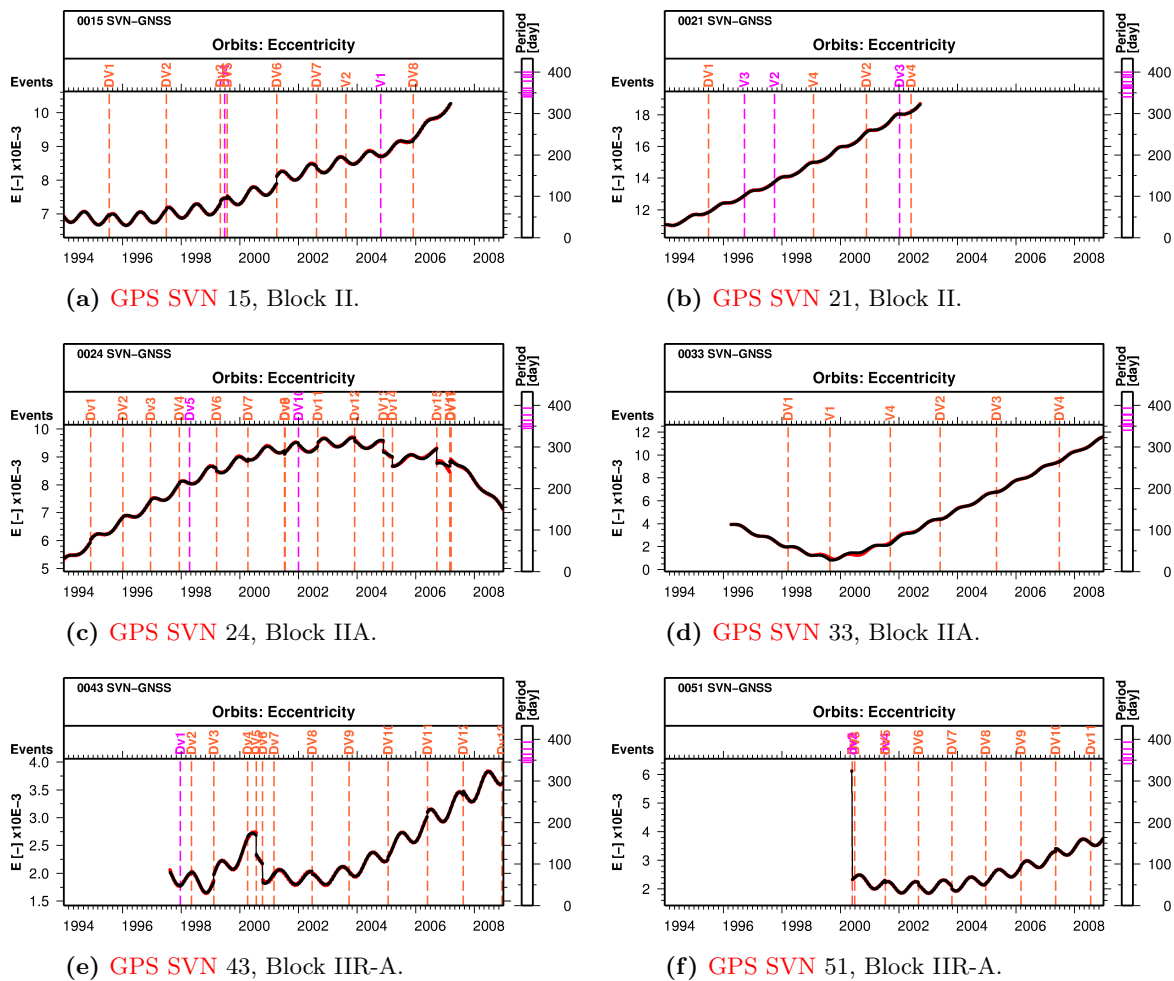


Figure 6.8: Evolution of the mean eccentricity of GPS satellites. The maneuvers identified in the analysis of the semi-major axis were introduced as known discontinuities.

Satellite maneuvers are meant to change the semi-major axis a . This can only be achieved by giving the satellite a pulse $T \cdot \Delta t$ in the tangential direction e_t (see (Beutler, 2005), Vol 1,

Eq. (6.91)₁). A pulse $T \cdot \Delta t$ cannot affect the orbital plane, i.e., the elements i and Ω (see (Beutler, 2005), Vol 1, Eq. (6.91)). The elements e , ω , and T_0 may be affected by a pulse in the direction e_t . The actual change does, however, highly depend on the true anomaly v (see (Beutler, 2005), Vol 1, Eq. (6.91)). It is in principle possible to perform the maneuver at a time, where one or two elements e , ω , T_0 are not affected by $T \cdot \Delta t$. If, e.g., the element e shall remain unaffected, one has to perform the thrust at a time t , where $\cos v = -e$, i.e., $v = \arccos(-e)$. This implies that the thrust would have to take place close to the semilatus rectum (i.e., for $v = \pm 90^\circ$). If the thrust $T \cdot \Delta t$ is performed at $v = 0$ (perigee) or $v = 180^\circ$ (apogee) the elements T_0 and ω are not affected by a thrust $T \cdot \Delta t$, but the eccentricity e would suffer a maximum change. From (Beutler, 2005), Vol 1, Eq. (6.91)₂ we know that

$$\Delta e = \frac{2}{V_0} (\cos(v) + e) \Delta V . \quad (6.8)$$

For a $\Delta a = 20$ km, i.e., $\Delta V = 1.46$ m/sec (see Eq. (6.7)), the maximum change in eccentricity reaches 0.00037. For a $\Delta V = 200$ mm/sec, the average instantaneous pulse associated with repositioning maneuvers of GPS satellites to keep them in their assigned slots, the corresponding maximum change in eccentricity is 0.000051.

FODITS was used to analyze the evolution of the eccentricity by providing the ground truth (i.e., the epochs of the discontinuities) as known. The settings were the following: The overall level of significance was set to $U_t = 0.0001$. Changes in drift were identified and, after each discontinuity, the procedure proposed a new change in drift. The minimum interval length between successive drift changes was $\Delta t_v = 1.0$ year. For each series 10 periodic functions were proposed between 340 and 400 days.

Figure 6.8 illustrates the evolution of the mean eccentricity for the same SVNs of Fig. 6.2. In all results the algorithm introduced periodic functions to optimally represent the time series. The discontinuities added from the ground truth are typically small. By confronting Figs 6.8 and 6.2 we notice however that the visible discontinuities in the evolutions of the mean eccentricity are associated with the large maneuvers visible in the evolutions of the semi-major axis. The largest discontinuity was found in the evolution of the mean eccentricity of SVN 51. From the analysis of the mean semi-major axis we known that the maneuver was carried out to position the satellite in its slot.

Figure 6.9 shows the histograms of the discontinuities identified in the analysis of the mean eccentricity of all SVNs. The largest number of discontinuities had values smaller than 0.00015. According to Eq. (6.8), by assuming $\cos v = 1$ ($v = 0^\circ$), a discontinuity of 0.00015 in the eccentricity evolution corresponds to a discontinuity of 3.98 km (or 291 mm/s). From Section 6.2.1 we know that the repositioning events to keep the satellites in the assigned slot are carried out by pulses between 150 mm and 200 mm, thus comparable to when maneuvers are carried out with $v = 0^\circ$. This concludes that these typical maneuvers of GPS satellites are not executed by requiring a minimum change in the eccentricity.

Beutler (2005) predicts that the evolution of the eccentricity of GPS satellites increases with time due to the resonance perturbations. Figure 6.10a illustrates the mean numerical eccentricity evolution of the GPS satellites between 1994 and 2008 as a function of their lifetime as obtained from the analysis. Generally, we observe an ascending trend. A better

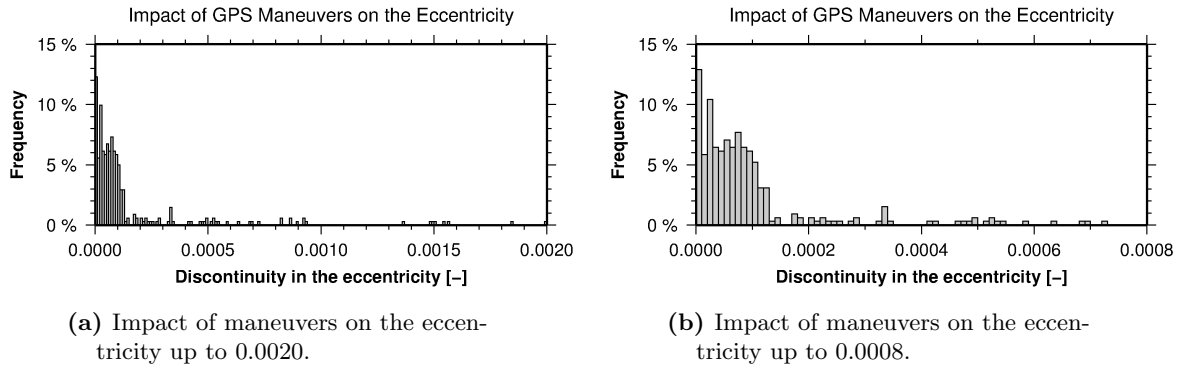


Figure 6.9: Mean numerical eccentricity evolution of GPS satellites between 1994 and 2008.

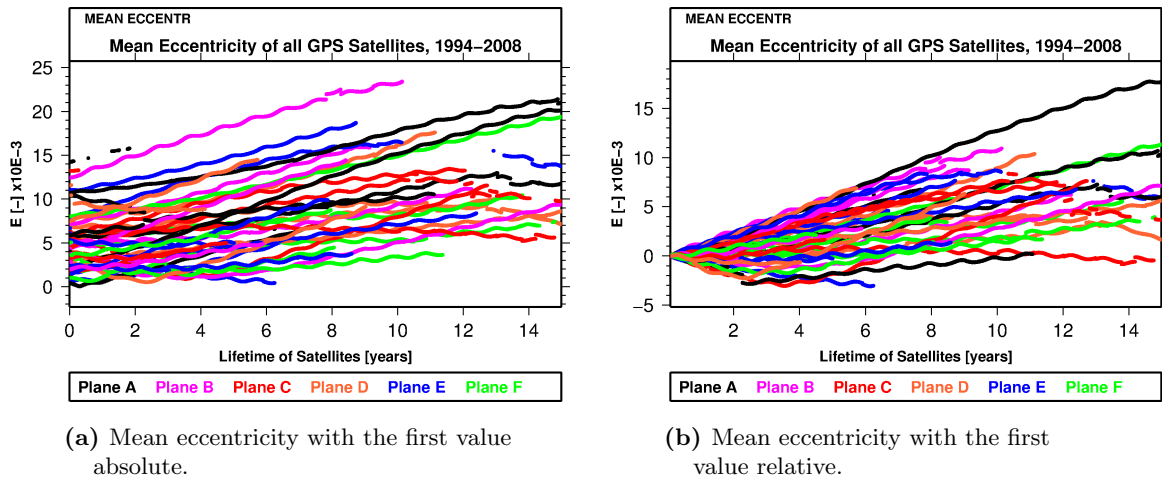


Figure 6.10: Mean numerical eccentricity evolution of GPS satellites between 1994 and 2008.

view is given by Fig. 6.10b, where all eccentricity evolutions were reset after 30 days of their lifetime—the interval in which the eccentricity evolution have discontinuities due to the improvements associated with the initial orbit determination. The general ascending trend is clear. The maximum increase rate of the eccentricity is about 0.001/yr. Figure 6.10b tells moreover that there is no evidence of plane-specific ascending trends.

6.2.3 Analysis of the Mean Ascending Node and Inclination

The development of the mean right ascension of the ascending node is dominated by the almost linear regression of the node. This effect is mainly due to the oblateness of the Earth. Assuming a value of $C_{20} \approx 1.082 \cdot 10^3$, Beutler (2005) obtains:

$$\dot{\Omega} \approx -\frac{10.0^\circ \cos(i)}{(a/R)^{3.5} \cdot (1 - e^2)^2} = -0.0388^\circ/\text{day} , \quad (6.9)$$

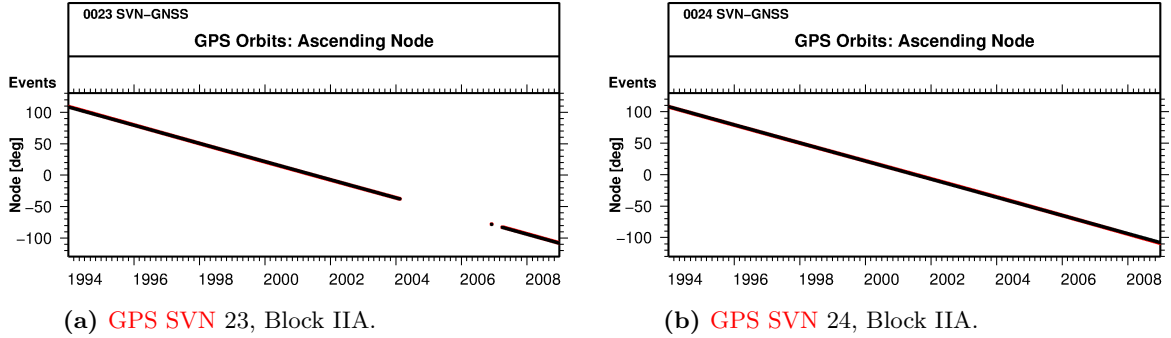


Figure 6.11: Analysis of the mean right ascension of the ascending node Ω of GPS satellites. (Red) time series. (Black) functional model.

where R is the equatorial radius of the Earth. Moreover, the numerical value was obtained by assuming $a = 26,560$ km, $i = 55^\circ$, and $e = 0.001$ (see Table 2.2).

From Figs. 6.11a and 6.11b we obtain values of $\dot{\Omega} = -0.039567 \pm 0.000002^\circ/\text{day}$ and $\dot{\Omega} = -0.039488 \pm 0.000002^\circ/\text{day}$ for SVNs 23 and 24, respectively. These values are slightly larger (in absolute value) than the value in Eq. (6.9). This is not surprising, because the terms $C_{2i,0}$, $i = 2, 3, 4, \dots$ and the luni-solar perturbations generate a regression of the node, as well.

Once the regression rate of the ascending node $\dot{\Omega}$ is known, we may compute the so-called draconitic year, i.e., the time period T_{drac} it takes the Sun to assume the same position w.r.t. the orbital plane. Assuming that the Sun moves in the equatorial plane, T_{drac} follows from the equation

$$T_{drac} = 365.25 \cdot \left(1 - \dot{\Omega} \cdot \frac{365.25}{360} \right)^{-1}. \quad (6.10)$$

For a typical GPS satellite, i.e., by applying Eq. (6.9) in Eq. (6.10), $T_{drac} = 351.43$ years (see also Table 2.2). For the entire GPS constellation, as obtained as average from the analysis with in total 49 SVNs, this period is $T_{drac} = 351.08 \pm 0.01$ years. The difference between the approximated and the mean T_{drac} values is likely due to the forces not considered in the approximation (e.g., perturbations of Moon and Sun).

The annual regression of the GPS constellation, as emerging from our analysis, is $\dot{\Omega} = -14.53 \pm 0.80^\circ/\text{yr}$. The constellation thus needs 24.78 years to carry out one entire revolution in the inertial system.

Figure 6.12a illustrates the evolution of the inclinations of all SVNs obtained from the CODE processing. Satellites in the same orbital plane have the same color (see legend). The colors highlight that satellites in the same orbital plane have approximately the same long-period evolution. The inclinations of satellites in adjacent orbital planes are shifted by about $+60^\circ$. This has to be expected because of the arrangement of the six orbital planes in the equator.

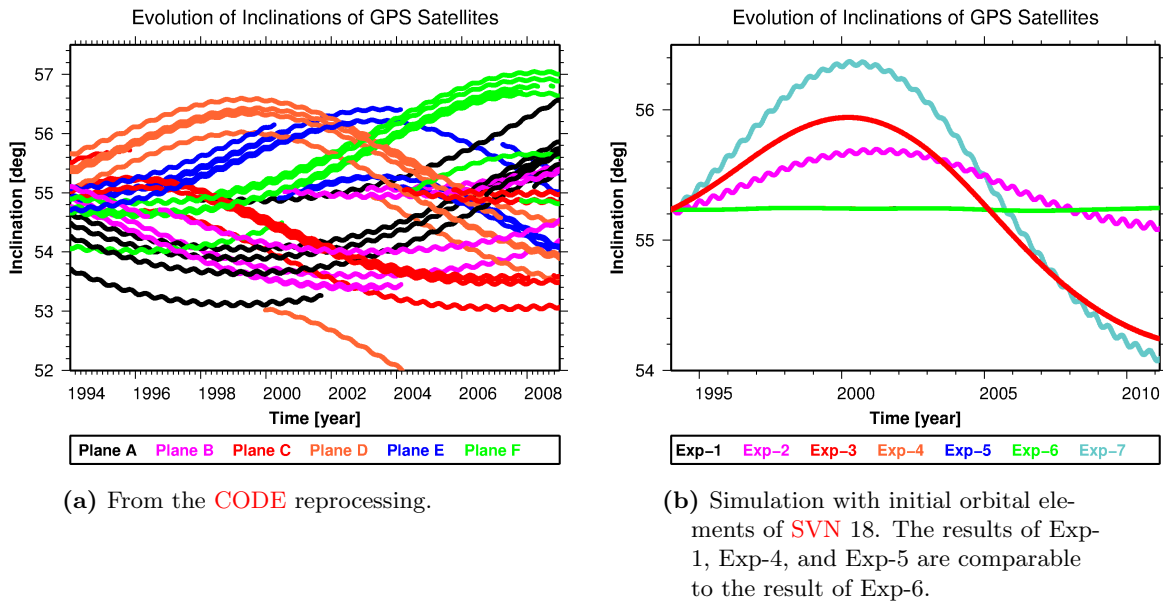


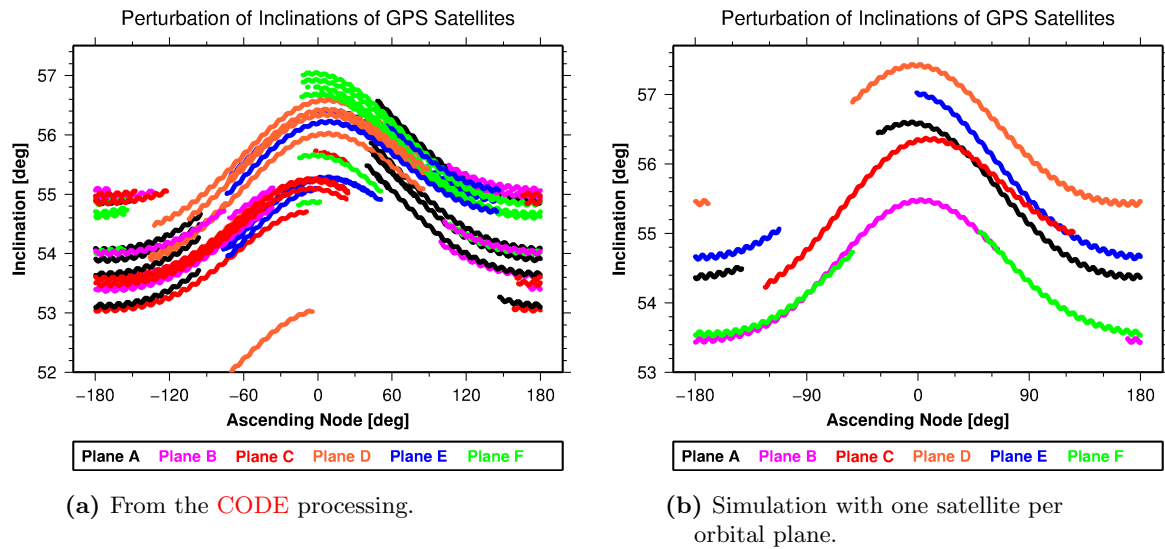
Figure 6.12: Evolution of the inclination of GPS satellites. In Fig. (6.12b) the result of Exp-1, Exp-4, and Exp-5 are comparable to that of Exp-6.

Figure 6.12b documents the results of seven experiments (Exp-1 to Exp-7) to understand short- and long-period perturbations of the inclination evolutions in Fig. 6.12a. All experiments were based on numerically integrating the orbit of SVN 18 with the initial state vector corresponding to January 2, 1994, see Table 6.3. For all experiments the Earth potential JGM3 (Tapley et al., 1996) was used up to degree and order 12. Exp-1 was carried out without additional accelerations, Exp-2 by accounting for the attraction of the Sun, Exp-3 by accounting for the attraction of the Moon, Exp-4 by accounting for the attraction of ocean tides using the model CSR3.0 (Eanes and Bettadpur, 1996), Exp-5 by accounting for the correction due to General Relativity, Exp-6 by accounting for a simple model for the direct radiation pressure, and Exp-7 by accounting for all mentioned forces (similar as the CODE solution). As the figure shows it, the two major contributions are due to the Sun (Exp-2) and the Moon (Exp-3), while all other contributions are in comparison negligible. The gravitational perturbation of the Sun is responsible for the perturbation with the period of half GPS draconitic year, i.e., about 175.7 days, also visible in the inclination evolution of all SVNs in Fig. 6.12a.

Figure 6.13a shows the inclination as a function of the right ascension of the ascending node for all GPS satellites. The figure shows that the dominating perturbation of the inclination equals one revolution of the constellation in the inertial system, i.e., of about 25 years. The osculating elements of one GPS satellite per orbital plane (see Table 6.3) given on 2 January, 1994, were used for the simulation of the inclination as a function of the ascending node. Figure 6.13b shows the result. The result of the numerical integration is comparable to the one obtained from the CODE processing shown in Fig. 6.13a.

Table 6.3: Osculating elements adopted for the simulations. Reference epoch 2 January, 1994.

	PRN	SVN	a [km]	e	i°	Ω°	ω°	μ°
Exp 1-7	18	2	26,558.4257	0.004471	55.2360	0.7575	-168.9217	285.5909
Plane A	9	39	26,561.0979	0.015140	54.4898	116.2226	-301.8950	223.1749
Plane B	2	13	26,560.9740	0.012441	54.7676	-36.7257	-154.5044	327.8517
Plane C	31	31	26,561.0911	0.004456	55.0133	24.3738	33.8150	0.3370
Plane D	17	17	26,559.4209	0.007312	55.4243	88.9962	104.5647	57.3769
Plane E	14	14	26,560.3447	0.003547	55.0634	146.3926	-188.9418	214.5176
Plane F	1	32	26,558.7548	0.003468	54.7316	-154.2636	-63.1851	259.7851

**Figure 6.13:** Inclination versus right ascension of ascending node of **GPS** satellites.

6.3 Evolution of Mean Elements of GLONASS Satellites

Since June 8, 2003, **CODE** simultaneously processes data from both, **GPS** and **GLONASS**³ satellites in a rigorous combined **GNSS** analysis. The number of active **GLONASS** satellites between 2003 and 2008 increased from 10 to 16 (**Dach et al., 2009**). On 24 December, 2011, the number is 24, see Table 2.2.

GLONASS satellites are characterized by a slot number and **SVNs** like **GPS** satellites, see Table A.2. Figure 6.14 illustrates the evolution of the elements for **SVN 791**. Eclipsing phases are marked by gray vertical lines. For a **GLONASS** satellite the maximum length of an eclipse phase is about 53 minutes (**Dilssner et al., 2011**), 3 minutes shorter than for a **GPS** satellite—due to a slightly smaller semi-major axis causing a larger mean motion (see Table 2.2).

From Sect. 2.2.1 we know that **GLONASS** orbits are commensurable with a ratio of 17:8 with the Earth’s rotation. As such orbits are far from the deep 2:1 resonance of the **GPS**

³[IGSMail-4371]: **IGS GLONASS** tracking data.

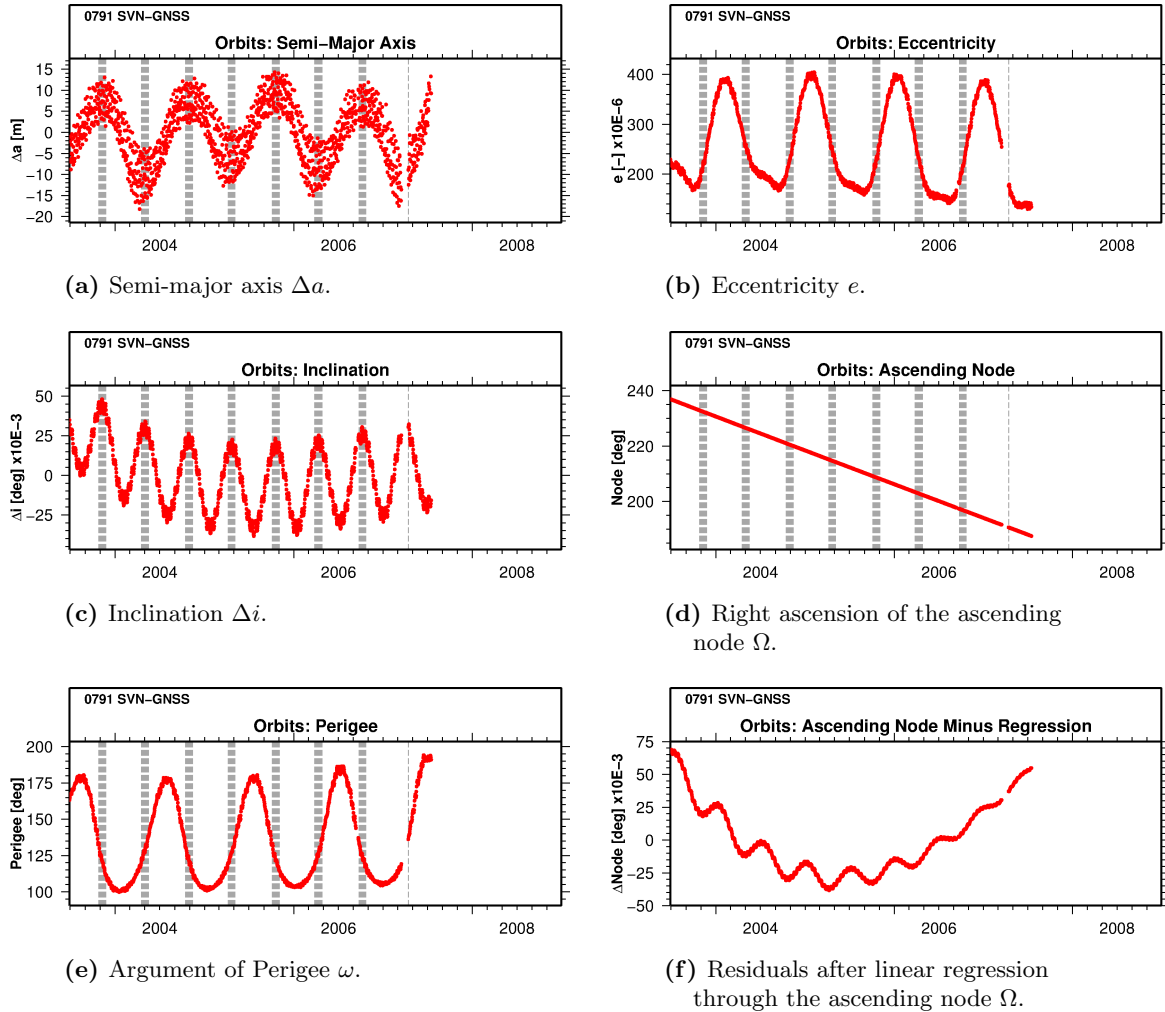


Figure 6.14: Evolution of mean elements of the **GLONASS SVN** 791, plane 3, **PRN** 122 from 25-Dec-2002 to 25-Oct-2007. Daily eclipsing phases are shown by the gray dashed vertical lines.

orbits, satellites of the **GLONASS** constellation do not need to be regularly repositioned. Figure 6.14a shows an example. The same figure also shows that the perturbation has the period of one **GLONASS** draconitic year, i.e., nominally of 353.37 days (see Table 2.2). From the analysis in Sect. 6.2.3 we know that the perturbation is due to the gravitational attraction by the Sun. The amplitude of the perturbation is about 10 m, therefore clearly smaller than the km-size amplitudes of the **GPS** satellites (Hugentobler, 1997). The 10 m scattering of the semi-major axis is due to the fact that osculating elements are extrapolated only down to 1 second (see Sect. 6.1). The same scattering is present in Fig. 6.2a, too, however not visible due to the repositioning events of **GPS** satellites.

Similarly as for **GPS**, the perturbation of one **GLONASS** draconitic year is present in the semi-major axis, in the eccentricity, and in the argument of Perigee. The inclination

evolution is perturbed by a period of half draconitic year.

6.3.1 Analysis of the Mean Semi-Major Axes

The **FODITS** analysis for the evolution of the semi-major axis of **GLONASS** satellites had the following settings. The overall level of significance was set to $U_t = 0.005$. Changes in drift were identified and, after each discontinuity, the procedure proposed a new change in drift. The minimum size accepted for a discontinuity (i.e., repositioning event) was 8 m. The minimum interval length between successive drift changes was $\Delta t_v = 1.0$ year. For each series 10 periodic functions were sought between 340 and 390 days.

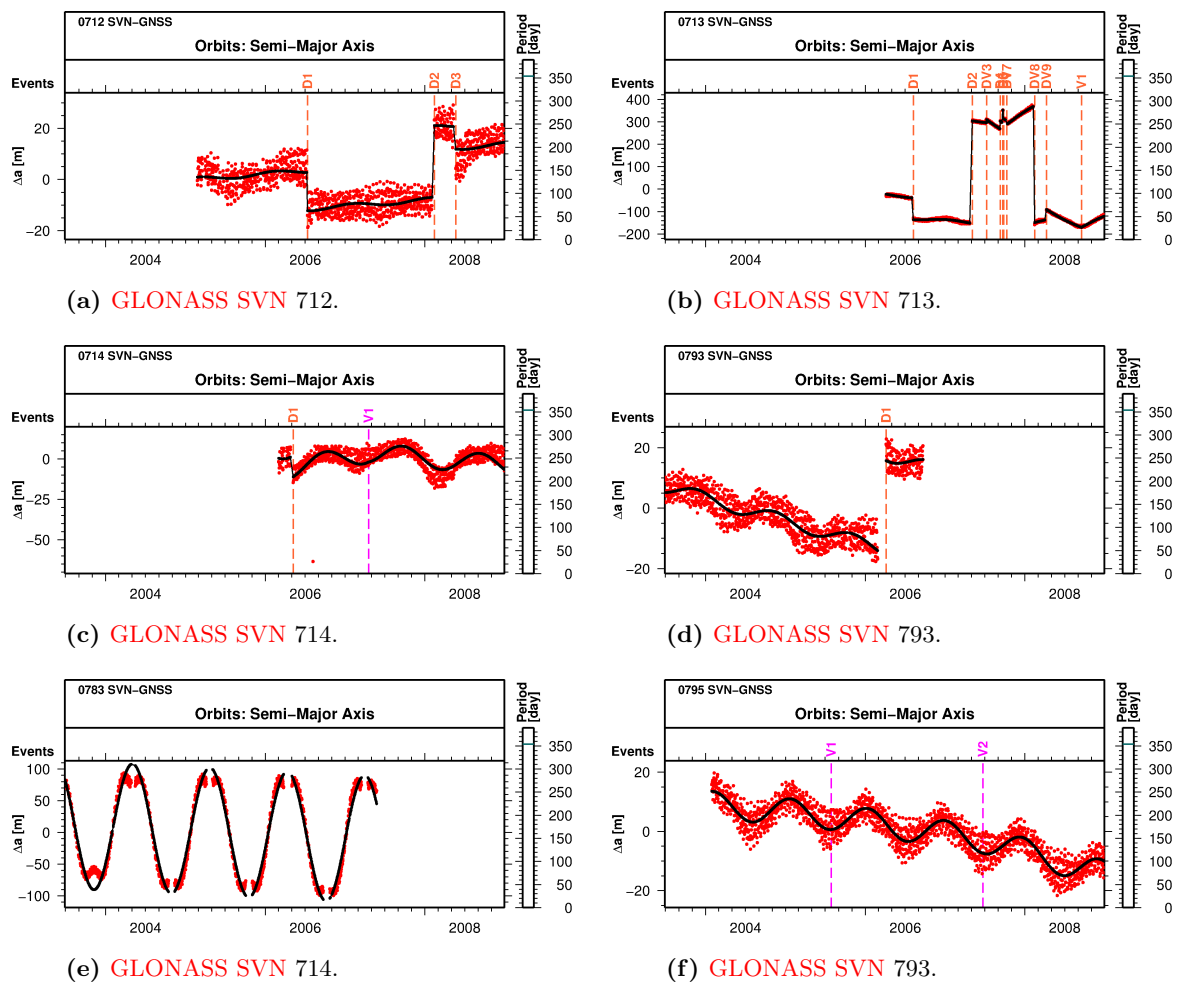


Figure 6.15: FODITS analyses of the semi-major axis evolution of **GLONASS** satellites. (D) identified maneuver. (V) change in drift. (Red) time series. (Black) functional model. The periodic function of 354 days was proposed to facilitate the analysis.

Figure 6.15 documents the results of six series of the evolution of the **GLONASS** semi-major axes. The automated analysis could not identify all maneuvers (e.g., see Fig. 6.15b).

Therefore, for **SVN** 712 and **SVN** 713 the analysis was supported by an **EVL** file, see Section 3.2.5. For **SVN** 712, **SVN** 714, and **SVN** 793, the identified discontinuities are smaller than 50 m. The discontinuity of 31.5 m estimated for the **SVN** 793 on 28 February, 2006, is associated with a change from slot 123 to slot 120⁴. For **SVN** 713 the discontinuities have sizes of up to about 550 m. For a **GLONASS** satellite a discontinuity of 100 m corresponds to an instantaneous velocity change of about 7.75 mm/sec, see Eq. (6.7). The largest maneuver registered (-520.26 ± 1.37 m for **SVN** 713 on 14 February, 2008) was performed by an instantaneous velocity change of 42.61 ± 0.10 mm/sec. From two IGSMAIL⁵⁶ it is known that **SVN** 712 accomplished other repositioning events after 2009, first of which with an instantaneous velocity change of -26.8 mm/sec in the along-track direction (and following ones of about the same amount). It is known that **SVN** 714 has a slightly different behavior than other **GLONASS** satellites (e.g., Dach et al., 2011). Its evolution of the semi-major axis shows a 354 days' variation with amplitude of ± 100 m. Moreover, Fig. 6.15e shows that at the minima and maxima of such variation the **SVN** 714 was regularly excluded from the data processing. Last, Fig. 6.15f shows a secular lowering of the semi-major axis of **SVN** 793.

6.3.2 Analysis of the Mean Eccentricity

The analysis of the evolution of the mean eccentricity was carried out with the following settings. The overall level of significance was set to $U_t = 0.001$. Changes in drift were identified and, after each discontinuity, the procedure proposed a new change in drift. The minimum interval length between successive drift changes was $\Delta t_v = 0.2$ year. For each series 20 periodic functions were proposed between 340 and 390 days.

Figure 6.16 illustrates the evolution of the mean eccentricity for the same **SVNs** of Fig. 6.15. Let us begin by the analysis of satellite **SVN** 712, see Fig. 6.16a. In order to model the variation of the amplitude of the 354 days' signal the algorithm added 6 periodic functions to the functional model. The largest discontinuity identified (DV2) was 0.000044. A similar evolution of the mean eccentricity is obtained from the analysis of satellite **SVN** 713, see Fig. 6.16b. Fig. 6.16c, on the other hand, shows a signal of one order of magnitude smaller in amplitude than the same signal of other **GLONASS** satellites. By looking at Fig. 6.16a one notices a similar signal superimposed. We conclude therefore that a similar signal is present in all evolutions of the mean eccentricity. The largest identified discontinuity (0.00072) was found in the series of **SVN** 793, see Fig. 6.16d. From the above analysis of the semi-major axis we know that **SVN** 793 had a slot change. Similar changes in the mean eccentricity of **GPS** satellites were associated with changes in the semi-major axis of 40 km if carried out for $v = 0^\circ$. The last two examples, see Figs. 6.16e and 6.16f, show a secular variation.

Figure 6.17 shows the evolution of the mean eccentricity of all **GLONASS** satellites. Compared to the **GPS** satellites, which have an increase of the mean eccentricity of about

⁴See <ftp://ftp.unibe.ch/aiub/BSWUSER50/GEN/SATELLIT>.

⁵[IGSMail-6415] GLONASS DV event with respect to R07/712.

⁶[IGSMail-6416] Re: GLONASS DV event with respect to R07/712.

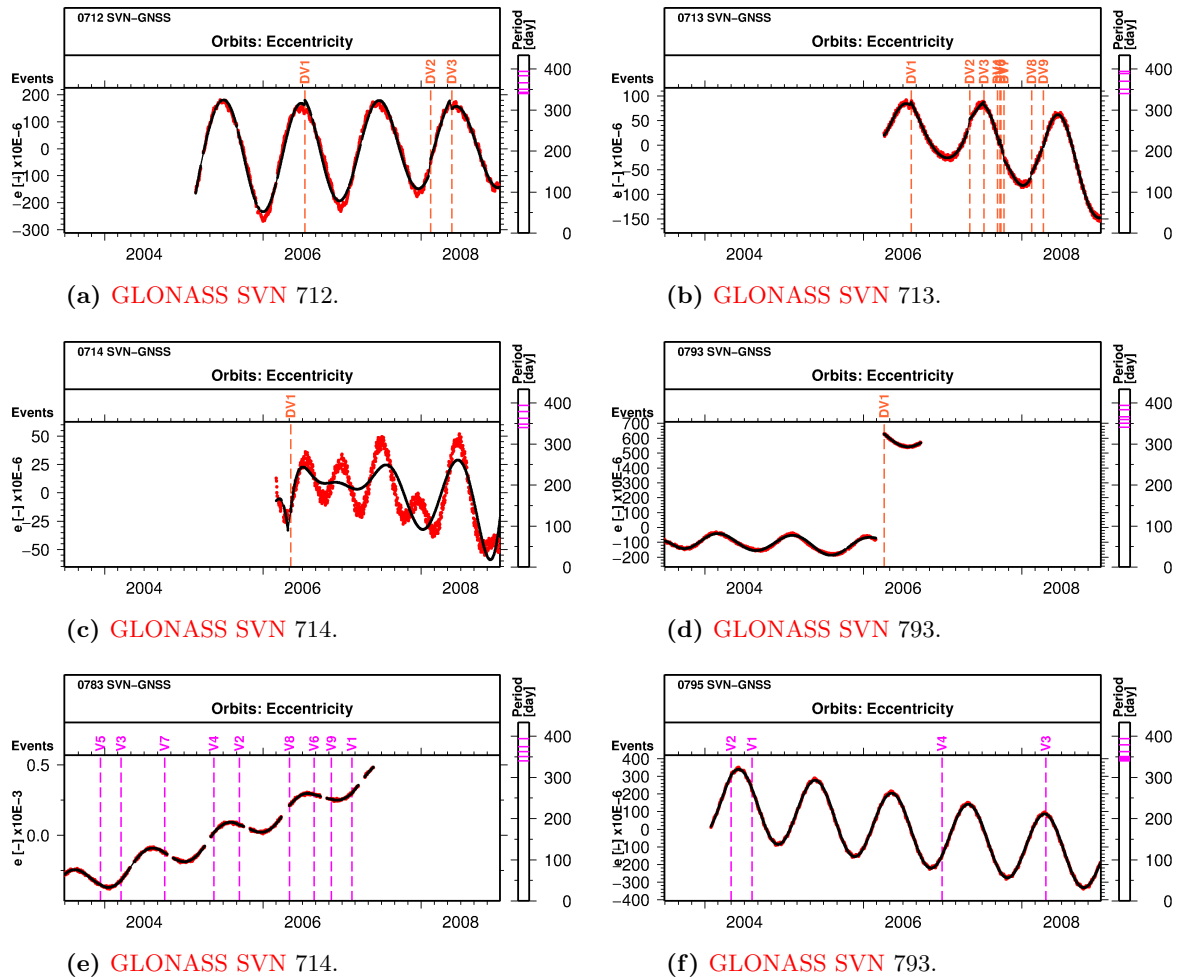


Figure 6.16: Evolution of the mean eccentricity of **GLONASS** satellites. The maneuvers identified in the analysis of the semi-major axis were introduced as known discontinuities.

0.001/yr, **GLONASS** satellites have a decrease of about 0.00005/yr. **GLONASS** satellites are indeed not in a deep 2:1 resonance as the **GPS** satellites. No evidence of plane-specific behavior can be seen.

6.3.3 Analysis of the Mean Ascending Node and Inclination

The nominal daily regression of the right ascension of the ascending node $\dot{\Omega}$ derived from the approximation with the only oblateness perturbation (6.9) is for a typical **GLONASS** satellite of $-0.033150^\circ/\text{day}$. According to Eq. (6.10) this value gives a nominal draconitic year of 353.37 days, also see Table 2.2.

As for **GPS** satellites, the draconitic year of **GLONASS** satellites can be derived from the secular regression of the right ascension of the ascending node (see Sect. 6.2.3). Figure 6.18

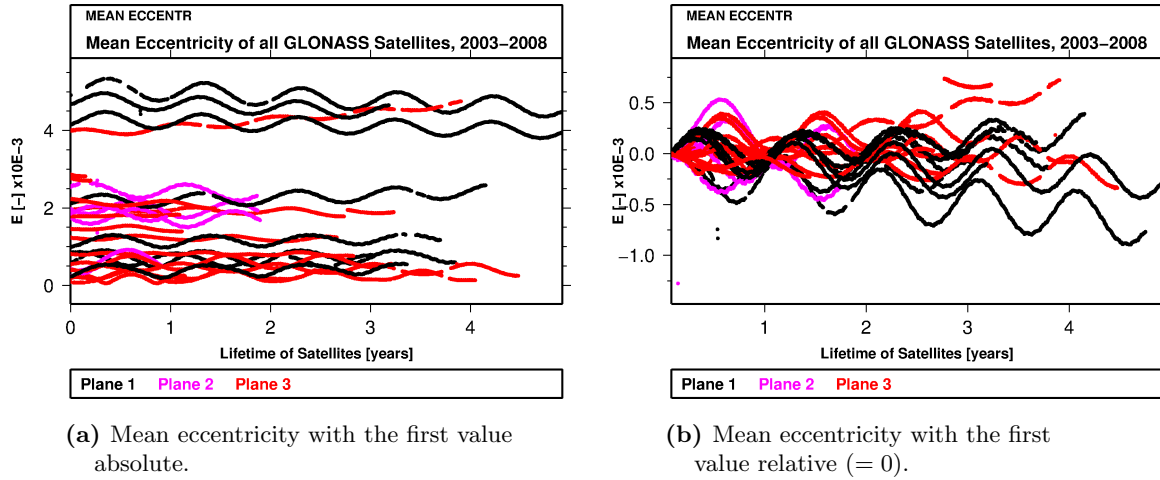


Figure 6.17: Mean numerical eccentricity evolution of **GLONASS** satellites between 2003 and 2008.

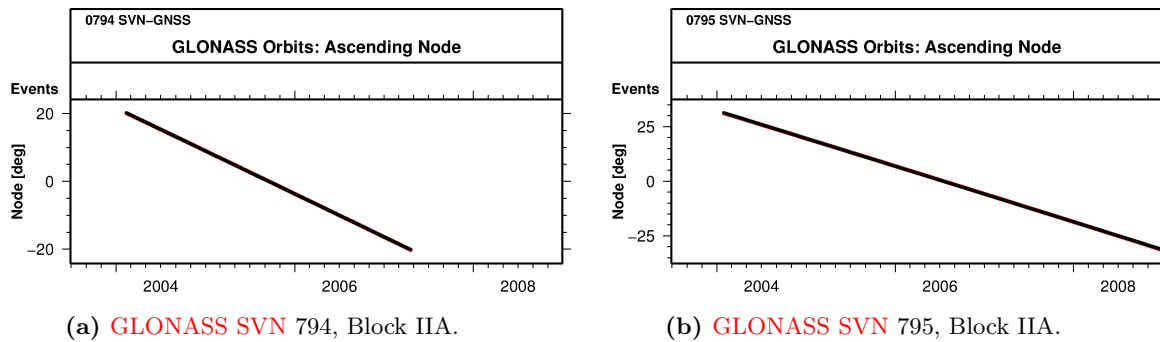


Figure 6.18: Analysis of the right mean ascension of the ascending node Ω of **GLONASS** satellites. (Red) time series. (Black) functional model.

documents the **FODITS** analysis for two **SVNs**. For **SVN** 794 we obtain $\dot{\Omega} = -0.034702 \pm 0.002716^\circ/\text{day}$ (i.e., $T_{drac} = 352.83 \pm 0.93$ days) and for **SVN** 795 $\dot{\Omega} = -0.034874 \pm 0.003667^\circ/\text{day}$ (i.e., $T_{drac} = 352.77 \pm 1.27$ days). The averaged value from the 29 analyzed **SVN** series, on the other hand, gave for the **GLONASS** constellation a daily rate of the right ascension of the ascending node $\dot{\Omega} = -0.033963 \pm 0.000772^\circ/\text{day}$, which corresponds to a draconic year of $T_{drac} = 353.09 \pm 0.02$ days. To accomplish one revolution in inertial system the **GLONASS** constellation takes therefore about 29 years.

One might expect that $\dot{\Omega}$ is larger for **GLONASS** than for **GPS**, because **GLONASS** satellites are flying at a lower altitude. The small value is however caused by the higher inclination.

7 Summary and Outlook

This work had the focus on the analysis of GNSS-derived station coordinate time series. The algorithm developed for the analysis, now embedded in the program **Find Outliers and Discontinuities in Time Series (FODITS)** of the **Bernese Software (BSW)**, tries to optimally represent the time series by a functional model including discontinuities, velocity changes, outliers, and periodic functions. The analysis always starts by fitting the functional model which describes a polynomial of first degree through the time series. Successively, known earthquakes, equipment changes, periodic functions, and other predefined elements are checked for significance. Significant elements are added to the functional model starting with the largest and ending with the smallest. When no more known elements give significant contributions, the algorithm begins to search for candidate elements, which remove the largest discrepancy between the functional model and the time series. The most probable candidate is eventually added to the functional model, provided it is significant, and the procedure begins again. The iterative procedure stops when no additional elements are found.

The algorithm implemented in **FODITS** was derived from the **Detection Identification Adaptation (DIA)** procedure proposed by (Teunissen and Kleusberg, 1998b). From that procedure the algorithm **FODITS** took over in particular the iteration principle to add elements to the functional model (from the largest to the smallest) and the statistical test proposed in the identification step. In this work the latter statistical test could be reduced to an absolute value of the sum of residuals. Such simplification was made on one hand to render the search test for discontinuities less CPU-time intensive than the original test of the **DIA** procedure, and on the other hand to propose the epoch of the most probable discontinuity even in the case when the analyzed time series are provided without their **Variance-Covariance Information (VCI)**. Figure 7.1 shows the time series of the search test (in blue) after the first iteration step of the algorithm while analyzing the time series of the North component of station Ponta Delgada in Portugal (in red). First, we note that the search is robust against "outliers". This is due to the fact that the sum underlying the search is in principle an integral of the residuals in time. Second, the discontinuity could be found despite the fact that there was not a sharp jump. Such a characteristic is in particular important to identify small offsets in long time series. The search could be furthermore optimized to be efficient also in the presence of data gaps, not unusual case in time series of geophysical parameters.

The algorithm implemented in **FODITS** was validated internally and externally. Internal validations were carried out for the identification part in particular, using synthetic time series. An external validation was performed by the **Detection of Offsets in GPS Experiment (DOGEx)**, an international experiment to test automated procedures to analyze time series.

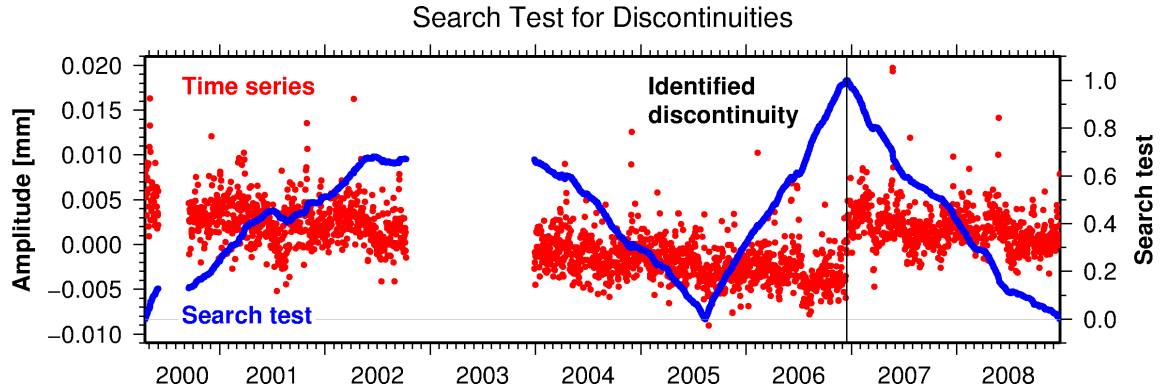


Figure 7.1: Search test for discontinuities in the North component of daily **CODE** coordinates of station Ponta Delgada, Portugal. Data gaps were added in the time series.

FODITS obtained good marks in this test (King and Williams, 2011).

The algorithm with the adopted search test for discontinuities aims at modifying the functional model until the resulting time series of residuals are normally distributed. No validation of the stochastic model is therefore yet carried out. Two different statistical tests were used: one for outliers and one for all other elements of the functional model. Such a distinction was made because outliers have a smaller impact on the functional model than the other elements. A unique statistical test for all elements was not found. Another improvement, in particular in view of CPU-time consumption, could be achieved by changing from the batch solution to the Kalman filter approach, as proposed by Salzmann (1993). For long time series the Kalman approach become more CPU-time effective than the least squares approach. The post-seismic relaxation phase after an earthquake cannot adequately represented in the functional model of **FODITS** so far. This remains as a task for the future improvement of the program.

The first goal of the analysis is to perform a quality assessment for station coordinate time series in cumulated multi-year solutions. The strategy is simple: the model of the coordinate time series in the cumulated solution is the functional model obtained in the analysis. The validation of the quality assessment was first carried out internally with 234 station coordinate time series of daily and weekly solutions obtained from the first **Center for Orbit Determination in Europe (CODE)** reprocessing efforts for the **International GNSS Service (IGS)**. The analysis took about 20 minutes for the daily series and 5 minutes for the weekly series. By comparing the multi-year solutions before and after quality assessment we obtained an improvement of the a posteriori **RMS** of unit weight from 3.47 mm to 1.30 mm for daily series and from 1.52 mm to 1.32 mm for weekly series. By comparing the number of identified events in the series before and after cleaning the coordinate time series, we observed a reduction of about 97% of the discontinuities and almost 100% of outliers for daily series, 92% of the discontinuities and 88% of the outliers for weekly series. Weekly coordinate time series showed a smaller **RMS** than daily series, but the weekly time series showed less clear signatures than the daily ones due to the reduction of data points by a factor of 7. The external validation was carried out by comparing the

discontinuities obtained from the analysis of weekly series to the known discontinuities in the **ITRF2008/IGS** solution (for the same time interval). The **FODITS** analysis found 354 discontinuities, the external solution **ITRF2008/IGS** had 256, and the number of common discontinuities was about 135 (with a window of tolerance of ± 11 days).

Ideally, the analysis of daily and weekly coordinate series had to be carried out by adopting the **ITRF2008/IGS** solution as known in a hierarchical sense, i.e., the list of **ITRF2008/IGS** discontinuities had to be added as known in the analyses. This procedure allows it to prepare a correct set of a priori coordinates and velocities consistent with the validity intervals in the **ITRF2008/IGS** solution.

The impact of the quality assessment of coordinate time series was checked in parameter time series such as that for the geocenter, for the scale, and for the **ERPs**. For geocenter and scale parameters, we saw a significant reduction of offsets and drifts with respect to the multi-year solution. For the geocenter, offsets were reduced by a factor larger than 4 and drifts by a factor larger than 5. After quality assessment geocenter offsets are within a 3σ interval, and geocenter drifts are within a 1σ interval, i.e., geocenter drifts are no more significant. For the scale the offset was reduced by a factor larger than 1.2 and the drifts by a factor of larger than 2.2. Nevertheless, all offsets and drifts (before and after quality assessment) were not significantly different from zero. The impact on the series of **ERPs** is significant. The discontinuities in the series before quality assessment partially or even completely disappeared. The **RMS** of the estimates improved at least by 20% and the formal errors by 13%.

The time series of the geocenter, of the scale, and of the coordinates were spectrally analyzed. Both, daily and weekly series had an annual signal of the same amplitude. In the series of the geocenter and of the coordinates we found evidence of the spectral lines associated with the draconitic year of the **GPS** constellation. In the Z-component of the geocenter time series we found the odd harmonics ($350.51/n$, with $n = 3, 5, 7$) and in the coordinate time series we found the even harmonics ($350.51/n$, with $n = 4, 6$). From this perspective the geocenter and the coordinate time series are complementary. No trace of these harmonics were found in the scale series. In the short-period part of the periodograms of the daily geocenter, scale, coordinate parameter time series we generally found spectral lines at 13.66 days (Lunar fortnightly). In the weekly series of these parameters we generally found a spectral line of 14.35 days of unknown origin. Stacked power spectra of station coordinate time series were generated to determine the noise characteristics. We found that both, daily and weekly coordinate time series, mainly contain a combination of white noise and flicker noise.

Seasonal signals were found in the analysis of coordinate time series. We found that both, phases and amplitudes of the annual signals are regionally correlated. Similar results were found by, e.g., [Dong et al. \(2002\)](#); [Ostini et al. \(2007\)](#). The semi-annual signal is more visible in the Up component at high latitudes in the Northern hemisphere. In an attempt to understand the source for the signals, we found that the periodic variations in the scale time series may be explained as the mean sum of the Up components for all stations.

Program **FODITS** was also used to analyze the evolution of the mean orbital elements of **GPS** and **GLONASS** satellites. **CODE** keeps track of all maneuvers of **GPS** satellites since

2004. Such logs were used as a known truth to test the sensitivity of the **FODITS** detection of discontinuities in the mean semi-major axes' evolutions. Two strategies were tested for the detection of discontinuities: The first proposed additional changes in drift and periodic functions as candidates. The second proposed only additional changes in drift. The former strategy introduced more errors than the latter strategy, and the latter strategy identified less discontinuities than the former strategy. The results were however comparable: for both strategies about 93% of discontinuities correctly identified and about 2% wrongly identified. For a more reliable identification of maneuvers in the evolution of the semi-major axis we concluded that the algorithm **FODITS** should consider changes in phase for the periodic functions. The ground truth was added to the analysis as known. The maneuvers to keep the satellites in their assigned slots were generally made with velocity changes of about 200 mm/s, while the maneuvers to move the satellites from one slot to another by velocity pulses that can reach even more than 6.0 m/s. The analysis found also not significant maneuvers. As the **GLONASS** satellites are not in a deep, but only in a shallow, 2:1 resonance with the Earth's rotation, no constellation-keeping maneuvers are visible in the evolution of the semi-major axes. Few maneuvers about of < 40 mm/s were identified. The evolution of the mean eccentricity of **GPS** satellites shows a continuous increase as a function of their lifetime. This result, which is explained by the 2:1 resonance with the Earth's rotation, confirms the prediction formulated in (Beutler, 2005). No such increase occurs for **GLONASS** satellites. The length of the draconitic year of a **GNSS** constellation can be derived from the regression of the right ascensions of the ascending nodes. The periods are **SVN**-specific and vary as a function of time. The mean value for the **GPS** constellation was computed to be $T_{drac} = 351.08 \pm 0.01$ years, while for the **GLONASS** constellation the computed period was $T_{drac} = 353.09 \pm 0.02$ days.

The program **FODITS**, developed in the context of this work, has been integrated in the **BSW**. This component is particularly important in the era of large networks and reprocessing efforts. Its efficiency has been shown with examples and applications.

A GPS and GLONASS Satellites

Table A.1: Information on all GPS satellites in the interval from 1994 to 2008. Source: <ftp://ftp.unibe.ch/aiub/BSWUSER50/GEN/SATELLIT.I08>

SVN	COSPAR	W ¹	P ²	Block	PRN	From	To
SVN09	1984-059A	C	520	Block I	PRN13	13-Jun-84	21-Jun-94
SVN10	1984-097A	A	519	Block I	PRN12	08-Sep-84	27-Mar-96
SVN11	1985-093A	C	521	Block I	PRN03	09-Oct-85	14-Apr-94
SVN13	1989-044A	B	880	Block II	PRN02	10-Jun-89	13-May-04
SVN14	1989-013A	E	880	Block II	PRN14	14-Feb-89	16-Apr-00
SVN15	1990-088A	D	880	Block II	PRN15	01-Oct-90	14-Mar-07
SVN16	1989-064A	E	880	Block II	PRN16	18-Aug-89	14-Oct-00
SVN17	1989-097A	D	880	Block II	PRN17	11-Dec-89	24-Feb-05
SVN18	1990-008A	F	880	Block II	PRN18	24-Jan-90	19-Aug-00
SVN19	1989-085A	A	880	Block II	PRN19	21-Oct-89	12-Sep-01
SVN20	1990-025A	B	880	Block II	PRN20	26-Mar-90	14-Dec-96
SVN21	1990-068A	E	880	Block II	PRN21	02-Aug-90	28-Jan-03
SVN22	1993-007A	B	975	Block IIA	PRN22	03-Feb-93	07-Aug-03
SVN23	1990-103A	E	975	Block IIA	PRN23	26-Nov-90	17-Feb-04
					PRN32	02-Dec-06	n.d. ⁵
SVN28	1992-019A	C	975	Block IIA	PRN28	10-Apr-92	16-Aug-97
SVN29	1992-089A	F	975	Block IIA	PRN29	18-Dec-92	24-Oct-07
SVN30	1996-056A	B	975	Block IIA	PRN30	12-Sep-96	04-Aug-11
SVN31	1993-017A	C	975	Block IIA	PRN31	30-Mar-93	25-Oct-05
SVN32	1992-079A	F	975	Block IIA	PRN01	22-Nov-92	17-Oct-08
SVN33	1996-019A	C	975	Block IIA	PRN03	28-Mar-96	n.d. ⁵
SVN36	1994-016A	C	975	Block IIA	PRN06	10-Mar-94	n.d. ⁵
SVN37	1993-032A	C	975	Block IIA	PRN07	13-May-93	15-Jan-08
					PRN01	23-Oct-08	07-Jan-09
SVN38	1997-067A	A	975	Block IIA	PRN08	06-Nov-97	n.d. ⁵
SVN40	1996-041A	E	975	Block IIA	PRN10	16-Jul-96	n.d. ⁵
SVN41	2000-071A	F	1100	Block IIR-A	PRN14	10-Nov-00	n.d. ⁵
SVN43	1997-035A	F	1100	Block IIR-A	PRN13	23-Jul-97	n.d. ⁵
SVN44	2000-040A	B	1100	Block IIR-A	PRN28	16-Jul-00	n.d. ⁵
SVN45	2003-010A	D	1100	Block IIR-A	PRN21	31-Mar-03	n.d. ⁵
SVN46	1999-055A	D	1100	Block IIR-A	PRN11	07-Oct-99	n.d. ⁵
SVN47	2003-058A	E	1100	Block IIR-B	PRN22	21-Dec-03	n.d. ⁵
SVN48	2008-012A	A	1100	Block IIR-M	PRN07	15-Mar-08	n.d. ⁵
SVN51	2000-025A	E	1100	Block IIR-A	PRN20	11-May-00	n.d. ⁵
SVN52	2006-042A	A	1100	Block IIR-M	PRN31	25-Sep-06	n.d. ⁵
SVN53	2005-038A	C	1100	Block IIR-M	PRN17	26-Sep-05	n.d. ⁵
SVN54	2001-004A	E	1100	Block IIR-A	PRN18	30-Jan-01	n.d. ⁵
SVN55	2007-047A	F	1100	Block IIR-M	PRN15	17-Oct-07	n.d. ⁵

Table A.1: To be continued in the next page.

⁵Not yet decommissioned on 24 December, 2011.

Table A.1: Continuation from the previous page.

SVN	COSPAR	W ³	P ⁴	Block	PRN	From	To
SVN56	2003-005A	B	1100	Block IIR-A	PRN16	29-Jan-03	n.d. ⁵
SVN57	2007-062A	C	1100	Block IIR-M	PRN29	20-Dec-07	n.d. ⁵
SVN58	2006-052A	B	1100	Block IIR-M	PRN12	17-Nov-06	n.d. ⁵
SVN59	2004-009A	C	1100	Block IIR-B	PRN19	20-Mar-04	n.d. ⁵
SVN60	2004-023A	F	1100	Block IIR-B	PRN23	23-Jun-04	n.d. ⁵
SVN61	2004-045A	D	1100	Block IIR-B	PRN02	06-Nov-04	n.d. ⁵

Table A.2: Information on all GLONASS satellites in the interval from 2003 to 2008. Source: <ftp://ftp.unibe.ch/aiub/BSWUSER50/GEN/SATELLIT.I08>

SVN	COSPAR	W ⁶	P ⁷	Block	PRN	From	To
SVN701	2003-056A	1	1415	GLONASS-M	PRN106	10-Dec-03	27-Apr-10
SVN712	2004-053B	1	1415	GLONASS-M	PRN107	26-Dec-04	14-Dec-11
SVN713	2005-050B	3	1415	GLONASS-M	PRN124	25-Dec-05	28-Feb-10
SVN714	2005-050A	3	1415	GLONASS-M	PRN123	28-Feb-06	18-Mar-10
SVN715	2006-062C	2	1415	GLONASS-M	PRN114	25-Dec-06	15-Dec-10
SVN716	2006-062A	2	1415	GLONASS-M	PRN115	25-Dec-06	n.d. ¹⁰
SVN717	2006-062B	2	1415	GLONASS-M	PRN110	25-Dec-06	n.d. ¹⁰
SVN718	2007-052C	3	1415	GLONASS-M	PRN117	26-Oct-07	15-Dec-10
SVN719	2007-052B	3	1415	GLONASS-M	PRN120	26-Oct-07	n.d. ¹⁰
SVN720	2007-052A	3	1415	GLONASS-M	PRN119	26-Oct-07	n.d. ¹⁰
SVN721	2007-065A	2	1415	GLONASS-M	PRN113	25-Dec-07	n.d. ¹⁰
SVN722	2007-065B	2	1415	GLONASS-M	PRN109	25-Dec-07	30-Sep-10
SVN723	2007-065C	2	1415	GLONASS-M	PRN111	25-Dec-07	n.d. ¹⁰
SVN724	2008-046A	3	1415	GLONASS-M	PRN118	25-Sep-08	n.d. ¹⁰
SVN725	2008-046B	3	1415	GLONASS-M	PRN121	25-Sep-08	n.d. ¹⁰
SVN726	2008-046C	3	1415	GLONASS-M	PRN122	25-Sep-08	28-Feb-10
SVN728	2008-067C	1	1415	GLONASS-M	PRN102	25-Dec-08	n.d. ¹⁰
SVN729	2008-067B	1	1415	GLONASS-M	PRN108	25-Dec-08	n.d. ¹⁰
SVN765	1995-009A	3	900	GLONASS	PRN120	01-Jan-96	27-Feb-06
SVN770	1994-050C	2	900	GLONASS	PRN114	01-Jan-96	24-Dec-06
SVN776	1995-068C	2	900	GLONASS	PRN109	01-Jan-96	24-Dec-07
SVN777	1995-009C	3	900	GLONASS	PRN119	01-Jan-96	24-Dec-05
SVN778	1995-068B	2	900	GLONASS	PRN115	07-Apr-99	24-Dec-06
SVN781	1995-037B	2	900	GLONASS	PRN110	01-Jan-96	24-Dec-06
SVN782	1995-068A	2	900	GLONASS	PRN113	01-Jan-96	24-Dec-07
SVN783	2000-063C	3	900	GLONASS	PRN118	13-Oct-00	24-Sep-08
SVN787	2000-063A	3	900	GLONASS	PRN117	13-Oct-00	25-Oct-07
SVN788	2000-063B	3	900	GLONASS	PRN124	13-Oct-00	24-Dec-05
SVN789	2001-053B	1	1415	GLONASS	PRN103	01-Dec-01	24-Dec-08
SVN791	2002-060A	3	1480	GLONASS	PRN122	25-Dec-02	25-Oct-07
SVN792	2002-060C	3	1480	GLONASS	PRN121	25-Dec-02	24-Sep-08
SVN793	2002-060B	3	1480	GLONASS	PRN123	25-Dec-02	27-Feb-06
					PRN120	28-Feb-06	25-Oct-07

Table A.2: To be continued in the next page.¹⁰Not yet decommissioned on 24 December, 2011.

Table A.2: Continuation from the previous page.

<i>SVN</i>	<i>COSPAR</i>	<i>W</i> ⁸	<i>P</i> ⁹	Block	<i>PRN</i>	From	To
SVN794	2003-056B	1	900	GLONASS	PRN102	10-Dec-03	24-Dec-08
SVN795	2003-056C	1	900	GLONASS	PRN104	10-Dec-03	13-Dec-09
SVN796	2004-053A	1	900	GLONASS	PRN101	26-Dec-04	13-Dec-09
SVN797	2004-053C	1	900	GLONASS	PRN108	26-Dec-04	24-Dec-08
SVN798	2005-050C	3	900	GLONASS	PRN119	25-Dec-05	25-Oct-07
					PRN122	26-Oct-07	24-Sep-08

B The Tool for the Spectral Analysis

This appendix introduces the tool used in this work to spectrally analyze the time series. A least squares approach to compute stacked spectra of more than 200 station coordinate time series is too CPU-time intensive. By a **Discrete Fourier Transform (DFT)** approach the CPU-time efficiency improves, but the spectral resolution diminishes. The **FFT** approach proposed here, based on extending the time series by zero-padding (i.e., completion with zeros), provides both, a CPU-time efficient computation and an higher spectral resolution. No effective more information is however gained.

The **DFT** of the sequence x_n of N values, or time series, reads

$$\mathbf{X}_k = \sum_{n=0}^{N-1} x_n e^{-j \frac{2\pi}{N} nk} , \quad (\text{B.1})$$

where \mathbf{X}_k is a complex number. k is of length N (k runs from 0 to $N - 1$).

The **FFT** is a CPU-time efficient algorithm to compute the **DFT**. The **FFT** approach requires however that N is a power of two.

Geophysical time series have often missing epochs. The **DFT** assumes however that the sequence x_n consists of equidistant epochs. Thus, in order to compute the **DFT**, one has first to "fill" the gaps. The completion of the gaps with zeros is called zero-padding. Let us assume to have a sequence x_n with L observations, with $L < N$. Let us add zeros into the epochs of missing data as well as at the end of the sequence in order to have N data points:

$$x_n = \{0, x_1, \dots, x_l, 0, 0, x_{l+1}, \dots, x_{L-1}, 0, 0, \dots, x_{N-1} = 0\} . \quad (\text{B.2})$$

The **DFT** may now be computed in the same way as by Eq. (B.1) with

$$\mathbf{X}_k = \sum_{n=0}^{L-1} x_n e^{-j \frac{2\pi}{N} nk} = \sum_{n=0}^{N-1} x_n e^{-j \frac{2\pi}{N} nk} . \quad (\text{B.3})$$

The extension by zero-padding is useful to have more resolution in the frequency domain, however without gaining more effective information. To obtain the amplitude of the spectrum one has to normalize \mathbf{X}_k dividing it by the number of epochs L . Before applying the **FFT** the time series x_n must be "detrended", i.e., removal of the best fit of a polynomial of order k ($k = 1$ in this work).

Figure B.1 shows the **FFT** with zero-padding and **DFT** of the same time series. The time series (in red) consist of 782 data points, have weekly spacing, and have no missing epochs.

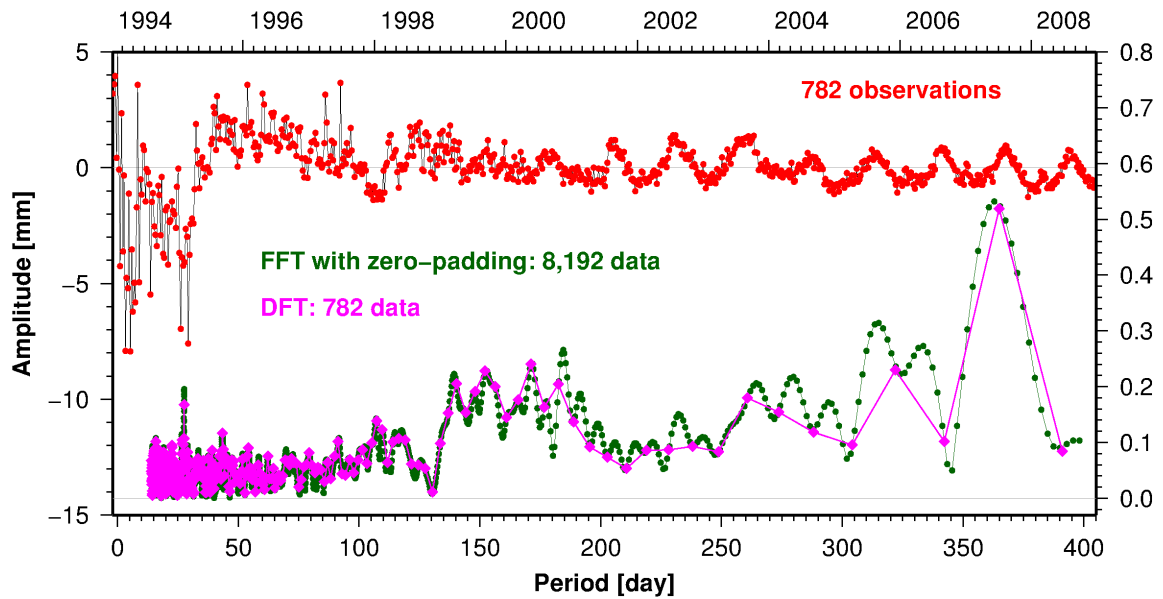


Figure B.1: Validation of the FFT approach with zero padding with a least squares approach. The top x-axis (time) and left y-axis (amplitude) refer to the one-dimensional time series. The bottom x-axis (period) and right y-axis (amplitude) refer to the spectral analysis of the time series.

For the **FFT** the original time series were first extended by zero-padding to the next power of two, i.e., to 1024 data points. Then, the resulting series were furthermore extended by zero-padding to a total of 8,192 data points. The **DFT** consists of 782 values, while the **FFT** of 8,192. Both spectral analyses are shown in the periodogram up to a period of 400 days. The **DFT** (in magenta) coincides with the **FFT** (in green) in all its points.

Acknowledgements

I would like to express my deepest gratitude to PDDr. Rolf Dach for teaching me, for guiding me, for given me always pertinent inputs and feedbacks, for always showing me the correct way to face problematics, and especially for being an excellent example.

I am indebted to Prof. Dr. Gerhard Beutler for teaching me astronomy and space geodesy from the beginning of my education at the university, for giving me the opportunity to be part of the AIUB group, for giving me precise, important and meaningful advice, for the experience I could collect during these years.

My appreciation goes to everyone of the AIUB group for supporting me always with everything with motivation. Special thanks are addressed to Prof. Dr. Adrian Jäggi who assisted me throughout the education, to Prof. Dr. Urs Hugentobler who introduced me to the topic of this work, to Prof. Dr. Werner Gurtner and Prof. Dr. Thomas Schildknecht for their advice during the education, to Dr. Michael Meindl, Dr. Stefan Schär, Dr. Heike Bock, Dr. Claudia Flohrer, Dr. Simon Lutz, Dr. Daniela Thaller, Dr. Lars Prange, Dr. Ulrich Meyer, Dr. Etienne Orliac, and Krzysztof Sośnica for their important contributions.

I would like to thank Dr. Matt King and Dr. Simon Williams. Their DOGEx (Detection of Offsets in GPS timeseries Experiment—Working Group 3 of COST Action ES0701 "Improved Constraints on Models of Glacial Isostatic Adjustment") importantly helped us in improving the efficiency of the algorithm embedded in the analysis tool of this work.

Special thanks are addressed to my family, my friends, and all who contributed in supporting me throughout these years.

Last but not least, I would like to thank the Center for Orbit Determination in Europe (CODE) for funding the project of this work.

Bibliography

- Agnew, D.C. (1992), The Time-Domain Behavior of Power-Law Noises, *Geophysical Research Letters*, 19(4), 333–336, Feb. 1992. 29, 30
- Altamimi, Z., X. Collilieux, J. Legrand, B. Garayt, and C. Boucher (2007), ITRF2005: A new release of the International Terrestrial Reference Frame based on time series of station positions and Earth Orientation Parameters, *Journal of Geophysical Research*, 112(B09402). 2, 28
- Altamimi, Z., X. Collilieux, and L. Métivier (2011), ITRF2008: an improved solution of the international terrestrial reference frame, *Journal of Geodesy*. 2, 3, 7, 84, 86
- Amiri-Simkooei, A.R., C.C.J.M. Tiberius, and P.J.G. Teunissen (2007), Assessment of noise in GPS coordinate time series: Methodology and results, *Journal of Geophysical Research*, 112(B07413), 591–603. 21, 30
- Ammon, C.J., C. Ji, H.-K. Thio, D. Robinson, S. Ni, V. Hjorleifsdottir, H. Kanamori, T. Lay, S. Das, D. Helmberger, G. Ichinose, J. Polet, and D. Wald (2005), Rupture Process of the 2004 Sumatra-Andaman Earthquake, *Science*, 308, 5725 pp., 11331139. 63
- Ashby, N. (2003), Relativity in the Global Positioning System, *Living Reviews in Relativity*, 6. 11
- Baarda, W. (1968), A testing procedure for use in geodetic networks, *Netherlands Geodetic Commission, Publication on Geodesy, New Series 2, No. 5 Delft*, The Netherlands. 41, 49
- Barnett, V., and T. Lewis (1994), *Outliers in statistical data*, John Wiley & Sons Ltd., Chichester, U.K., 3rd edition. 3, 49
- Beutler, G. (2004), Revolution in Geodesy and Surveying, Presentation at the plenary session of the FIG Working Week 2004, May 2004. 1, 7, 9
- Beutler, G. (2005), *Methods of Celestial Mechanics*, Springer-Verlag, Berlin, Heidelberg, New York. 10, 16, 18, 24, 30, 35, 56, 115, 116, 117, 119, 127, 128, 129, 142
- Beutler, G., E. Brockmann, W. Gurtner, U. Hugentobler, L. Mervart, and M. Rothacher (1994), Extended orbit modeling techniques at the CODE Processing Center of the International GPS Service (IGS): Theory and initial results, *Manuscripta Geodaetica*, 19, 367–386. 25, 28

- Beutler, G., E. Brockmann, U. Hugentobler, L. Mervart, M. Rothacher, and R. Weber (1996), Combining Consecutive Short Arcs into Long Arcs for Precise and Efficient GPS Orbit Determination, *Journal of Geodesy*, 70, 287–299. [25](#), [29](#)
- Beutler, G., H. Drewes, and A. Verdun (2004), The New Structure of the International Association of Geodesy (IAG) Viewed from the Perspective of History, *Journal of Geodesy*, 77, 566–575. [7](#)
- Beutler, G., A. Jäggi, U. Hugentobler, and L. Mervart (2006), Efficient satellite orbit modelling using pseudo-stochastic parameters, *Journal of Geodesy*, 80, 353–372, 10.1007/s00190-006-0072-6. [25](#)
- Blewitt, G. (2003), Self-consistency in reference frames, geocenter definition, and surface loading of the solid Earth, *Journal of Geophysical Research*, 108(B2), 2103. [93](#)
- Blewitt, G., and D. Lavallee (2002), Effect of annual signals on geodetic velocity, *Journal of Geophysical Research*, 107(B7), 2145, Fall Meeting Suppl., Abstract G11C-05. [38](#)
- Blewitt, G., P. Clarke, and D. Lavallee (2000), Spatially coherent oscillations in longitude and latitude linked to seasonal variation in Earth’s shape, *Eos Transactions AGU*, 81(48), 332, Fall Meeting Suppl., Abstract G11C-05. [34](#)
- Bock, H. (2004), *Efficient Methods for Determining Precise Orbits of Low Earth Orbiters Using the Global Positioning System*, Geodätisch-geophysikalische Arbeiten in der Schweiz, Band 65, Schweizerische Geodätische Kommission, Institut für Geodäsie und Photogrammetrie, Eidg. Technische Hochschule Zürich, Zürich. [24](#)
- Bock, H., R. Dach, A. Jäggi, and G. Beutler (2009), High-rate GPS clock corrections from CODE: support of 1 Hz applications, *Journal of Geodesy*, 83(11), 1083–1094. [29](#)
- Böhm, J., A. Niell, P. Tregoning, and H. Schuh (2006), Global Mapping Function (GMF): A new empirical mapping function based on numerical weather model data, *Geophysical Research Letters*, 33, L07304. [28](#)
- Böhm, J., R. Heinkelmann, and H. Schuh (2007), Short Note: A global model of pressure and temperature for geodetic applications, *Journal of Geodesy*. [28](#)
- Bossler, J.D., R.B. McMaster, C. Rizos, and J.B. Campbell (2010), *Manual of Geospatial Science and Technology*, CRC, 2nd edition edition. [14](#)
- Brockmann, E. (1997), *Combination of Solutions for Geodetic and Geodynamic Applications of the Global Positioning System (GPS)*, Geodätisch-geophysikalische Arbeiten in der Schweiz, Band 55, Schweizerische Geodätische Kommission, Institut für Geodäsie und Photogrammetrie, Eidg. Technische Hochschule Zürich, Zürich. [22](#), [27](#), [71](#)
- Calais, E. (1999), Continuous GPS measurements across the Western Alps, 1996-1998, *Geophysics Journal International*, 138, 221–230. [30](#), [106](#)
- Casella, G., and R.L. Berger (2001), *Statistical Inference*, Duxbury Press, 2nd edition edition. [42](#)

- Chen, J.L., C.R. Wilson, R.J. Eanes, and R.S. Nerem (1999), Geophysical interpretation of observed geocenter variations, *JGR*, 104, 2683–2690. [98](#)
- Collilieux, X., and G. Wöppelmann (2010), Global sea-level rise and its relation to the terrestrial reference frame, *Journal of Geodesy*. [3](#)
- Collilieux, X., T. van Dam, J. Ray, D. Coulot, L. Métivier, and Z. Altamimi (2011), Strategies to mitigate aliasing of loading signals while estimating GPS frame parameters, *Journal of Geodesy*. [99](#), [102](#), [104](#)
- Dach, R., G. Beutler, H. Bock, P. Fridez, A. Gäde, U. Hugentobler, A. Jäggi, M. Meindl, L. Mervart, L. Prange, S. Schaer, T. Springer, C. Urschl, and P. Walser (2007), *Bernese GPS Software Version 5.0*, Astronomical Institute, University of Bern, Bern, Switzerland, jan 2007, User manual. [2](#), [5](#), [13](#), [16](#), [19](#), [23](#), [27](#), [39](#), [50](#), [71](#), [73](#)
- Dach, R., E. Brockmann, S. Schaer, G. Beutler, M. Meindl, L. Prange, H. Bock, A. Jäggi, and L. Ostini (2009), GNSS Processing at CODE: Status Report, *Journal of Geodesy*, 83(3–4), 353–365. [117](#), [123](#), [132](#)
- Dach, R., J. Böhm, S. Lutz, P. Steigenberger, and G. Beutler (2010), Evaluation of the Impact of Atmospheric Pressure Loading Modeling on GNSS Data Analysis, *Journal of Geodesy*. [3](#), [35](#)
- Dach, R., R. Schmid, M. Schmitz, D. Thaller, S. Schaer, S. Lutz, P. Steigenberger, G. Wübbena, and G. Beutler (2011), Improved antenna phase center models for GLONASS, *GPS Solutions*, 15(1), 49–65, 01 2011. [15](#), [26](#), [135](#)
- Delle Donne, D., A.J.L. Harris, M. Ripepe, and R. Wright (2010), Earthquake-induced thermal anomalies at active volcanoes, *Geology*, 38(9), 771–774. [33](#), [34](#)
- Dick, W.R., and B. Richter (eds.) (2008), *IERS Annual Report 2006*, Frankfurt am Main: Verlag des Bundesamts für Kartographie und Geodesie, International Earth Rotation and Reference Systems Service, Central Bureau. [2](#), [8](#)
- Dilssner, F., R. Dach, R. Schmid, T.A. Springer, and J. Dow (2011), The GLONASS-M satellite yaw-attitude model, *Advances in Space Research*, 47, 160–171. [132](#)
- Dong, D., T. Yunck, and M. Heflin (2003), Origin of the International Terrestrial Reference Frame, *Journal of Geophysical Research*, 108(B4, 2200). [93](#)
- Dong, P., P. Fang, Y. Bock, M.K. Cheng, and S. Miyazaki (2002), Anatomy of apparent seasonal variations from GPS-derived site position time series, *Journal of Geophysical Research*, 107(B4). [34](#), [103](#), [141](#)
- Dow, J.M., R.E. Neilan, and C. Rizos (2009), The International GNSS Service in a changing landscape of Global Navigation Satellite Systems, *Journal of Geodesy*, 83, 191198. [1](#)
- Drewes, H. (2008), Geodesists Handbook 2008, *Journal of Geodesy*, 82, 661–846, 10.1007/s00190-008-0259-0. [7](#)

- Eanes, R., and S. Bettadpur (1996), The CSR 3.0 global ocean tide model, Center for Space Research, Austin, Texas, Technical Memorandum CSR-TM-96-05. [28](#), [131](#)
- Ergintav, S., S. McClusky, E. Hearn, R. Reilinger, R. Cakmak, T. Herring, H. Ozener, O. Lenk, and E. Tari (2009), Seven years of postseismic deformation following the 1999, M=7.4 and M=7.2, Izmit-Düzce, Turkey earthquake sequence, *Journal of Geophysical Research*, *114*(B07403). [29](#), [38](#), [78](#)
- Ferland, R., and M. Piraszewski (2009), The IGS-combined station coordinates, Earth rotation parameters and apparent geocenter, *Journal of Geodesy*, *83*(3–4), 385–392. [38](#)
- Ge, M., G. Gendt, G. Dick, F.P. Zhang, and C. Reigber (2005), Impact of GPS satellite antenna offsets on scale changes in global network solutions, *Geophysical Research Letters*, *33*(L06310). [99](#)
- Gendt, G. (2006), IGS switch to absolute antenna model and ITRF2005, IGS Mail No. 5438, IGS Central Bureau Information System. [2](#), [28](#)
- Gendt, G., Z. Altamimi, R. Dach, W. Söhne, T. Springer, and the GGPS Prototype Team (2009), GGSP: Realisation and Maintenance of the Galileo Terrestrial Reference Frame, presented at the *COSPAR Colloquium, 2nd International Colloquium — Scientific and Fundamental Aspects of the Galileo Programme*, October 2009. [35](#), [40](#)
- Görres, B., J. Campbell, M. Becker, and M. Siemes (2006), Absolute calibration of GPS antennas: laboratory results and comparison with field and robot techniques, *GPS Solutions*, *10*(2), 136–145. [15](#)
- Gurtner, W. (1994), RINEX: The Receiver-Independent Exchange Format, *GPS World*, *5*(7), 48–52, July 1994. [2](#)
- Habrich, H. (1999), *Geodetic Applications of the Global Navigation Satellite System (GLONASS) and of GLONASS/GPS Combinations*, Ph.D. dissertation, Astronomical Institute, University of Berne, Berne, Switzerland. [115](#)
- Hefty, J., M. Rothacher, T.A. Springer, R. Weber, and G. Beutler (2000), Analysis of the First Year of Earth Orientation Parameters with a Sub-Daily Resolution gained at the CODE Processing Center of the IGS, *Journal of Geodesy*, *74*, 479–487. [28](#)
- Hilla, S. (2002), Extending the Standard Product 3 (SP3) Orbit Format, in *Proceedings of the IGS Network, Data, and Analysis Center Workshop, Towards Real Time*, edited by P. Tetreault, Ottawa, Canada, April 8–11, 2002. [8](#)
- Hugentobler, U. (1997), *Astrometry and Satellite Orbits: Theoretical Considerations and Typical Applications*, Ph.D. dissertation, Astronomical Institute, University of Berne, Berne, Switzerland. [133](#)
- Hugentobler, U. (2006), GPS week 1400 model changes made at CODE, IGS Mail No. 5518, IGS Central Bureau Information System. [2](#)

- Hugentobler, U., S. Schaer, R. Dach, M. Meindl, and C. Urschl (2004), Routine Processing of Combined Solutions for GPS and GLONASS at CODE, Presentation at the IGS Workshop., March 2004. [26](#)
- Hugentobler, U., M. Meindl, G. Beutler, H. Bock, R. Dach, A. Jäggi, C. Urschl, L. Merivart, M. Rothacher, S. Schaer, E. Brockmann, D. Ineichen, A. Wiget, U. Wild, G. Weber, H. Habrich, and C. Boucher (2006), CODE IGS Analysis Center Technical Report 2003/2004, in *IGS 2004 Technical Reports*, edited by Ken Gowey *et al.*, IGS Central Bureau, Jet Propulsion Laboratory, Pasadena, California, USA, in press. [119](#)
- Jäggi, A. (2007), *Pseudo-Stochastic Orbit Modeling of Low Earth Satellites Using the Global Positioning System*, Geodätisch-geophysikalische Arbeiten in der Schweiz, Band 73, Schweizerische Geodätische Kommission, Institut für Geodäsie und Photogrammetrie, Eidg. Technische Hochschule Zürich, Zürich. [25](#)
- Jäggi, A., H. Bock, R. Pail, and H. Goiginger (2008), Highly-Reduced Dynamic Orbits and their Use for Global Gravity Field Recovery: a Simulation Study for GOCE, *Stud Geophys Geod*, *52(3)*, 341–359. [25](#)
- Kern, M, T. Preimesberger, M. Allesch, R. Pail, J. Bounman, and R. Koop (2005), Outlier detection algorithms and their performance in GOCE gravity field processing, *Journal of Geodesy*. [49](#)
- King, M.A., and C.S. Watson (2010), Long GPS coordinate time series: Multipath and geometry effects, *Journal of Geophysical Research*, *115*(B04403). [77](#)
- King, M.A., and S.D.P. Williams (2009), Apparent stability of GPS monumentation from short-baseline time series, *Journal of Geophysical Research*, *114*(B10403). [4](#), [21](#), [30](#), [35](#)
- King, M.A., and S.D.P. Williams (2010), The Detection of Offsets in GPS Experiment (DOGEx): Call for Participation, in *IGS Workshop*, Newcastle upon Tyne, UK, 28 June – 2 July 2010, Poster. [68](#), [69](#)
- King, M.A., and S.D.P. Williams (2011), G23A-0810 The Detection of Offsets in GPS Experiment (DOGEx), in *IUGG Meeting*, Melbourne, Australia, 28 June – 7 July 2011, Poster. [68](#), [69](#), [124](#), [140](#)
- King, M.A., R. Coleman, P.J. Morgan, and R.S. Hurd (2007), Velocity change of the Amery Ice Shelf, East Antarctica, during the period 1968–1999, *Journal of Geophysical Research*, *112*(F01013). [52](#)
- King, M.A., C.S. Watson, N.T. Penna, and P.J. Clarke (2008), Subdaily signals in GPS observations and their effect at semiannual and annual periods, *Geophysical Research Letters*, *35*(L03302). [35](#)
- Kleijer, F. (2002), Time Series Analysis of the Daily Solutions of the AGRS.NL Reference Stations, in *Vertical Reference Systems*, vol. 124, edited by H. Drewes *et al.*, International Association of Geodesy Symposia, Springer-Verlag Berlin Heidelberg New York. [4](#)

- Koch, K.R. (1999), *Parameter Estimation and Hypothesis Testing in Linear Models*, Springer, Berlin Heidelberg New York, 2nd updated and enlarged edition edition. 19, 22, 42
- Kositsky, A.P., and J.-P. Avouac (2010), Inverting geodetic time series with a principal component analysis-based inversion method, *Journal of Geophysical Research*, 115, B03401. 38
- Kouba, J. (2008), A simplified yaw-attitude model for eclipsing GPS satellites, *Journal of Geodesy*, 13, 1–12. 117
- Kouba, J. (2009), A guide to using International GNSS Service (IGS) products, May 2009. 8
- Krügel, M., D. Thaller, V. Tesmer, M. Rothacher, D. Angermann, and R. Schmid (2007), Tropospheric parameters: combination studies based on homogeneous VLBI and GPS data, *Journal of Geodesy*, 81, 515–527. 99
- Lacy, M.C. de, M. Reguzzoni, F. Sansò, and G. Venuti (2008), The Bayesian detection of discontinuities in a polynomial regression and its application to the cycle-slip problem, *Journal of Geodesy*, 82, 527–542. 4
- Langbein, J., and H. Johnson (1997), Correlated errors in geodetic time series: Implications for time-dependent deformation, *Journal of Geophysical Research*, 102(B1), 591–603, January 1997. 4, 21, 29, 30, 105
- Larson, K.M., M. Poland, and A. Miklius (2010), Volcano monitoring using GPS: Developing data analysis strategies based on the June 2007 Kilauea Volcano intrusion and eruption, *Journal of Geophysical Research*, 115, B07406. 29
- Luzum, B., J. Ray, M. Carter, and F. Josties (2001), Recent improvements to IERS Bulletin A combination and prediction, *GPS Solutions*, 4 (3), 3440. 28, 110
- Lyard, F., F. Lefevre, T. Letellier, and O. Francis (2006), Modelling the global ocean tides: modern insights from FES2004, *Ocean Dynamics*, 56(5–6), 394–415, December 2006. 28
- Mader, Gerald L. (1999), GPS Antenna Calibration at the National Geodetic Survey, *GPS Solutions*, 3, 50–58, 10.1007/PL00012780. 15
- Mao, A, C.G.A. Harrison, and H.T. Dixon (1999), Noise in GPS coordinate time series, *Journal of Geophysical Research*, 104(B2), 27972818. 21, 29, 30, 105, 106, 107
- Mathews, P., T. Herring, and B. Buffett (2002), Modeling of nutation and precession: New nutation series for non-rigid Earth and insights into the Earths interior, *Journal of Geophysical Research*, 107(B4), 27972818. 28, 110
- McCarthy, D.D., and G. Petit (2003), IERS Conventions, 21, International Earth Rotation and Reference Systems Service, Paris, France, IERS Technical Note. 2, 7, 28

- Meindl, M., S. Schaer, U. Hugentobler, and G. Beutler (2004), Tropospheric Gradient Estimation at CODE: Results from Global Solutions, in *Applications of GPS Remote Sensing to Meteorology and Related Fields*, vol. 82(1B) of *Journal of the Meteorological Society of Japan*, edited by R. A. Anthes et al., pp. 331–338, Meteorological Society of Japan. 17
- Melbourne, W.G. (1985), The Case for Ranging in GPS Based Geodetic Systems, in *Proceedings of the 1st International Symposium on Precise Positioning with the Global Positioning System*, edited by Clyde Goad, pp. 373–386, US Department of Commerce, Rockville, Maryland. 27
- Menge, F., G. Seeber, C. Völksen, G. Wübbena, and M. Schmitz (1998), Results of Absolute Field Calibration of GPS Antenna PCV, in *Proceedings of the ION GPS-98*, Nashville, Tennessee. 15
- Mervart, L. (1995), *Ambiguity Resolution Techniques in Geodetic and Geodynamic Applications of the Global Positioning System*, Geodätisch-geophysikalische Arbeiten in der Schweiz, Band 53, Schweizerische Geodätische Kommission, Institut für Geodäsie und Photogrammetrie, Eidg. Technische Hochschule Zürich, Zürich. 16, 17, 19, 27
- Montenbruck, O., T. van Helleputte, R. Kroes, and E. Gill (2005), Reduced dynamic orbit determination using GPS code and carrier measurements, *Aerospace Science and Technology*, 9(3), 261–271. 25
- Nathan, L.K., J. Wang, and C. Rizos (2010), Generalised measures of reliability for multiple outliers, *Journal of Geodesy*. 49
- Nerem, R.S., R.J. Eanes, J.C. Ries, and G.T. Mitchum (2000), The Use of a Precise Reference Frame for Sea Level Change Studies, in *Towards and Integrated Global Geodetic Observing System (IGGOS)*, edited by R. Rummel et al., pp. 8–12, Springer-Verlag, Munich. 4
- Ostini, L. (2007), Analysis of GNSS Station Coordinate Time Series, Master’s thesis, Astronomisches Institut Universität Bern. 4, 35, 103
- Ostini, L., G. Beutler, R. Dach, U. Hugentobler, M. Ploner, S. Schaer, and C. Urschl (2007), Near-Seasonal Periods in GNSS Station Coordinate Time Serie, in *EGU General Assembly*, Vienna, Austria, April 16–20 2007, Poster. 99, 103, 104, 141
- Ostini, L., R. Dach, M. Meindl, S. Schaer, and U. Hugentobler (2008a), FODITS: A New Tool of the Bernese GPS Software, in *Subcommission for the European Reference Frame (EUREF)*, edited by J.A. Torres and H. Hornik. 2, 4, 31, 36, 69
- Ostini, L., R. Dach, M. Meindl, S. Schaer, and U. Hugentobler (2008b), FODITS: A New Tool of the Bernese GPS Software to Analyze Time Series, in *EUREF 2008 Symposium*, International GNSS Service, Brussels, Belgium, June 18–21 2008, Poster. 31
- Ostini, L., R. Dach, M. Meindl, U. Hugentobler, S. Schaer, and G. Beutler (2010a), FODITS: A time series analysis tool, in *IGS Workshop*, International GNSS Service, Newcastle upon Tyne, Jun 2010, Poster. 5, 31

- Ostini, L., R. Dach, S. Schaer, U. Hugentobler, M. Meindl, and G. Beutler (2010*b*), Time Series Analysis using FODITS, in *COST ES0701 WG 1-3 meeting*, Nottingham, UK, Mar 2010, Poster. [5](#), [31](#)
- Pearlman, M.R., J.J. Degnan, and J.M. Bosworth (2002), The International Laser Ranging Service, *Advances in Space Research*, *30*(2), 135–143, July 2002. [1](#)
- Peltier, W.R. (1976), Glacial-Isostatic Adjustment—II. The Inverse Problem., *Geophysical Journal of the Royal Astronomical Society*, *46*, 669705. [29](#)
- Peltier, W.R., and J.T. Andrews (1976), Glacial-Isostatic Adjustment—I. The Forward Problem., *Geophysical Journal of the Royal Astronomical Society*, *46*, 605646. [29](#)
- Penna, N.T., and M.P. Stewart (2003), Aliased tidal signatures in continuous GPS height time series, *Geophysical Research Letters*, *30*(23)(2184). [35](#)
- Penna, N.T., M.A. King, and M.P. Stewart (2007), GPS height time series: Short-period origins of spurious long-period signals, *Journal of Geophysical Research*, *112*(B02402). [35](#)
- Perfetti, N (2006), Detection of station coordinate discontinuities within the Italian GPS Fiducial Network, *Journal of Geodesy*. [4](#)
- Petit, G., and B. Luzum (2010), IERS Conventions, *36*, International Earth Rotation and Reference Systems Service, Paris, France, IERS Technical Note. [2](#), [7](#), [98](#), [102](#)
- Petrov, L., and J.P. Boy (2004), Study of the atmospheric pressure loading signal in very long baseline interferometry observations, *Journal of Geophysical Research*, *109*, B03405. [35](#)
- Plag, H.-P., and M. Pearlman (2009), *Global Geodetic Observing System - Meeting the Requirements of a Global Society on a Changing Planet in 2020*, Springer. [9](#)
- Ray, J., Z. Altamimi, X. Collilieux, and T. van Dam (2008), Anomalous Harmonics in the Spectra of GPS position Estimates, *GPS Solutions*, *12*(1), 55–64. [4](#), [21](#), [29](#), [30](#), [35](#), [98](#), [105](#)
- Rockwell (1984), Rockwell International Corporation, *ICD-GPS-200*, Satellite Systems Division, September 1984, GPS Interface Control Document. [16](#)
- Romero, N. (2010), IGS Infrastructure: Accomplishments and Challenges, Presentation at IGS Workshop 2010., June 2010. [15](#)
- Rothacher, M. (1998), Recent Contributions of GPS to Earth Rotation and Reference Frames, Habilitation (2nd Ph.D.), University Press, University of Berne. [16](#)
- Rothacher, M., and R. Schmid (2002), ANTEX: The Antenna Exchange Format 1.0, Position Paper and presentation at IGS Workshop, April 8-11, 2002, Ottawa, Canada., April 2002, available at <http://www.iers.org>. [8](#), [15](#)

- Rothacher, M., and R. Schmid (2006), ANTEX: The antenna exchange format, version 1.3, IGS Central Bureau Information System. [8](#), [15](#)
- Rothacher, M., T.A. Springer, S. Schaer, and G. Beutler (1997), Processing Strategies for Regional GPS Networks, in *Proceedings of the IAG General Assembly in Rio, September, 1997*, Springer. [28](#)
- Rothacher, M., T.A. Springer, G. Beutler, R. Dach, U. Hugentobler, D. Ineichen, S. Schaer, U. Wild, A. Wiget, E. Brockmann, C. Boucher, E. Reinhard, and H. Habrich (1999), Annual Report 1998 of the CODE Analysis Center of the IGS, in *IGS 1998 Technical Reports*, edited by Ken Gowey *et al.*, pp. 61–73, IGS Central Bureau, Jet Propulsion Laboratory, Pasadena, California, USA, November 1999. [115](#)
- Rülke, A., R. Dietrich, M. Fritsche, M. Rothacher, and P. Steigenberger (2008), Realization of the Terrestrial Reference System by a reprocessed global GPS network, *Journal of Geophysical Research*, *113*(B08403). [3](#)
- Saastamoinen, I.I. (1973), Contribution to the theory of atmospheric refraction, *Bulletin Géodésique*, *107*, 13–34. [28](#)
- Salzmann, M. (1993), Least Squares Filtering and Testing for Geodetic Navigation Applications, *Publication on Geodesy 37*, Netherlands Geodetic Commission, Delft. [4](#), [42](#), [140](#)
- Santamaría-Gómez, A., M.-N. Bouin, and X. Collilieux (2011), Correlated errors in GPS position time series: Implications for velocity estimates, *Journal of Geophysical Research*, *116*(B01405). [30](#)
- Scargle, J.D. (1982), Studies in astronomical time series analysis. II. Statistical aspects of spectral analysis of unevenly spaced data, *The Astronomical Journal*, *263*, 835–853. [30](#)
- Schaer, S. (1999), *Mapping and Predicting the Earth's Ionosphere Using the Global Positioning System*, vol. 59 of *Geodätisch-geophysikalische Arbeiten in der Schweiz*, Schweizerische Geodätische Kommission, Institut für Geodäsie und Photogrammetrie, Eidgenössische Technische Hochschule Zürich, Zürich, Switzerland. [16](#), [19](#), [29](#)
- Schaer, S., W. Gurtner, and J. Feltens (1998), IONEX: The IONosphere Map EXchange Format Version 1, in *Proceedings of the IGS Analysis Center Workshop*, edited by J. M. Dow *et al.*, pp. 233–247, ESA/ESOC, Darmstadt, Germany, February 9–11, 1998. [8](#)
- Schlüter, W., and D. Behrend (2007), The International VLBI Service for Geodesy and Astrometry (IVS): current capabilities and future prospects, *Journal of Geodesy*, *81*(6–8), 379–387, June 2007. [1](#)
- Schmid, R., and M. Rothacher (2003), Estimation of elevation-dependent satellite antenna phase center variations of GPS satellites, *Journal of Geodesy*, *77*(7–8), 440–446. [15](#), [28](#)
- Schmid, R., P. Steigenberger, G. Gendt, M. Ge, and M. Rothacher (2007), Generation of a consistent absolute phase center correction model for GPS receiver and satellite antennas., *Journal of Geodesy*, *81*(12), 781–798. [3](#)

- Schupler, B.R., R.L. Allshouse, and T.A. Clark (1994), Signal Characteristics of GPS User Antennas, Allied Signal Technical Services Corporation. 15
- Segall, P., and J.L. Davis (1997), GPS applications for geodynamics and earthquake studies, *Annu. Rev. Earth Planet. Sci.* 23, 201–336. 1, 29, 38, 52
- Sella, G., T.H. Dixon, and A. Mao (2002), REVEL: A model for Recent plate velocities from space geodesy, *Journal of Geophysical Research*, 107(B4,2081). 29
- Sella, G., S. Stein, T.H. Dixon, M. Craymer, T.S. James, S. Mazzotti, and R.K. Dokka (2007), Observation of glacial isostatic adjustment in "stable" North America with GPS, *Geophysical Research Letters*, 34(L02306). 29
- Springer, T.A. (2000), *Modeling and Validating Orbits and Clocks Using the Global Positioning System*, Geodätisch-geophysikalische Arbeiten in der Schweiz, Band 60, Schweizerische Geodätische Kommission, Institut für Geodäsie und Photogrammetrie, Eidg. Technische Hochschule Zürich, Zürich. 27
- Standish, E. (1998), JPL planetary and lunar ephemerides, DE405/LE405, *Publication on Geodesy F-98-048*, Interoffice Memorandum IOM 312, JPL, Pasadena, California. 28
- Steigenberger, P. (2009), *Reprocessing of a global GPS network*, Ph.D. dissertation, Fakultät für Bauingenieur- und Vermessungswesen, TU München, Dissertation. 2, 3, 12, 26, 27, 28
- Steigenberger, P, S. Schaer, S. Lutz, R. Dach, L. Ostini, U. Hugentobler, H. Bock, A. Jäggi, M. Meindl, and D. Thaller (2009a), CODE Contribution to IGS Reprocessing: Status and Perspectives, in *EGU General Assembly*, Vienna, Austria, April 2009, Poster. 2, 26
- Steigenberger, P., M. Rothacher, R. Dietrich, M. Fritsche, A. Rülke, and S. Vey (2009b), Reprocessing of a global GPS network, *Journal of Geophysical Research*, 111(B5(B05402)). 113, 114
- Tapley, B., M. Watkins, J. Ries, G. Davis, R. Eanes, S. Poole, H. Rim and B. Schutz, C. Shum, R. Nerem, F. Lerch, J. Marshall, S. Klosko, N. Pavlis, and R. Williamson (1996), The Joint Gravity Model 3, *Journal of Geophysical Research*, 28(101(B12)). 28, 131
- Teunissen, P. J. G., and A. Kleusberg (eds.) (1998a), *GPS for Geodesy*, Springer. 17
- Teunissen, P.J.G., and A. Kleusberg (eds.) (1998b), *GPS for Geodesy*, chapter Quality Control and GPS, Springer-Verlag, Berlin, Heidelberg, New York. 4, 31, 41, 42, 49, 139
- Thaller, D. (2008), Inter-technique combination based on homogeneous normal equation systems including station coordinates, Earth orientation and troposphere parameters, *Scientific Technical Report STR08/15*, Deutsches GeoforschungsZentrum, PhD thesis. 16, 23, 110
- Tregoning, P., and C. Watson (2009), Atmospheric Effects and Spurious Signals in GPS Analyses, *Journal of Geophysical Research*, (B09403). 104

- Tregoning, P., and C. Watson (2011), Correction to Atmospheric Effects and Spurious Signals in GPS Analyses”, *Journal of Geophysical Research*, 116(B02412). 104
- Tregoning, P., P.J. Morgan, and R. Coleman (2004), The effect of receiver firmware upgrades on GPS vertical timeseries, *Cahiers du Centre Européen de Géodynamique et de Séismologie*, 23, 37–46. 14
- van Dam, T.M., and T.A. Herring (1994), Detection of atmospheric pressure loading using Very Long Baseline Interferometry measurements, *Journal of Geophysical Research*, 99(B3), 4505–4517. 34
- van Dam, T.M., J. Wahr, Y. Chao, and E. Leuliette (1997), Predictions of crustal deformation and of geoid and sea-level variability caused by oceanic and atmospheric loading, *Geophysics Journal International*, 129, 507–517. 35
- Watson, C., R. Burgette, P. Tregoning, N. White, J. Hunter, R. Coleman, R. Handsworth, and H. Broksma (2010), Twentieth century constraints on sea level change and earthquake deformation at Macquarie Island, *Geophysics Journal International*, Jun. 2010. 63
- Williams, S.D.P. (2003), Offsets in Global Positioning System time series, *Journal of Geophysical Research*, 108(B6)(2310). 3, 4, 21, 41, 46, 75
- Williams, S.D.P. (2008), CATS: GPS coordinate time series analysis software, *GPS Solutions*, 12, 147–153. 4
- Williams, S.D.P., Y. Bock, P. Fang, P. Jamason, R.M. Nikolaidis, L. Prawirodirdjo, M. Miller, and D.J. Johnson (2004), Error analysis of continuous GPS position time-series, *Journal of Geophysical Research*, 109(B03412). 21, 29, 30, 106, 107
- Willis, P., H. Fagard, P. Ferrage, F.G. Lemoine, C.E. Noll R. Noomen, M. Otten, J.C. Ries, M. Rothacher, L. Soudarin, G. Tavernier, and J.J. Valette (2010), The International DORIS Service, Toward maturity, in DORIS: Scientific Applications in Geodesy and Geodynamics, *Advances in Space Research*, 45(12):1408–1420. 1
- Wöppelmann, C., C. Letetrel, A. Santamaria, M.-N. Bouin, X. Collilieux, Z. Altamini, S.D.P. Williams, and B. Martin Miguez (2009), Rates of sea-level change over the past century in a geocentric reference frame, *Geophysical Research Letters*, 36(L12607). 3
- Wöppelmann, G., B. Martin Miguez, M.-N. Bouin, and Z. Altamimi (2007), Geocentric sea-level trend estimates from GPS analyses at relevant tide gauges world-wide, *Global and Planetary Change*, 57, 396–406, June 2007. 3
- Wübbena, G. (1985), Software Developments for Geodetic Positioning with GPS Using TI 4100 Code and Carrier Measurements, in *Proceedings First International Symposium on Precise Positioning with the Global Positioning System*, edited by Clyde Goad, pp. 403–412, US Department of Commerce, Rockville, Maryland. 27
- Wübbena, G., M. Schmitz, F. Menge, V. Böder, and G. Seeber (2000), Automated Absolute Field Calibration of GPS Antennas, in *Proceedings of the ION GPS-00*, Salt Lake City, Utah. 15

- Wübbena, G., M. Schmitz, G. Boettcher, and C. Schumann (2006), Absolute GNSS antenna calibration with a robot: repeatability of phase variations, calibration of GLONASS and determination of carrier-to-noise pattern, in *International GNSS Service: Analysis Center Workshop, May 08–12, 2006*, edited by T. Springer *et al.*, Darmstadt, Germany, apr 2006. [15](#)
- Yagi, Y., M. Kikuchi, and T. Sagiya (2001), Co-seismic slip, post-seismic slip, and aftershocks associated with two large earthquakes in 1996 in Hyuga-nada, Japan, *Earth Planets Space*, *53*, 793–803. [34](#)
- Yibin, Yao (2006), Earth rotation parameter estimation by GPS observations, *Geo-Spatial Information Science*, *9*, 260–264, 10.1007/BF02826737. [110](#)
- Zhang, J., Y. Bock, H.O. Johnson, P. Fang, S.D.P. Williams, J. Genrich, S. Wdowinski, and J. Behr (1997), Southern California Permanent GPS Geodetic Array: error analysis of daily position estimates and site velocities, *Journal of Geophysical Research*, *102(B8)(2310)*, 18,035–18,055. [21](#), [29](#), [30](#), [106](#)
- Zhu, S.Y., F.-H. Massmann, Y. Yu, and Ch. Reigber (2003), Satellite antenna phase center offsets and scale errors in GPS solutions, *Journal of Geodesy*, *76*, 668–672. [99](#)